LARGE-SCALE PATTERNED OXIDE NANOSTRUCTURES:

FABRICATION, CHARACTERIZATION AND APPLICATIONS

A Dissertation
Presented to
The Academic Faculty

by

Xudong Wang

In Partial Fulfillment
of the Requirements for the Degree
Doctor of Philosophy in the
School of Materials Science and Engineering

Georgia Institute of Technology
December, 2005

LARGE-SCALE PATTERNED OXIDE NANOSTRUCTURES:

FABRICATION, CHARACTERIZATION AND APPLICATIONS

Approved by:

Dr. Zhong Lin Wang, Advisor
School of Materials Science & Engineering
Georgia Institute of Technology

Dr. C. P. Wong
School of Materials Science& Engineering
Georgia Institute of Technology

Dr. Brent Wagner
Georgia Tech Research Institute
Georgia Institute of Technology

Dr. Christopher J. Summers, Co-Advisor
School of Materials Science & Engineering
Georgia Institute of Technology

Dr. Russell D. Dupuis
School of Electrical and Computer
Engineering
Georgia Institute of Technology

Date Approved: Nov. 18, 2005

ACKNOWLEDGEMENTS

First of all, I would like to express my thanks to both of my advisors, Dr. Zhong L. Wang and Dr. Christopher J. Summers, who were always encouraging me, guiding me, giving me chances to try and allowing me to grow. From them, I learned the ways to create ideas, to organize research and to present results, which will greatly benefit me in my future career. I would also like to thank my committee members: Dr. C. P. Wong, Dr. R. D. Dupuis and Dr. Brent Wagner.

During my PhD program, I feel very lucky that I was involved in the research conducted by two excellent groups—Wang's group and Summers' group. Many thanks to my group members who were helping me with my research. Especially, Dr. Y. Ding was always the first people I would seek help from for my TEM work. Dr. Elton Graugnard was very helpful in my ALD and PL work and also enriched my knowledge about vacuum techniques. Additionally, I would like to thank my officemates, namely Daniel Moore, William Hughes, Brent Buchine and Chris Ma, who improved my language skill, brought me the American culture and made me quickly adapt to this new place.

I feel sorry that I couldn't meet my parents for such a long time. But I really appreciate everything that I have taken from them: the optimism, the persistence, and the intelligence, without which I would never achieve success. To this point, I would like to thank the visa official who finally issued them visa to attend my commencement. My Aunt Liza and Uncle Bill are the only relatives I have here. Their love and care warms me and makes me feel strong. Although I am a foreigner, because of them, I have never felt lonely in family holidays.

Most importantly, I am very grateful for my wife, who always stays with me, supports me, and cares me. I would never go this far without her.

TABLE OF CONTENTS

LIST OF TABLES

LIST OF FIGURES

x

LIST OF ABBREVIATIONS

1D	Quasi One Dimensional
2D	Two Dimensional
0D	Zero Dimensional
LED	Light Emitting Diodes
(HR)TEM	(High-Resolution) Transmission Electron Microscope
SWNT	Single-Wall Carbon Nanotube
MWNT	Multi-Wall Carbon Nanotube
SPM	Scanning Probe Microscopy
AFM	Atomic Force Microscopy
FET	Field Effect Transistor
SEM	Scanning Electron Microscope
VS	Vapor-Solid
VLS	Vapor-Liquid-Solid
PL	Photoluminescence
FWHM	Full Width at Half Maximum
EDS	Energy-Dispersive X-ray Spectrum
NSL	Nanosphere Lithography
PS	Polystyrene
SDS	Sodium Dodecyl Sulfate
SSDP	Substrate Surface Dispersing Process
WSDP	Water Surface Dispersing Process
ALD	Atomic Layer Deposition
PMMA	Polymethyl Methacrylate

MOCVD	Metal Organic Chemical Vapor Deposition
XRD	X-Ray Diffraction
PC	Photonic Crystal

SUMMARY

Nanotechnology is experiencing a flourishing development in a variety of fields covering all of the areas from science to engineering and to biology. As an active field in nanotechnology, the work presented in this dissertation is mostly focused on the fundamental study about the fabrication and assembly of functional oxide nanostructures. In particular, *Zinc Oxide*, one of the most important functional semiconducting materials, is the core objective of this research, from the controlled growth of nanoscale building blocks to understanding their properties and to how to organize these building blocks. Thermal evaporation process based on a single-zone tube furnace has been employed for synthesizing a range of 1D nanostructures. By controlling the experimental conditions, different morphologies, such as ultra-small ZnO nanobelts, mesoporous ZnO nanowires and core-shell nanowire were achieved. In order to pattern the nanostructures, a large-scale highly-ordered nanobowl structure based on the self-assembly of submicron spheres was created and utilized as patterning template. The growth and patterning techniques were thereafter integrated for aligning and patterning of ZnO nanowires. The aligning mechanisms and growth conditions were thoroughly studied so as to achieve a systematic control over the morphology, distribution and density. The related electronic and electromechanical properties of the aligned ZnO nanowires were investigated. The feasibility of some potential applications, such as photonic crystals, solar cells and sensor arrays, has also been studied. This research may set a foundation for many industrial applications from controlled synthesis to nanomanufacturing.

CHAPTER 1

INTRODUCTION

During the revolution of the electronic industry over the past half century, the understanding and applications of electronic phenomena and materials have experienced a tremendous advancement. The technology relies on electron operated devices and circuits, such as transistors, capacitors, inductors, interconnects and dielectrics. For the development of microelectronics, Moore's Law predicted that circuit performance doubles every 18 months, and this law has held for more than 30 years. Nowadays, current semiconductor technology can achieve a single transistor with a size below 50 nanometers, almost the size limit for electrical isolation. So, what will be the direction for future technology developments? Generally, minimizing the cost of fabrication and further shrinking device size through another new technology, or concept, are two widely accepted answers. Over the last decade, nanotechnology, as a new concept impacting the fields of physics, chemistry, electronics and optics, has experienced a flourishing development and is believed to be the next generation of technologies in human's history.

In the long history of industrial engineering, microelectronics has been the only technology characterized by length only occurred in microelectronics. Now, nomination of nanotechnology is the second time. Nanotechnology can be defined as the creation and utilization of materials, devices, and systems through the control of matter on the nanometer-scale, which is, at the level of atoms or assembles of atoms, molecules, supermolecular structures, and with at least one characteristic dimension measured in nanometers (1-100 nm).

Phenomena at the nanometer scale expose a completely new world. The properties of matter at the nanoscale are not as predictable as those observed at larger

dimensions. Important changes in behavior are caused not only by the continuous modification of characteristics with diminishing size, but also by the emergence of totally new phenomena such as quantum confinement. For example, the color of light emitting from semiconductor nanoparticles varies with their sizes;[1] the melting temperature of gold nanoparticles drops dramatically when their size is lower than 20nm;[2] nanostructured ceramics and metals have greatly improved mechanical properties, both in ductility and strength.[3] Designed and controlled fabrication and integration of nanomaterials and nanodevices is therefore a revolutionary new science and technology.

Nanotechnology is also promoting the unprecedented understanding of materials and devices and impacts many fields. All natural materials and systems establish their foundation at the nanoscale; therefore controlling matter at the atomic or molecular levels means tailoring fundamental properties, phenomena, and processes exactly at the scale where basic properties are initiated. Nanotechnology could impact the production of virtually every human-made object – from automobiles and electronics to advanced diagnostics, surgery, advanced medicines, and tissue and bone replacements. To build electronic devices at the nanometer scale, for example, it is essential to understand the interaction between atoms and molecules, how to manipulate them, how to keep them stable, how to communicate signals between them, and enface their properties with the real world. This goal requires new knowledge, new tools, and new approaches.

Top-down and bottom-up are two distinct concepts for realizing structures and devices in nanometer scale. Top-down approaches start from bulk materials, which are sculpted into nanosized features by carving, milling, etching and patterning. Lithography methods are typical examples of this approach, and have been dominating technique in microelectronic engineering for fabricating integrated circuits (ICs). Controlled by powerful computers and software, a device dimension, location and organization can be achieved with a very high precise. However, inevitably, the high precision always comes at a high cost, especially when the size is below 100 nanometer. Fortunately, nature has

already provided many good examples in overcoming this challenge: in biological systems, the genetic codes and sequence guide and control the self-assembling process of supermolecules or proteins for forming higher level more complex functional and living structures. This is the bottom-up approach—constructing structures or devices from the basic building blocks, such as atoms, molecules and supermolecular clusters.
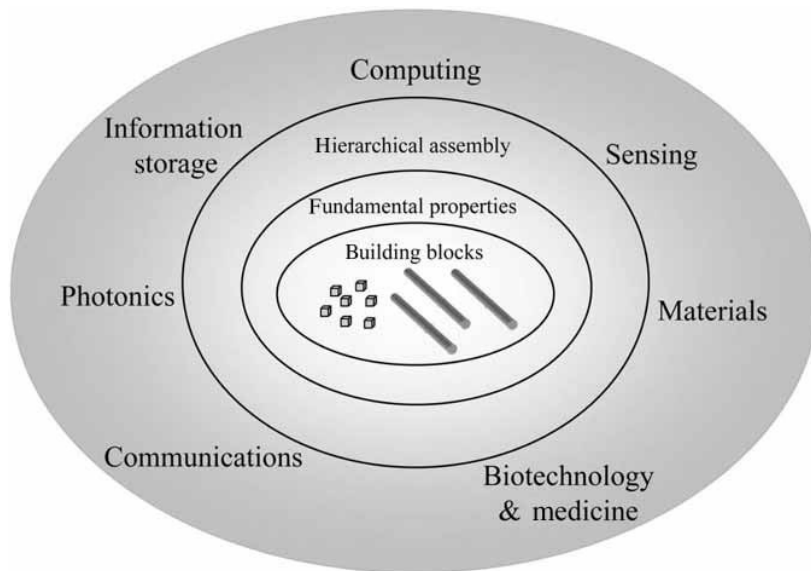
Figure 1.1: Overview of the bottom-up paradigm for nanotechnology.

A roadmap of this bottom-up paradigm has been presented by Lieber,[4] as shown in Figure 1.1. Underpinning this bottom-up paradigm is the controlled growth of nanoscale materials, the fundamental building blocks, pursued within the disciplines of materials science and chemistry. This level has been the most active area in nanotechnology and a large variety of morphologies has been discovered or created. By understanding the physics and chemistry behind the growth, the ultimate goal is to control with atomic precision the morphology, structure, composition, and size of nanoscale materials, so as to enable precise control over the properties of the resulting nanomaterials.

Beyond fabrication, property investigation or characterization of new nanomaterials is another important and fundamental part of the bottom-up paradigm. These studies will expand our understanding of the basic science and new or improved properties related to size, structure and composition. Moreover, knowing the physics of their properties will also enable us to make rational predictions and possibly define new device concepts unique to the nanoscale building blocks.

Finally, in order to fully exploit and utilize those novel properties into a wide range of devices, rational methods must be developed for hierarchical assembly, which involves at least an integration of numerous functional nanomaterials and/or single device element for achieving a complex, preprogrammed action. This includes patterned materials growth on a designed substrate; large-scale, parallel integration of nanowires, nanoparticles, and functional groups; interconnection among the components; and defect-tolerated path design following neuron networks. To today, the major challenge is the simultaneous, parallel fabrication of large arrays of nanodevices under precisely controlled conditions and repeatability. A possible solution is to integrate top-down and bottom-up approaches, such as generating large-scale patterns through a lithography technique and controlling the local configuration by a self-assembly process.

This dissertation will be focused on ZnO, one of the most important functional semiconducting oxides, covering from the controlled growth of nanoscale building blocks to understanding their properties and how to organize these building blocks. The main text of this dissertation is organized into seven chapters: The next chapter (Chapter 2) gives a general review on one-dimensional (1D) nanostructures, including their definitions and classifications, the major fabrication methods and mechanisms, and their properties and current applications. Chapter 3 details the experimental equipment and procedures employed in this work. Chapter 4 presents three new morphologies of 1D nanostructure, including ultra-small ZnO nanobelts, mesoporous ZnO nanowires and core-shell nanobelt. A newly-developed self-assembly technique is presented in Chapter

5, in which the large-scale highly-ordered nanobowl structure is created based on submicron spheres monolayer self-assembly technique and is utilized as a platform for nanostructure patterning. The growth and patterning techniques are integrated in Chapter 6 for aligning and patterning of ZnO nanowires. The aligning mechanisms, techniques, the related property investigation and potential applications are introduced and discussed in details. The future work and conclusion is given in the final two chapters (Chapter 7 and 8), respectively.

CHAPTER 2

ONE-DIMENSIONAL NANOSTRUCTURES

Nanomaterials and systems can be rationally designed to exhibit many novel and unique physical, chemical, and biological phenomena because of their small size. Depending on dimensionalities, nanomaterials can be classified as two-dimensional thin/nano layers, one-dimensional nanowires and zero-dimensional quantum dots.

Extensive research has been conducted on two-dimensional (2D) nanostructures owing to the well-developed thin-film deposition technique, such as molecular beam epitaxy (MBE).[5] The quantum well laser is a successful example of a commercialized 2D nanostructure device.[6] In the past two decades, zero-dimension (0D) quantum dots have experienced rapid development due to their ultra-small size induced quantum confinement effects, which impacts density of states.[7] Various chemical methods have been developed for making quantum dots from a wide range of materials with well-controlled morphologies. Novel quantum devices, such as quantum dot lasers,[8] single electron transistors[9] and light emitting diodes (LEDs)[10] have been realized and intensively studied.

Since the discovery of carbon nanotubes, quasi-one-dimensional (1D) nanostructures have become an important focus of research in nanoscience and nanotechnology. Their 1D structure enables unique quantum effects that directly impact the electronic and optical properties. Therefore, they are showing great potential both in understanding size-dependent electrical, optical, thermal and mechanical properties and in fabricating nanosized electrical junctions, optoelectronic and electromechanical devices.[11]

2.1 Definition and Classification of 1D Nanostructures

According to their morphologies, 1D nanostructures are generally defined and classified into three main categories: *nanotube, nanowire* and *nanobelt*. In this section, the definitions, representative structures and the related characters of these three types of 1D nanostructures will be introduced.

2.1.1 Nanotube

A nanotube is a tubular 1D nanostructure whose diameter is within nano-regime (<100nm), while the length could be as long as a few centimeters. As one of the first discovered 1D nanostructures, the carbon nanotube is the most intensively studied nanotube structure in the areas of syntheses, property characterization, and applications.

In the early 1990s, Iijima found a needle-like structure that was ~4-30 nm in width and ~1 μm in length from the cathode-discharged by-products of graphite rods.
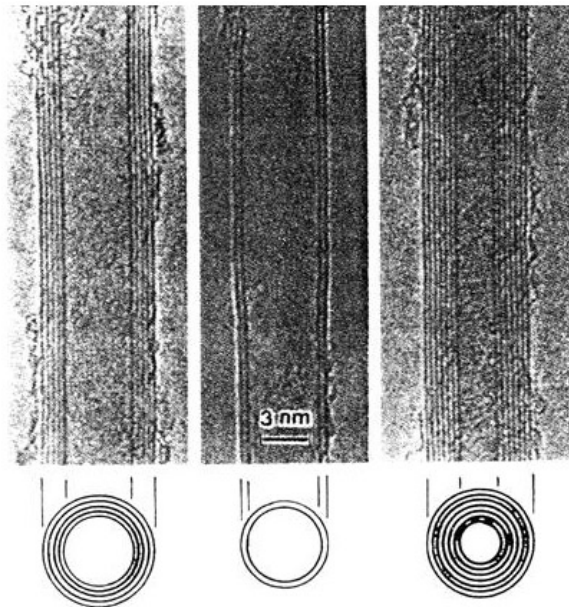
Figure 2.1: TEM image of carbon nanotubes with different diameters and graphite layers.

High resolution transmission electron microscopy (HRTEM) revealed that this structure was composed by coaxial rolls of graphite sheets, where the distance between each roll was identical to the lattice constant along the *c*-axis of graphite, which is ~0.34 nm, as shown in Figure 2.1. Thus, this structure was named *Carbon Nanotube*[12]. Subsequent research discovered that carbon nanotubes could be either semiconducting or metallic depending on their diameter and the rolling direction of the graphite sheet. Owing to their unique structure and properties, carbon nanotubes have attracted intensive research interests.
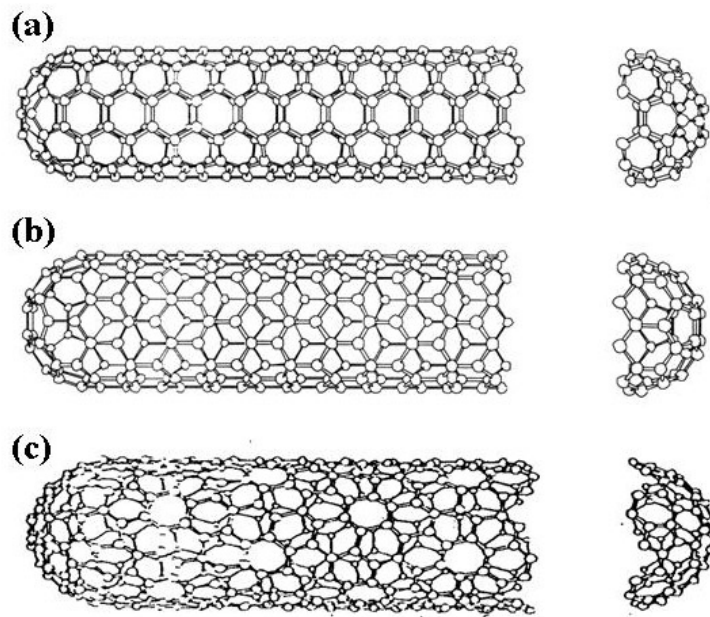
Figure 2.2: Schematic structure of carbon nanotubes. (a) armchair structure; (b) zigzag structure; (c) helical structure.

As shown in Figure 2.2, HRTEM studies revealed that each layer of a carbon nanotube is a seamless cylinder formed by "rolling up" a graphite sheet composed of a hexagonal network of carbon atoms. According to the rolling direction of the graphite sheet, each cylinder can be categorized into non-helical and helical structures.

In the non-helical structure, the chain of carbon atom hexagons is either parallel or perpendicular to the axis of the carbon nanotube. Consequently, the carbon nanotube is

called an *armchair* structure when it has a parallel configuration; while the perpendicular configuration is called a *zigzag* structure. Figure 2.2 shows the single wall carbon nanotubes with different structures. Both ends of nanotubes are treated as a half of a C_{60} molecule (bucky ball). Once the caps of a carbon nanotube are formed by cutting a C_{60} molecular normal to its five-fold axis, an armchair carbon nanotube is constructed, as shown in Figure 2.2a. On the other hand, a zigzag structure is resulted from the caps formed by cutting a C_{60} molecular normal to its three-fold axis, as shown in Figure 2.2b.[13] Both armchair and zigzag are non-helical structures, which exhibit a high symmetry and non-*achiral* property.[14]

However, in most carbon nanotube structures, their carbon hexagon chains and axis are not perfectly aligned as in the non-helical structure. There is always an angle between the axis and carbon hexagon chains.[15] Carbon nanotubes with such a configuration are called helical structure, as shown in Figure 2.2c. Due to the lower symmetry of this structure, helical carbon nanotube exhibits an *achiral* property.

Based on the structure property, the single-shell conformation of a carbon nanotube can be precisely defined by the diameter d_t and the rolling angle θ (due to the symmetry of the carbon hexagon, the angle θ is always less than 30º). Although the valid combination of d_t and θ could be infinite, when the boundary condition is considered, a carbon nanotube can only be formed with a limited number of d_t and θ value sets. Therefore, indexing a carbon nanotube by d_t and θ has been utilized as a simply and clear method to describe its structure.[16]

As illustrated in the schematic two-dimensional graphite sheet shown in Figure 2.3a, the chiral vector is defined by:

$$\vec{C}_h = n\vec{a}_1 + m\vec{a}_2 \tag{2.1}$$

where $\vec{a}_1$ and $\vec{a}_2$ are unit vectors, n and m are integers. θ is defined by the angle between the reference axis $\overrightarrow{OZ}$ and the helical vector $\overrightarrow{OA}$. When $\theta = 30º$, the carbon nanotube has
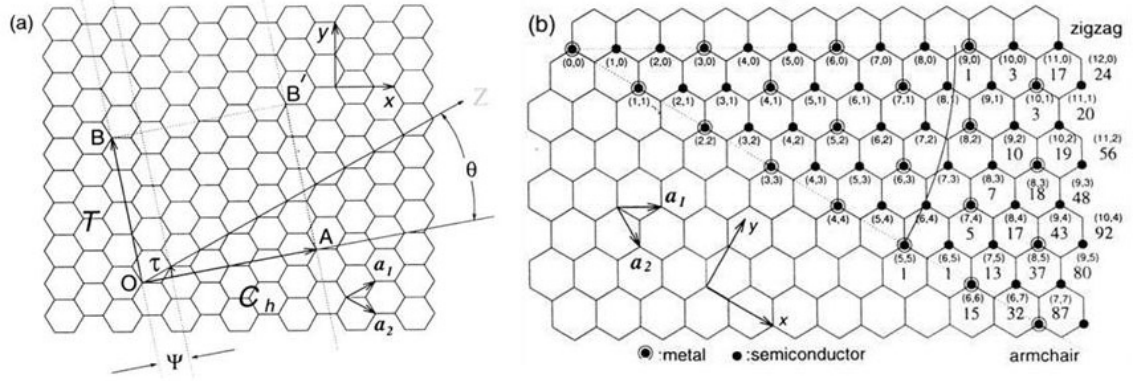
Figure 2.3: Schematic of a graphite sheet showing different rolling directions to form carbon nanotubes.

an armchair structure; while a zigzag structure is formed when $\theta = 0°$. Single-wall carbon nanotube rolled along any other arbitrary angle can be defined by the chiral vector with a certain set of (n, m) value, as shown in Figure 2.3b.[17] In the situation that $0° < \theta < 30°$, each combination of (n, m) represent a different rolling condition, which exclusively includes all of the possible rolls due to the symmetric graphite structure. In this way, the armchair and zigzag structures can be written as (n, n) and $(n, 0)$, respectively. The chiral or helical carbon nanotubes are expressed when m has a non-zero value and is not equal to n.

The diameter d_t and rolling angle θ of a carbon nanotube can also be written in terms of n and m, as illustrated in equation 2.2 and 2.3:

$$d_t = C_h/\pi = \sqrt{3}a_{c-c}\left(n^2 + nm + m^2\right)^{\frac{1}{2}}/\pi \tag{2.2}$$

$$\theta = tg^{-1}\left[\sqrt{3}m/(m + 2n)\right] \tag{2.3}$$

where $C_h = \left|\vec{C}_h\right|$ and a_{c-c} is the distance between two closest carbon atoms (~0.1421 nm). It is clear that larger n, m value defines a carbon nanotube with larger diameter.

Discussed above are the carbon nanotubes with only one layer: so-called single-wall carbon nanotubes (SWNTs). In reality, many carbon nanotubes are composed of

multiple graphite cylinders that are sheathed one by one coaxially. These are named multi-wall carbon nanotubes (MWNTs). The number of the layers can vary from two to tens, while the spacing between each layer is kept at 0.34 nm. Correspondingly, the diameter of multi-wall carbon nanotubes ranges from a few nanometers to ~100 nanometers, while the length could be as long as several centimeters[18]. Due to the increased stability and durability of MWNTs relative to SWNTs, the more robust MWNTs are expected to have greater potential for applications exploiting the exceptional mechanical strength and stiffness and the very high thermal conductivity of carbon nanotubes.[19]

Theoretical calculation has shown that the electronic properties of SWNTs are very sensitive to structure.[20] Depending on the chiral indices (n, m), carbon nanotubes can serve as metals or semiconductors with various energy gaps. The armchair (n, n) SWNTs are always metals. For the case where $n \neq m$, but $n - m = 3j$, where j is a nonzero integer, the SWNTs are narrow-bandgap semiconductors, which behave like metals at room temperature. SWNTs are large-bandgap semiconductors only when $n - m = 3j \pm 1$. The energy gap value also relies on the diameter of the carbon nanotube, d_t, where the bandgap decreases with increasing diameter. For example, a (7, 1) SWNT would be metallic at room temperature, whereas an (8, 0) SWNT would be semiconducting.

As a consequence of their exceptional electronic properties and unique structures, carbon nanotubes are extremely promising building blocks for novel nano-devices, such as field effect transistors (FETs), sensors, field emitting sources, diodes, fuel cells. Some prototypes have already been realized in the laboratory. However, for the commercialization of carbon nanotube electronic devices, it is essential to have a source of low-cost, single-phase material, preferably with the same (n, m) indices. Although progress has been made both in improving the synthesis to create more uniform carbon nanotubes, and the separation techniques for separating the metallic from semiconducting

carbon nanotubes[21], challenges still exist in acquiring large quantity of carbon nanotubes with a reasonably high purity.

2.1.2 Nanowires

Although carbon nanotubes are very promising for electronic devices due to their tunable electric properties, challenges still exist. From the current fabrication techniques, mono-structured carbon nanotubes, e.g. carbon nanotubes with the same rolling direction and diameter, are still impossible to be achieved in a large quantity, which severely limits the application and commercialization of carbon nanotubes in electronic devices. Recently, nanowires have become the focus of intensive research for applications in mesoscopic physics and nano devices fabrication.[22] Unlike carbon nanotubes, the structure of nanowires can be well controlled by the synthesis conditions. Thus, uniform properties can be achieved in crystal structure, chemical composition, growth direction and even length and diameter.

The *nanowire* is a terminology represents any wire-like structure that has a diameter less then 100 nanometers. The composition can be single crystal, poly-crystal, amorphous or organic chains. Single crystalline nanowires are the most intensively studied structure owing to their unique electronic, optical, mechanical and magnetic properties.[4, 23] A single-crystal nanowire grows along a specific axial direction, whereas their side surfaces may or may not be well-defined. The cross-section of a nanowire can be round, hexagonal or polyhedron according to the crystallography of the material. The length of a nanowire varies from a few hundred nanometers to microns or even millimeters; however, its thickness is always negligibly small comparing to its length. Sometimes, the terminology *nanorod* is also applied to describe a short nanowire with lengths ranging from tens to hundreds of nanometers.

The essence of nanowire formation is crystallization, a process that has been investigated for hundreds of years. The evolution of a solid from a vapor, liquid or solid phase involves two fundamental steps: nucleation and growth. As the concentration of the building blocks (atoms, ions or molecules) becomes sufficiently high, they aggregate into small clusters through either homogeneous or heterogeneous nucleation. With a continuous supply of the building blocks, these nuclei serve as seeds for further growth to form a long-range-ordered, crystalline lattice. In addition, the building blocks also need to be supplied at a well-controlled rate in order to obtain crystals with a homogeneous composition and uniform morphology.

Nanowire structures are ideal systems for studying transport processes of one-dimensionally confined objects and related fundamental phenomena, but also for
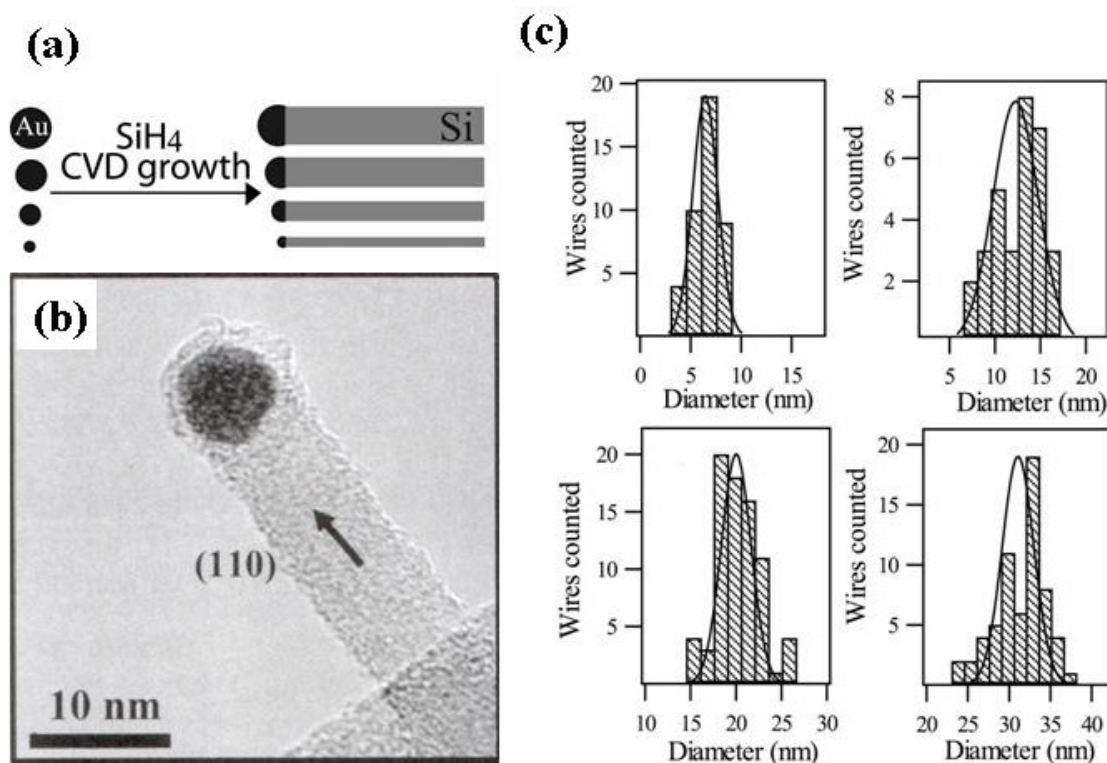
Figure 2.4: (a) Schematic of the size control. (b) TEM image of a silicon nanowire catalyzed by a gold nanoparticle with identical size. (c) Size distribution of the as-synthesized silicon nanowires catalyzed by gold nanoparticles with sizes of 5, 10, 20 and 30 nm, respectively.

developing new generation nanodevices with high performance. Therefore, size control is fundamental for other property investigations.

Catalyst confined growth has been demonstrated as a successful example to precisely control the diameter of nanowires. As illustrated in Figure 2.4a, the diameter of a silicon nanowire can be confined by the gold nanoparticles during the growth. By using mono-distributed gold colloidal as catalyst, Cui et al experimentally proved this concept through a chemical vapor deposition process using SiH_4 as a precursor.[24] The transmission electron microscope (TEM) image shows that the as-synthesized silicon nanowire exhibited an almost identical width as the gold nanoparticle on its tip (Figure 2.4b). The size relationship was established by varying the gold nanoparticles' diameters: 5(4.9±1.0), 10(9.7±1.5), 20(19.8±2.0), and 30(30.0±3.0). Statistic of data acquired by TEM measurements revealed that the corresponding widths of the nanowires were 6.4±1.2, 12.3±2.5, 20±2.3, and 31.7±2.7, as shown in Figure 2.4c.

So far, the smallest size that can be achieved by this method is ~1 nm. However, since silicon is easily oxidized, silicon nanowires are always covered by a 1-3 nm thick amorphous silica layer. From Figure 4.2b, a thin layer of silica can be clearly observed around the nanowire and catalyst tip. Although theoretical calculations demonstrated that silicon nanowires would exhibit strong quantum confinement for diameters smaller than 5 nm[25], the presence of the insulating silica shell has limited the further investigations on size-induced quantum effects. Therefore, it is essential to achieve a stable and defect-free silicon surface for silicon nanowires.

Also using gold nanoparticles as a catalyst, Ma et al recently made single-crystal silicon nanowire with a diameter of only 1.3 nm from SiO powder and H_2 under 1200ºC.[26] The oxide shell on the as-synthesized nanowires surface was removed by HF, which also introduced H atoms onto the silicon surface preventing further oxidation.[27] Thus, stable silicon nanowires were achieved. A high-resolution scanning tunneling
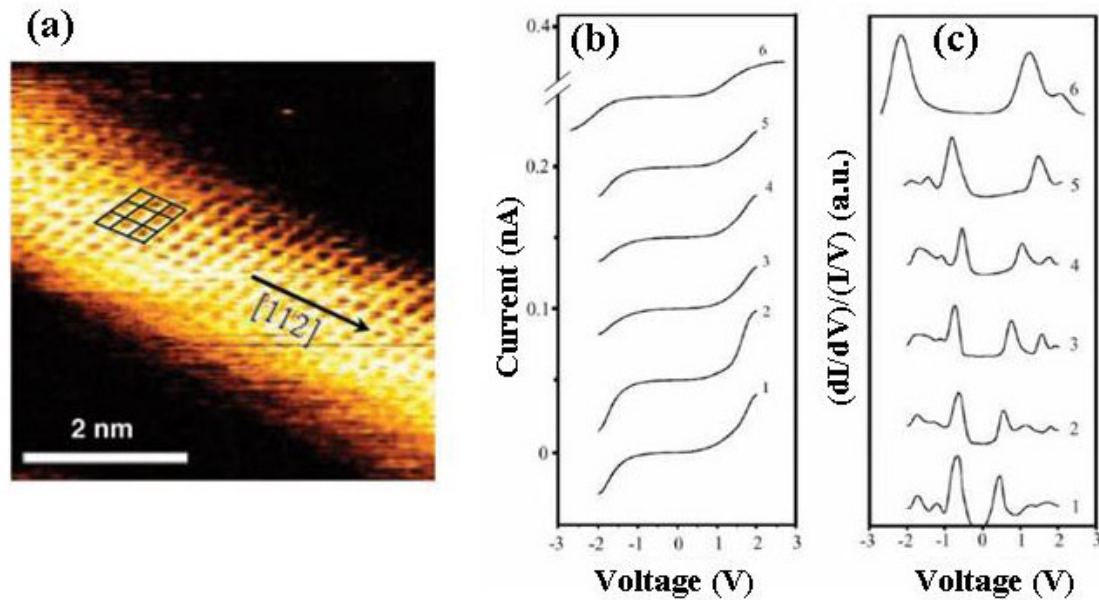
Figure 2.5: (a) High-resolution STM image of a 2-nm-wide Si nanowire. (b) I-V curves obtained by STS on six Si nanowires; the diameters of wires 1 to 6 are 7, 5, 3, 2.5, 2, and 1.3 nm, respectively. (c) The corresponding normalized tunneling conductances.

microscope (STM) image of a stabilized silicon nanowire is shown in Figure 2.5, where the crystalline surface can be clearly distinguished and its growth direction is shown to be along the [112] direction. The quantized energy gap was determined by the scanning tunneling spectra (STS). Figure 2.5b shows the I-V curves of six silicon nanowires with diameters of 7, 5, 3, 2.5, 2, and 1.3 nm respectively. Figure 2.5c shows the corresponding *(dI/dV)/(I/V)* curves, which are proportional to the state density of electrons. With the decreasing diameter, the distance between two main peaks increases, representing the increasing of the energy bandgap. Therefore, stabilized silicon nanowires provided an ideal specimen for investigating quantum effects in 1D nanostructures.

2.1.3 Nanobelts

Since the first discovery by Pan et al in 2001, nanobelts, also sometimes called nano-ribbons, have attracted more and more interests due to their unique morphology and
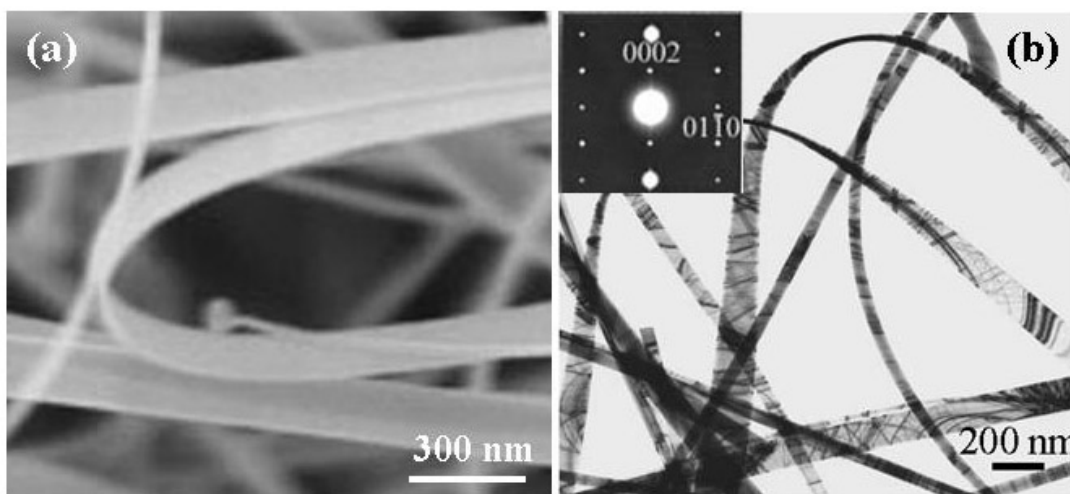
Figure 2.6: Typical SEM (a) and TEM (b) images of ZnO nanobelt. Inset is the diffraction pattern recorded on a single nanobelt showing the growth direction and side surfaces.

shape-induced physical, electronic and optical properties. The nanobelt represents a quasi-one-dimensional nanostructure that not only has a specific growth direction but also its top/bottom surfaces and side surfaces exhibit well-defined crystallographic facets (Figure 2.6). For example, a typical ZnO nanobelt[28] has a growth direction along [0001], the top/bottom surfaces are $\pm(2\bar{1}\bar{1}0)$ and the side surfaces are $\pm(01\bar{1}0)$, as shown in the insert of Figure 4.1b. The as-synthesized metal oxide nanobelts exhibit a rectangular-like cross-section and are single crystalline and structurally uniform. Nanobelts are nanowires that have well-defined structure. This is an important characteristic because the properties of nanobelts are strongly shape and structure dependent, especially when their sizes approach a few nanometers.

Nanobelts represent a unique group of nanostructures from semiconducting oxides to II-VI and III-V compounds and to structural ceramics. Starting from ZnO nanobelts, this family of nanobelts is a flourishing and new area of focus in nanoscience and nanotechnology. Based on their composition, nanobelts can be classified into three categories.

Binary oxide nanobelts: The belt morphology was firstly discovered in semiconducting oxides. Table 2.1 summarizes the nanobelt structures of function oxides discovered so far, including ZnO[28], SnO_2[29], Ga_2O_3[30], In_2O_3[31], CdO[28], PbO_2[32], MoO_3[33], MgO[34], CuO[35], and Al_2O_3[36]. Although these materials belong to different crystallographic families, they have a common faceted nanobelt structure. Each type of nanobelt is defined by its crystallographic structure, a unique growth direction, and specific top/bottom surfaces and side surfaces. Some of the materials can grow along different crystal directions, which can be controlled by choosing specific experimental conditions.

Table 2.1: Crystallographic geometry of functional oxide nanobelts

Nanobelt	Crystal structure	Growth Direction	Top Surface	Side surface
ZnO	Wurtzite	[0001], [01$\bar{1}$0] or [2$\bar{1}$$\bar{1}$0]	{2$\bar{1}$$\bar{1}$0} or {0001}	{01$\bar{1}$0}, {0001} or {2$\bar{1}$$\bar{1}$0}
Ga_2O_3	Monoclinic	[001] or [010]	{100} or {100}	{010} or {10$\bar{1}$}
t-SnO_2	Rutile	[101]	{10$\bar{1}$}	{010}
o-SnO_2	Orthorhombic	[010]	{100}	{001}
In_2O_3	C-Rare earth	[001]	{100}	{010}
CdO	NaCl	[001]	{100}	{010}
PbO_2	Rutile	[010]	{201}	{10$\bar{1}$}
MoO_3	Orthorhombic	[001]	{010}	{100}
MgO	Face Center Cubic	[100]	{001}	{010}
CuO	monoclinic	[10$\bar{1}$]	{110}	{001}
Al_2O_3	Hexagonal	[0001]	{01$\bar{1}$0}	{11$\bar{2}$0}

Table 2.2: Crystallographic geometry of functional non-oxide nanobelts

Nanobelt	Crystal structure	Growth Direction	Top Surface	Side surface
ZnS	Wurtzite	[01$\bar{1}$0]	{11$\bar{2}$0}	{0001}
CdSe	Wurtzite	[01$\bar{1}$0]	{11$\bar{2}$0}	{0001}
GaN	Wurtzite	[10$\bar{1}$0]	{01$\bar{1}$0}	{0001}
GaP	Zinc blende	[111]	{100}	{0$\bar{1}$1}
AlN	Wurtzite	[0001]	{11$\bar{2}$0}	{01$\bar{1}$0}

Compound semiconductor nanobelts: More and more functional non-oxide nanobelts have also been synthesized by various approaches. They are mostly II-VI or III-V compounds that have shown interesting physical or chemical properties in bulk or other nano-morphologies. The structures are summarized in Table 2.2. ZnS[37] and CdSe[38] nanobelts, II-VI compounds with the wurtzite crystal structure, have been recently synthesized. Analogous to ZnO nanobelts, these nanobelts exhibit polarized side surfaces that induce anisotropic growth, forming a one-side structure with teeth, a so-called "nanosaw".[39] Some other important III-V semiconducting materials, such as GaN[40], GaP[41], and AlN[42] have also been reported to exhibit belt-like morphology. These nanobelts are single crystal and have specified growth directions and side facets.

Multi-element nanobelts: Because of high stoichiometry requirements, the formation of multi-element nanobelts is restricted by the evaporation method, the traditional pathway to grow a nanobelt. However, through some chemical routes, a limited number of three-component nanobelts can be synthesized in solution. For example, bismuth oxide bromide[43] and $BaCrO_4$[44] nanobelts have been prepared through a hydrothermal route and a reverse micelles directed synthesis, respectively. Another type of nanobelt was achieved by doping. By using a nanobelt as a template and doping with another element resulted in a new type of nanostructure. Mn doped ZnO nanobelts have been fabricated by ion implanting Mn^{2+} into as-synthesized ZnO nanobelts, which have very interesting applications in spintronics[45]. Nitrogen doped GaP nanobelts have been achieved by growing GaP nanobelts in a NH_3 atmosphere[41] and showed interesting optical properties.

Off all these structures, the ZnO nanobelt is the most intensively studied. Novel morphologies and properties have been discovered by controlling the geometry and crystallography. Although ZnO crystal can be either Wurtzite or Zinc Blend, ZnO nanobelts are always hexagonal Wurtzite. The $\{0001\}$, $\{01\bar{1}0\}$ and $\{2\bar{1}\bar{1}0\}$ are the three

Figure 2.7: Schematic of typical types of ZnO nanobelts with different growth directions and side surfaces.

surface groups with the lowest energy, which comprise the "out" surfaces of any ZnO nanobelts. Figure 2.7 shows three different types of ZnO nanobelts geometries constructed from different crystal surfaces. These structures can be achieved by controlling the growth rate of different crystal surfaces during deposition. The configuration shown in Figure 2.7a is the most commonly discovered nanobelt structure, while the other two shown in Figure 2.7b and c are normally induced by the presence of defects. It is important to notice that the {0001} are polar surfaces. Therefore, for the configuration shown in Figure 2.7c, the majority of the nanobelt surface is polarized, thus it's called polar-nanobelt. Due to the polarization, this nanobelt can be treated as a planar capacitor. The dipole moment between the two parallel polar surfaces induces coiling of the nanobelt during the growth and new-morphologies, such as nano-helix[46] and nano-rings[47] are thus formed.

2.2 Growth Mechanisms of 1D Nanostructures

As mentioned previously, the essence of forming 1D nanostructures is crystallization from vapor, liquid or solid phases. The most adaptable growth of 1D nanostructure is still believed to be from the vapor phase because the transportation and concentration control of the building blocks are relatively easy. Two primary growth mechanisms of the nucleation and growth from vapor source are widely accepted amongst the one-dimensional nanostructure synthesis community: the vapor-solid (VS) process and the vapor-liquid-solid (VLS) process. Both will be described in detail in the following sections.

2.2.1 Vapor-Solid Process

Although the exact mechanism responsible for 1D growth directly from the vapor phase is still not fully understood, this approach has been explored by many research groups to synthesize 1D nanostructures from a variety of materials. As early as 1950s, it was reported that acicular structured oxides of metals such as Cu, Cr, Fe, Pb, Ti, W, and Zn could be produced on the external surfaces of the corresponding metals when they were heated in air at certain temperatures.[48] Frank's dislocation growth mechanism[49] had been believed for the growth of crystal whiskers, in which a screw dislocation with its Burgers' vector parallel to the growth direction provides self-perpetuating growth steps on the tip so that the tip is an efficient sink for adsorbing atoms. However, no one has been able to observe the proposed screw dislocation in the final product. Now it is generally accepted that the control of supersaturation is a prime consideration in obtaining 1D nanostructures.[23]

The VS process is believed to be a kinetics driven anisotropic crystallization process. From experimentally and theoretically studies on the kinetics of nanowire

growth,[50, 51] The 2D nucleation probability (P_N) on the surface of a nanowire was established to be

$$P_N = B\exp(-\frac{\pi\sigma^2}{k^2 T^2 \ln\alpha})$$ (2.4)

where B is a constant; σ is the surface energy of the solid nanowire; k is the Boltzmann constant; T is absolute temperature; α is the supersaturation ratio determined by $\alpha=p/p_0$ (p is the actual vapor pressure and p_0 is the equilibrium vapor pressure corresponding to T). According to Equation 2.4, the lower the surface energy, the larger the 2D nucleation probability. On the other hand, an atom adsorbed on a low-energy surface has a low binding energy and a high probability of desorption. Competition and coordination of these two effects are responsible for the formation of the low-index crystal planes enclosing the 1D nanostructures. The temperature and the supersaturation ratio are two parameters controlled by experimental conditions. Higher temperature and larger supersaturation ratios facilitate 2D nucleation, resulting in the formation of films. As for

Figure 2.8: (a-e) A proposed growth mechanism for ZnO nanobelts through a VS process. (f, g) The growth front and end of a ZnO nanobelt showing no trace of catalyst.

the nucleation and growth of wire-like structures, lower temperature and smaller supersaturation ratios are preferred. Therefore, in VS growth process, temperature and supersaturation ratio are the two dominant factors controlling the morphology of deposited products.

Therefore, the VS growth can be considered as starting from "self-catalytic" initiation. When there is no catalyst used in the synthesis, the formation of 1D nanostructures is normally dominated by the VS process, such as the growth of oxide nanobelts structures[28]. A possible mechanism has been proposed on VS growth of ZnO nanobelts[52], as illustrated in Figure 2.8. After vaporization at high temperature, the ZnO molecules condensed onto the substrate placed on the lower temperature region (Figure 2.8a) and the cation-anion will be arranged in such a way that a proper cation-anion coordination is preserved to balance the local charge and structural symmetry forming a small nucleus (Figure 2.8b). Newly arriving molecules will continue to deposit on the formed nucleus while the local vapor supersaturation is remained. Due to the high mobility of the molecules at the deposition temperature (~800ºC), the molecules accumulated onto the rough growth front or edges, resulting in an expanded surface area (Figure 2.8c). The rough structure of the tip leads to a rapid accumulation of incoming molecules, resulting in the fast formation of a nanobelt (figure 2.8d) and after some time a long nanobelt is formed (Figure 2.8e). Figure 2.8f and g show tips of ZnO nanobelts, in which the growth fronts are a rounded, indicating their atomic-scale roughness with the presence of steps, ledges, and kinks, where the molecules are most likely to stay resulting in an anisotropic 1D growth.

2.2.2 Vapor-Liquid-Solid Process

Since the nucleation and growth are only controlled by the temperature and supersaturation ratio, it is hard to achieve precise control over the growth. Improved

control can be realized by introducing a metal catalyst to guide the precipitation such that now growth is typically through a VLS process. Compared to VS process, the mechanism of VLS process is much better understood.

Figure 2.9: Schematic steps of the growth of a nanowire via VLS process.

The VLS process was originally discovered by Wagner et al to produce silicon whiskers in 1964,[53] and later adapted to one-dimensional nanostructure growth by Lieber, Yang, and many other research groups.[54, 55] Figure 2.9 demonstrates the major steps of a VSL process using gold catalyst for growing ZnO nanowires. With the existence of ZnO vapor, the solid gold nanoparticles (Figure 2.9a) form liquid alloy droplets once the deposition temperature rises above the eutectic temperature of Au and ZnO (Figure 2.9b). The incoming ZnO vapor causes the percentage of the ZnO component in the droplet to increase and ultimately supersaturates. ZnO is precipitated out at the solid-liquid interface (Figure 2.9c), and growth continues until the source vapor is cut off or the temperature drops below its eutectic point (Figure 2.9d).

This mechanism has been confirmed by in-situ TEM observations of Ge nanorod growth in a TEM chamber equipped with a temperature-controllable stage, where GeI_2 and Au was used as the vapor source and catalyst, respectively.[56] Figure 2.10 shows a

Figure 2.10: A series of TEM images showing the growth of a Ge nanowire from a gold nanoparticle. (a) gold catalyst; (b-c) formation of Ge-Au alloy; (d-e) starting of precipitation; (f) grown Ge nanowire.

series of TEM images sequentially recorded during the growth of a Ge nanorod. These images clearly show the VLS steps including formation of the alloy (Figure 2.10a-c), precipitation (Figure 2.10d), and nanowire growth (Figure 2.10e-f). Therefore, in the VLS process, the 1D growth is induced and dictated by the liquid alloy droplets, which serve as the source reservoir during the growth and restrict the lateral growth of the nanowires.

For VLS growth, it is very important to select the right metal catalyst. As a major requirement, there should exist a good solvent capable of forming a liquid alloy with the source material, and ideally they should be able to form eutectic compounds. In addition, the catalyst should be chemically stable with respect to the source material and oxygen as there is always the inclusion of trace amounts of O_2 in the reaction systems. Consequently, gold, as a noble catalyst, is the first choice for catalyzing a VLS growth of various materials.[24, 57]

There are several benefits in applying the VLS process for 1D nanostructure growth. The first is dimensionality control. It has been demonstrated that the diameter of the catalyst directly affects the cross-section of the resulting 1D nanostructures.[24, 58] In

24

addition to size control, the VLS affords the capability of site-specific growth. The catalysts act as preferential nucleation sites, allowing for patterned or arrays of nanostructures to be synthesized.[57] Moreover, VLS provides the ability to synthesize aligned nanostructures, once a single crystal substrate is carefully chosen based on their lattice parameters. This has already been demonstrated for ZnO nanowires and a sapphire substrate.[55] One of the challenges faced by the VLS process is the limitation in forming 1D nanostructures with complex components, because the simpler phases always tend to be precipitated from the alloy when the alloy is formed by multiple elements. For example, it seems impossible to fabricate three- or four-element piezoelectric or superconducting 1D nanostructures, such as PZT, through a VLS process.

2.3 Properties and Potential Applications

Compared with bulk materials, 1D nanostructures exhibit distinct mechanic, electronic, optical, chemical and physical properties owing to their large surface-to-volume ratio and possible quantum-confinement effects. For instance, ceramic nanobelts showed great flexibility compared to bulk material[28]; quantized conductance has been observed on SWNTs[59]; and the light-emitting[55] and field-emission[60] efficiency was greatly enhanced by the wire-like morphologies. It is obvious that 1D nanostructures with well-controlled dimensions, composition, and crystallinity represent a new class of material system for investigating structure related properties and applications. In this section, the property investigation and the related applications will be reviewed in the fields of mechanics, electronics, optoelectronics and optics.

2.3.1 Mechanical Properties and Nano Balance

Characterizing the mechanical properties of individual 1D nanostructure is a challenge to most existing testing and measuring techniques because of the following constrains. First, the size (diameter and length) is small, prohibiting the applications of the well-established testing techniques. Tensile and creep testing require that the size of the sample be sufficiently large to be clamped rigidly by the sample holder without sliding. This is impossible for 1D nanomaterials using conventional means. Secondly, the small size of the nanostructure makes their manipulation rather difficult, and specialized techniques are needed for picking up and installing individual nanostructures. Therefore, new methods and methodologies must be developed to quantify the properties of individual nanostructure.

Due to the extremely small size that cumbers the manipulation of nanostructures, property measurement using a microscope is required. A modern TEM is a powerful tool that can not only provide a real space resolution better than 0.2 nm, but also give quantitative chemical and electronic analysis from a region as small as 1 nm. Integrating the structural information of a nanostructure provided by TEM with the properties measured in-situ from the same nanostructure[61] provides an ideal technique for

Figure 2.11: A transmission electron microscope and a schematic diagram of a specimen holder for in-situ measurements.

understanding the property-structure relationship. This is a powerful technique that can simultaneously provide the properties and structure of an individual nanomaterial.

To perform property measurements on a 1D nanostructure, a TEM compatible specimen holder was built for applying a voltage across a 1D nanostructure and its counter electrode (Figure 2.11).[62] In the specimen loading area, an electromechanical system was built that allows the lateral movement of the tip, while applying a voltage across the 1D nanostructure with the counter electrode. With this system, both the static and dynamic properties of the 1D nanostructures can be obtained by applying controllable static and alternating electric fields. Also, the microstructure of the measured object can be fully characterized by electron imaging, diffraction and chemical analysis techniques.

Figure 2.12: TEM image showing one-dimensional nanostructures at the end of the electrode and the other counter electrode. A constant or alternating voltage can be applied to the two electrodes to induce electrostatic deflection or mechanical resonance.

The 1D nanostructure was directly imaged under TEM (Figure 2.12), and electron diffraction patterns and images can be recorded from the 1D nanostructure to reveal both the surface and the intrinsic structure of the 1D nanostructure. This is a unique advantage over the SPM techniques.

Figure 2.13: Nanotube response to resonant alternating applied potentials. (a) In the absence of a potential; (b) Resonant excitation of the fundamental mode of vibration ($v_1 = 530$ kHz); (c) Resonant excitation of the second harmonic ($v_2 = 3.01$ MHz).

The first measurements were carried out for multiwalled carbon nanotubes.[63] Because of the sharp needle shape of a carbon nanotube, it can be easily charged by an externally applied voltage; the induced charge is distributed mostly at the tip of the carbon nanotube and the electrostatic force results in the deflection of the nanotube. Alternatively, for an alternating voltage, the charge on the tip of the nanotube is oscillated and consequently the electric force. If the applied frequency matches the natural resonance frequency of the nanotube, mechanical resonance is induced. By tuning the applied frequency, the first and the second harmonic resonances were observed (Figure 2.13), and the frequencies were accurately measured. Resonance is nanotube selective because the natural vibration frequency depends on the tube diameter (D), the length (L), the density (ρ), and the bending modulus (E_b) of the nanotube:

$$v_i = \frac{\beta_i^2 D}{8\pi L^2} \sqrt{\frac{E_b}{\rho}}$$

(2.5)

where β = 1.875 and 4.694 for the first and the second harmonics. In the above formation, the nanotube is assumed to be solid and the inner radius of the tube is ignored and the bending modulus of carbon nanotubes has been measured as a function of its diameter. The bending modulus is as high as 1.2 TPa (as strong as diamond) for nanotubes with diameters smaller than 8 nm, and as low as 0.2 TPa for tubes with diameters larger than 30 nm. A decrease in bending modulus as the tube diameter increases is a result of the rippling effect of the nanotube.

Figure 2.14: (a) Schematic geometry shape of a nanobelt. A selected ZnO nanobelt at stationary (b), the first harmonic resonance in x direction, v_{x1} = 622 kHz (c), and the first-harmonic resonance in y direction, v_{y1} = 691 kHz (d). (e) An enlarged image of the nanobelt and its electron diffraction pattern (inset). (f) A resonance peak measured from another ZnO nanobelt. The resonance occurs at 230.9 kHz.

This method has also been extended to other 1D nanostructures such as ZnO nanobelts. Due to the mirror symmetry and its rectangular cross-section of ZnO nanobelts (Figure 2.14a), there are two distinct fundamental resonance frequencies corresponding to vibration in the thickness and width directions. From the classical elasticity theory for a rectangular beam, the fundamental resonance frequency corresponding to the thickness direction (x-axis) is

$$v_x = \frac{\beta_i^2 T}{4\pi L^2}\sqrt{\frac{E_x}{3\rho}} \qquad (2.6)$$

Where β_i is a constant for the ith harmonic: $\beta_1=1.875$ and $\beta_2=4.694$; E_x is the bending modulus for the vibration along x-axis, ρ, L, W, and T is the density, length, width and thickness of the nanobelt respectively. The corresponding resonance frequency along the width direction (y-axis) is given by:

$$v_y = \frac{\beta_i^2 W}{4\pi L^2}\sqrt{\frac{E_y}{3\rho}} \qquad (2.7)$$
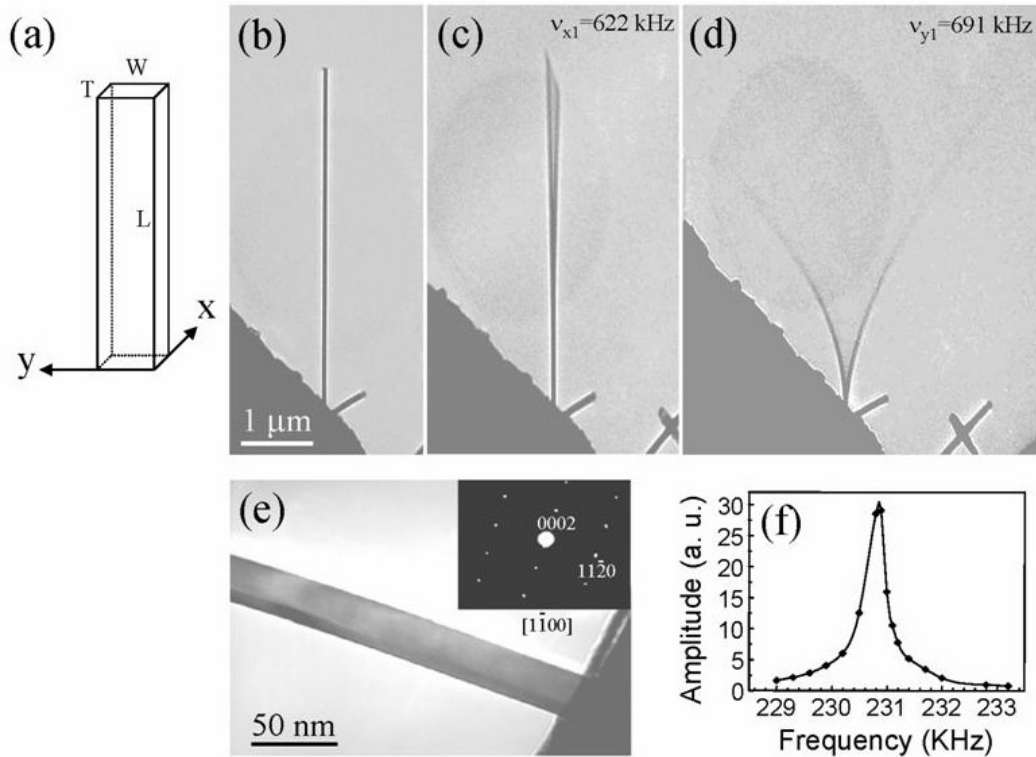
These two modes are decoupled and can be observed separately in experiments. By changing the frequency of the applied voltage, two fundamental frequencies in orthogonal directions transverse to the nanobelt were found.[64] Figures 2.14c and d show the harmonic resonance with the vibration planes nearly perpendicular and parallel to the viewing direction, respectively. When calculating the bending modulus, it is critical to accurately measure the fundamental resonance frequency (v_1) and the size (L and T or W) of the investigated ZnO nanobelts. To determine v_1, one end of nanobelt was tightly fixed, and the resonant excitation was carefully checked around the half value of the resonance frequency to ensure it is the fundamental frequency

The geometrical parameters are key for accurate derivation of the mechanical property from the measured resonance frequencies. Thus, specimen holder was rotated about its axis so that the nanobelt is aligned perpendicular to the electron beam, thus, the

real length (L) of the nanobelt can be obtained. The normal direction of the wide facet of the nanobelt was determined by the electron diffraction pattern, $[2\bar{1}\bar{1}0]$ for the ZnO. Then the nanobelt was tilted from its normal direction by rotating the specimen holder, and the tilting direction and angle determined from the corresponding electron diffraction pattern. As shown in the inset of Figure 2.14e, the electron beam direction is $[1\bar{1}00]$. The angle between $[1\bar{1}00]$ and $[2\bar{1}\bar{1}0]$ is 30°, i.e. the normal direction of the wide facet of the nanobelt is 30° tilted from the direction of the electron beam. Using the projected dimension measured from the TEM image (Figure 2.14e), the geometrical parameters were determined to be $W = 28$ nm and $T = 19$ nm. Based on the experimentally measured data, the bending modulus of the ZnO nanobelts was calculated from Equation 2.6 and 2.7 to be ~ 52 GPa. This value for the modulus cannot be directly compared to Young's modulus of ZnO ($c_{33} = 210$ GPa, $c_{13} = 104$ GPa)[65], because the shape of the nanobelt and the anisotropic structure of ZnO are convoluted in the measurement. The bending modulus measured by the resonance technique, however, is in excellent agreement with the elastic modulus measured by nanoindentation for the same type of nanobelts.[66]
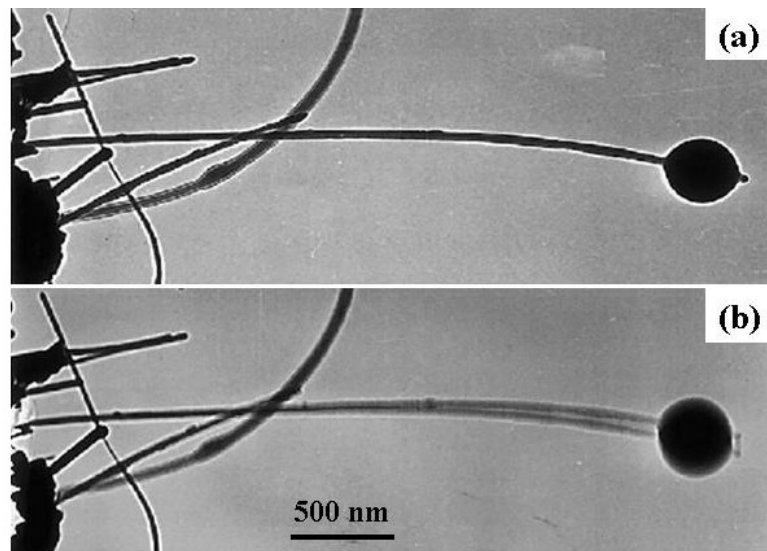
Figure 2.15: A small particle attached at the end of a carbon nanotube at (a) stationary and (b) first harmonic resonance ($v = 0{:}968$ MHz).

The methods introduced above are also well suited to measure masses in the picogram-to-femtogram mass range, as demonstrated in Figure 2.15, which shows the resonance of a carbon particle that is attached to the end of a nanotube. Analogous to a spring balance, where the mass of a particle attached at the end of the spring can be determined if the vibration frequency is measured (provided the spring constant is calibrated), a very small mass attached to the tip of the nanowire can be determined by measuring the change in resonance frequency. More than ~40% drop was observed in the resonance frequency as a result of adding a small mass to the tip. The mass of this particle was found to be M = 22±6 fg (1fg = 10^{-15}g), which is near that calculated from the measured geometry, assuming bulk amorphous carbon density—that is, M ≈ 30 fg. This nanobalance is the most sensitive and smallest balance in the world, and potentially can have applications in measuring the mass of large biomolecules and biomedical particles, such as virus.

2.3.2 Electronic Properties and Nano Sensors

The Field Effect Transistor (FET) is one of the most important building blocks for modern microelectronic devices. They are so named because a weak electrical signal applied to gate electrode amplifies an electrical field from source to drain electrodes. This field flips from positive to negative when the incoming signal does, and controls a second current traveling through the rest of the transistor. Nowadays, however, by traditional thin-film/lithography, it's becoming harder and harder to achieve the increase transistors' density at the rate predicted by Moore's law. As a result, new types of transistors, such as novel nanostructures based FETs, are attracting great research interests. As for 1D nanomaterials, their large surface to volume ratio and their function as quasi-one dimensional conductive elements simultaneously confer upon them high sensitivity and size-dependent transduction of the chemical processes occurring at their surface into

functional electrical signals.[11] As a result, the FET is one of the most frequently fabricated devices using 1D nanostructures in order to realize their potential for applications in sensing, switching, and even logic circuit.[67]

2.3.2.1 1D Nanomaterials Based FETs

The oxide nanobelt is a structurally perfect and geometrically uniform 1D nanostructure showing confined side surfaces and a rectangular cross section. By forming metal electrode/nanobelt electrical contacts and capacitively coupling the nanostructure to a nearby gate electrode, FETs were produced based on ZnO and SnO$_2$ nanobelts for the exploration of new physical and chemical properties.[68]
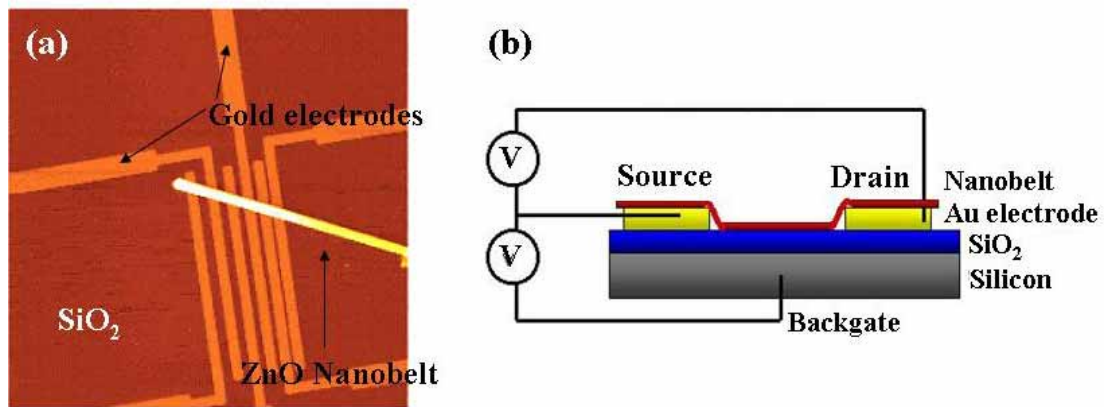
Figure 2.16: (a) AFM image of a FET built using a single ZnO nanobelt on gold electrodes; (b) a schematic diagram of the FET device.

SnO$_2$ FETs were fabricated by depositing SnO$_2$ nanobelt dispersions onto SiO$_2$ / Si (p+) substrates, followed by treatment in an oxygen atmosphere at 800 ºC for 2 h. The SiO$_2$/Si substrates were then spin-coated with PMMA, baked, exposed to electron-beam lithography for the definition of electrode arrays, and developed. A 30-nm-thick layer of titanium was deposited by electron-beam evaporation to serve as the source and drain electrodes, and the remaining PMMA was lifted off in hot acetone. An alternative way of

contacting the nanostructures was to deposit dispersed ZnO nanobelts on predefined gold electrode arrays. In both cases, the SiO_2 gate dielectric thickness was 120 nm and the back gate electrode was fabricated by evaporation of gold on the Si (p+) side of the substrate. The electrode gaps between source and drain were varied from 100 nm to 6 μm. Figure 2.16a shows a FET fabricated using a single ZnO nanobelt to the design principle given in Figure 2.16b.
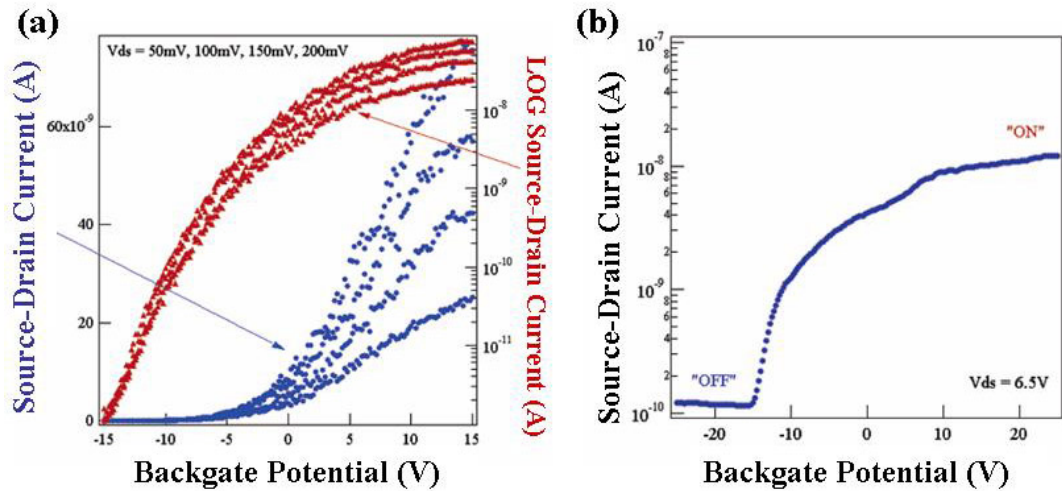
Figure 2.17: (a) Source-drain current versus gate bias for a SnO_2 FET in ambient; (b) Source-drain current vs gate bias for a ZnO FET in ambient.

A typical SnO_2 FET pretreated in a 1atm oxygen atmosphere at 800 ºC demonstrated a gate-threshold voltage of -2.5 V, a current switching ratio I(ON)/I(OFF) of nearly 10000, and (ignoring voltage drops at the Ti contacts) a peak conductivity of 8.14 $(\Omega \cdot cm)^{-1}$, as shown in Figure 2.17a. Measured conductivities ranged from 4 to 15 $(\Omega \cdot cm)^{-1}$. The typical leakage conductance between electrodes under ambient conditions was measured to be between 20 and 80 pS and was gate-bias independent. In most cases, the switching ratios of the FETs were limited by this background conductivity. From an analysis of the transconductance, dI_d/dV_g, for gate biases above the threshold bias, the electron mobility of an n-type field effect transistor can be estimated if the geometry of the device is known. Without subtracting voltage drops at the contacts, from analysis of

Figure 2.17a the electron mobility in the SnO_2 nanobelt was estimated to be ~35 cm^2/Vs. Other measured SnO_2 nanobelt FETs exhibited electron mobility ranging from 10 to 125 cm^2/Vs.

A typical ZnO FET showed a gate threshold voltage of -15 V, a switching ratio of nearly 100, and a peak conductivity of 1.25×10-3 $(\Omega \cdot cm)^{-1}$, as shown in Figure 2.17b. A completely analogous behavior has also been observed for carbon nanotubes deposited on top of Au electrodes or covered by Ti electrodes.[69]

As one of the best-studied 1D nanostructures, Si nanowires can be prepared as single-crystal structures with diameters as small as 2-3 nm and have been shown, for both *p*-type and *n*-type materials, to exhibit performance characteristics comparable to or better than the best achieved in the microelectronics industry.[70]
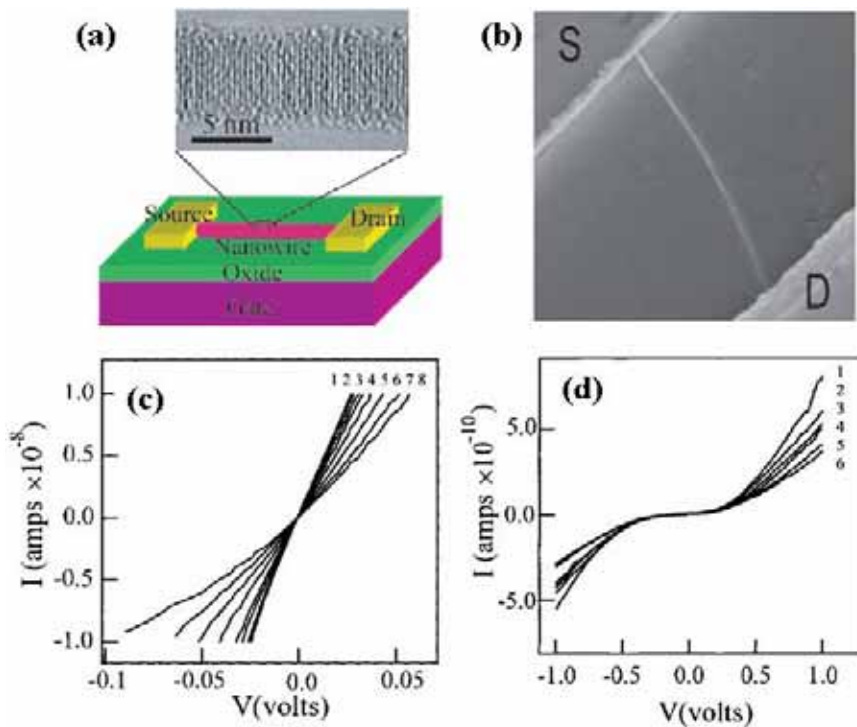
Figure 2.18: (a) Schematic of a Si nanowire FET; (b) SEM image of the FET; (c) I-V data recorded on a 150 nm wide B-doped Si nanowire; curves 1-8 correspond to V_g = -20, -10, -5, 0, 5, 10, 15, and 20 V, respectively; (d) *I-V* data recorded on a 60 nm wide P-doped Si nanowire, curves 1-6 correspond to V_g = 20, 5, 1, 0, -20, and -30 V, respectively.

As shown in Figure 2.18a, the Si nanowire FET had a similar configuration as that

of the nanobelt FET.[71] In the measurements, the gate electrode was used to vary the

electrostatic potential of the Si nanowire while measuring the current versus voltage of

the nanowire. The change in conductance of the Si nanowire as a function of gate voltage

can be used to distinguish whether it is *p*-type (boron doped) or *n*-type (phosphorus

doped) since the conductance will be of opposite sign for increasing positive (negative)

gate voltages. Typical gate-dependent current versus bias voltage (*I-V*) curves recorded

on p-type and n-type Si nanowires are shown in Figure 2.18c and d, respectively. For a *p*-

type Si nanowire, when V_g was made increasingly negative (positive), the conductance

increases (decreases). The V_g dependence of an *n*-type SiNW was opposite of that

observed for the *p*-type SiNWs. The *I-V* curve recorded on the *n*-type nanowire was also

nonlinear, which indicates non-ideal contact between the electrodes and nanowire.
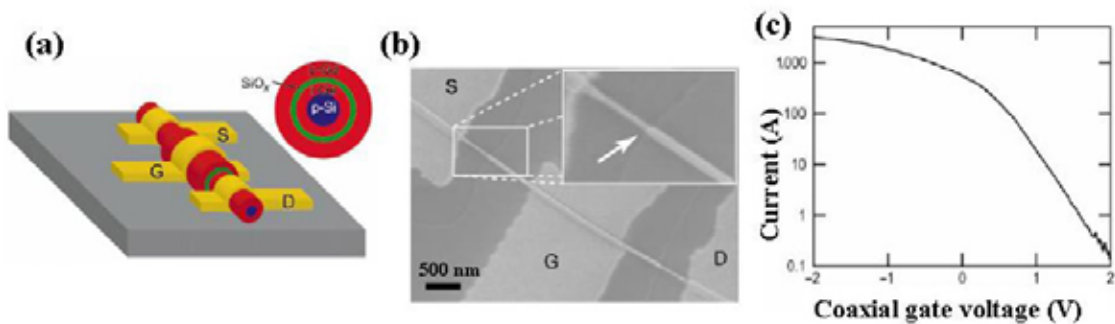
Figure 2.19: (a) Schematic of a coaxially-gated nanowire FET; (b) SEM image of a coaxial
transistor; (c) Gate response of the coaxial transistor at $V_{SD} = 1V$, showing a maximum
transconductance of 1500 nAV^{-1}.

Semiconductor heterostructures with modulated composition and/or doping

enable passivation of interfaces and the generation of devices with diverse functions.

Recently, low-temperature hetero-epitaxial growth has been achieved on crystalline

germanium–silicon and silicon–germanium core–shell/multi-shell structures, in which

band-offsets drive hole injection into either germanium core or shell regions. Using the

core-multi-shell nanowires, a coaxially gated nanowire FET was fabricated.[72] As show in Figure 2.19a, the core-shell nanowire started with a *p*-doped Si core (blue, 10 nm) with subsequent layers of *i*-Ge (red, 10 nm), SiO_x (green, 4 nm), and *p*-Ge (5 nm). Source and drain electrodes were deposited after etching the Ge and SiO_x layers to expose the core layers. The gate electrodes were defined in a second step without any etching before contact deposition (Figure 2.19b). Thus, the source (S) and drain (D) electrodes are contacted to the inner *i*-Ge core, while the gate electrode (G) is in contact with the outer *p*-Ge shell and electrically isolated from the core by the SiO_x layer (Figure 2.19a).

The coaxial geometry offers advantages for nano-FETs, such as a capacitance enhancement compared to standard planar gates used in nanowire and nanotube FETs, and might be best compared to double-gated structures being investigated for advanced planar devices.[73] The nanowire building blocks used to fabricate coaxial FETs consisted of a core–multi-shell structure: *p*-Si/*i*-Ge/SiO_x/*p*-Ge, where the active channel is the *i*-Ge shell. The source, drain and gate contacts were made by selective etching and metal deposition onto the inner *i*-Ge shell and outer *p*-Ge shell, respectively. Significantly, transport measurements made on these initial devices show very good performance characteristics (Figure 2.19c) with transconductance values up to 1,500 nAV^{-1} for a 1-V source–drain bias. The values for the coaxial nanowire FET thus probably represent a lower limit to what may be achieved. For example, minimizing SiO_x trap states, which can compensate the applied gate voltage, reducing the gate dielectric thickness, and/or substituting high-K dielectrics should lead to improvements in transistor performance.

2.3.2.2 FET Sensors

The dependence of the conductance on gate voltage makes FETs natural candidates for electrically based sensing since the electric field resulting from binding of a charged species to the gate dielectric is analogous to applying a voltage using a gate electrode. This idea for sensing with FETs was introduced several decades ago[74],

although the limited sensitivity of these planar devices has precluded them from having a large impact. Using semiconducting 1D nanostructures as FET elements can overcome the sensitivity limitations of previous planar FET sensors since binding to the surface of a nanowire leads to depletion or accumulation of carriers in the 'bulk' of the nanometer-diameter structure (versus only the surface region of a planar device) thereby greatly increasing the sensitivity to the point that single-molecule detection might become possible.

Nanobelts of semiconducting oxide, with a rectangular cross section in a ribbon-like morphology, are very promising for sensors due to the fact that the surface to volume ratio is very high, the oxide is single crystalline, the faces exposed to the gaseous environment are always the same and the small size is likely to produce a complete depletion of carriers inside the belt.[75] In the sensors based on single crystalline nanobelts, almost all of the adsorbed species are active in producing a surface depletion layer. Free carriers should cross the belts bulk along the axis in a FET channel-like way. Beside,
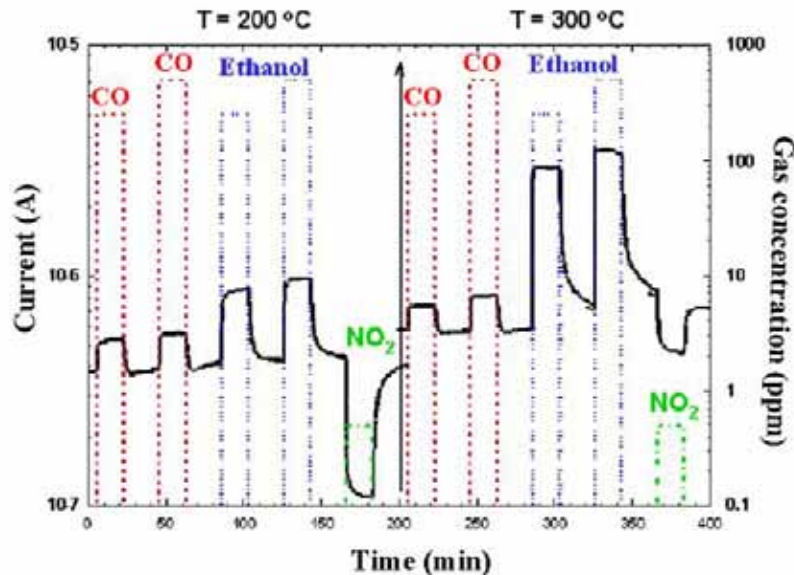
Figure 2.20: Response of the conductance through SnO_2 nanobelts FET to the concentration of the surface adsorbed CO, ethanol and NO2 gases at two different temperatures.

38

since the size of the depletion layer for tin oxide, due to oxygen desorption, penetrates 50 nm or more through the bulk, the belts are probably almost depleted of carriers as a pinched-off FET because of belt thickness is typically less than 50 nm. The presence of poisoning species should switch the structures from pinched-off to conductive channel, strongly modifying the electrical properties.

Figures 2.20 reports the isothermal response of the current flowing through the tin oxide nanobelts[75] at a operating temperature of 400°C and 30%RH (relative humidity at 20°C), as two square concentration pulses of CO (250 and 500 ppm, respectively) are fed into the test chamber. The electric current increases by ~60% and 100% with the introduction of 200 and 500 ppm CO. The sensor response, defined as the relative variation in conductance due to the introduction of gas, is about $\Delta G/G = 0.9$. Figure 2.20 also shows the isothermal response of the current flowing through the nanobelts as a square concentration pulse of 0.5 ppm nitrogen dioxide is fed into the test chamber for similar conditions. The sensor response is $\Delta G/G = -15.5 = -1550\%$, which is extremely high and sensitive. This means that the sensitivity of the sensor is at the level of a few ppb.

Biological macromolecules, such as proteins and nucleic acids, are typically charged in aqueous solution and, as such, can also be detected readily by FETs based on semiconducting nanowires. A general sensing device can be configured from the high performance, nanowire FETs, as illustrated in Figure 2.21a, where specific sensing is achieved by linking a recognition group to the surface of the nanowire.

An example of detecting proteins in solution was carried out by using p-type Si nanowire devices in which the molecule biotin, which binds with high selectivity to the protein streptavidin, was linked to the oxide surface of the nanowires.[76] When solutions of streptavidin protein are delivered to nanowire sensor devices modified with biotin receptors, we find that the conductance increases rapidly to a constant value, and that this conductance value is maintained after the addition of pure buffer solution, as shown in
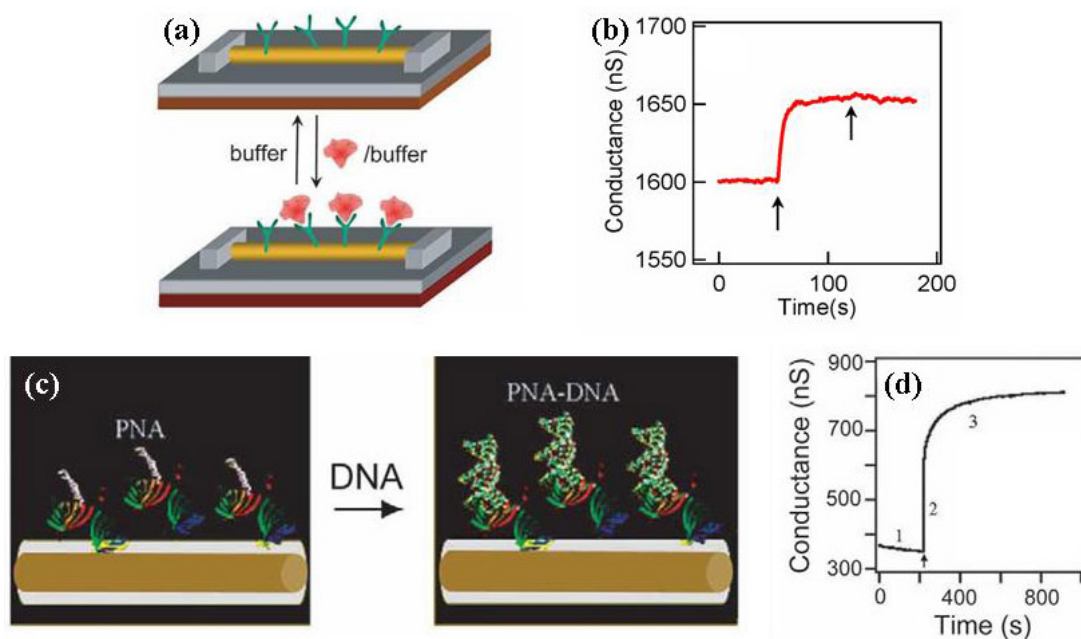
Figure 2.21: (a) Schematic of a SiNW FET configured as a bio-sensor with antibody receptors before and after target proteins; (b) Plot of conductance versus time for a biotin-modified SiNW FET showing the response to streptavidin; (c) Schematic of a PNA modified SiNW FET before and after duplex formation with target DNA. (d) SiNW FET DNA sensing where the arrow corresponds to the addition of DNA sample.

Figure 2.21b. These results are consistent with the net negative charge on streptavidin at the pH of these experiments (i.e. causing accumulation of carriers in *p*-type material) and the very small dissociation rate of the streptavidin-biotin system, respectively.

More recently, Si nanowire FETs have been investigated as sensors for the detection of single-stranded DNA[77], where the binding of this negatively charged polyanionic macromolecule to *p*-type nanowire surfaces leads to an increase in conductance. Recognition of the DNA target molecules was carried out with a complementary sequence of single-stranded material, such as peptide nucleic acids (PNAs), as illustrated in Figure 2.21c. Studies of *p*-type Si nanowire devices modified with a PNA receptor designed to recognize wild type versus the DF508 mutation site in the cystic fibrosis transmembrane receptor gene show that the conductance increases following addition of a 60 fM wild-type DNA sample solution, as shown in Figure 2.21d.

The increase in conductance for the *p*-type Si nanowire device is consistent with an increase in the negative surface charge density associated with the binding of negatively charged DNA at the surface. The sequence specificity in these experiments is a critical first step toward the development of the nanowire devices for genetic-based disease detection.

In general, 1D nanomaterials' large surface-to-volume ratio, ultra-thin channel and high structural uniformity provided the FETs with enhanced electron-transporting properties. As a result, although the 1D-nanostructure-based FETs are still prototype devices, they already show reliable and unique applications in solid state sensor system. They are readily integrated into miniaturized systems, and, moreover, recognizing the fact that 1D nanostructure FETs transfer chemical/biological binding events into electronic/digital signals suggests the potential for a highly sophisticated interface between nanoelectronic and biological information processing systems in the future.

2.3.3 Optical Properties and Nano Lasers

It is well known that quantum confinement plays an important roll in define the energy levels in 0D nanomaterials (quantum dots).[78] This principle is also applicable to 1D nanostructures once their diameter is below the Bohr radius (normally ~6 nm). For instance, Korgel et al found that the absorption edge of Si nanowires was significantly blue shifted comparing to bulk silicon with an indirect bandgap of ~1.1eV. A ~120meV blue shift was also observed on ZnO nanobelts less than 6nm wide with respect to 200nm-wide ZnO nanobelts.[79] In addition to quantum confinement, the 1D morphology naturally acts as a waveguide with a dimension less than the wavelength of light. Due to the large interface between the low-refractive-index air and the high-refractive-index crystal, most of the light waves can be confined inside the crystal body and a large output can only be detected at both ends.[80] The combination of light generation and specific

axially guiding properties enabled semiconducting nanowires to be a Fabry-Perot cavity and lasing phenomena have been discovered on ZnO[55], GaN[81] and CdS[82] nanowires once the excitation energy was higher than their thresholds.

As discussed previously, ZnO is one of the most intensively studied and widely utilized optoelectronic materials owing to its wide energy bandgap (3.37 eV) and large exciton banding energy (60 meV). As a result, ZnO 1D nanomaterials are a very promising optoelectronic material for future nano-photonic devices. Photoluminescence (PL) spectra can provide useful information on light emitting properties as well as the electronic characteristics, such as bandgap structure, carried dynamics and defects effects. Room-temperature PL of ZnO 1D nanostructures normally exhibits two distinct peaks: a narrow band-edge emission peak at 385 nm and a broad defect emission peak at 510 nm, as shown in Figure 2.22a. The near-UV PL arises from free- and donor bound exciton recombination, while the green defect PL is believed to be caused by paramagnetic oxygen vacancies[83] and/or Zn interstitials.
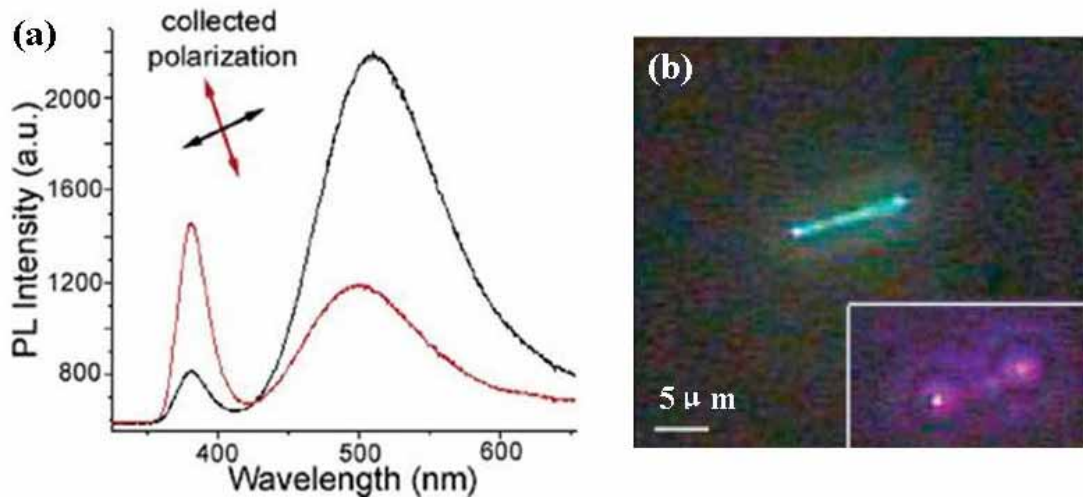
Figure 2.22: (a) PL spectra of a ZnO nanowire excited with unpolarized 325 nm light. The emission was collected with a polarizer aligned either along the major axis (black curve) or perpendicular to it (red curve). (b) Far filed PL image of the nanowire. Inset shows a stimulated emission image of the waveguided band edge emission under pulsed excitation.

Strong polarization of the PL has also been observed on a single ZnO nanowire.[84] Figure 2.22a shows two PL spectra recorded along and perpendicular to the axis of a ZnO nanowire supported by sapphire substrate. The corresponding luminescence image is shown in Figure 2.22b. Both of the spectra and the image present the UV emission is more likely guided along the axis, while green emission is preferred along the normal direction. It can be concluded that the variations in polarization for band edge and defect emission result from different dipole orientations. As the case for UV luminescence shown in the inset of Figure 2.22b, the observation of strong emission at both ends indicates that the wave was strongly guided along the wire axis due to coupling to guided cavity modes. Alternatively, since the PL efficiency coupling to axially guided modes varies inversely with the wavelength of light, a strong axial radiation can be observed at longer wavelengths, as shown in Figure 2.22b.
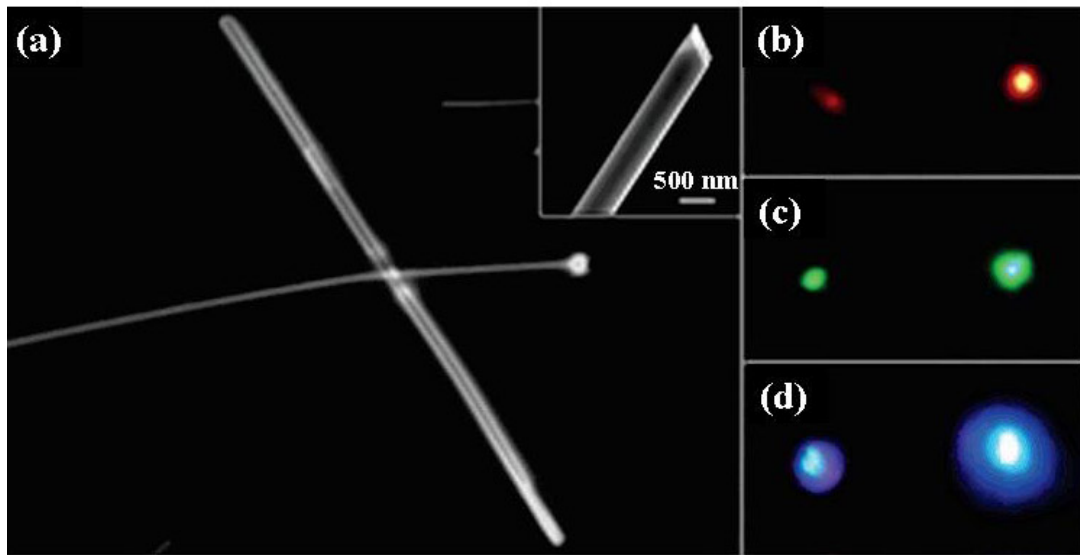
Figure 2.23: (a) Dark-field/PL image of the light exiting end of a SnO_2 nanobelt waveguide supported by a larger belt. Inset: An angled SEM image showing the rectangular cross-section of one of the ends of the nanobelt. (b-d) True color images of monochromatic 652, 532, and 442 nm light waveguiding through the nanobelt.

As introduced previously, of all the 1D nanostructures, nanobelts have the best defined crystal structure and morphology. Their flat surface can almost act as a perfect mirror that reflects lights down the axis. Recently, SnO_2 nanobelts have been revealed to be an excellent subwavelength waveguides of UV and visible light.[80] Non-resonant waveguiding in a single nanobelt has been achieved by focusing laser diodes on one end of the nanobelt. Figure 2.23 shows a 425 μm long nanobelt with a wide (~1 mm) belt across one of the ends. The rectangular cross section of the nanobelt was 520 nm wide and 275 nm thick, shown in the inset of Figure 2.23. Monochromatic red, green, and blue light were injected into the left end of the long nanobelt and emitted at another end on the right, as shown in Figure 2.23b-d, respectively. The images reveal that the shorter wavelengths were better confined and guided than the longer wavelengths. Here, the nanobelt can be treated as a cylindrical waveguide surrounded by air. The calculated cutoff diameters for higher order optical modes are approximately 270, 220, and 180 nm for 652, 532, and 442 nm light. These approximations are in reasonable agreement with the sizes of the nanobelt, even though substrate-induced losses and other effects were
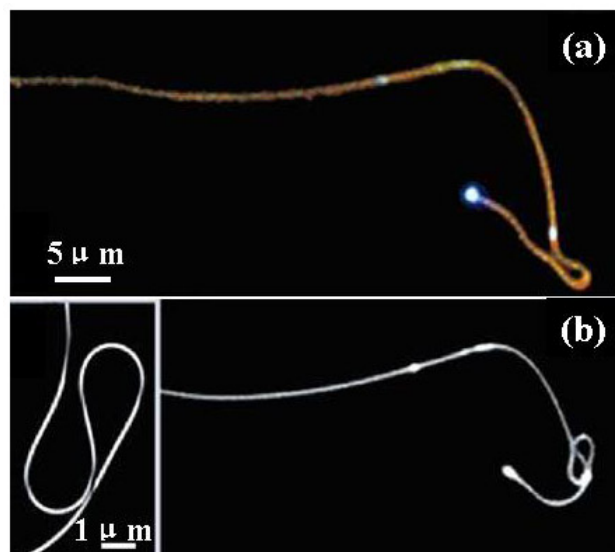
Figure 2.24: True color dark-field/PL image of a nanobelt waveguide showing a sharp curvature; (b) Dark-field/PL image after fashioning two tight loops; inset is a SEM resolving an S-turn of the nanobelt waveguide.

44

ignored. The actual losses of nanobelt waveguides were also measured to be ~10 db/cm for wavelengths between 400 and 550 nm. Even with these reported losses, however, nanobelt waveguides are able to guide light over hundreds of microns, which is adequate for most applications.

Moreover, nanobelt structures are of sufficient length and strength to be manipulated on surfaces to form various waveguide assemblies. Once the nanobelts were placed on the substrate, Van der Waals force between the substrate and nanobelt should prevent elastic recoil of the structure. For example, a high-aspect ratio nanobelt (dimensions: 275 nm by 150 nm by 785 μm) was bent into a tight U shape (Figure 2.24a) with a radius of curvature ~1μm to illustrate the high flexibility of these structures. Additionally two tight loops and a tight S turn were made as shown in Figure 2.24b and the inset. The sharp bend induced minimal losses and no measurable decrease in the output of the waveguide was observed. In general, twists and bends with radii of 1 μm do not disrupt the optical confinement and the ability of these structures to route light across hundreds of micrometers (Figure 2.24a and b).
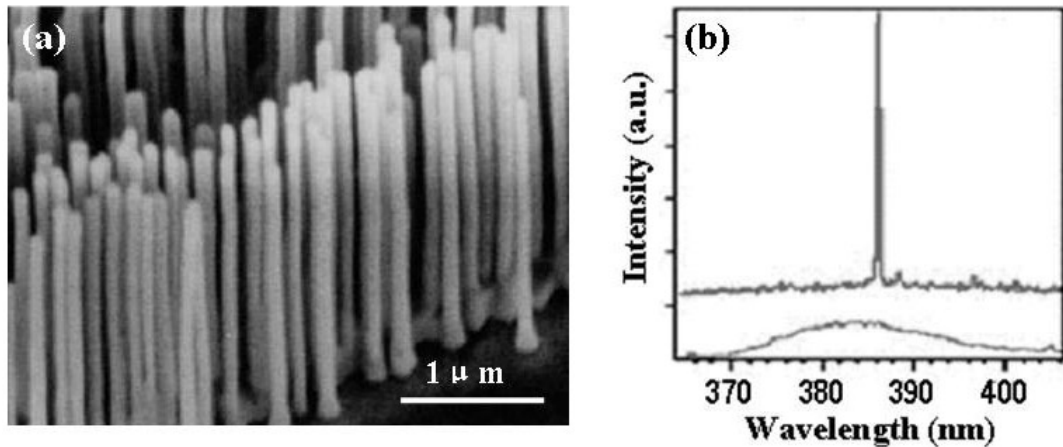
Figure 2.25: (a) SEM image of the vertical aligned ZnO nanowires grown on sapphire substrate. (b) The power-dependent emission spectra recorded from the aligned ZnO nanowires, with the excitation energy being below (bottom) and above (top) the threshold.

Nanowires with flat ends can also be exploited as nanoscale optical resonance cavities for lasing. The first nanowire lasing phenomenon was discovered on aligned ZnO nanowires grown on sapphire substrate (Figure 2.25a).[55] In this configuration, one end of the nanowire was the epitaxial interface between sapphire and ZnO and the other end is the flat top (0001) plane of hexagonal ZnO nanowire. Considering the refractive indices of sapphire (1.8), ZnO (2.5), and air (1.0), both ends of the nanowires serve as good mirrors to form an optical cavity. This nature cavity/waveguide structure provided a simple approach to the fabrication of nanoscale optical resonance cavities without cleavage and etching. A Nd:YAG (yttrium-aluminum-garnet) laser was applied to excite the aligned ZnO nanowires to lase. Figure 2.25b shows the emission spectra recorded at different pumping powers. When the excitation power was below the threshold, a broad spontaneous luminescence peak with a full width at half maximum (FWHM) was observed ~17 nm (the bottom curve in Figure 2.25b). Once the excitation power was increased over the threshold (~40 kW/cm^2), a sharp peak with much higher intensity was observed (the top curve in Figure 2.25b). The line width of this peak was 50 times narrow than the spontaneous emission peak. The narrowing of the peak width and rapid increase in intensity are strong indications of stimulated emission in the aligned nanowires.
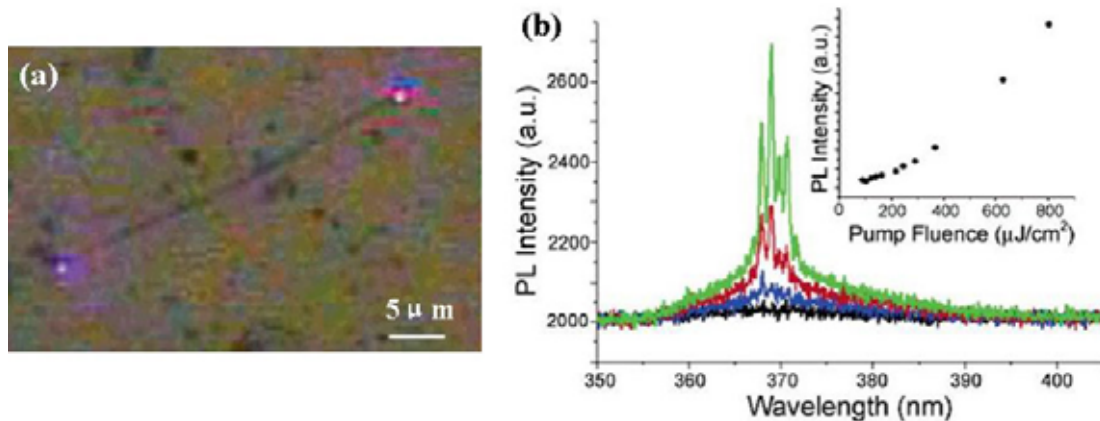
Figure 2.26: (a) Far-field PL/bright-field image of a GaN nanowire pumped above the lasing threshold. (b) Power dependence spectra of a GaN nanowire under nanosecond excitation. Spectra taken at 142, 218, 292, and 368 μJ/cm^2. Inset is the power curve of the same wire.

46

This concept of using will-cleaved nanowires as a natural laser cavity has also been extended to other semiconducting materials. Almost 10 years after the first achievement of room temperature lasing in a GaN thin film (1990s)[85], lasing effects in GaN single nanowire has been observed.[81] Figure 2.26a shows optically pumped (310 nm, 4.0 eV) laser emission from a single, isolated GaN nanowire on sapphire substrate. The GaN nanowire was ~40 μm long and ~300 nm wide. The localization of the bright emission at the ends of the wire indicated strong waveguiding behavior and that the cavity modes were Fabry–Perot (axial). Below the lasing threshold, the image had minimal contrast, and the PL spectrum was broad and featureless, as shown by the black curve in Figure 2.26b. As the pump power approached the threshold (in this case ~700 nJ/cm^2), several sharp (FWHM<1.0 nm) features appear in the spectrum, indicating the onset of stimulated emission (Figure 2.26b blue curve). Additional laser modes appear as the excitation intensity is further increased (Figure 2.26b, red and green curves). At even higher pump intensities, laser emission was detected, but at a lower energy (>380 nm), indicating a shifting of the gain curve due to bandgap renormalization. This is probably the result of the formation of an electron–hole plasma, which is the dominant lasing mechanism for GaN at high temperatures because of its weakly bound excitons (~25 meV) and coulombic screening at high excitation intensities.[86] For example, under nanosecond excitation, we typically observe a 2-3 orders of magnitude increase in P_{th} (Figure 2.26b, inset) when pumping with a laser ~100 times longer than the radiative lifetime (> 100 ps).

Similar lasing effects have also been discovered on single-crystal CdS nanowires.[82] A single CdS nanowire supported by a silicon substrate was excited by a frequency doubled Ti:sapphire laser pulses. As shown in Figure 2.27a, the excited CdS nanowire exhibited emission from the excitation region and 20 μm away at the nanowire end, demonstrating excellent waveguiding properties. PL spectra recorded at 4.2 K from a 40 μm long, 100 nm wide CdS nanowire as a function of excitation power are shown
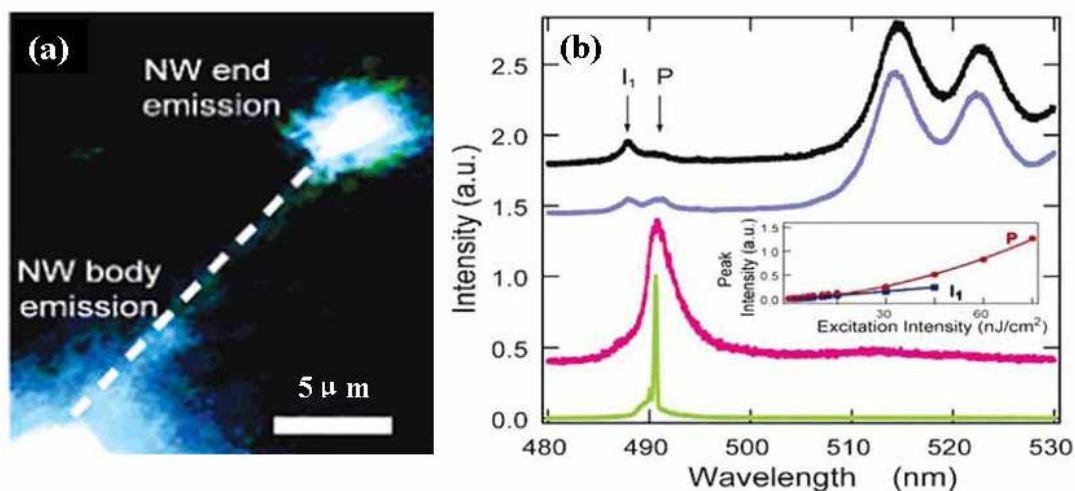
Figure 2.27: (a) PL image showing luminescence from the excitation area (lower left) and one end (upper right) of a CdS nanowire. (b) PL spectra of CdS nanowire end emission recorded at 4.2 K with excitation powers of 0.6, 1.5, 30, and 240 nJ/cm^2 for the black, blue, red, and green curves, respectively. Inset shows peak intensity of I_l (black squares) and P (red circles) bands versus incident laser power.

in Figure 2.27c. Also similar results were observed for nanowires with diameters ranging from 80-150 nm for length between 30-50 μm. The low excitation intensity (0.6 nJ/cm^2) PL spectrum reveals a number of well-defined, reproducible features in the 488 to 530 nm range, with peaks at 488.8(I_l), 490.5(P), 513, 522, and 530 nm corresponding to neutral acceptor bound excitons[87], exciton-exciton scattering[88], free electron-bound hole radiative recombination, and the LO phonon progressions of the free electron-bound hole transitions[89], respectively.

Excitation power dependent measurements (Figure 2.27b) show that the P-band intensity increases rapidly and becomes dominant at higher excitation powers. At high excitation intensities the P-band is the dominant feature in the PL spectra and furthermore shows a superlinear increase in the PL intensity above a threshold pumping power of 200 nJ/cm^2 (inset, Figure 2.27b). Above this threshold the PL spectrum collapses to a narrow peak at 490.5 nm with a line width of 0.3 nm, indicative of lasing.

48

The position and the power dependence of the PL spectrum strongly suggest that the lasing mechanism in CdS nanowires at 4.2 K is due to an exciton-exciton process.

Until now, most research interests have been focused on 1D nanomaterials in the areas of fabrication, characterization and applications. Novel properties and phenomena have been discovered in these fields; while more questions are raised simultaneously. For instance, various fabrication methods have been created and studied for making 1D nanostructures but it is still essential to increase the yields and improve uniformity for commercialization. An increasing number of proof-of-concept nanodevices have been realized in the laboratory with promising applications; however, the lack of efficient manipulation techniques that can achieve parallel processing and integrating nanodevices is still a big gap between scientific models and real products. In this dissertation, the effort has been to propose feasible solutions by applying self-assembly technique to order and align nanostructures at a very large scale.

CHAPTER 3

FABRICATION METHODOLOGY

The synthesis of nanomaterials is one of the most active fields in nanotechnology. Various 1D nanostructures have been fabricated through a number of approaches including thermal evaporation[28], laser ablation[58], template-assisted growth[90], arc discharge[91], lithography[92] and the sol-gel method[93]. Of these, thermal evaporation is normally the first choice as it is simple to setup and gives acceptable control of the self-assembly process. Consequently, this method has been very successful and versatile in fabricating nanobelts and nanowires with various characteristics.

In the experiments reported in this work, thermal evaporation process based on a single-zone tube furnace has been employed for synthesizing all of the 1D nanostructures, which compose the core of this dissertation. Therefore, the discussion of the research will start with this chapter to describe the details of the thermal evaporation system utilized for the entirety of this work. The thermal evaporation technique is a very simple process in which solid or powder source material is vaporized at elevated temperatures and then the resultant vapor phase(s) is condensed under certain conditions (temperature, pressure, atmosphere, substrate, etc.) to form the desired nanostructures.

The thermal evaporation system used throughout the entirety of the fabrication was comprised of two basic components: a furnace and pressure system. The furnace system provides the fundamental temperature control of the reaction chamber for nanostructure deposition; while the pressure system was responsible for the evaporation and deposition pressure condition inside the reaction chamber. Both systems and the basic control principles will be described in detail in this chapter.

3.1 Furnace System

A schematic of the furnace system is shown in Figure 3.1. A Thermolyne 79300 single zone split tube furnace was used as the heat source. Exposed heating element coils embedded into a ceramic fiber insulation provided the capability of rapidly ramping the temperature up to 1200 °C in only 20 minutes. The heating rate of the furnace was controlled by a digital C1 programmable controller with one stored program of eight segments. Each segment of the program consisted of three parts: a ramp rate (ranging from 1 °C/min to 60 °C/min), a temperature set point (ranging from 100°C to 1200°C), and a dwell time (ranging from 0.1 min to 999.9 min). An alumina tube with a length of 30", 1.75" outer diameter and 1.50" inner diameter was placed inside the tube furnace. Because the furnace chamber is only 24" in length, the alumina tube protruded six inches on either side of the furnace. Both ends of the tube were covered by stainless steel end caps and sealed with O-rings. Cooling water was circulated inside the cover caps to achieve a reasonable temperature gradient in the tube. One end cap was fitted with a gas inlet connection for introducing the inert carrier gas into the system and a quartz window
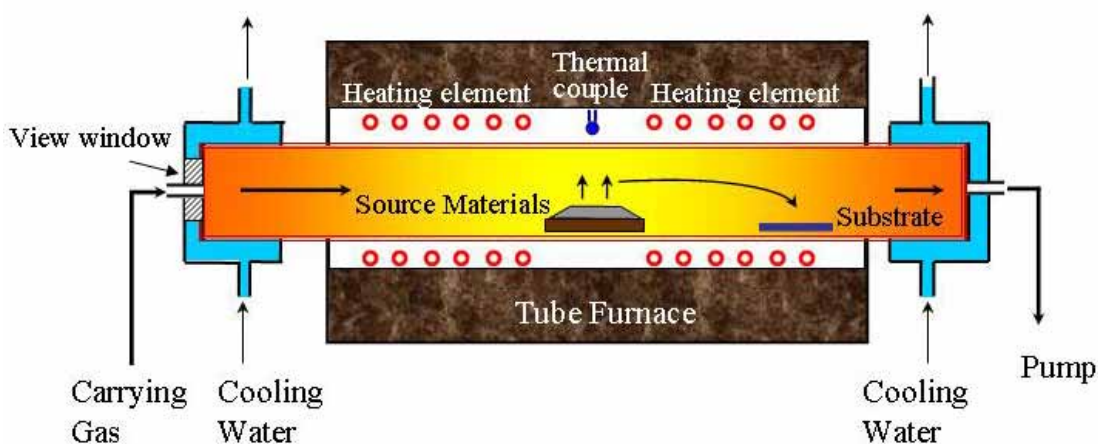
Figure 3.1: Schematic of the furnace system for thermal evaporation.

was also screwed on this end cap to monitor the evaporation process inside the tube. Another end cap was connected to the pressure system, which exhausted the waste gases into a hood.

In this system, the alumina tube acts as the reaction chamber for evaporation and deposition. Generally, high purity source powders loaded in an alumina boat were located in the middle of the furnace, the highest temperature region. The desired nanostructures were deposited on substrates placed a set distance away from the source in the down-stream direction of the carrier gas.
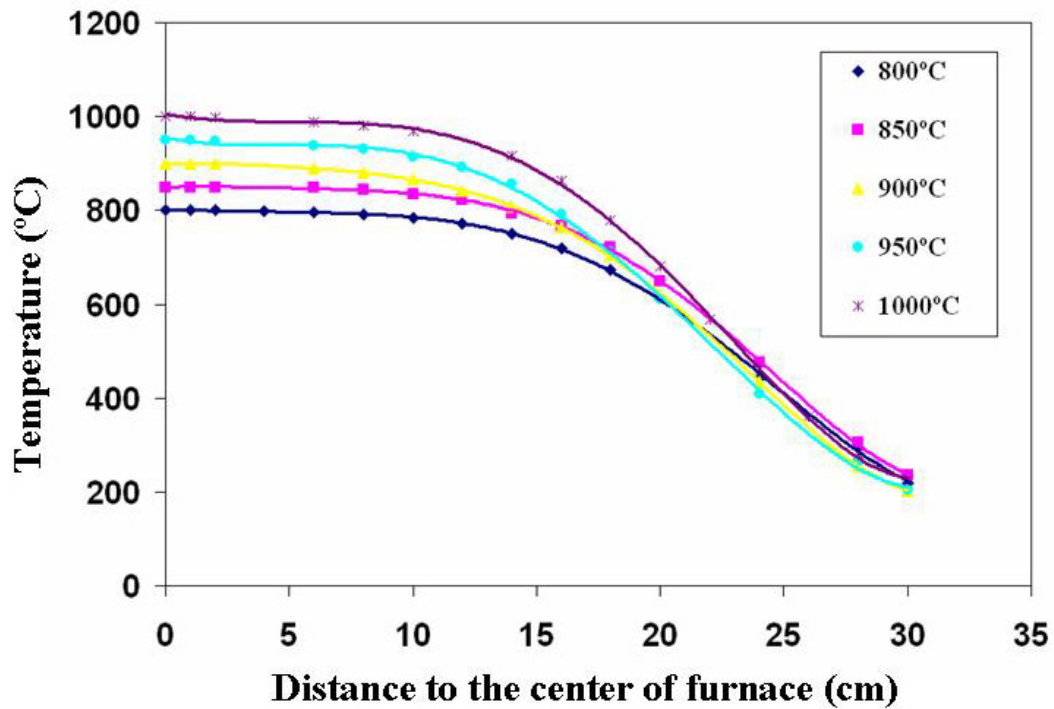
Figure 3.2: Temperature profile measured inside the alumina tube (from the center to the outside of the furnace) for different source temperatures.

Temperature control is one of the most important parameters for synthesis and was measured by a thermal couple placed at the center of the furnace chamber, but outside of the alumina tube. As a single zone furnace, this temperature readout is the only

feedback available to control the temperature inside the furnace. Therefore, it is essential to know the temperature gradient along the horizontal direction and the local deposition temperature is coupled for the distance from the substrate to tube center. As such, the temperature gradients for several different furnace temperatures were measured. An S-type thermocouple element (Platinum 10% Rhodium) sheathed in an alumina sleeve, was inserted into the furnace while under a 300mbar vacuum. A series of data points were taken at various positions within the furnace, so that the temperature gradient across the entire furnace could be extrapolated. Although all of the data for the measured temperature gradients were taken using a 300 mbar chamber pressure, previous unpublished studies demonstrated no change in the temperature gradient with varied chamber pressure, which is to be expected. Figure 3.2 shows the data for five distinct source temperatures and their corresponding temperature gradients. A best-fit curve was calculated for each. These equations were then used to extrapolate the local substrate temperature with the corresponding source temperatures for synthesis run.

3.2 Pressure System

The pressure system comprised three distinct parts. Following the direction of the gas flow, they were carrier gas introduction, pressure monitor and control and pump, as shown in Figure 3.3.

The carrier gas module was comprised by gas cylinders and mass flow controllers. The gases used in the system include N_2, Ar and O_2, and each was individually connected to an Aalborg mass flow controller to regulate the gas flow rate through the chamber. The
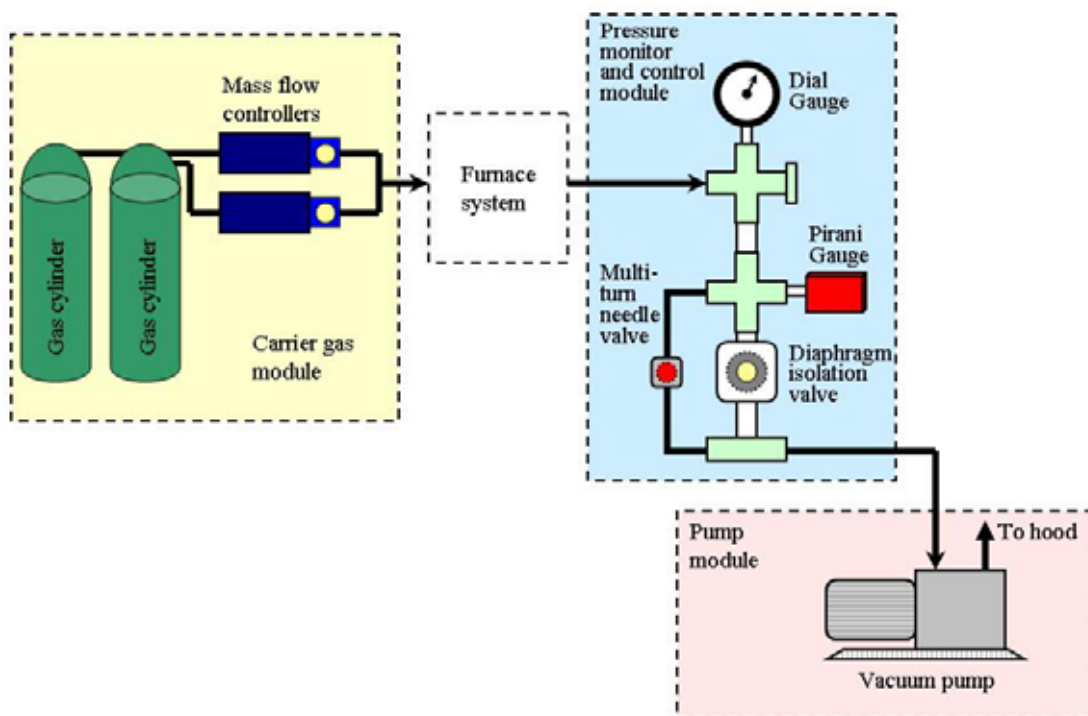
Figure 3.3: Schematic of the pressure system for thermal evaporation.

maximum flow rates of N_2, Ar and O_2 were 200, 100 and 10 standard cubic centimeter per minute (sccm) respectively, and were controlled to within 2% of their maximum flow rate. All of the outlets of the mass flow controllers were joined via 1/4" plastic tubing, and were connected to the gas inlet port of the end cap.

The pressure monitor and control module was connected to the outlet of the furnace system. The high vacuum conditions were measured by a BOC Edwards analog Pirani vacuum gauge series 500 with a working range from 100 to 10^{-3} mbar. The low vacuum level was detected by a BOC Edwards analog dial vacuum gauge series CG16K over the pressure range from 10 to 1000 mbar. In addition to monitoring the chamber pressure, two valves were incorporated in order to control the chamber pressure with coarse and fine adjustments. The coarse valve was a BOC Edwards diaphragm isolation valve. The

primary purpose of this valve is to fully open the system to the mechanical pump and purge

the chamber. A fine adjustable Cole-Palmer multi-turn needle valve was then used during

synthesis to make small pressure adjustments and to achieve and maintain a stable reaction

chamber pressure.

A BOC Edwards RV8 Hydrocarbon rotary vacuum pump was used to maintain the

vacuum of the system. The mechanical pump has a pumping rate of 8.0 m^3/h and an

ultimate vacuum of $2x10^{-3}$ mbar. Despite the fact that excess oxygen content can have an

adverse effect on deposition, this system was found to be sufficient. The mechanical pump

was connected to the vacuum controlling module by a 3-ft, 2-inch-wide flexible stainless

steel tube and the outlet is directly connected to the hood exhausting system.

3.3 Basic Procedure of Thermal Evaporation Technique

Before starting the synthesis, the reaction chamber was pre-pumped down to the

lowest possible pressure, which was normally $\sim2\times10^{-3}$ Torr, to remove the residue O_2 in

the system. Then the furnace was heated to the reaction temperature at a specific heating

rate. Meanwhile, an inert carrier gas, such as argon or nitrogen, was introduced into the

system at a constant flow rate to bring the pressure in the chamber back to a relatively

high value (different pressures were required by different source materials and final

deposited nanostructures). The reaction temperature and pressure were held constant

during the deposition. When the reaction was completed, the furnace was cooled down to

room temperature with flowing inert gas. Normally, the system pressure was kept at the

reaction pressure to prevent subsequent decomposition of the grown nanostructures.

This is the basic procedure to grow nanostructures through a thermal evaporation

process. In reality, the deposition is very sensitive to many system parameters, such as

temperature, temperature gradient and pressure. Different morphologies can be achieved by a small change of one of those parameters. One of the goals of this dissertation is to establish how these parameters determine the final nanostructure properties. The details of the fabrication conditions and the resulting 1D nanostructures will be presented in Chapter 4 and Chapter 6.

CHAPTER 4

1D ZNO NANOSTRUCTURES WITH CONTROLLED

MORPHOLOGIES

Chapter 3 described a tube furnace system used for the thermal evaporation of synthesizing 1D nanostructures. Despite its simple configuration, this system has been very successful in fabricating nanobelts and nanowires with various characteristics. The basic process is to sublimate source material(s) in powder form at high temperature, and the subsequent deposition of the vapor in a certain temperature region to form desired nanostructures. By monitoring the growth conditions, including the evaporation temperature, chamber pressure, deposition temperature and catalyst, the resulting 1D nanostructures could be controlled in shape, length, thickness and composition. In this chapter, three new types of 1D ZnO nanostructures, ultra-thin ZnO nanobelts, mesoporous ZnO nanowires and ZnS-ZnO nanocables are described to show the controllability on the morphology of ZnO nanostructures.

4.1 Ultra-Thin ZnO Nanobelts

In general, it is believed that nanostructures less than 10 nm in size are possible to show quantum confinement effects. Nanowires of a few nanometers in diameter have been synthesized for InP[58] and Si[26] by using nanoparticles as catalysts or using single-wall carbon nanotubes as templates. However, due to the fact that solid-vapor phase synthesis typically occurs at high temperature between 700-1300 ºC, the synthesis of small size (<10 nm) ZnO nanobelts requires an innovative approach. By using a thin film of metallic tin as catalyst, ultrasmall single-crystalline zinc oxide nanobelts can been

synthesized in large quantity by a carbon-thermal evaporation process[79]. The nanobelts have an average width of 5.5 nm and a narrow size distribution of ±1.5 nm, and should be good candidates for investigating size induced electrical and optical properties of functional oxides.

4.1.1 Fabrication Method

The ultrasmall nanobelts were synthesized using a novel catalyst in the thermal evaporation system described in Chapter 3. A 1 cm × 1 cm silicon wafer was used as the supporting substrate, which was pre-cleaned by a 2:1 mixture (by volume) of H_2SO_4 (98%) and H_2O_2. Instead of using traditional dispersive nanoparticles as the catalyst for size-controlled seeding growth[58], a uniform thin film (~10 nm) of tin was coated on the silicon substrate. A thermal evaporator with a quartz crystal thickness monitor was used to reproducibly obtain the exact film thickness for the tin layer. For nanobelt growth, an equal molar of ZnO powder and graphite powder were grounded together and loaded into an alumina boat. The source materials were located at the center of an alumina tube and the substrate was place downstream (15-20 cm) from the center. A horizontal tube furnace was used to heat the tube to 900˚C at a rate of 50˚C/min and the temperature was held for 10 minutes under a pressure of 300 mbar with a constant argon flow at 20-30 sccm. The reaction was terminated by turning off the furnace and the tube was cooled down naturally to room temperature. The as-synthesized products were examined by SEM and TEM.

4.1.2 Structure Characterization

The morphology of the ZnO nanobelts was firstly examined by SEM. Figure 4.1a shows a low magnification SEM image of the ultra small ZnO nanobelts obtained from
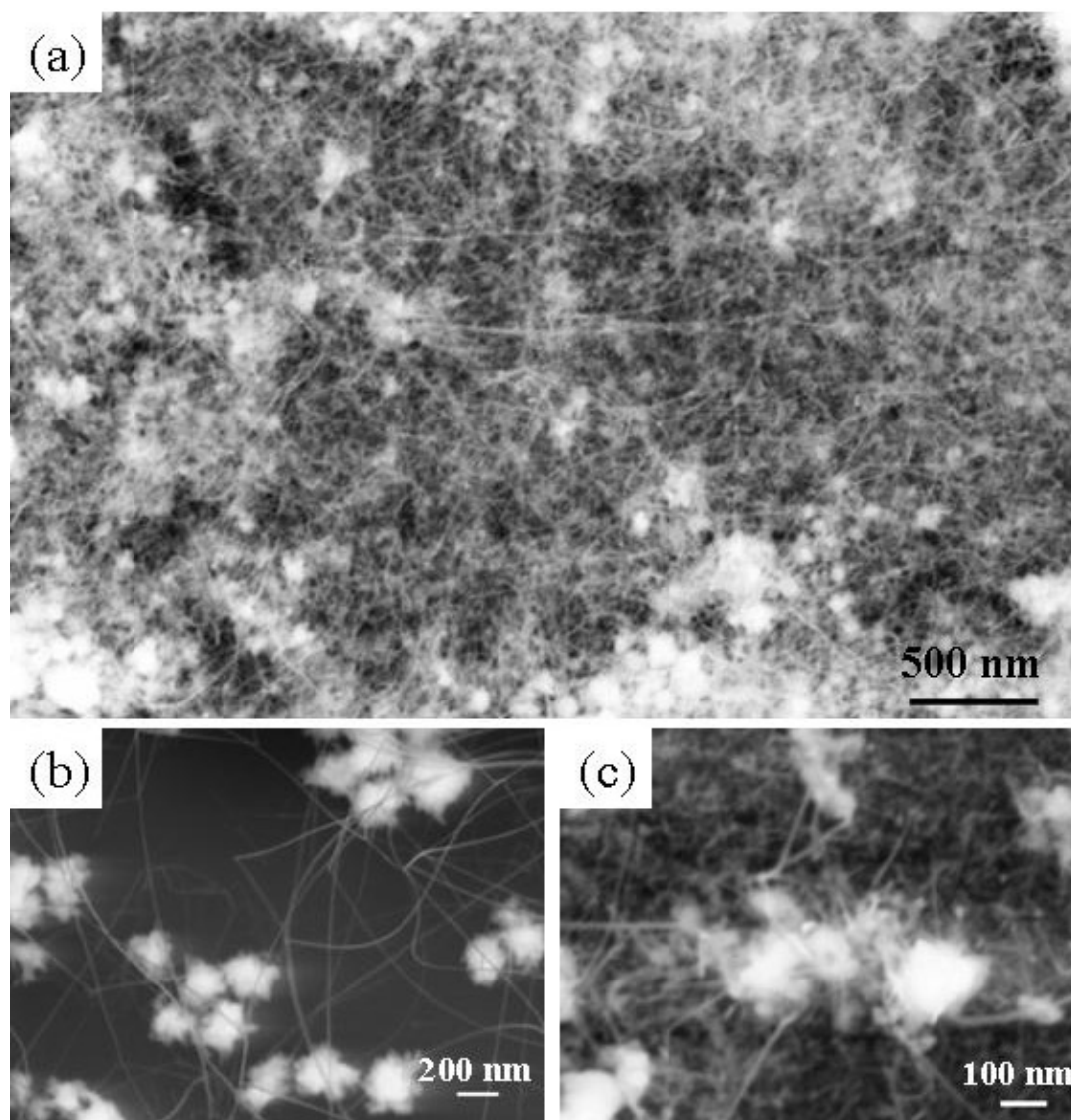
Figure 4.1: SEM images of ultrathin ZnO nanobelts grown on tin-coated silicon substrate. (a) Low-magnification image, (b) higher-magnification image showing tin catalysts, (c) higher-magnification image showing ZnO nanobelts extended out from tin balls.
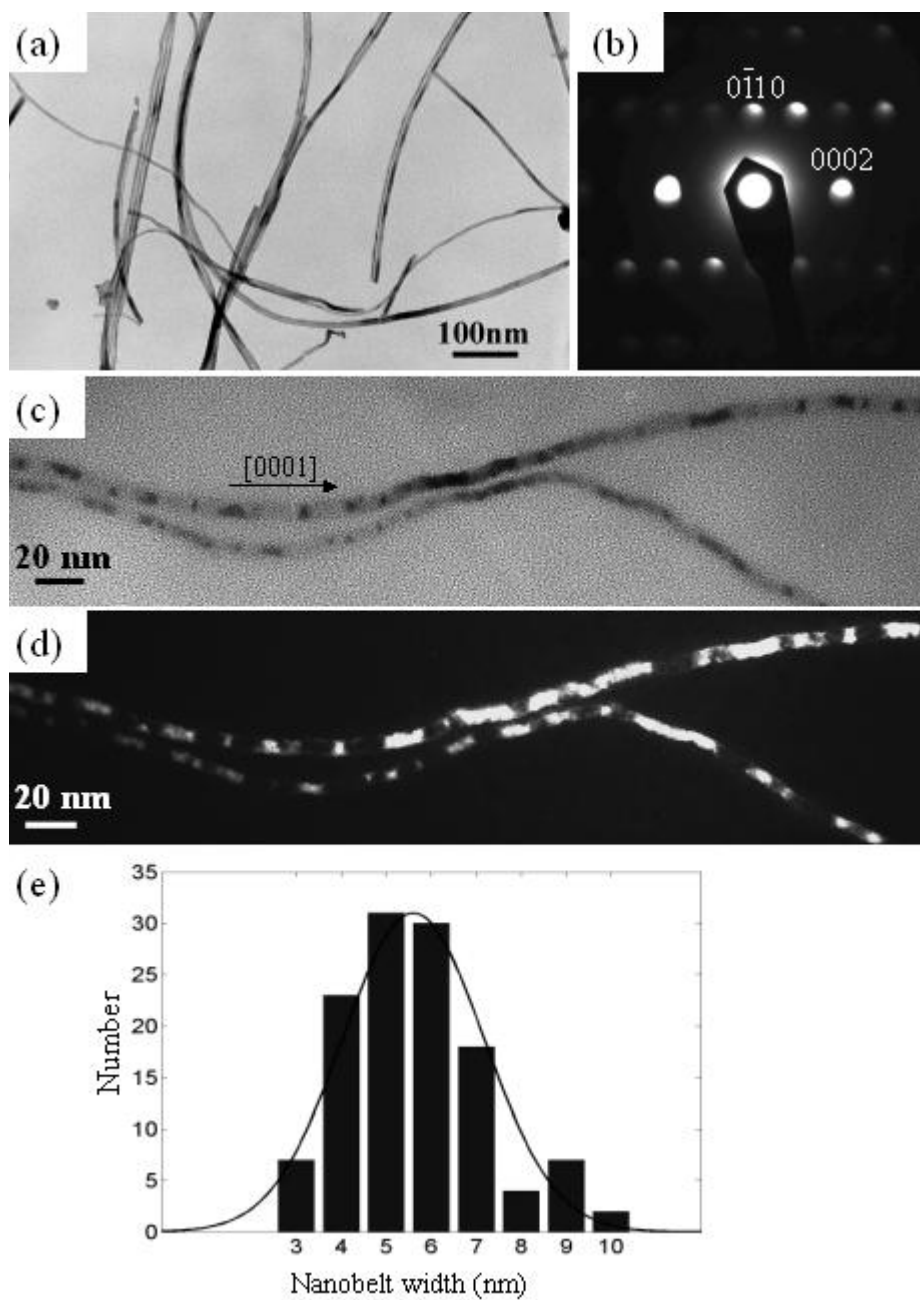
Figure 4.2: (a) Low-magnification TEM image showing the size uniformity of ZnO nanobelts. (b-d) Diffraction pattern, bright field image, and dark field image of ZnO nanobelts that have a belt-like morphology. (e) Size distribution of as-synthesized ZnO nanobelts.

60

growth on a silicon wafer coated with a 10 nm tin layer. Because the mutual solubility of silicon and tin is limited, during the initial heating process, the thin tin layer agglomerates into balls due to surface tension. The white balls in Figure 4.1b then become the tin catalyst for nanobelt growth. The lengths of the nanobelts are typically a few microns and exhibit a uniform size distribution. The ZnO nanobelts extend out from the tin balls and cover the whole substrate with a reasonably yield, which can be seen more clearly in a higher magnification SEM image given in Figure 4.1c.

By measuring over 120 nanobelts from randomly recorded TEM images, the average diameter of the nanobelts was determined to be 5.5 nm with a standard deviation of ± 1.5nm. As shown in figure 4.2e, most nanobelts are in the range of 4-7 nm indicating very good size uniformity. A sample exhibiting this size uniformity and distribution is presented by the TEM image shown in figure 4.2a.

Figure 4.2b shows an electron diffraction pattern recorded from a relatively large ZnO nanobelt shown in Figure 4.2c. The diffraction pattern corresponds to the $[2\bar{1}\bar{1}0]$ zone axis of wurtzite ZnO, and displays the fastest growth direction of ZnO nanobelts is being [0001]. The contrast in Figures 4.2c and 4.2d is due to bending induced strain, and the image indicates the equal projected thickness of the nanobelt. The top surfaces of the nanobelts are $(01\bar{1}0)$ and the side surfaces are $(2\bar{1}\bar{1}0)$. All of these structural confinements are consistent with previous reported experimental results on ZnO nanostructures.

High-resolution TEM has been employed to study the strain release mechanism in ZnO nanobelts (Figure 4.8). All of the nanobelts display a single crystalline structure with the (0001) fringes of spacing 5.1 Å. Due to the root-growth process; the bending of the nanobelts introduces a large local strain. This is demonstrated by the fact that a nanobelt 10 nm in width is straight (Figure 4.3a), while a thin nanobelt, 5 nm in width, shows a curly shape (Figure 4.3b). The strain in the thicker nanobelt is released by creating stacking faults perpendicular to the growth direction of the nanobelts (Figure
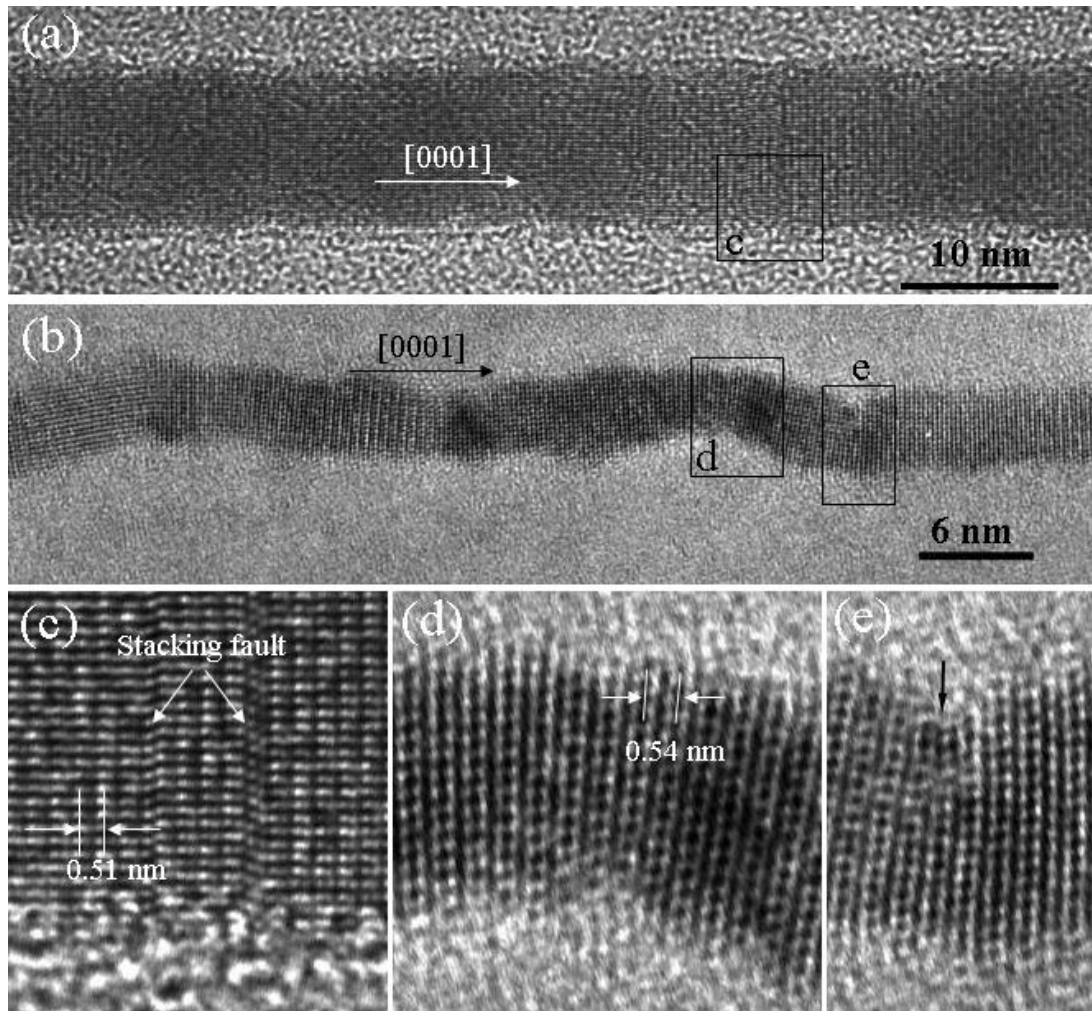
Figure 4.3: High-resolution TEM images of (a) 10 nm-wide and (b) 5 nm-wide ZnO nanobelts. (c-e) The enlarged images from areas c, d, and e marked in (a) and (b), respectively, showing strain-induced change in interplanar distance and an edge dislocation in the nanobelt.

4.3c). For the ~5 nm nanobelt, besides stacking faults, distortion in the orientation of the (0001) atomic planes (Figure 4.3d) and edge dislocations (Figure 4.3e) are introduced to accommodate the local deformation. The interplanar distance can be expanded to ~ 5.4 Å at the exterior arc and compressed to ~ 4.8 Å at the inner arc to accommodate the local strain. This is possible for narrow nanobelts. The creation of edge dislocations in oxide nanobelts is rare.
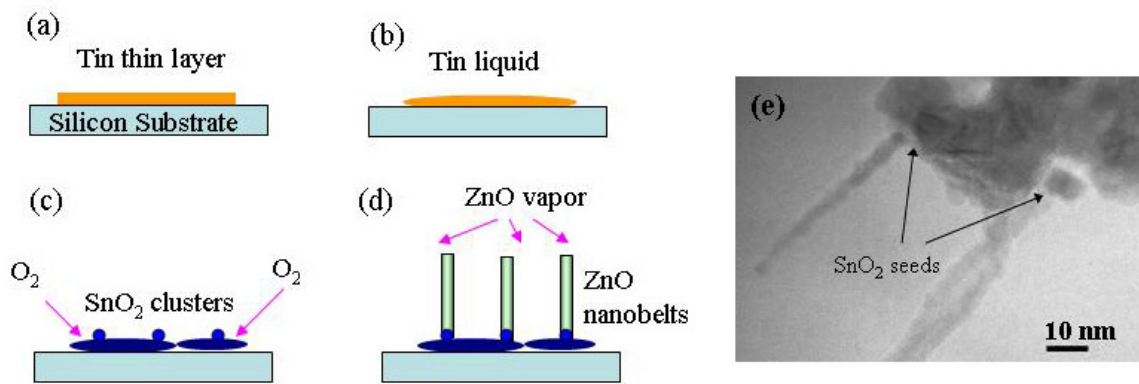
Figure 4.4: (a-d) Schematic steps of the growth of ZnO nanobelts on tin catalyst. (e) ZnO nanobelts growing on the top of tin oxide.

4.1.3 Growth Mechanism

Unlike other reported metal-seeded VLS growth techniques, which normally have a metal ball at the tip of the nanowires, these nanobelts have clean tips. Thus, this growth was very likely through the VS process, where tin oxides only served as the nucleation sizes to initiate the growth. The schematic growth processes are illustrated in Figure 4.4. Since tin has a very low melting point (232 ˚C), it was molten before the ZnO vapor was formed in the reaction tube (Figure 4.4a and 4.4b), even though the substrate deposition temperature was lower than that of the ZnO source. The molten tin can be oxidized at the growth temperature[94] by the residue oxygen inside the tube and form very small tin oxide

particles as well as relatively big tin oxide clusters(Figure 4.4c). Once the temperature became high enough to evaporate ZnO, ZnO vapor inside the tube gradually became supersaturates and ZnO started depositing around those nucleation seeds. By keeping a reasonable vapor pressure of ZnO in the furnace, the ZnO nanobelts continued to grow from the nucleation sites through a VS process same as how the normal ZnO nanobelts were formed (Figure 4.4d),[52] while their width were confined by the initial tin oxide particles. Figure 4.4e shows a TEM image of the ZnO nanobelts grown on top of the tin oxide nanoparticles, which supports this catalyst-assisted VS growth. Therefore, the effective catalyst that confined the size of ZnO nanobelts were self-formed during the growth. This is in contrast to conventional VLS growth, where a pre-treatment of catalyst is traditionally necessary for size determination. Thus, this method provided a much simpler way to fabricate ultra thin ZnO nanobelts at lower cost and at large quantity and can be extended to a variety of inorganic materials.
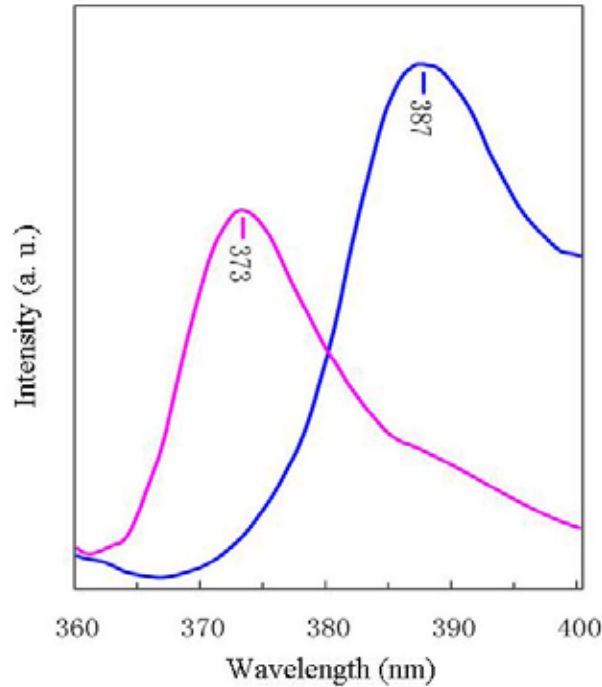
Figure 4.5: Photoluminescence spectra acquired from ~200-nm wide ZnO nanobelts (blue line) and 6 nm-wide ZnO nanobelts (pink line).

4.1.4 PL Properties

To examine the size induced quantum effect in the ultra thin ZnO nanobelts, PL measurements were performed at room temperature using a Xe lamp with an excitation wavelength of 330 nm. Figure 4.5 compares the PL spectra recorded from the ZnO nanobelts synthesized previously that have an average width of ~ 200 nm and the PL from the ultra thin ZnO nanobelts with an average width of 5.5 nm. The 387 nm peak corresponds to a 3.2 eV spontaneous emission of the normal ZnO nanobelts, as reported previously[95]. This emission lies at an energy considerably below that of the band gap (3.37 eV) of ZnO is a result of exciton-exciton collision. From this model the energy of the resulting photon can be given by

$$P_n = E_{ex} - E_b^{ex}(1-\frac{1}{n^2}) - \frac{2}{3}kT \quad (n = 2, 3, 4 \ldots) \tag{4.1}$$

where P_n is the photon energy, E_{ex} the free-exciton emission energy, E_b^{ex} the binding energy of the exciton, n is the quantum number of the envelope function, and kT is the thermal energy. However, in contrast, the ultra thin ZnO nanobelts exhibit a near band edge emission at 373 nm (3.32 eV). We suggest that the increase in photon energy is due to an increase in E_{ex}, which indicates quantum confinement due to the reduced size of the nanobelts.

4.2 Mesoporous Single-Crystal ZnO Nanowires

Porous materials have exhibited a wide variety of application in bioengineering, catalysis, environmental engineering and sensor systems owing to their high surface-to-volume ratio. Normally, most mesoporous structures are composed of amorphous materials[96] and the porosity is achieved by solvent-based organic or inorganic reactions[97]. There are few reports of mesoporous structures based on crystalline materials. Through

the thermal-evaporation technique, we found a new wurtzite ZnO nanowire structure that is single crystal but composed of mesoporous walls/volumes. The highly porous ZnO nanowires were also enclosed by a thin layer of epitaxial Zn_2SiO_4 at the exterior surface, which was formed during synthesis performed with the use of a silicon substrate. These high-porosity single-crystal wire-like structures have potential applications as filters, catalysts support and gas sensors.

4.2.1 Fabrication Method

The fabrication was performed in the furnace system for thermal evaporation process. In a typical experiment, a {111} orientated silicon substrate was cleaned by a 2:1 mixture (by volume) of H_2SO_4 (98%) and H_2O_2 and a 10 nm thin film of tin was coated onto the silicon substrate using a thermal evaporator with a quartz crystal thickness monitor for obtaining exact tin film thickness. Part of the silicon substrate was covered from tin deposition in order to investigate the catalyst effects. 2 gram of ZnO powder (99.9%) was loaded into an alumina boat and placed in the center of an alumina tube. The tin coated silicon substrate was located about 12 cm downstream from the source. Both ends of the tube were water cooled to achieve a reasonable temperature gradient. The tube was firstly pumped down to $5x10^{-3}$ torr at room temperature and then heated to 800 ºC at a rate of 25ºC/min. After holding this temperature for 20 minutes, the furnace was heated up to 1300 ºC at a rate of 20ºC/min. Meanwhile, a constant Ar gas was introduced at 20 sccm to bring the pressure back to 300 torr. This condition was held for 30 minutes to achieve the final nanostructures geometry. Then the furnace was shut down and cooled to room temperature under an Ar flow.

4.2.2 Structure Characterization

The morphology of the porous ZnO nanowires was first examined by SEM. Figure 4.6a is a low magnification SEM image of the as-synthesized ZnO nanowires
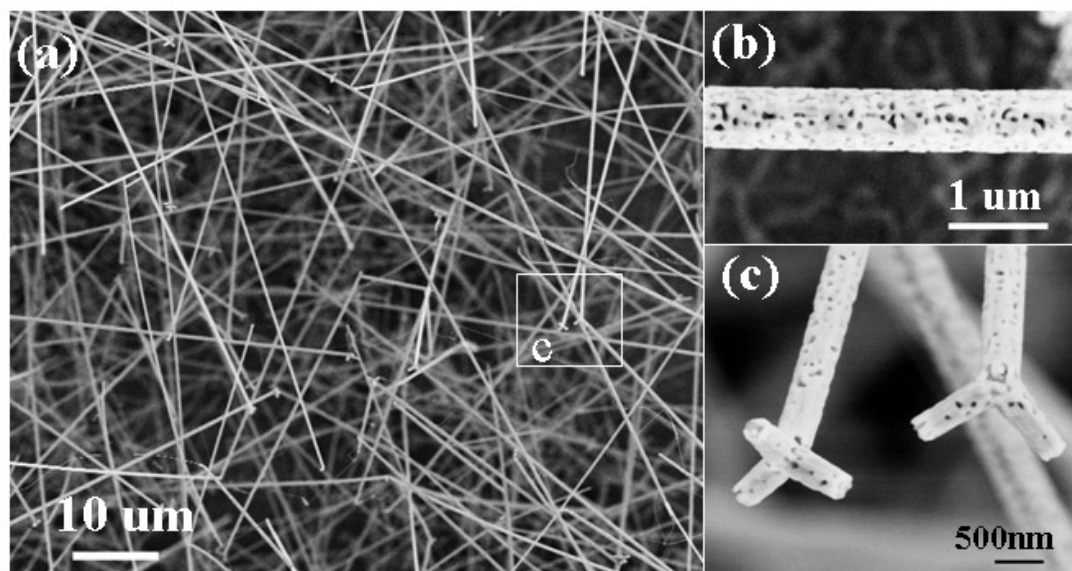
Figure 4.6: Low-magnification SEM image of high-porosity ZnO nanowires grown on a tin coated silicon substrate; (b) higher magnification SEM image showing high-porosity morphology; (c) a close-up view of the tetrapod structure.

deposited on a silicon substrate, where is coated with a thin layer of tin to act as a catalyst for growth. The typical length of the nanowires varies from 100 μm to 1 mm and the diameter is in the range of 50-500 nm. The porous structure of the ZnO nanowires is shown more clearly in a high magnification SEM image in Figure 4.6b, which display a hexagonal surface morphology. Moreover, most of the nanowires have the tetragonal configuration at the end as shown in Figure 4.6c.

On the silicon substrate surface not covered by tin, low-density ZnO tubular sprouts were found growing upwards from the silicon substrate as shown in Figure 4.7a. All of the sprouts have about the same length and diameter and exhibit high-porosity walls/volumes (Figure 4.7b), while their length are much shorter than the ZnO nanowires catalyzed by tin. Most of the sprout' legs retain the tetraleg structure, as indicated by arrowheads. Moreover, many sprouts can grow together in tightly confined regions and form partially aligned ZnO corral structures as shown in Figure 4.7c, where the tetraleg structure is identified at the side of the corral.
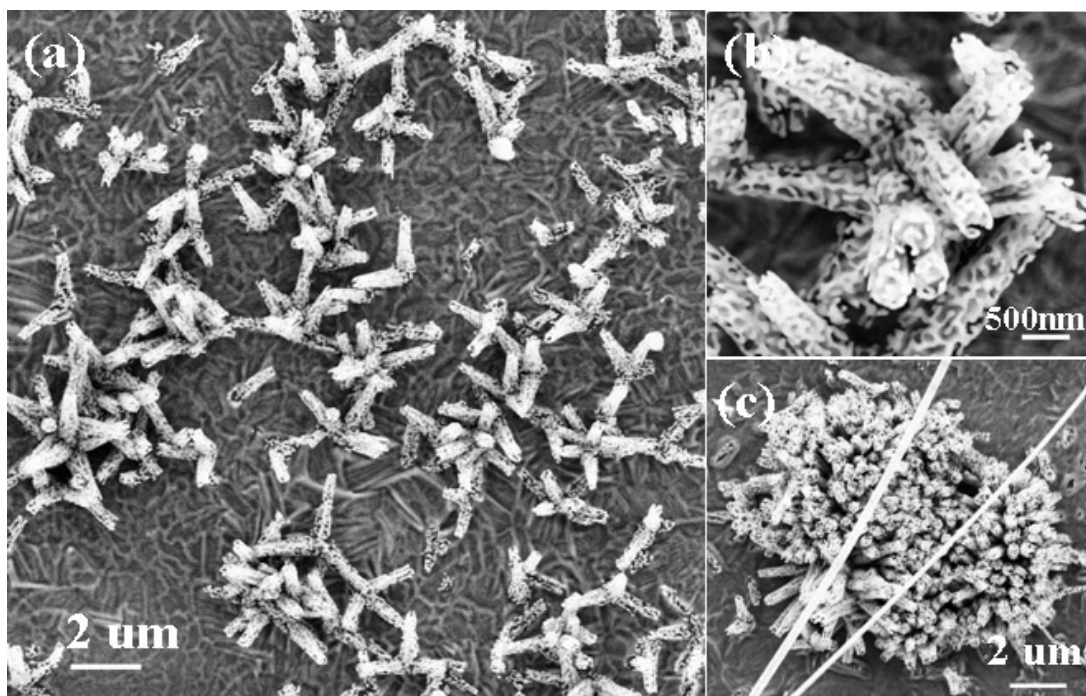
Figure 4.7: (a) Porous ZnO sprouts grown on the non-tin covered region; (b) A close view of the ZnO sprouts; (c) Partially aligned ZnO sprouts in the form of coral-like structure.
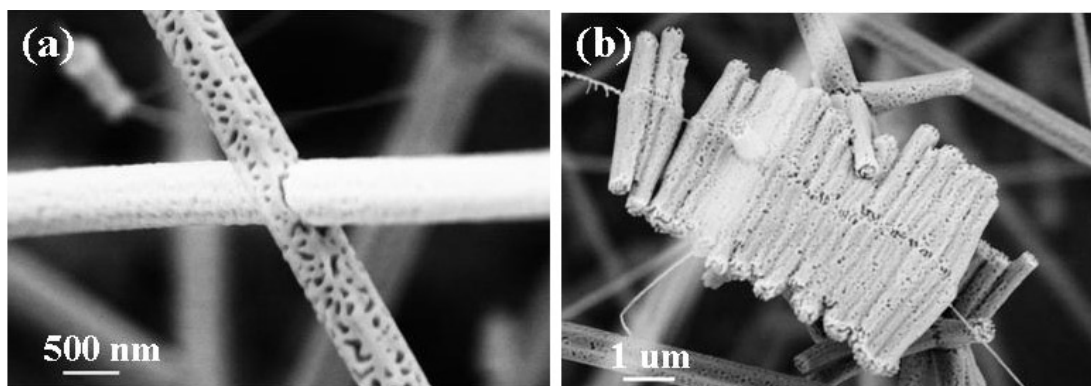
Figure 4.8: (a) A junction between two porous ZnO nanowires; (b) Rib-like structure formed by aligning porous ZnO nanorods side-by-side on a nanowire.

Crossed structures of two nanowires have also been observed (Figure 4.8a). The porosity in the nanowire is apparent, and its hexagonal shape is clearly visible. Arrays of short nanowires (nanorods) have also been formed, as presented in Figure 4.8b, which has a rib-like structure.

TEM studies were employed to examine the crystallography and the growth mechanism of the ZnO nanowires. The porous structure is clearly seen through the TEM image (Figure 4.9a). A corresponding electron diffraction pattern recorded from the nanowire is shown in Figure 4.9b, but it presents two sets of patterns: the brighter spots come from ZnO, which is the $[2\bar{1}\bar{1}0]$ zone axis pattern, displaying the nanowire axial direction of [0001]; the weaker diffraction spots correspond to a different phase. High resolution TEM image recorded from the side of the nanowire shows that the phase is sheathed on the surface of the nanowire and has an epitaxial orientation related to ZnO. In Figure 4.9c, on the top of the ZnO crystal, whose lattice fringe spacing of c = 0.52 nm perpendicular to the growth direction, a few fringes with a spacing of ~ 1 nm from the new phase are present and lie parallel to the wire axis.

Chemical analysis provides the first hint for defining the structure of the new phase. Energy-dispersive X-ray spectrum (EDS) (Figure 4.9e) recorded from the edge of the nanowire shown in Figure 4.9d indicates the presence of Zn, Si and O in the new phase. The atomic ratio of Si to Zn is about 2:3, which is smaller than the ratio in Zn_2SiO_4 due to the presence of a thin silica layer on the surface of the nanowire. In reference to the real space interplanar distance of ZnO, the corresponding reflection planes of the new phase can be determined from the electron diffraction pattern presented in Figure 4.9b. The diffraction pattern from the new phase can be indexed to be the [100] zone axis of Zn_2SiO_4. The orientation relationship between ZnO and Zn_2SiO_4 is:

(0001)ZnO || (001)Zn_2SiO_4, $[2\bar{1}\bar{1}0]$ ZnO || [100]Zn_2SiO_4. Structurally, Zn_2SiO_4 has an orthorhombic crystal structure with lattice constants of a = 0.9085 nm, b = 1.0625 nm and
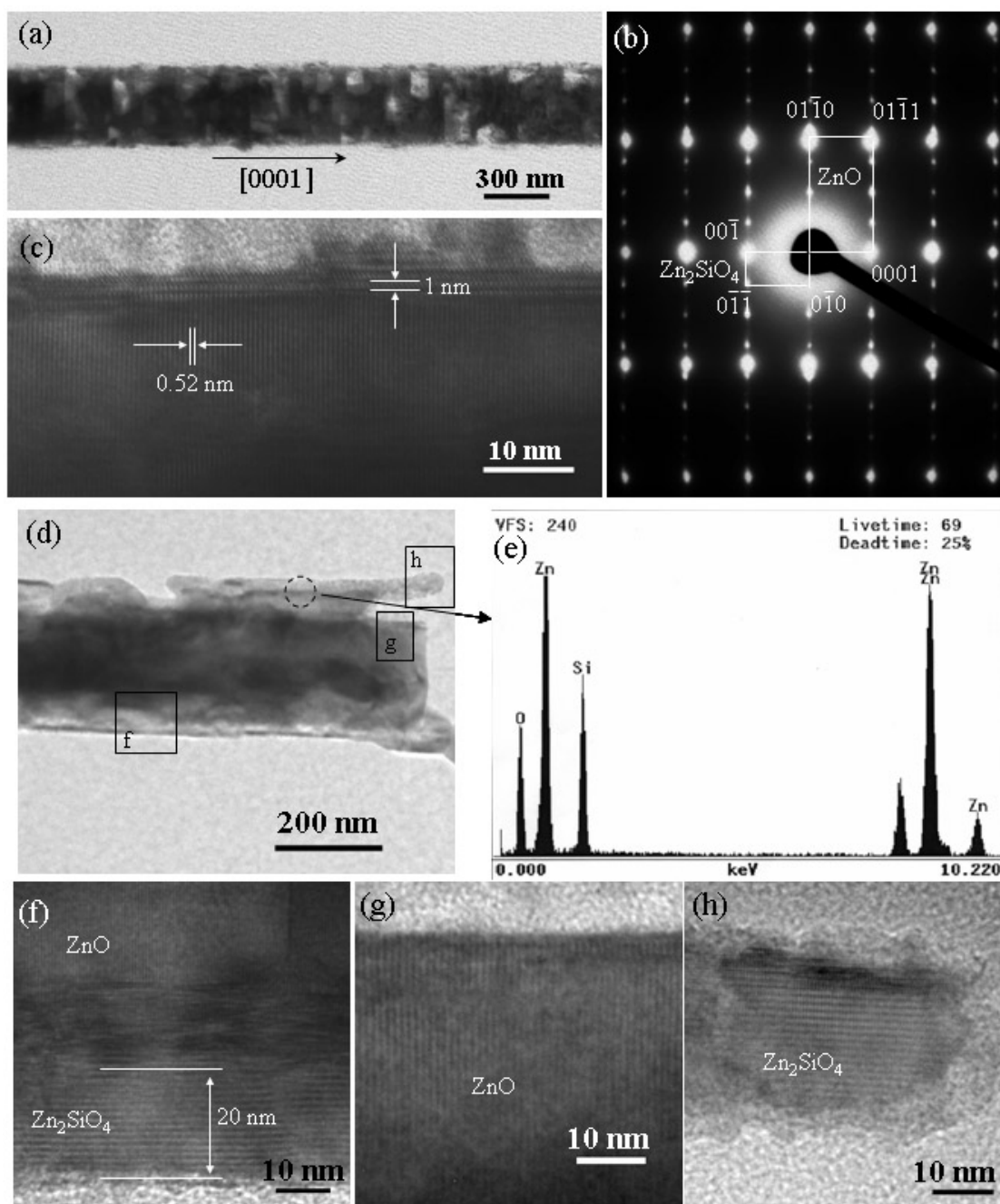
Figure 4.9: (a) Low-magnification TEM image of a porous ZnO nanowire and (b) corresponding diffraction pattern; (c) High-magnification TEM image taken on the edge of a porous ZnO nanowire; (d) Low-magnification TEM image of a porous ZnO nanowire covered by a thick layer of Zn_2SiO_4; (e) EDS spectra recorded on the Zn_2SiO_4 layer; (f-h) High-magnification TEM images recorded from the areas indicated in (d), showing the Zn_2SiO_4/ZnO interface, ZnO core and Zn_2SiO_4 shell, respectively.

70

c = 0.5962 nm. Figure 4.14f is a high-resolution TEM image that clearly shows the formation of the Zn_2SiO_4 layer. A 20 nm thick layer on the bottom is clearly single crystalline Zn_2SiO_4. Figure 4.9g shows the pure ZnO crystal lattice recorded at the end of the nanowire; the outer layer is shown in Figure 4.9h, which exhibits a pure Zn_2SiO_4 crystal structure surrounded by a thin layer of amorphous SiO_2.

4.2.3 Growth Mechanism

The formation of the tetraleg structure presented in Figures 4.6c and 4.7a indicate that the solid ZnO nanowire is formed first. According to the Iwanaga' model[98] (so-called octa-twin model[99]), the first homogeneous ZnO nuclei formed are octa-twins, and consist of eight tetrahedral-shape crystals, each consisting of three $\{11\overline{2}0\}$ pyramidal facets and one (0001) basal facet. The eight tetrahedral crystals are connected together by making the pyramidal faces contact one another to form an octahedron. The surfaces of the octa-twins are all basal planes, but the eight basal surfaces of the octa-twin are alternately the Zn-terminated (0001) surfaces and the oxygen-terminated $(000\overline{1})$ surfaces. Since the (0001) surface is chemically active, while the $(000\overline{1})$ surface is inert[39], the growth of nanowires along [0001] from the Zn-terminated (0001) surfaces results in the formation of the tetraleg. The four legs of each tetraleg structure are expected to have equivalent growth rates at least during the early growth stage, as supported by the image in Figure 4.7a recorded from an area uncovered with tin catalyst. In the region covered with tin, the leg that is directly in contact with the tin catalyst coated on the substrate surface is likely to grow much faster due to a vapor-liquid-solid growth mechanism occurring at the root (interface with the catalyst) than the legs that are grown by self-catalyzing[39] without the assistance of the tin catalyst, possibly resulting in the one-long leg structure presented in Figure 4.6c.
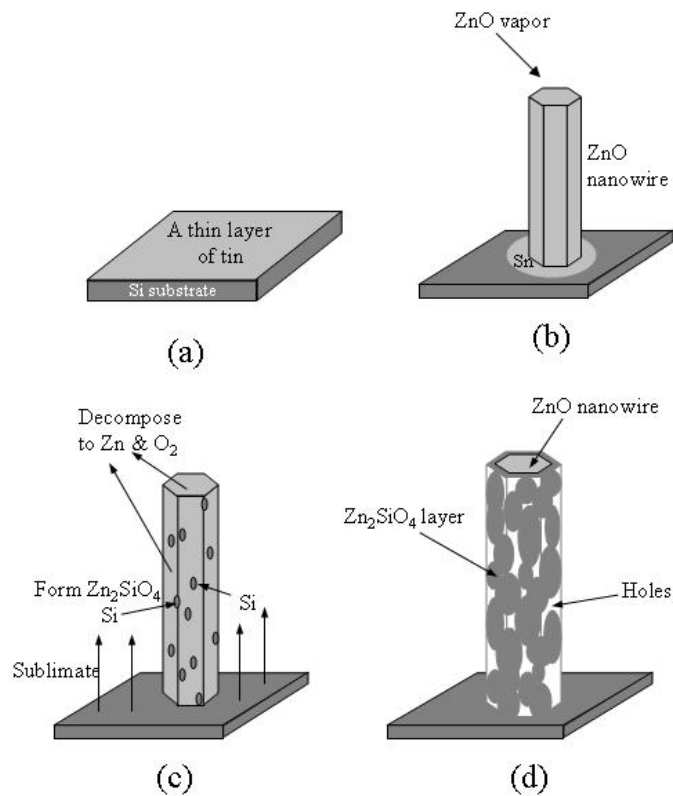
Figure 4.10: Schematic of the proposed growth mechanism for growth of high-porosity ZnO nanowires.

According to the TEM data, a possible growth mechanism is proposed in Figure 4.10. Starting from the tin catalyst deposited on the substrate as a thin film, ZnO nanowires were formed by supplying ZnO vapor from the source material (Figure 4.10a, b). In this high temperature deposition process, tin only served as the nucleation sites The nanowire grows along [0001] and its side surfaces are $\{2\bar{1}\bar{1}0\}$. In a high temperature region, ZnO nanowires can re-decompose into Zn vapor and O2, which can occur at a local substrate temperature of ~ 600 ℃. In the meanwhile, Si-O vapor sublimated from the silicon substrate can quickly deposited on the nanowire surface and diffuse into the ZnO lattice, resulting in the formation of a new phase, Zn_2SiO_4. The electronegativity of

Si is 1.9 and that of Zn is 1.65, which are quite close. Additionally, the atomic size of Si and Zn, 0.117 and 0.133 nm, respectively, are also comparable. Additionally ZnO and Si-O vapor can quickly combine to form a new phase:

$$2ZnO + SiO_2 \rightarrow Zn_2SiO_4 \qquad\qquad (4.2)$$

The newly formed Zn_2SiO_4 layer tends to have an epitaxial relationship with ZnO in order to reduce the interface lattice mismatch (Figure 4.10c). On the other hand, the lattice mismatch between $(0001)_{ZnO}$ and $(001)_{Zn2SiO4}$ is 14%, and between $(01\bar{1}0)$ ZnO and $4(010)_{Zn2SiO4}$ is 9%, Zn_2SiO_4 tends to form textured islands on the surface of ZnO, but they cannot form a continuous single-crystal film due to the large lattice mismatch; resulting in the growth of epitaxial Zn_2SiO_4 islands on the ZnO surface. The newly formed Zn_2SiO_4 may be more stable than ZnO at the local growth temperature. Therefore, there are open areas on the ZnO surface that are not covered by the Zn_2SiO_4 network. The evaporation of Zn-O from the open areas may form the porous in the volume of the nanowire. The sublimation of ZnO and growth of Zn_2SiO_4 proceed simultaneously and finally end with a high-porosity ZnO nanostructure (Figure 4.10d).

4.2.4 PL Properties

It is well known that Zn_2SiO_4 is a green luminescence material and ZnO has a near-UV luminescence. A PL system was used to characterize the optical properties of the porous ZnO nanowires that are enclosed by Zn_2SiO_4. The measurements were performed at room temperature using a 337 nm N_2 pulsed laser as the excitation light source. The laser repetition rate was 15 Hz, with 800 ps pulse duration at an average energy of 50 mW. As shown in Figure 4.11, a near-UV luminescence peak is observed at 387 nm, which is consistent with our previous results on other ZnO nanostructures. Additionally, a small green peak located at 512 nm is also observed (see the insert), which is attributed to by Zn_2SiO_4. It was reported that both pure[100] and magnesium doped[101] Zn_2SiO_4 bulk crystals
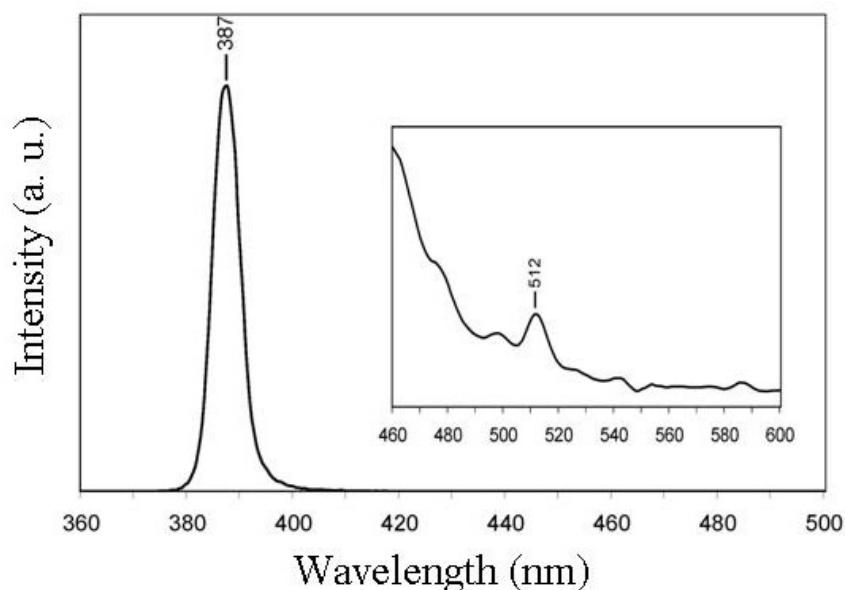
Figure 4.11: Photoluminescence spectra of high-porosity ZnO nanowires. The inset is an enlarged spectral region showing the luminescence peak contributed by Zn_2SiO_4.

have a luminescence peak at 525 nm. A shift of the peak to 512 nm in our case is possible owing to the small thickness of the Zn_2SiO_4 layer.

4.3 ZnS-ZnO Nanocables

As introduced in chapter 2, as-synthesized oxide nanobelts are pure, structurally uniform, single crystalline and mostly free from dislocations. They have a rectangular cross-section with typical widths of 100-300 nm, width-to-thickness ratios of 5-10 and lengths of up to a few millimeters.[28] The nanobelts are an ideal system for fully understanding dimensionally confined transport phenomena in functional oxides and building functional devices along individual nanobelts. Using as-synthesized ZnO nanobelts as a template, nanostructured ZnS nanocables and nantubes have been synthesized by chemical substitution reactions.[95] This template-assisted method is

demonstrated to be a unique technique for producing morphology controlled ZnS

nanostructures and can be a general approach for fabricating porous nanobelt based

porous structures of compound semiconductors.

4.3.1 Fabrication Method

The ZnO nanobelts were synthesized by a solid-vapor process using the

experimental setup described in Chapter 3.[28] Saturated H_2S-H_2O solution (>0.4%) was

filtered before reaction. 50 mg of ZnO nanobelts was added into 3 mL of pure ethanol.

After 10-minutes ultra-sonicating, a well-dispersed ZnO nanobelts suspension was

obtained, into which 30 mL of saturated H_2S solution was added. Then, the mixture was

sealed and allowed to stand for 24 hours at room temperature. The resulting ZnS-ZnO

nanocables and nanotubes were cleaned through three cycles of centrifugation (3000 rpm

/ 15 min) and redispersion in 10 mL of water, and dried in an isothermal oven at 90 ºC.
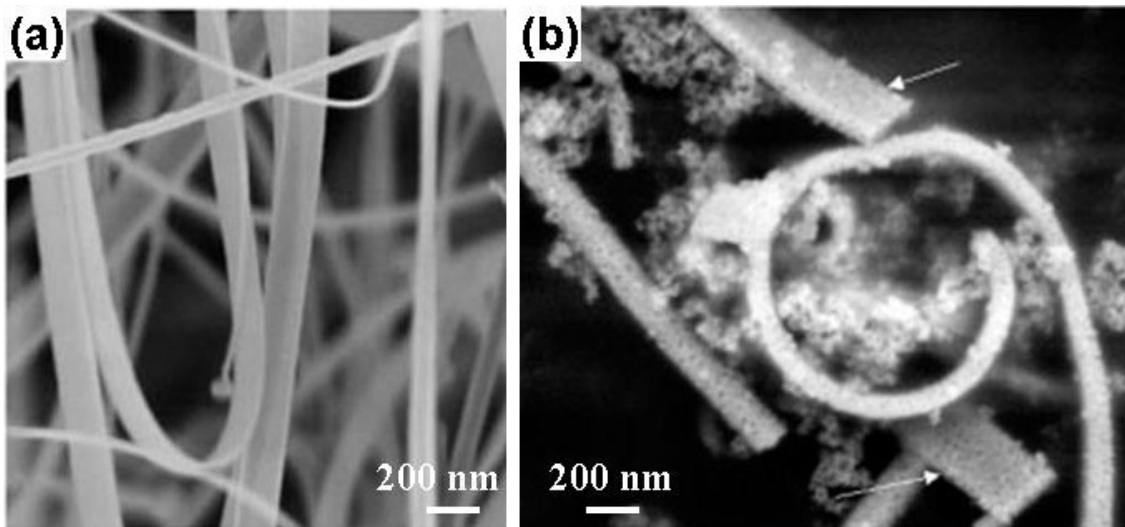
Figure 4.12: SEM images of ZnO nanobelts (a) pre- and (b) post-reaction with H2S showing the change of morphologies.

4.3.2 Structure Characterization

The structure change of the ZnO nanobelt prior and post reaction with H_2S was first observed in SEM. Figure 4.12a shows an SEM image of the as-synthesized ZnO nanobelts. A TEM image of the nanobelts is given in Figure 4.13a, clearly showing its uniformity in shape. The contrast observed on the nanobelts is due to bending induced strain, which is the so-called bending contour in electron diffraction.

Based on the geometrical shape of the nanobelt template, we anticipate receiving ZnS nanostructures based on reaction:

$$ZnO + H_2S \rightarrow ZnS + H_2O \qquad (4.3)$$

Figure 4.12b shows an SEM image of the converted ZnS nanobelts. Indeed, besides some particle shaped reaction byproducts, nanobelts of ZnS have been formed, as indicated by arrowheads. However, the nanobelts exhibited porous surfaces with pore sizes of ~ 30 nm. A rolled nanobelt is also presented in the image, which was possibly produced by the reaction-induced surface tension; such a shape was rarely observed for the as synthesized ZnO nanobelts. TEM analysis shows that the converted ZnS nanobelts have two types of structural configurations: rectangular ZnO-ZnS nanocables and ZnS nanotubes.

Figure 4.13b shows a low magnification TEM image of the ZnO-ZnS nanocables, with a single crystal ZnO as the core and the nanostructured ZnS as the shell. The interface between the shell and the core is fairly sharp and there appear no intermediate layer. A clearer picture of the structure is given in Figure 4.13c, which displays a composite nanocable with a broken ZnS surface layer. Electron diffraction recorded from the nanocable display a spotted pattern that corresponds to the $[2\bar{1}\bar{1}0]$ zone axis of ZnO and a set of ring diffraction pattern, which fits very well to zinc blend structured ZnS. This is consistent with other studies that, for small particles, low temperature synthesis forms zinc blend structure[102], while high temperature synthesis results in Wurtzite
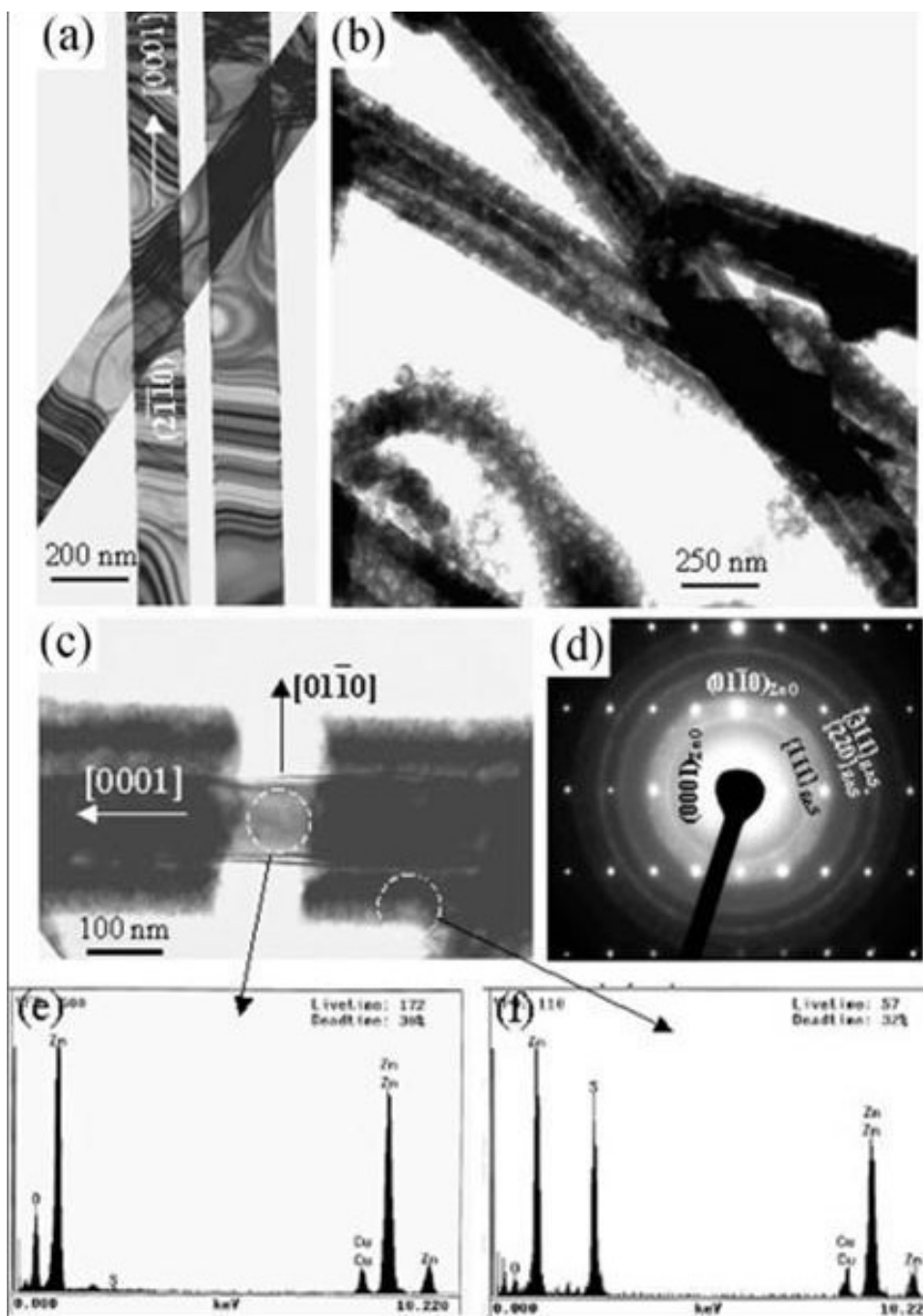
Figure 4.13: TEM images of ZnO nanobelts (a) pre- and (b) post-reaction with H$_2$S, showing the formation of ZnO-ZnS nanocable structure. (c) A ZnO-ZnS nanocable structure with a broken ZnS shell, and (d) a corresponding electron diffraction pattern recorded from the region, showing the present of a single-crystal ZnO core and the nanostructured ZnS shell. (e,f) EDS spectra acquired from the regions indicated in (c), which prove the local chemical position (the C and Cu lines come from the supporting films and copper grid used for TEM analysis, respectively).

structure[103]. Real space distances measured from the rings also fit the expected interplanar spacings for ZnS. EDS analysis shows that the core is mainly composed of Zn and O, and the shell is Zn and S (The Cu and C signals are from the TEM grid) (Figures 4.13d, 4.13e). Therefore, the core is single crystalline ZnO and the shell is nanocrystalline ZnS.

The other structural configuration is ZnS nanotubes, as shown in Figure 4.14a. The tubular shape of the ZnS nanostructured wall is apparent, and there is some porosity in the tube wall. The wall thickness can be as thick as ~100 nm and as thin as 30 nm (Figure 4.14b). Electron diffraction shows the random orientations of the ZnS nanocrystallites.

High-resolution TEM shows that the ZnS layer is composed of small size nanocrystals of an average size ~ 7 nm (Figure 4.15). The lattice symmetry from a [110] projected image (inset) displays the two sets of {111} fringes and {002} fringes.
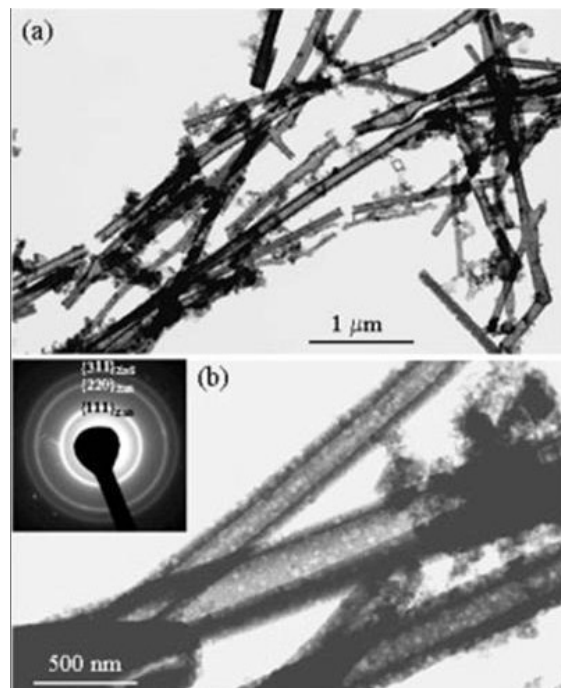
Figure 4.14: Low-magnification and higher magnification TEM images of ZnS nanotubes. The inset is an electron diffraction pattern recorded from the tubes, which can be indexed to be ZnS zinc blend structure.
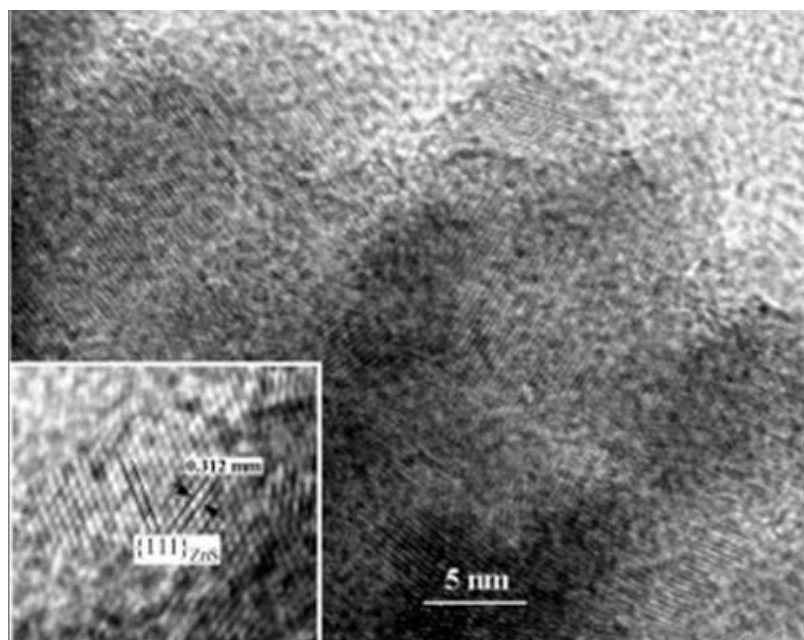
Figure 4.15: High-magnification TEM image of ZnS nanocrystallites in the shell of a ZnO-ZnS nanocable, showing their grain size, crystallinity, and distribution.

The conversion of ZnO nanobelts into ZnS nanocrystallite structured nanocables and nanotubes occurred in solution. The nanocable is formed by a direct reaction of H_2S with the surface layer of ZnO with the presence of water as follows:

$$ZnO + H_2O \rightarrow Zn^{2+} + 2(OH)^- \tag{4.4}$$

$$H_2S \rightarrow H^+ + (HS)^- \rightarrow 2H^+ + S^{2-} \tag{4.5}$$
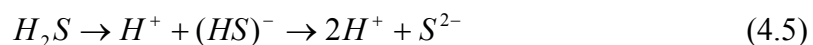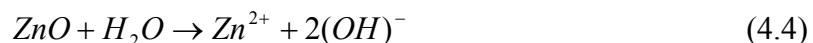
Due to the limited solubility of ZnO in water, the reaction is essentially a substitution reaction, thus, the nanocable still preserve the rectangular cross-section. The pores in the structures are produced due to two factors. The excess H_2O produced in the reaction may present in the structure and form the pores. From the structural point of view, ZnS has the zinc blende structure (cubic) with a = 0.54109 nm, ZnO has the Wurtzite structure (hexagonal) with a = 0.3249 nm ad c = 0.52065 nm; both of them are incompatible in structure. Thus, the substitution reaction is unlikely to produce single

79

crystalline ZnS. The formation of nanocrystallites is expected especially when the reaction temperature was at room temperature.

The formation of nanotubes is possible if the Zn^{2+} and $(OH)^-$ ions are mobile in the solution, so that they can diffuse through the porous ZnS wall and combine with the H^+ and S^{2-} ions in the solution, resulting in the formation of an empty tubular structure.

4.3.3 PL Properties

PL spectra were acquired at room temperature by placing ZnO nanobelts on an Al_2O_3 substrate, and the data shown are the processed results that have removed the contribution from Al_2O_3. PL measurements of ZnS-ZnO nanocables and the standard ZnS were performed on their dry powders, respectively. Photon excitation was stimulated using a Beamlok 2085-15 Ar ion laser (275 nm) and the spectra were acquired by an Isa 270m spectrometer and photomultiplier tube (PMT).
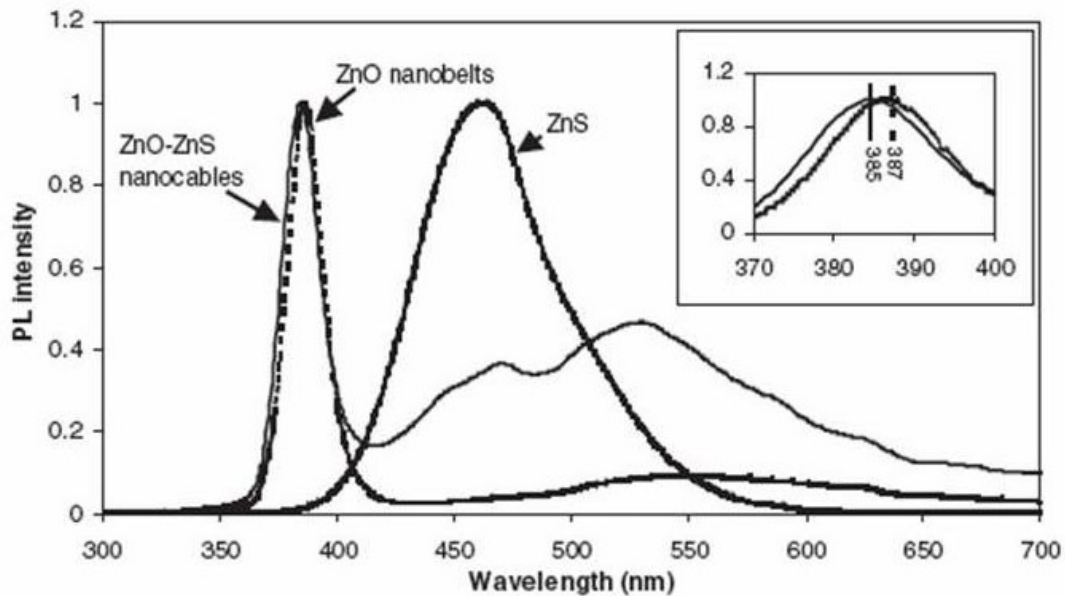
Figure 4.16: Photoluminescence spectra acquired from the as-synthesized ZnO nanobelts, the standard ZnS sample, and the ZnO-ZnS nanocables. The inset is the enlargement of the peaks around 385 nm, showing a ~2nm blue shift for the ZnO-ZnS nanocables.

A comparison of the PL spectra recorded from the as-synthesized ZnO nanobelts, the ZnO-ZnS nanocables and ZnS powders is given in Figure 4.16. The peak located at ~ 385 nm corresponds to the 3.2 eV bandgap transition of ZnO. A small blue shift of ~ 2 nm for the ZnO-ZnS nanocables is observed (see the inset) that is possibly due to the reduced size of the ZnO cores especially in the thickness direction of the nanobelt. The peak located at 470 nm is contributed by ZnS, and the broad peak at 550 nm is a resultant contribution from ZnO and ZnS.

CHAPTER 5

SELF-ASSEMBLY TECHNIQUES OF NANO-PATTERNS

Before we going to the details of growing aligned ZnO nanowires, the self-assembly technique for patterning the catalysts should be introduced first in order for a good understanding of the aligning technique. All of the following three patterning techniques, including monolayer of submicron spheres, nanobowl arrays and free-standing nanobowl sheets, are based on self-assembly process. These techniques not only provided a low-cost platform to pattern the aligned nanowires, but more important, they were new approaches of integrating bottom-up and top-down processes for economical large-scale fabrication of nanodevices.

5.1 Self-Assembly of Submicron Sphere Monolayers

The self-assembly technique of monolayer of submicron sphere has been investigated for years as the template for deposition mask, which is also known as *Nanosphere Lithography* (NSL) technique. NSL is an inexpensive, inherently parallel, high-throughput, and materials general nanofabrication technique that is now being employed in laboratories around the world.[104] The basic idea of this technique is to utilize a single layer of highly-packed polymer spheres as a mask. Through the space between the spheres, materials can be deposited to generate a hexagonal dots pattern or beams can selectively etch the exposed substrate. The resultant patterns have an in-plane shape and inter-particle spacing determined by the projection of the nanosphere mask interstices onto the substrate.

The first successful large-scale monolayer of polystyrene (PS) micron sphere was achieved by spin-coating technique mimicking the process of forming a thin layer of photo-resister.[105] However, the grain size (the sphere-arrangement with the same orientation) in the as-formed monolayer is very small (mostly just a few microns). Therefore, the resulting patterns couldn't show a long-range order, which highly limited the application of those monolayers as deposition masks. Recently, the monolayer generation methods have been largely improved by many research groups for the studies of size-dependent optical[106], magnetic[107], catalytic[108], thermodynamic[109], and electrical transport[110] properties of materials. In this section, two novel processes for making sphere monolayers that were used and developed in our lab will be introduced. Both of them have successfully achieved fairly large single monolayer grains from a few hundred microns to a few millimeters.
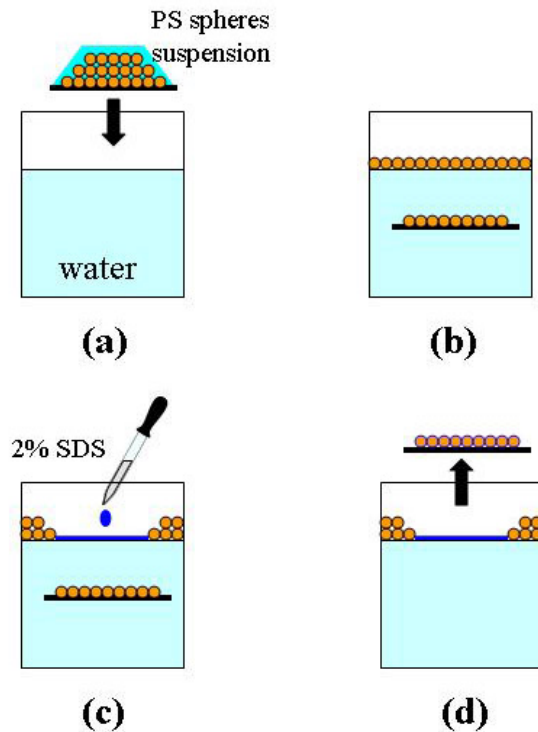
Figure 5.1: Schematic procedure of making PS monolayer on silicon substrate through substrate surface dispersing process.

5.1.1 Substrate Surface Dispersing Process

This technique was originally created in our laboratory using mono-dispersed PS spheres as building blocks. The concentration of the PS suspensions was 10% spheres and the diameter of the spheres applied for monolayer formation was 895 nm. Before dispersion, a 1 cm × 1 cm single-crystal silicon substrate was sonicated for 20 minutes in a 2% Hellmanex II solution to achieve a completely hydrophilic surface. The procedure has four steps as shown in Figure 5.1 schematically.

(1) 1 to 2 drops of the PS sphere suspension was applied to the surface of the substrate. After holding the substrate stationary for ~1 minute to obtain a good dispersion and a full coverage of the suspension on the substrate, the substrate was then slowly immersed into deionized water (Figure 5.1a).

(2) Once the suspension contacted the water's surface, PS spheres was quickly dispersed onto water surface due to the concentration and surface tension gradient until only a single layer of spheres left on the substrate surface. Then the substrate was continuing immersed into water, where the monolayer on the substrate was protect (Figure 5.1b).

(3) A few drops of 2% dodecylsodiumsulfate (SDS) solution were slowly added to the water surface to change the surface tension. The layer of PS spheres that remained suspending on the water surface was immediately pushed aside due to the change of surface tension. As a result, a clear area was created on the water surface, where the surface tension had been modified by the surfactant (Figure 5.1c)

(4) The substrate was lifted up through the clear area. No additional PS spheres were dispersed into water from the substrate due to the coverage of SDS (Figure 5.1d). Moreover, some SDS was transferred to the PS sphere monolayer during the lifting and helped to binding the spheres together. The substrate was subsequently dried in air during sonicating to avoid sphere

clustering, thus a monolayer of PS sphere was eventually achieved. Since the monolayer of PS spheres was directly formed on the substrate surface, this process was named as *substrate surface dispersing process* (SSDP).
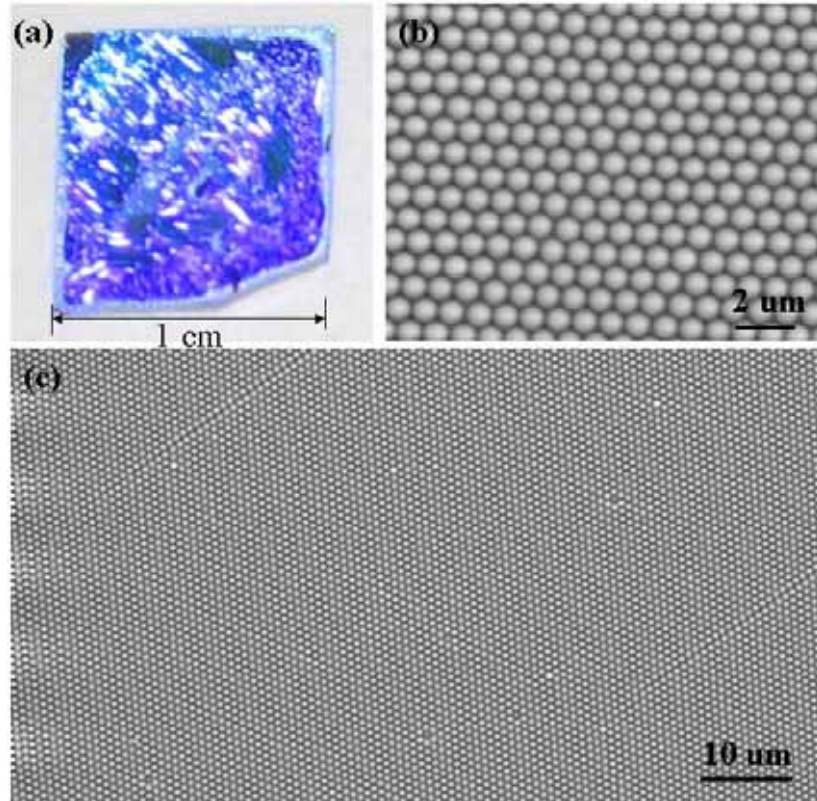
Figure 5.2: (a) Optical image of a monolayer of self-assembled polystyrene submicron spheres on an alumina substrate. (b, c) Low and high magnification SEM images, respectively, of a selfassembled monolayer of polystyrene spheres.

Figure 5.2a shows an optical image of the self-assembled monolayer structure formed by this technique. The substrate was 90% covered by the monolayer while the different colors represent different domains of the monolayer, which were formed as a consequence of different orientations of the sphere arrays. The area of a single domain can reach a few square millimeters. The detailed organization of the spheres was investigated by SEM. Figure 5.2c is a low magnification SEM image, which shows a relatively large area of the self-assembled monolayer. The ordering is reasonably good

85

although point defects and stacking faults are observed in some areas, which are produced by a variation in sphere size. A closer examination presented in figure 1b shows a perfectly ordered array.
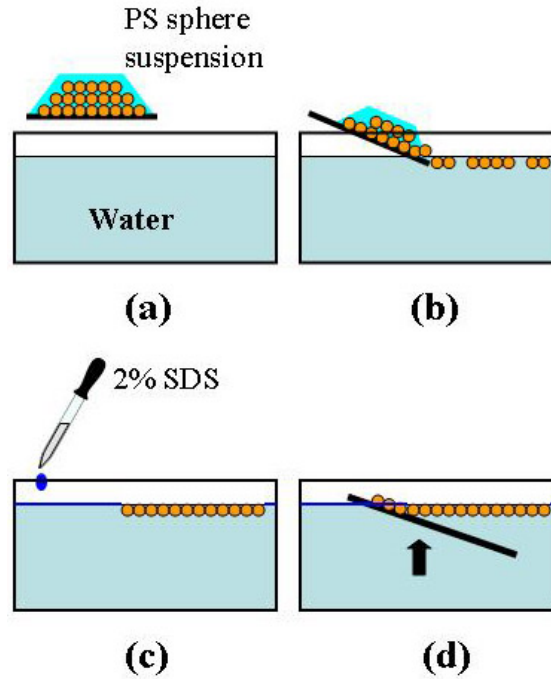
Figure 5.3: Schematic procedure of making PS monolayer on silicon substrate through water surface dispersing process.

5.1.2 Water Surface Dispersing Process

Although the SSDP can provide a fairly large single grain monolayer, a similar process has been developed to increase the single grain size into millimeter or even centimeter regime. In this process, 10% (by weight) mono-dispersed PS spheres (500 nm) water suspension was first diluted by mixing with equal amount of ethanol. A 2 cm × 2 cm piece of (100) orientated silicon substrate was clean by ultrasonicating in acetone for 30 minutes before using. As shown in Figure 5.3 schematically, four major steps are included for making monolayers.

(1) A small drop of the ethanol diluted PS sphere suspension was applied onto the pre-cleaned silicon substrate and evenly distributed to cover the whole substrate surface using a plastic pipette tip. A glass vessel with a diameter of 15 cm was filled with deionized (DI) water and sit still to acquire a steady water surface (Figure 5.3a).

(2) The silicon substrate was slowly tilted and touched the water surface with one side, at which the PS spheres can quickly disperse away from the substrate forming an unordered monolayer on water surface. In order for a complete dispersion, the substrate was slowly immersed into the water until all the PS spheres were distributed (Figure 5.3b).

(3) To consolidate the spheres, the water surface tension was modified by the adding one drop of 2% SDS solution into the vessel. Thus, a large area of monolayer with highly ordered spheres was obtained and freely floated on the water surface (Figure 5.3c).

(4) The floating monolayer can be lifted up by another piece of silicon wafer and formed a highly ordered monolayer on the wafer surface after drying in air (Figure 5.3d). During this process, the monolayer of PS spheres was first assembled on the water surface, thus, it was named as *water surface dispersing process* (WSDP).

In this process, a much larger monolayer can be formed on the water surface, which can be lifted by multiple substrates with smaller sizes. So, it is more efficient method for parallel assembly of monolayer structures. However, the dispersion of PS spheres is highly depended on their size and the water to ethanol ratio. In order to acquire monolayer with different sized PS sphere, more investigations are needed to find out the optimal ethanol percentage corresponding to different sphere sizes.

5.1.3 Comparison of These Two Processes

Although both processes described above have been successfully used for assembling PS sphere monolayer in large area, their different mechanisms equipped them with different merits. In general, WSDP is more efficient and easier to conduct, so it's more frequently used in my experiments for mask or pattern generation when the size variance was not required. However, SSDP has to be used for assembling big particles. An itemized comparison of these two processes is listed in table 5.1

Table 5.1: Comparison of SSDP and WSDP techniques.

	SSDP	WSDP
PS sphere size range	500 nm to 5μm	100 nm to 1μm
Optimal sphere size	~1μm	~500 nm
Substrate requirement	Complete hydrophilic	Hydrophilic/Hydrophobic
Substrate coverage	>90%	100%
Single grain size in monolayer	1 mm^2	1 cm^2
Defects in monolayer	Point, line, multilayer	Point, line, overlay spheres

Shown by table 5.1, WSDP exhibits more advantages over SSDP. Because in SSDP, the substrate performed as sphere distributor as well as monolayer supporter, it has to be complete hydrophilic in order for a good monolayer quality. In WSDP, by decoupling the sphere distribution function from monolayer lifting, more flexibility is added to the choice of supporting substrates. For example, a large area monolayer has been successfully transported to a hydrophobic polymer coated substrate.[111]

WSDP is better for assembly smaller sized sphere, while SSDP is bigger size favorable. This is because in WSDP, the high-packed arrangement of sphere was self-assembled on water surface by "pushing" from surfactant molecules. The big spheres were more difficult to be pushed around forming an ordered structure. On the contrary,

SSDP requires the spheres to stay still on the substrate and additional spheres to diffuse away. When the spheres were too small (<500 nm), incomplete monolayer or disordered structures were more likely to be formed.

In SSDP, a highly ordered monolayer was assembled during the drying process; while in WSDP, the highly ordered structure was formed on water surface before lifting. A size-shrinkage was always induced when the spheres re-arranged from disordered to ordered structure. Thus, it was inevitable that the substrate cannot be fully covered by the ordered monolayer through SSDP, of which the highest coverage was around 90%. However, 100% substrate coverage could easily be achieved through a WSDP due to the pre-assembled ordered structure before drying. The bigger single grain size of WSDP is also attributed to this advantage.

Due to the sphere size variation, defects are inevitable in the monolayer assembled through either process. The most common defects are point defects and line defects. Many experiments revealed that the densities of those defects are not depend on how the monolayer is formed but significantly relies on the uniformity of spheres. Double-layer or multi-layer was usually found in the monolayer formed by SSDP due to the incomplete dispersing of spheres. WSDP can achieve very large area of pure single layer of spheres. However, additional sphere may also be pushed onto the monolayer when it's floating on water surface. This issue would become more significant when the surfactant was over used.

In general, WSDP exhibits more advantages over SSDP. When the sphere size was within the applicable region of WSDP, this process was always used. Nevertheless, SSDP was still a good substitution to compensate the size limitation of WSDP. Both techniques were investigated in my experiments and contributed to pattern- or template-generation in a wide size range.

5.2 TiO₂ Nanobowl Arrays

As introduced in the previous section, monolayer self-assembly of PS submicron spheres on a flat substrate is an effective and economic technique for fabricating patterns on a relatively large scale. In addition to this versatile self-assembly technique, atomic layer deposition (ALD), in which film growth is a cyclic, multi-step process of alternating surface-limited chemical reactions, has been demonstrated to be a powerful technique for fabrication of high-quality and multifunctional thin films on various substrates. A diversity of nanostructures can be synthesized using ALD owing to its wide operation temperature and precursor adaptability. For example, by controlling the thickness of the uniformly deposited films, template assisted ALD process has been applied to the fabrication of inverse opal structures and 1D nanostructures. By combining the monolayer self-assembly technique and ALD, large-area TiO₂ nanobowl arrays have been first-time created as a new member in the family of nanomaterials.[112] The TiO₂ nanobowls exhibited smooth surfaces and uniform size and thickness, which can be used as ultra small containers for holding fluid of nano-scale volume or as size selectors and filters for submicron particles. The approach could be extended to a wide range of coating materials and substrates with controlled wall thickness and size. Before going to the detailed fabrication procedure, another key technology—ALD technique that was used to grow the nanobowls will be introduced first.

5.2.1 Atomic Layer Deposition Technique

ALD is a modification of the chemical vapor deposition process that is used to deposit monolayer films. The process was originally called atomic layer epitaxy (ALE) due to the epitaxial nature of the growth.[113] The more general term of ALD is used to

describe deposition of films where the film structure does not necessarily have the same structure as the growth substrate. ALD was originally developed for the deposition of ZnS:Mn and amorphous Al_2O_3 films. Materials that can be deposited using ALD include oxides, nitrides, II-VI compounds, III-V compounds, and single elements.[114] ALD films can be grown on amorphous and single crystal substrates.
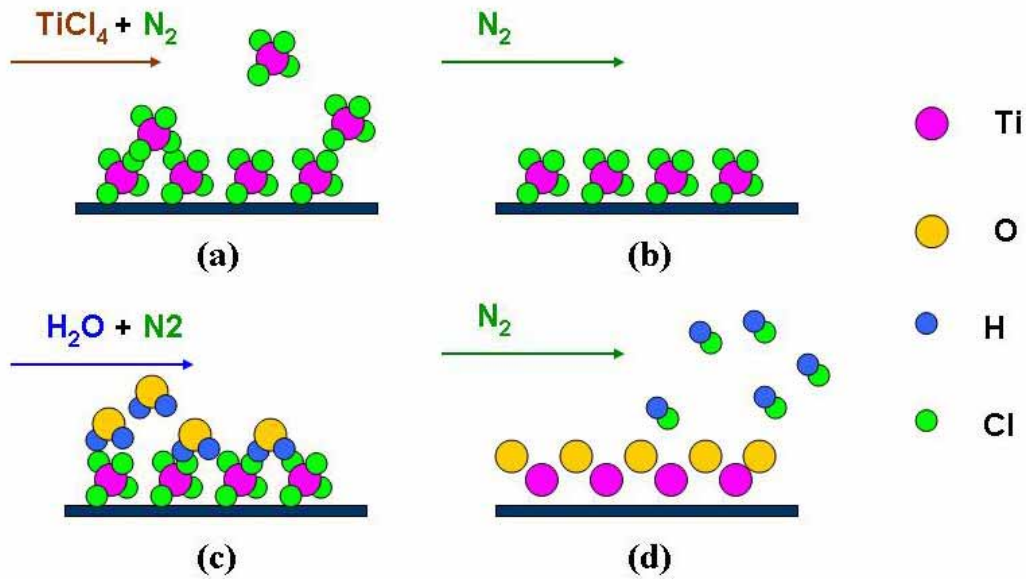
Figure 5.4: Schematic mechanism of forming TiO_2 atomic layer on a flat surface in ALD technique using $TiCl_4$ and H_2O as precursors.

The ALD process proceeds through saturative steps resulting in a constant thickness increase of conformal films. Using the formation of TiO_2 films as an example, a typical ALD process is schematically shown in Figure 5.4 following the chemical equation:

$$TiCl_4(g) + 2H_2O(g) \rightarrow TiO_2(s) + 4HCl(g) \qquad (5.1)$$
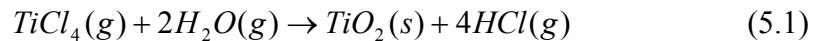
Metal precursor ($TiCl_4$) is first pulsed into the process chamber where it is chemisorbed on the surface of the substrate (Figure 5.4a). The chamber is then purged to remove any precursor still in the gas phase as well as any physisorbed reactant (Figure 5.4b). The second pulse of nonmetal precursor (H_2O) is now introduced into the chamber. The

nonmetal gas chemisorbs on the surface and undergoes an exchange reaction with the metal layer forming a metal-oxide molecular thin film (Figure 5.4c). Gaseous byproducts (HCl) are also produced which are removed with the subsequent purge. Any unreacted gas and physisorbed nonmetal reactant is also removed from the chamber during the purge (Figure 5.4d). Films are deposited one layer at a time due to the chemisorption of the reactants. Therefore, ALD is a self-controlling process.

ALD precursors must be volatile, thermally stable, and have rapid reaction with substrate surface groups.[115] The precursors must be thermally stable so that they do not decompose at higher temperatures leading to multilayer growth instead of the self-limited ALD growth. In addition to thermal stability, the precursor should not dissolve into the film or etch the film. Dissolution of the precursor into the film is another means for destroying the self-limiting growth mechanism, whereas precursor etching will inhibit film growth. However, dissolution of the precursor is rarely reported in the literature. Unlike CVD, aggressive reactions are preferable for ALD because of quicker reactions and shorter cycle times.

A wide variety of metal precursors have been studied, which fall into five categories: halides, alkyls, alkoxides, electropositive metals, and cyclopentadienyl compounds. Halide research has focused mainly on chlorides, but also on fluorides, bromides, and iodides.[115] Elemental metals such as Zn, Cd, and Hg have also been used as ALD sources. A limited number of precursors have been investigated for the nonmetal source. The majority of research has focused on hydrides such as H_2O, H_2S, NH_3, and AsH_3. Hydrogen peroxide (H_2O_2) has also been used as a nonmetal source.

5.2.2 Fabrication Procedure of TiO$_2$ Nanobowl Arrays

The experimental procedure for fabricating TiO2 nanobowl arrays includes four steps, as illustrated in Figure 5.5
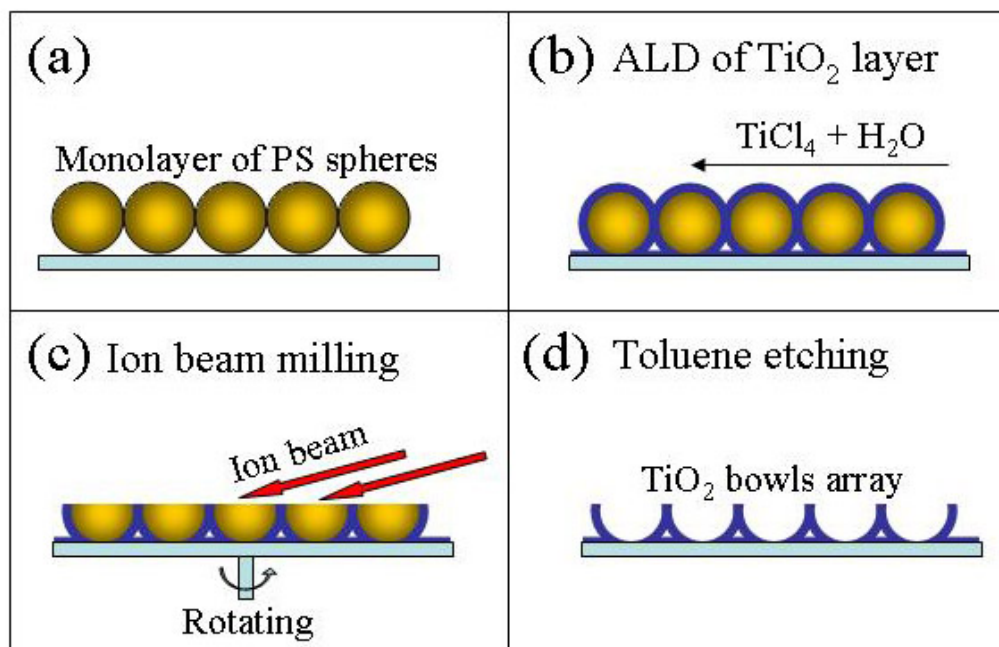
Figure 5.5: Experimental procedure for fabricating TiO_2 nanobowl arrays.

(1) *Self-assembly of a monolayer of polystyrene spheres.* Using WSDP that was explained in the first section, a large-area monolayer of PS spheres within a size of 500 nm was self-assembled on a 1 cm × 1 cm a-plane orientated sapphire substrate with hydrophilic surface (Figure 5.5a).

(2) *ALD of amorphous TiO₂ thin films.* The substrate with a monolayer of PS spheres was placed at the center of a quartz ALD chamber, which was kept at 80ºC during the entire growth process. Then, pulses of $TiCl_4$ vapor and H_2O vapor were introduced sequentially into the chamber under a vacuum of 4.5 torr. The pulse duration was 4 second, and the pulses were separated by N_2 purging gas for 10 second. A TiO_2 layer was slowly grown on the surfaces of the PS spheres and the substrate at a growth rate of 0.12 nm/cycle. The growth was terminated after 200 pulse cycles, which produced a uniform amorphous

TiO$_2$ layer of 24 nm in thickness deposited around the PS spheres (Figure 5.5b).

(3) *Ion milling.* An ion milling machine that was originally used for preparing TEM samples was used to remove the top half of the TiO$_2$ layer coated PS spheres. The ion beam with an intensity of 0.4 mA was generated by a high-voltage of 5 kV and stroke onto the sample surface at a grazing angle of 15º while the sample was continuously rotated. After 20-minute milling, the top half of the spheres was evenly removed (Figure 5.5c).

(4) *Toluene etching and annealing.* The PS hemispheres that left on the substrate were etched away by sonicating the substrate in toluene for 2~3 minutes, resulting in highly-ordered arrays of TiO2 nano-bowls (Figure 5.5d). The amorphous TiO2 nano-bowls can be converted into crystalline nano-bowls by annealing. After annealing at 850ºC for 2 hours in air, nano-bowls composed of nanocrystalline anatase TiO2 were received.

5.2.3 Morphology and Structure Characterization

The experimental results of each step described above were examined by SEM and the corresponding images are illustrated in Figure 5.6. Figure 5.6a shows a monolayer of self-assembled PS spheres coated with TiO$_2$, which exhibits a very smooth surface due to the low growth temperature. The spaces between the spheres are partially filled as a result of the TiO$_2$ growth. The sample surface after ion milling is shown in figure 5.6b. The bright triangles are TiO$_2$ shells with a uniform thickness of ~24 nm. This reveals that the growth per cycle of amorphous TiO$_2$ on the PS spheres is about 0.12 nm at 80ºC, a little higher than the growth rate at 100ºC, as expected from the increased number of hydroxyl groups present on the surface at low temperatures. The dark region
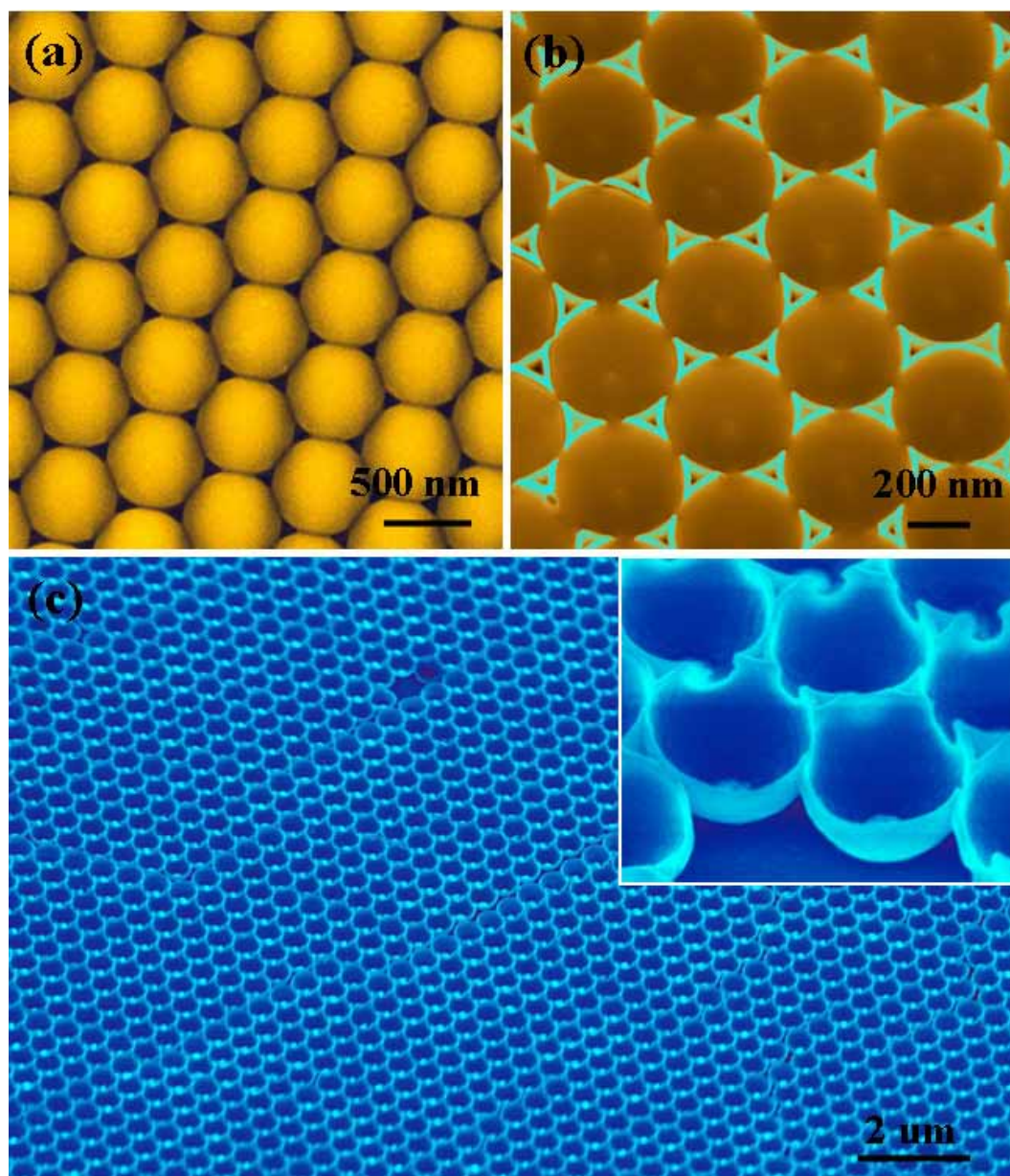
Figure 5.6: SEM images at each step of the nanobowl fabrication process: (a) Monolayer self-assembly of polystyrene spheres coated with TiO_2; (b) Ion beam milled surface of TiO_2 coated polystyrene spheres; (c) Low- and high- (inset) magnification SEM image of TiO_2 nanobowl arrays.

among the triangles is the milled polystyrene surface, which is slightly lower than the

TiO_2 surfaces owing to a higher milling rate of polystyrene.

Highly ordered arrays of TiO_2 nano-bowls were fabricated after toluene etching.

As shown in Figure 5.6c, the periodic structure was well preserved during the entire

process. No distortion was observed on the thin walls of TiO_2 after sonicating in toluene

for 1.5 minutes. The bright spot at the center of each bowl is the exposed Al_2O_3 substrate,

which was masked from TiO_2 deposition at the PS sphere contact points. The insert in

figure 5.6c is a high-magnification image of the TiO_2 bowls, from which the spherical

shape and the smooth interior surface of the bowls can be clearly seen. The notches

between the bowls are the result of the contact point between PS spheres.
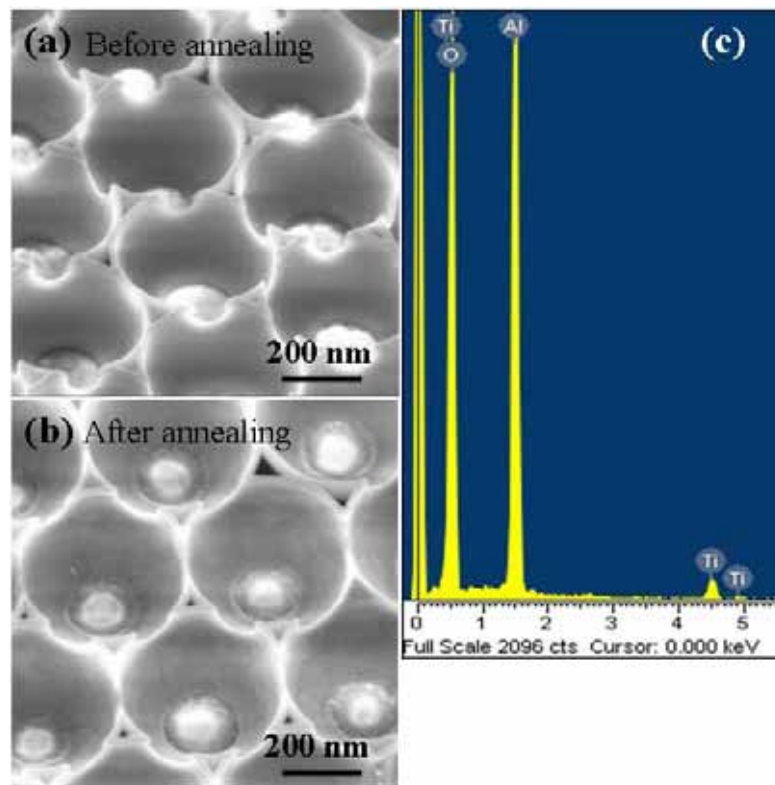
Figure 5.7: High-temperature annealing was used to transform the amorphous structured walls into polycrystalline walls. TiO_2 nanobowls before (a) and after (b) annealing at 850 °C. (c) EDS spectra recorded from the TiO_2 nanobowls after annealing.

The amorphous TiO_2 nano-bowls can be converted into polycrystalline nano-bowls by annealing. After annealing at 850ºC for 2 hours in air, nano-bowls composed of nano-crystallites were produced. Representative images of the TiO_2 bowls before and after annealing are shown in Figure 5.7a and b, respectively. By comparing these two pictures, no obvious size shrinkage was induced: the diameter of the bowls remains at ~460 nm and the thickness of the TiO_2 wall measured at the triangular region is also constant at 24~25 nm. Furthermore, the annealing process does not obviously change the smoothness of the interior surface, although there is a small roughness around the contact region between the TiO_2 bowls and the substrate. The chemical composition of the bowls after annealing is confirmed by EDS (Figure 5.7c). Besides Ti and O peaks, Al is also shown attributed to the substrate.
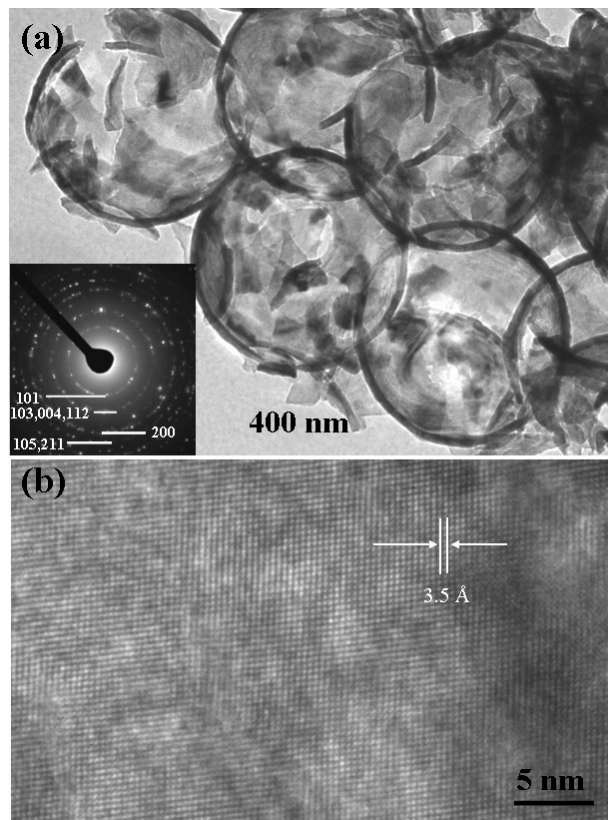
Figure 5.8: Crystallographic structure of the TiO_2 nanobowls. (a) Low magnification TEM image of TiO_2 nanobowls. (inset) Diffraction pattern recorded from TiO_2 nanobowls. (b) High-resolution TEM image of the wall of a TiO_2 nanobowl.

The crystallography of the annealed TiO_2 was examined using a Hitachi HF2000 TEM. A low-magnification TEM image is shown in Figure 5.8a. The TiO_2 bowls were broken for TEM the specimen preparation. However, their spherical shape can still be seen. The strong contrast of the wall is due to the larger projected mass thickness. The inset in Figure 5.8a is a typical diffraction pattern recorded on the TiO_2 bowls indicating their polycrystalline structure. The anatase crystal structure is confirmed by the diffraction pattern. Although the TiO_2 bowls exhibit a polycrystalline structure, their grain size is fairly large, typically 50 nm. A high-resolution TEM image recorded from a TiO_2 nanocrystal is shown in Figure 5.8b. The uniform lattice fringe spacing is indicative of the high quality of the nanocrystal. The distance between each fringe is about 3.5 Å corresponding to the inter-planar distance of {101}.

5.2.4 Potential Applications

As one of the important functional semiconductors, TiO_2 exhibits promising applications in solar cell[116], photocatalytic[117], photonic crystal[118], and photovoltaic[119] technology. As described above, robust and highly-ordered anatase TiO_2 nano-bowl arrays have been successfully fabricated, and their larger open surface area that could significantly increase the efficiency of surface related phenomena. The fabrication technique could also be applied to different substrates that have smooth and hydrophilic surfaces, such as silicon, glass, metals or even polymer. This will broaden its application in various fields. The nano-bowls could also be lifted-off the substrate to form monolayer submicron filters. Moreover, the thickness of the TiO_2 wall can be precisely tuned by varying the number of ALD cycles, and the bowl size can be adjusted by using different sized PS spheres suing the formation of the templates. Therefore, these nano-bowl arrays could be good candidates as size separators and containers for fine particles, or even for
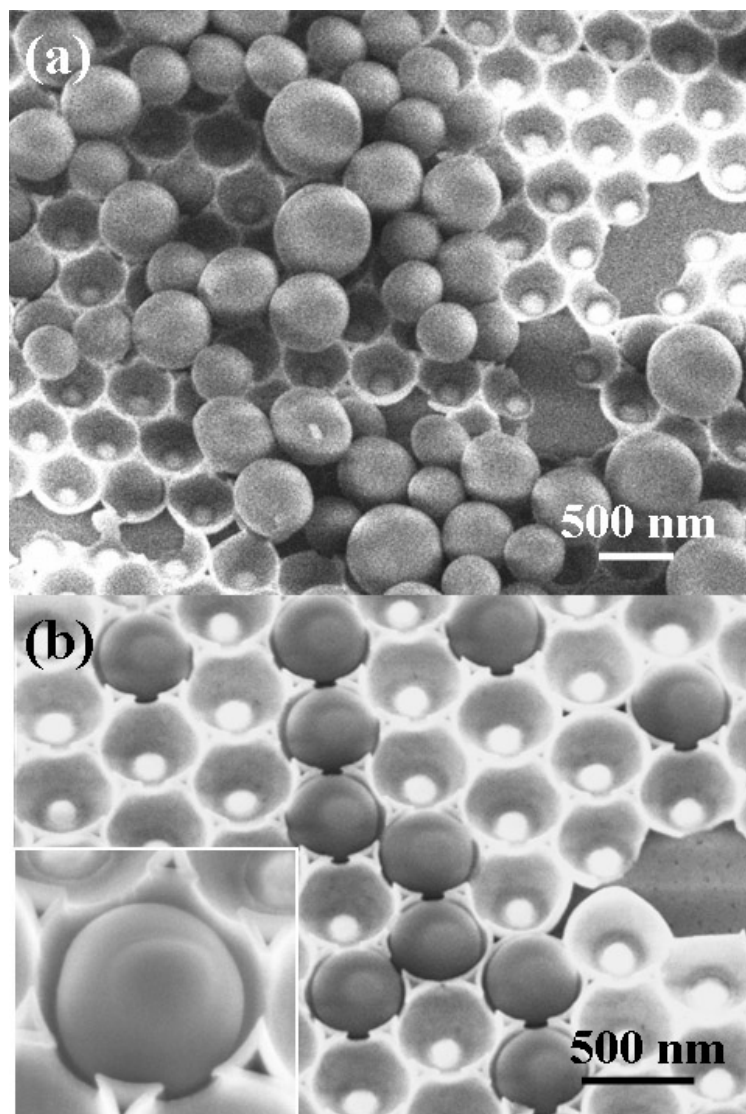
Figure 5.9: (a) Different sized PS spheres lying on the top of a TiO_2 nanobowl array after applying a drop of PS spheres with mixed sizes. (b) Only the smallest PS spheres remain after washing with ethanol. (inset) A 450 nm PS sphere confined inside a TiO_2 nanobowl.

bio species such as cells if the interior surface is coated with functional groups. The following experiment demonstrates this potential application.

A mixture of PS spheres with different sizes was used to demonstrate that the TiO_2 bowls can be used for selecting monosize submicron spheres. In the following experiment, equal amount of PS spheres of diameters 450 nm, 590 nm, 680 nm and 820 nm were added into 10 mL of ethanol, forming a 0.5% (by weight) PS spheres suspension. One droplet of the suspension was applied onto the crystallized TiO2 bowls and sonicated for 15 seconds. As shown in Figure 5.9a, PS spheres that are larger than the inner diameter of the TiO_2 bowls (~ 460 nm), are distributed on the top of the bowls. Only the smaller PS spheres with a diameter of 450 nm fell into the TiO_2 bowls. Then, a small amount of ethanol was sprayed onto the substrate to wash away the PS spheres. All of the larger spheres were flushed away, and only the small sized spheres remained inside the bowls (Figure 5.9b). The inset in Figure 5.9b shows that a PS sphere that is located inside a TiO_2 bowl is well surrounded and protected so that it was not flushed away by the ethanol. Due to the low concentration of PS spheres in suspension, only a small percentage of the TiO_2 bowls were occupied. A repeat of the above process may select all of the smaller spheres. This simple experiment illustrates that TiO_2 bowls arrays are useful for selecting particles smaller than their inner diameter.

In general, the large-area highly-ordered TiO_2 nano-bowls are a brand new morphology in the world of nano. Owing to the wide applications of TiO_2 crystals, this bowl structure could potentially be applied to solar cell, photocatalysis and photovoltaic technology with enhanced properties. The nano-bowls have been demonstrated for selecting spheres smaller than the inner diameter of the bowls. The approach presented in this section could be extended to a wide range of coating materials and substrates, with controlled wall thickness and size.

5.3 Large-Scale Free-Standing Nanobowl Sheets

Nanotechnology is experiencing a fast development in laboratories as well as in industry. Both bottom-up and top-down approaches have been employed for fabrication of nanometer-scale materials and devices[4]. In order to take advantage of both approaches and eventually lower the cost of production, techniques can be combined to generate patterns utilizing a top-down process, such as lithography, and control the local structure through a bottom-up process, such as self-assembly. However, challenges still remain in integrating bottom-up and top-down processes for economical large-scale fabrication of nanodevices. Since the cost increases exponentially when the pattern size created by lithography drops below 100 nm, it will greatly facilitate the commercialization of nanotechnology if a low-cost large-scale bottom-up process can be developed to extend or replace lithography techniques in the nanometer size range. In section 5.2, highly-ordered TiO_2 nanobowl arrays has been shown as a successful example in nano-patterning through a low-cost self-assembly technique. Although the nanobowl arrays have been demonstrated as a good candidate for surface-reaction-related nanodevices as well as a size selector, their inflexibility on substrates limits their adaptability and applications.

In this section, an improved bottom-up process will be described for fabrication of large-scale, free-standing nanobowl arrays with high flexibility in operation and manipulation. By introducing an organic buffer layer between the nanobowls and the substrate, a full layer (in centimeter range) of nanobowl arrays can be lift-up and deposited on any other substrate or even placed up-side-down forming small chamber arrays. Coating a copper TEM grid with this nanobowl sheet will be demonstrated, which can be utilized as a reusable mask for making catalyst or quantum dots arrays with precisely controlled sizes, distribution and density.[111]

101
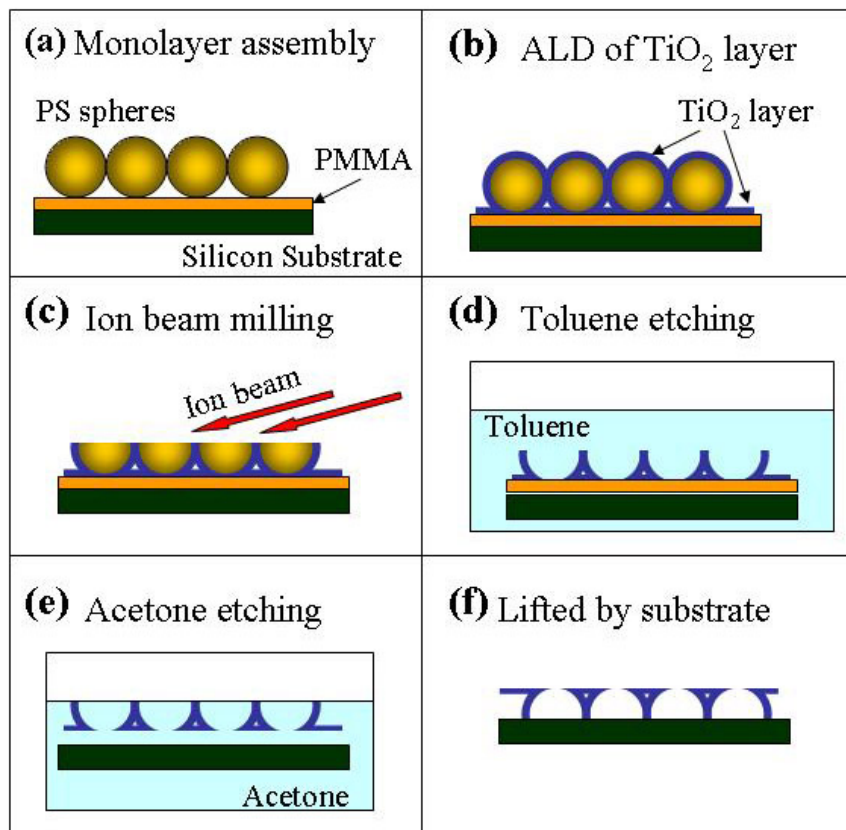
Figure 5.10: Schematic procedure for the fabrication of freestanding nanobowl sheets.

5.3.1 Fabrication Procedure

The basic fabrication strategy is based on the procedure for making regular nanobowl arrays and each step is shown in Figure 5.10 schematically. However, in order to eventually separate the nanobowl sheet from the substrate, a ~300 nm PMMA layer was first spin-coated onto a silicon substrate, which was used for supporting the nanobowl sheet, as illustrated in Figure 5.10a. A monolayer of PS spheres was self-assembled on a water surface through WSDP. Since this monolayer is easily destroyed when contacted by a hydrophobic surface, the PMMA coated silicon substrate was pre-immersed into a 2% SDS solution for 2 hours. After this treatment, a monolayer with an area of a few square centimeters can be smoothly transferred from the water surface onto

102

the PMMA layer without any distortion. A TiO$_2$ coating was then grown to a thickness of ~25 nm through a low temperature ALD process (80°C). It should be noted that the growth of TiO$_2$ occurred both around the PS spheres and on the PMMA layer, which composed spherical shells and a flat bottom surface, respectively (Figure 5.10b). The top-half of the TiO$_2$ coated PS spheres was evenly milled away by an argon ion beam in an ion milling machine (Figure 5.10c). The residual hemispheres of PS spheres were removed by toluene to achieve the nanobowl morphology (Figure 5.10d). To ensure the remaining spheres were completely removed, the substrate was normally sonicated in toluene for 2-3 minutes until bright optical diffraction from the ordered structure became clearly visible again. Although the PMMA is also soluble to toluene, it was protected by the TiO$_2$ coating and was not dissolved. By immersing the substrate in acetone overnight, the PMMA layer was slowly removed, creating a free-standing TiO$_2$ nanobowl sheet (Figure 5.10e), which floated to the acetone surface and could be lifted up by any other substrate with the bowls facing either away or toward the substrate (Figure 5.10f).
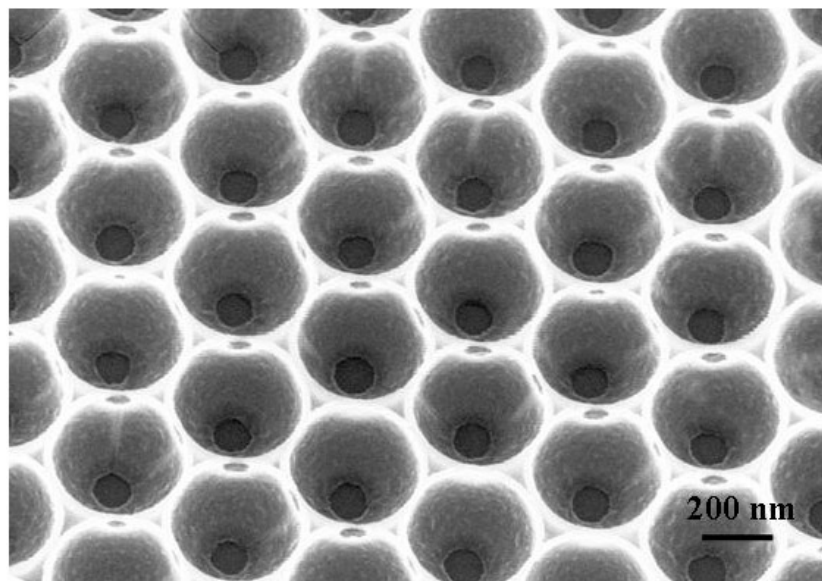
Figure 5.11: SEM image of TiO$_2$ nanobowl arrays on a PMMA layer.

103

A SEM image of as-synthesized TiO$_2$ nanobowl arrays on a PMMA layer is shown in Figure 5.11. Due to the good wetting between PS and PMMA, an almost identical and perfect small open circle was formed at the center of each nanobowl, from which the underneath PMMA layer can be seen. This shows that sonicating in toluene for a short period of time can completely remove the PS hemispheres while leaving the PMMA layer unaffected, even though both polymers are soluble to toluene. Similarly for the lift-off process in lithography, immersing in acetone for a long-time (normally around 10 hours) can slowly dissolve the PMMA layer away through the small open circles. Once the PMMA is completed removed, the nanobowl sheet separates from the supporting silicon substrate and is ready for further applications.

5.3.2 Nano-Dome Arrays

A piece of bowl-side-down nanobowl sheet is shown in Figure 5.12a, which was lifted from the acetone surface by another silicon substrate. The TiO$_2$ surface exhibits high flatness inherited from the supporting substrate. The open circles at the center of each nanobowl now become a hole-array when they are observed from the back side, while the high periodicity of the nanobowls remains unchanged. Behind the TiO$_2$ layer, all of the nanobowls are facing down and are actually supporting the whole layer from substrate. Owing to the identical height of each nanobowl attributing to the ion milling process, no fluctuation of the top layer can be observed. A high resolution SEM image of the back side is shown in Figure 5.12b, from which the identical shape and size of the holes are clearly demonstrated. Since the TiO$_2$ layer is only ~25 nm in thickness, the spherical nanobowl shape can still be seen by the electron beam through the top layer. This bowl-side-down configuration of the nanobowls is more clearly revealed by a view of the edge area (Figure 5.12c), where the smooth back of the nanobowls are exposed.
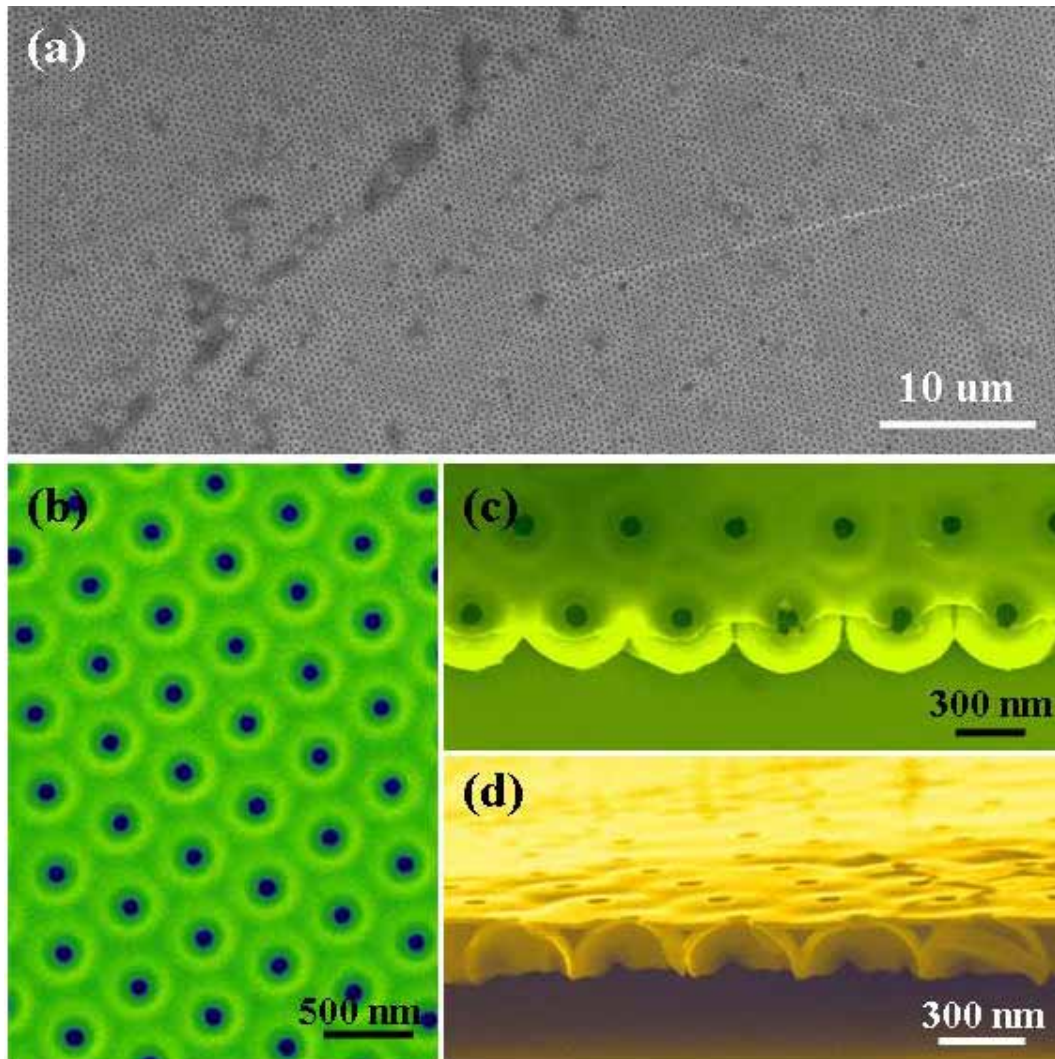
Figure 5.12: SEM images of nanobowl sheets: (a) Low magnification image of a bowl-side-down nanobowl sheet on a silicon substrate; (c) High magnification image of the back side of a nanobowl sheet; (d) Edge of a bowl-side-down nanobowl sheet; (e) Cross-section of a bowl-side-down nanobowl sheet.

From a side view of a cross section, as shown in Figure 5.12d, a good contact between the nanobowls and the substrate is evident. In this configuration, each nanobowl forms a dome with a size of a few hundred nanometers and there is only one "window" opened on the top of each dome. These domes are highly ordered and separated from each other, forming a two-dimensional nano-cell array. The cell is interconnected by a tiny tunnel at the bottom, which is actually the notch between the nanobowls resulted from the contact point between the PS spheres. On the other hand, it is also possible to completely separate each cell by milling over the contacting spot during ion milling process. Considering that the "window" is ~100 nm, which is comparable to the size of a single virus, this nano-cell array can be a good candidate for housing, filtering and separating viruses.

Because of the thin shell, the nanobowl sheet broke due to high stress when the size of a single piece was larger than ~0.3 mm^2 despite the high flexibility of amorphous TiO$_2$ layer. The general dimension was 0.5 mm x 0.5 mm for a freestanding sheet, which contained ~1 million ordered nanobowls. This is a reasonably large number considering the quantity of nano-cells that can be formed and used. However, it is still necessary to improve the size limit in order to achieve real large-scale fabrication and manipulation and eventually commercialization. The key issue is how to bind the entire sheet to an unbreakable framework, which can also be easily removed when needed.

5.3.3 Large-Scale Reusable Nano-Masks

By considering that PS does not dissolve in acetone while PMMA does, PS was chosen to be a binding material. As shown in Figure 5.13a, on top of the PMMA layer, another layer of PS (~100 nm in thickness) was spin-coated before loading the monolayer template of PS spheres. After using the procedure described above to form the hemispheres morphology shown in Figure 5.13a, the substrate was first immersed in
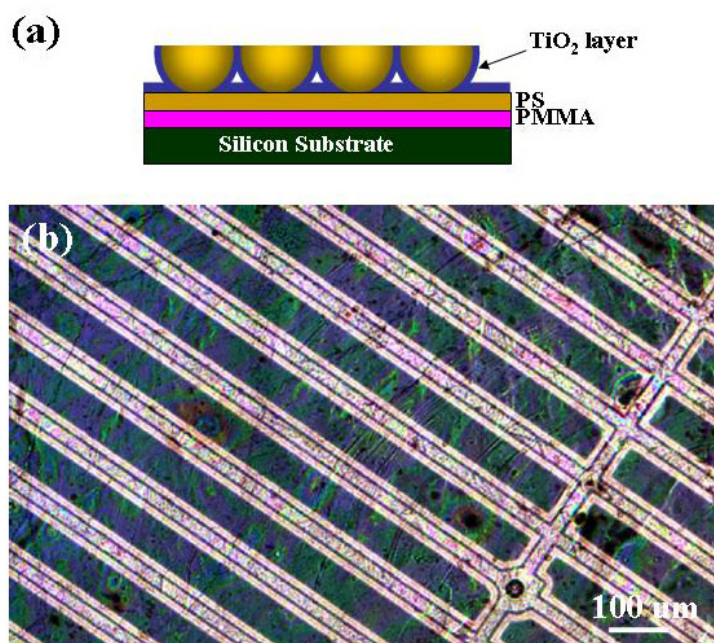
Figure 5.13: (a) Schematic of the modified configuration for fabricating stable large-area nanobowl sheets. (b) Optical image of a copper TEM grid covered by a large-area nanobowl sheet.

acetone overnight. Due to their different solubility, the PMMA layer between the silicon substrate and PS layer was completely removed so as to separate the half-sphere layer from substrate. Held together by a very flexible PS layer on the bottom, the thin TiO_2 nanobowl sheet can be made as big as a few square centimeters. This freestanding composite sheet can then be lifted up by another substrate or even a TEM grid. The final morphology of the nanobowl sheet was achieved by using toluene to remove the residual PS half spheres and the bottom PS layer. The resulting large-area nanobowl sheet did not break once supported by a solid substrate.

An optical microscope image of the nanobowl sheet supported by a copper TEM grid is shown in Figure 5.13b. The green and blue color was from light scattering upon the ordered structure. The total size of this nanobowl layer is 10 mm^2, which completely covered a standard TEM grid with a diameter of 3.05 mm. Van der Waals forces held the nanobowl sheet attached to the TEM grid, owing to the flat surface on the bottom of the

nanobowls. The open space between the copper bars is ~80 μm, which is within the size range that the TiO$_2$ layer itself can hold the nanobowls together without falling apart.
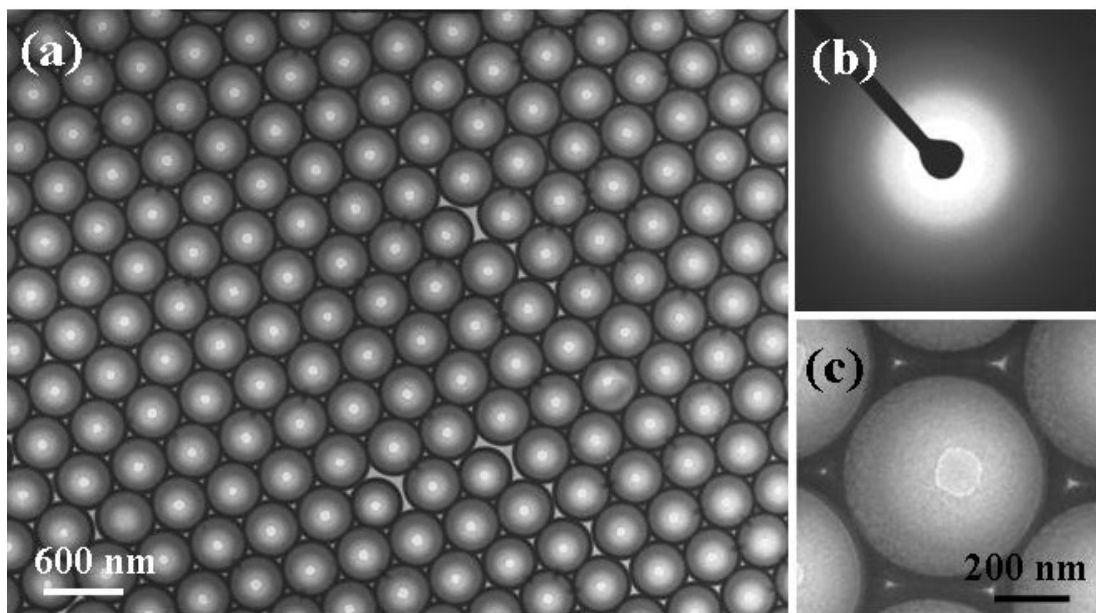
Figure 5.14: (a) A TEM image of the nanobowl sheet loaded on a TEM grid; (b) Electron diffraction of the amorphous TiO$_2$ nanobowl sheet; (c) A closer view of a single nanobowl.

Supporting by the TEM grid, TiO$_2$ nanobowl arrays can therefore be easily observed inside a TEM and a typical TEM image is shown in Figure 5.14a. Changing of contrasts clearly demonstrated the spherical shape, the circular holes and the walls of nanobowls, while the flat amorphous TiO$_2$ layer is not easily distinguished due to the absence of Bragg reflections from the sample (Figure 5.14b, c). This image also proves that the improved fabrication process has successfully transferred a large-area nanobowl sheet to a substrate without damaging its morphology and distribution.

Attaching the nanobowl sheet onto a TEM grid facilitated the easy manipulation and application of this nanobowl arrays. The 20-nm-thick sheet could be moved, tilted and placed by simply controlling the supporting TEM grid. In this configuration, the top-down (TEM grid) and bottom-up (nanobowl sheet) processes have been successfully
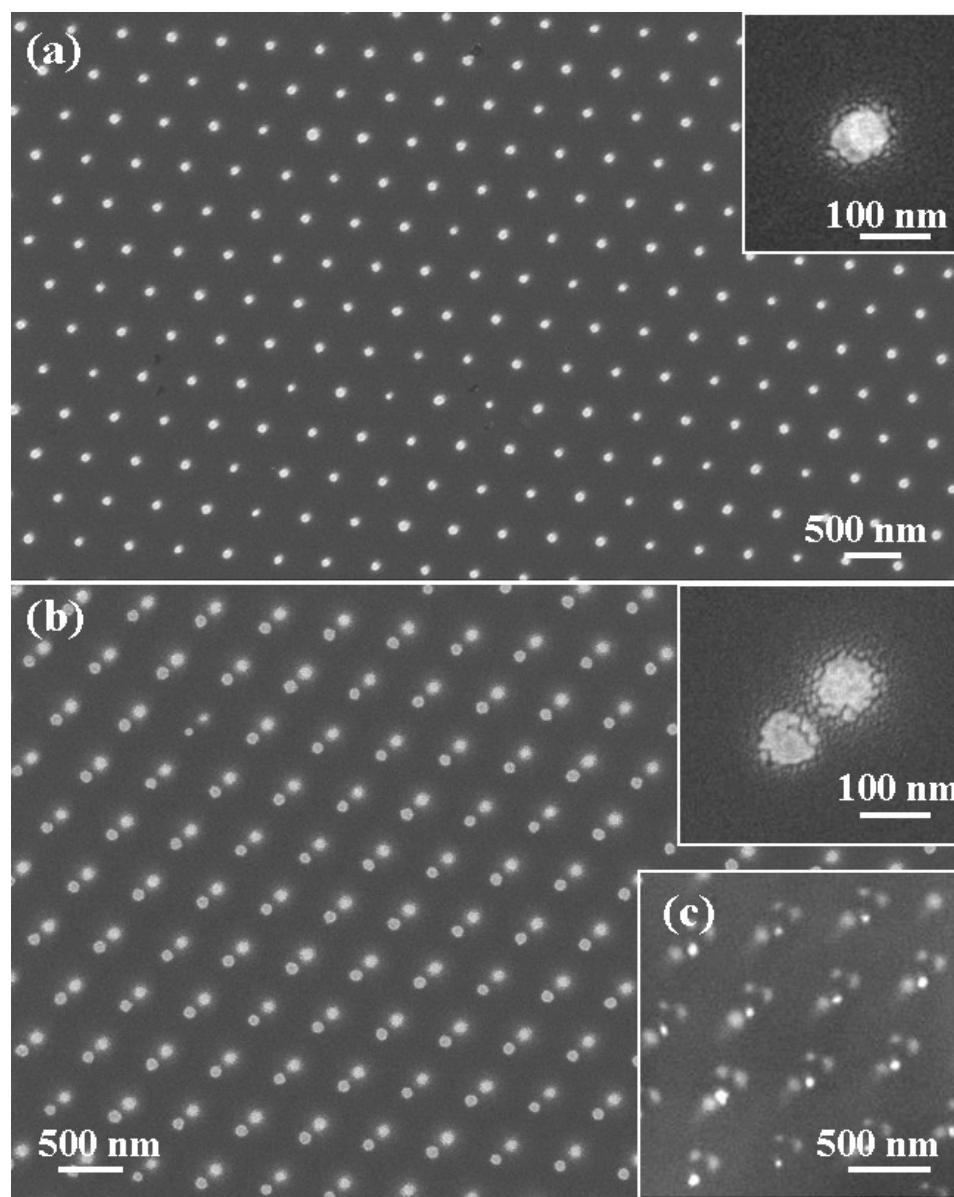
Figure 5.15: Gold dot patterns made through the nanobowl masks. (a) A triangular single-dot pattern and a close view of a single dot (inset); (b) A triangular double-dot pattern and a close view of a double-dot (inset); (c) A multi-dot pattern.

united and provide a very promising example for a low-cost and high-efficiency fabrication process for nano-scale features.

Taking the advantage of the open hole at the bottom of each nanobowl, the nanobowl coated TEM grid is demonstrated as a reusable mask for generating catalyst or quantum dots arrays with precise control of size and distribution. As mentioned previously, the open bottom is caused by the contact point between the spheres and substrate. Since the contacts between the PS spheres and the PS layer are fairly uniform, the size variation of the holes is within 5% (Figure 5.14a). Using the uniform and highly organized holes as a mask, triangular gold nanoparticle patterns were generated through thermal evaporation of a 20 nm gold layer, as shown in Figure 5.15a. Each gold dot exhibits a circular shape with a diameter of ~100 nm determined by the size of the holes (inset in Figure 5.15a). The distance between the gold dots is ~500 nm corresponding to the size of the PS sphere template (505 nm in diameter). Once the nanobowl mask was put up-side-down on the substrate, the walls of the nanobowls, whose height was precisely controlled by the time of ion-milling, separate the holes from target substrate with a certain distance so that various patterns can be generated through the mask by changing deposition angle[120], such as double-dots and multi-dots patterns (Figure 5.15b, c); or even circles by angularly rotating the substrate[121]. More important, this mask can be reused multiple times owing to the support from the TEM grid, which can be simply removed after deposition and put on another substrate manually without damaging the mask. This advantage can not be achieved by photoresist based lithography techniques.

In addition to the reusability, the hole-size on the mask can also be tuned precisely so as to achieve different particle sizes. The hole-diameter can be controlled by depositing additional TiO_2 on the nanobowls through low temperature ALD, in which the holes are gradually closed by the conformal TiO_2 coating. This additional ALD coating allows uniform control of the hole size with sub-nanometer precision. Figure 5.16 shows a series of TEM images of nanobowls after additional ALD growth with different
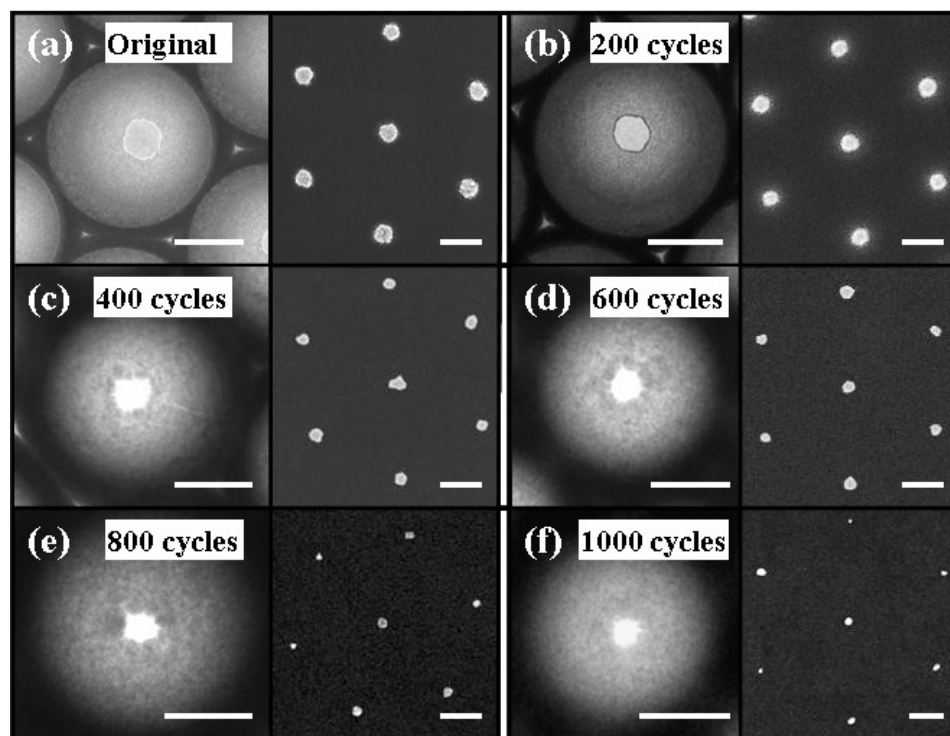
Figure 5.16: TEM images of the nanobowls after additional ALD growth of 0 (a), 200 (b), 400 (c), 600 (d), 800 (e) and 1000 (f) cycles. Besides each TEM image is the gold dot pattern generated through the corresponding nanobowl masks. All the scale bars represent 200 nm.

numbers of cycles. The average diameter of the original hole was 110 nm (Figure 5.16a) and after each increment of 200 ALD cycles, the average hole diameter was tuned to 105 nm, 86 nm, 64 nm, 48 nm and 37 nm, as shown in Figure 5.16b to f, respectively. Besides each image is a SEM image of the gold dots made through the corresponding nanobowl mask in a thermal evaporation process. Obviously, the dimensions of gold dots were very well determined by varying the hole diameters. Furthermore, this size control is practically continuous. According to the ALD growth rate, which is ~ 0.5 Å /cycle on average, the precision in size control can be as good as a few angstroms. However, the size uniformity might decrease when the dots get smaller. This is because the uniform ALD growth keeps the absolute size deviation unchanged in any hole dimensions, e. g. if

the mask starts with a hole size of 110±5nm, it will end up with 37±5nm after additional ALD growth, in which the variation is more significant.

In summary, a procedure has been created for fabricating free-standing, large-area, ordered TiO$_2$ nanobowl sheets at low-cost and without using clean-room facilities. Nano-cell arrays and reusable nano-scale masks are two new structures fabricated by manipulating the freestanding nanobowl sheets. Applications of the structures as masks have been demonstrated for fabricating nano-dot arrays with controllable size and distribution on a substrate. The formation of both bowl-side-down nanobowls and nanobowl masks presents successful examples of integrating top-down and bottom-up processes, which is the future of nanotechnology. The process has a great potential for scale-up, mass production and commercial applications.

CHAPTER 6

PATTERNED AND ALIGNED ZNO NANOWIRES

Discovery of semiconducting nanowires has provided us a new type of nanoscale building blocks with precisely controlled size, shape and composition. Moreover, new or enhanced properties have also been revealed due to their small sizes and high-quality crystal structures.[23] A diversity of novel applications has thus been proposed or even realized laboratorially in the fields of optics, electronics, mechanics and biomedical sciences.[4, 67] However, assembling nanowires into devices is still challenging because of the difficulties in manipulating structures of such small sizes. New tools and approaches must be developed to meet new challenges.

Although a wide range of novel approaches has been developed for fabrication of single nanodevices based on nanowires[11], a commercialized nano-manufacturing requires a simultaneous, parallel fabrication of a large amount of nanodevices under precisely controlled conditions and repeatability. This remains a major challenge to the development of nanotechnology, especially for nanoelectronics. The ultimate solution is self-assembly.[122] Like many biological systems, self-assembly is the most fundamental process for forming a functional and living structure. In general, self-assembly is the organization and pattern formed naturally by the fundamental building blocks such as molecules and cells. Designed and controlled self-assembly is a possible solution for future nano-manufacturing needs.

Aligned growth of nanowires is a simple but very efficient self-assembly technique for integrating nanowires into nanodevices, such as nanowire lasers[55], LEDs[123] or FETs[124]. In this chapter, the aligning mechanisms, techniques, the related property

113

investigation of ZnO nanowires and the potential applications will be introduced and discussed in details.

6.1 Alignment of ZnO Nanowires

As introduced previously, 1D ZnO nanostructures are considered as one of the most important semiconducting nanomaterials for fabricating nano-devices with applications in optics, electronics, mechanics and biomedical sciences.[125, 126] The attraction of ZnO is due to its high purity in crystallography, wide direct bandgap (3.37 eV), large excitation binding energy (60 meV), piezoelectricity and bio-compatibility as well as the diversive nanostructures.[127] VLS process is the most widely used technique for fabricating aligned ZnO nanowires because of its relatively low cost and simple procedure.[128] MOCVD has also been proved as an alternative method for aligning nanowires but with a much higher cost.[129] Wet chemistry process has recently been demonstrated as a powerful technique for growing aligned ZnO nanowires at a very low cost and over a very large surface area.[130] However, the density of nanowires grown on the surface cannot be controlled because the nanowires have to been grown in a very high density in order to have every nanowire pointing upwards.

Our goal is to explore the VLS process as a powerful but low-cost technique in large-scale aligned ZnO nanowires fabrication. In this section, the growth of aligned ZnO nanowires on sapphire and nitrides substrates will be presented.

6.1.1 Alignment of ZnO Nanowires on Sapphire Substrates

The large-scale perfect vertical alignment of ZnO nanowires has been firstly discovered on a-plane ((11$\overline{2}$0) crystal surface) orientated single-crystal aluminum oxide

(sapphire) substrates in 2001.[55] The general idea of this technique is to use gold nanoparticles as catalysts, in which the growth is initiated and guided by the Au particle and the epitaxial relationship between ZnO and Al_2O_3 leads to the alignment.

Unlike the normal VLS process, a moderate growth rate is required for the alignment since the catalyst need to melt, form alloy and precipitate step by step to achieve the epitaxial growth of ZnO on sapphire surface. Therefore, a relatively low growth temperature was always applied to reduce the vapor concentration. Mixing ZnO with carbon powder, which is so-called carbon-thermal evaporation, can reduce the vaporization temperature from 1300°C to 900°C,

$$ZnO(s) + C(s) \xleftrightarrow{\;900°C\;} Zn(v) + CO(v) \tag{6.1}$$
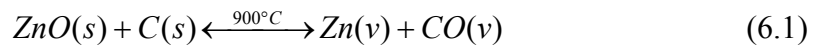
The above reaction is reversible in a relatively lower temperature. So when the Zn vapor and CO were transferred to the substrate region, they could react and became back to ZnO, which could be absorbed by gold catalyst and eventually formed ZnO nanowires through VLS process.

In our case, the growth condition is summarized as following.[131] The source materials contained equal amounts (by weight) of ZnO powder and graphite powder (0.8 gram each). The source materials were grounded and well mixed together. The mixture was loaded into an alumina boat that was placed at the center of an alumina tube with the substrate being positioned 10 cm downstream from the tube's center. Both ends of the tube were water cooled to achieve a reasonable temperature gradient. A horizontal tube furnace was used to heat the tube to 950°C at a rate of 50°C/min and the temperature was held for 20-30 minutes under a pressure of 300-400 mbar at a constant argon flow at 25 sccm. Then the furnace was shut down and cooled to room temperature under a flow of argon.

The typical morphology of the aligned ZnO nanowires on sapphire substrate is shown in Figure 6.1, a SEM image recorded at a 30° tilted view. All of the nanowires are perpendicular to the substrate surface and the darker dot on the top of each nanowire is
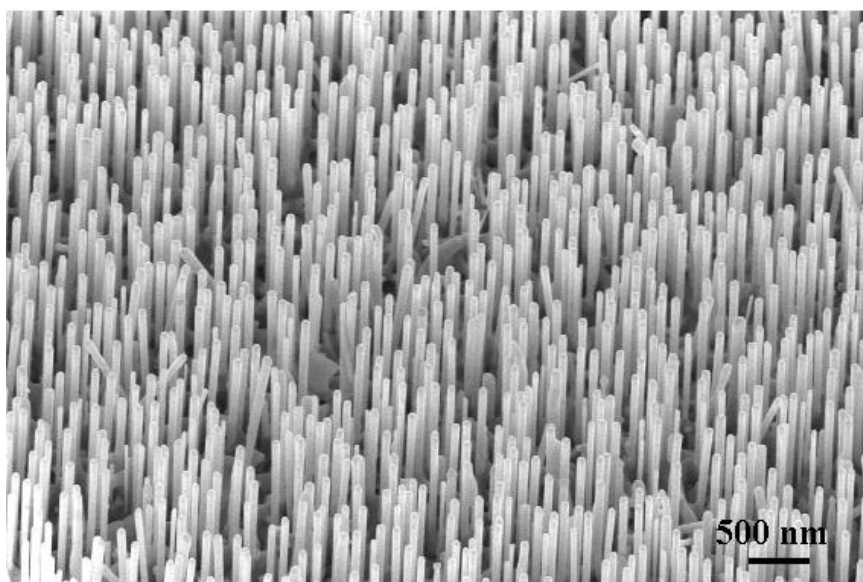
Figure 6.1: SEM image of aligned ZnO nanowires grown on sapphire substrate using a thin layer of gold as catalyst.

the gold catalyst. Due to the catalyst used in this sample is just a thin layer of gold (~5 nm), the distribution of the nanowires is random and there is no control over the nanowire's density.

From the application point of view, the density and distribution of aligned nanowires is very important since it is directly related to how the nanowires interact with each other optically, electronically and mechanically. Take field emission as an example, an array of densely packed nanowire greatly reduces the field enhancement effect of the nanowire tip, while too loosely distributed nanowires cannot meet the desired requirement of high emitting points. It is strongly desired to systematically control the density and distribution of the aligned nanowires, so that an optimal performance can be achieved by optimize the space between the aligned nanowires when their morphologies already meet the requirements. By combining this surface epitaxial approach with the self-assembly-based nanosphere-monolayer masking technique that was introduced in Chapter 5, large-area hexagonal arrays of aligned ZnO nanowires has been successfully achieved. This approach opens the possibility of creating patterned 1D nanostructures for
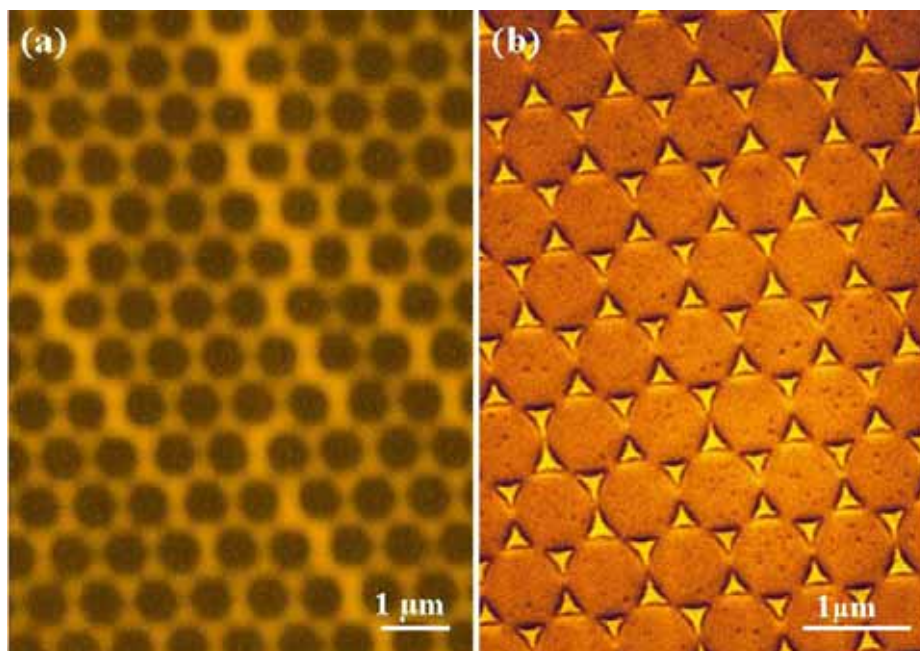
Figure 6.2: SEM images of gold catalyst patterns generated by (a) sputtering and (b) thermal evaporation process using PS monolayer as mask.

applications as sensor arrays, piezoelectric antenna arrays, optoelectronic devices, and interconnects.

During the process, a monolayer of 890 nm PS spheres was first self-assembled on a 1 cm × 1 cm *a*-plane orientated sapphire substrate. Then gold was either sputtered or thermally evaporated onto the self-assembled monolayer structure through this mask; as a result, two different patterns were obtained. For the sputtered coatings the high mobility of the gold atoms during the sputtering process, resulted in gold covering every available area, even beneath the spheres. Therefore, after etching away the PS spheres using toluene, this technique produced a honeycomb-like hexagonal gold pattern, as shown by the SEM images in Figure 6.2a. However, by using a thermal evaporator, which provides a line of sight vapor stream, the gold particles were only deposited onto areas of the substrate that were not shadowed by the PS spheres. After etching away the PS spheres, a highly ordered hexagonal array of gold spots was formed on the substrate (Figure 6.2b).
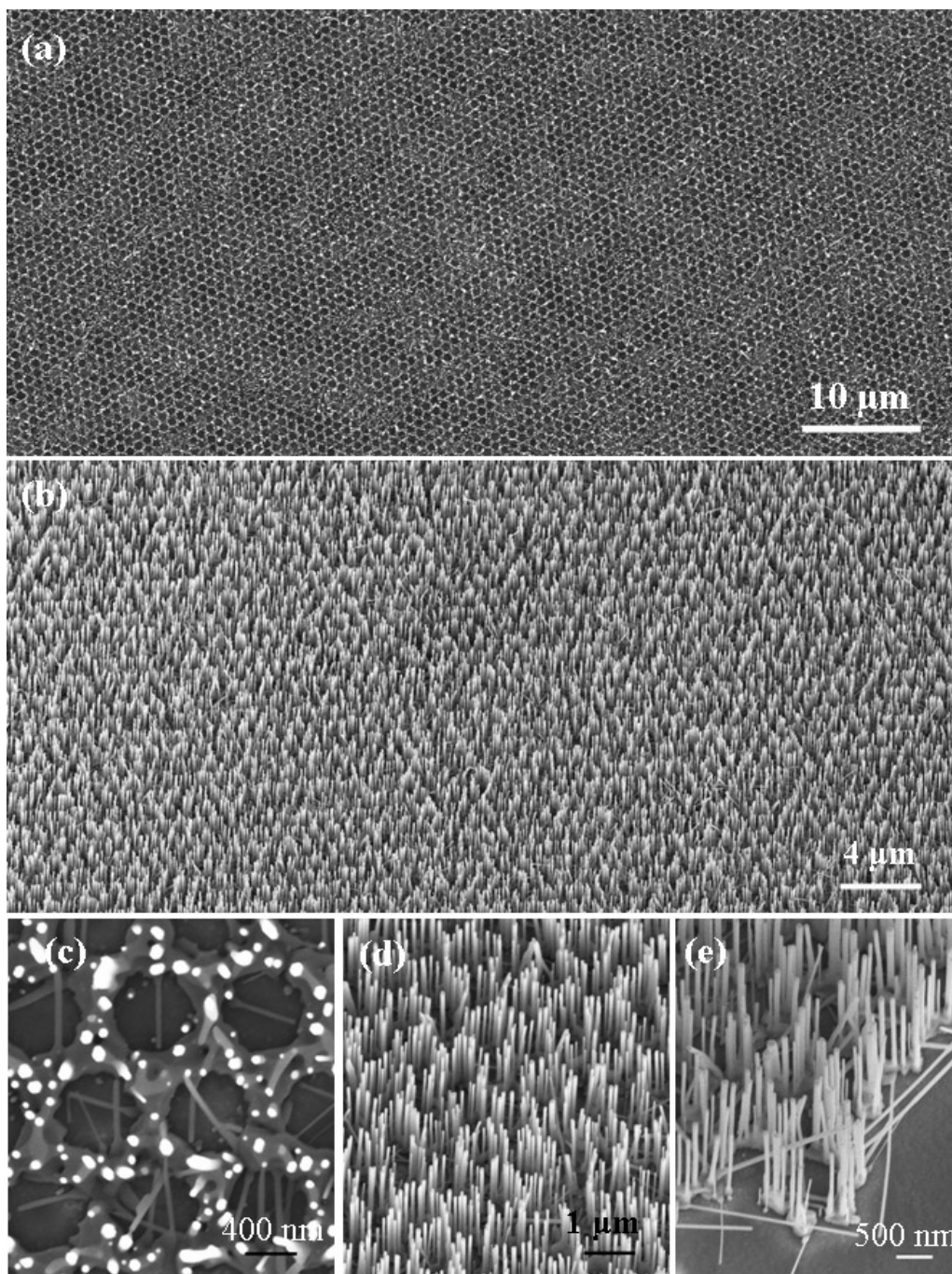
Figure 6.3: (a) A low magnification top-view SEM image of aligned ZnO nanorods grown onto a honeycomb catalyst pattern as shown in Fig. 6.2a. (b) A side view of the aligned ZnO nanorods at an angle of 30º. (c, d) A top and a 30º view of aligned ZnO nanorods, where the hexagonal pattern is apparent. (e) Aligned ZnO nanorods at the edge of the growth pattern.

The honeycomb-like gold pattern covered sapphire substrate was then used to growth the aligned ZnO nanowires through the carbon-thermal evaporation process. The as-synthesized results are presented by SEM images in Figure 6.3. Figure 6.3a shows a top view of the ZnO nanorod arrays over a large area. It is clear that the honeycomb-like arrangement of the gold pattern was preserved during the growth process. A magnified image of the top view is shown in Figure 6.3c. Each white spot represents one ZnO nanowire oriented perpendicular to the sapphire substrate and at the tip is a gold particle. Some ZnO nanowires that grew sideways were also observed. A 30° side view of the arrays (Figure 6.3b) shows clearly the well-aligned growth of the ZnO nanowires. The hexagonal arrangement of the aligned ZnO nanowires can be clearly distinguished in the magnified image shown in Figure 6.3d. All of the ZnO nanowires have about the same height, of about 1.5 μm and their diameters range between 50 and 150 nm. By changing the growth time the height of the ZnO nanowires could be varied from a few hundred nanometers to a few micrometers. Figure 6.3e is a higher magnification SEM image taken at the edge of an array. It clearly demonstrates that most of the ZnO nanowires
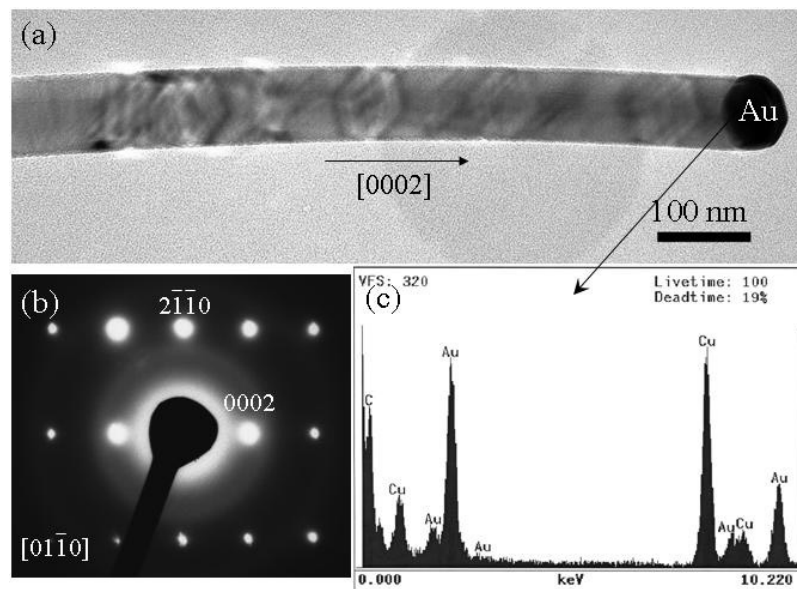
Figure 6.4: (a) TEM image of a ZnO nanorod with an Au particle at the end. (b) Electron diffraction pattern of a nanorod. (c) EDS spectrum recorded from the catalyst particle.

grow perpendicular to the substrate (that is, vertically), but that a few can also grow parallel to the substrate, and have a growth root from the same catalyst particle that promotes vertical nanowire growth.

TEM was used to characterize the crystallography of the ZnO nanowires. Figure 6.4a shows a ZnO nanowire with a catalyst particle at the tip. The contrast observed along the length of the nanorod displays the hexagonal cross section of the ZnO nanowire. An electron diffraction pattern recorded from the nanowire indicates that the nanowire grows along [0001] and its side surfaces are defined by $\{2\bar{1}\bar{1}0\}$ (Figure 4b). The tip of the nanowire was confirmed to be a gold particle from EDS (Figure 4c), where the copper and carbon signatures are from the copper TEM grid coated with a carbon film.

6.1.2 Alignment of ZnO Nanowires on Nitrides Substrates

The orientation of ZnO nanowires can be well aligned on sapphire substrates; however, two intrinsic problems associated with this technique are still limiting its application to devices. Al_2O_3 is a non-conductive material, making it difficult to utilize the aligned ZnO nanorods for electronic and optoelectronic devices. Also due to the surface crystal structure, a lateral growth of side branches close to the substrate surface is almost inevitable during the early stages of growth. For technological applications, it is highly desirable to grow ZnO nanorods on a conductive or semiconductive substrate in order to fabricate heterostructure devices and to make electronic measurements. GaN, an important optoelectronic material with the same crystal structure as ZnO, has been used as a substrate for growing aligned ZnO nanorods by the metalorganic chemical vapor deposition (MOCVD) process due to their very close lattice match.[129] However, since no catalyst was used in this process, there was no control over the site distribution and density of the nanostructures.

Taking the advantage of the site selectability of VLS process, we successfully grew prefect aligned ZnO nanowires on semiconducting GaN, $Al_{0.5}Ga_{0.5}N$ and AlN thin-film substrates using gold pattern as catalyst.[132] In our experiments, the MOCVD technique was employed for growing GaN, AlN and AlGaN epilayers[133], which served as the substrate for the subsequent growth of ZnO nanorods. Undoped c-plane-oriented GaN and AlN thin films were grown on a-plane sapphire substrates to thicknesses of 2 μm and 500 nm, respectively. $Al_{0.5}Ga_{0.5}N$ epitaxial layers with a thickness ~205 nm were grown on a 500 nm-thick AlN buffer layer grown on c-plane orientated sapphire substrate. A 7~8 nm-thick ~5 x 5 mm^2 gold catalyst layer was then deposited by plasma sputtering onto the epitaxial nitride substrates. The ZnO nanorods were grown through a vapor-liquid-solid process using a mixture of equal amounts (by weight) of ZnO and graphite powders that were loaded in an alumina boat located at the center of an alumina tube. To facilitate the reaction 2% (1sccm) oxygen was mixed with argon carrier gas at a flow rate of 49 sccm and the substrates were placed down stream in a temperature zone at ~850˚C. A horizontal tube furnace was used to heat the source materials to 950˚C at a rate of 50˚C/min and the temperature was held at the peak temperature for 30 minutes under a pressure of 30 mbar. Then the system was slowly cooled to room temperature under an argon flow.

A typical low-magnification SEM image of the as-synthesized ZnO nanowires grown on GaN is shown in Figure 6.5a. All of the ZnO nanowires are straight and perpendicular to the substrate with a high uniformity across the entire substrate, indicating that this technique can be scaled up for large-area production. As shown from a higher magnification SEM image in Figure 6.5b, the ZnO nanowires exhibit uniform diameter. Figure 6.5c shows a top view of the aligned ZnO nanowires, where only the very bright gold catalyst tips can be observed. It also confirms that almost every single nanowire is perpendicular to the substrate and that there are no side branches, which is
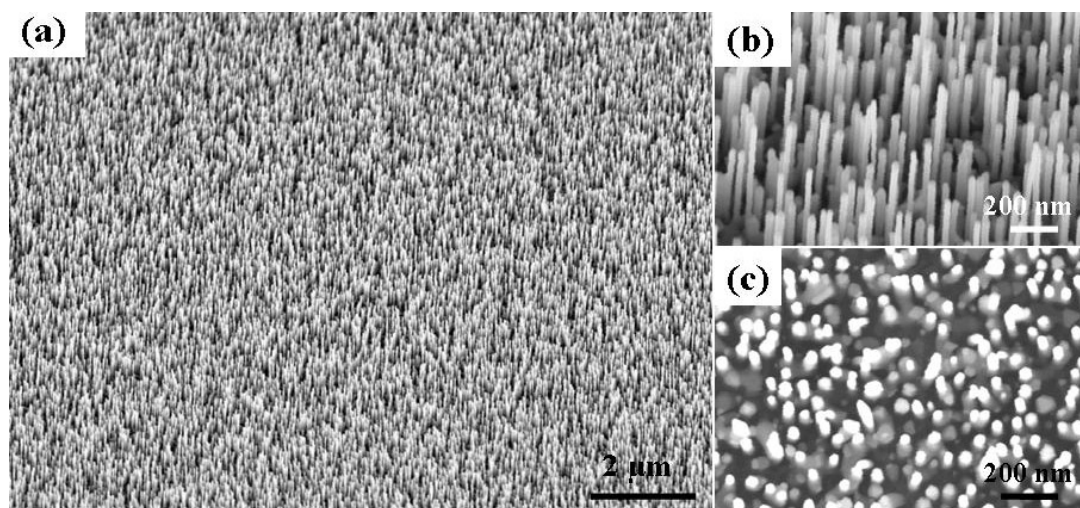
Figure 6.5: SEM images of aligned ZnO nanorods grown on a GaN substrate . (a) Low-magnification 30º side-view image; (b) High-magnification 30º side-view image; (c) High-magnification top-view image.

generally unavoidable when sapphire is used as substrate.

Highly aligned ZnO nanowires were also grown on $Al_{0.5}Ga_{0.5}N$ and AlN substrates under the same growth conditions, even though the lattice mismatch for these materials are larger than for GaN. Figure 6.6a~c gives the X-ray diffraction (XRD) spectra of the aligned ZnO nanorods samples grown on GaN, $Al_{0.5}Ga_{0.5}N$, and AlN substrates, respectively. In all three spectra, only diffraction from (0002) and (0004) atomic planes of ZnO are observed at 34.63º and 72.76º, respectively, indicating the high degree of nanowires alignment and their epitaxial relationship with the substrate. From the lattice constants of wurtzite GaN: a = 3.190 Å and c = 5.189 Å and wurtzite ZnO: a = 3.249Å and c = 5.207 Å, the lattice mismatch between the (0001) planes is 1.9%. Thus, in the XRD spectrum (Figure 2a), the peak from the GaN (0002) plane overlaps that of ZnO, while a double shoulder is observed on the (0004) peak. For the AlGaN system, although the lattice constant decreases from 3.190 (GaN) to 3.15 ($Al_{0.5}Ga_{0.5}N$) and to 3.110 (AlN) Å; and their lattice mismatch correspondingly increases from 1.8%, 3.0% to 4.3%; the epitaxial relationship is preserved as supported by the XRD spectra shown in
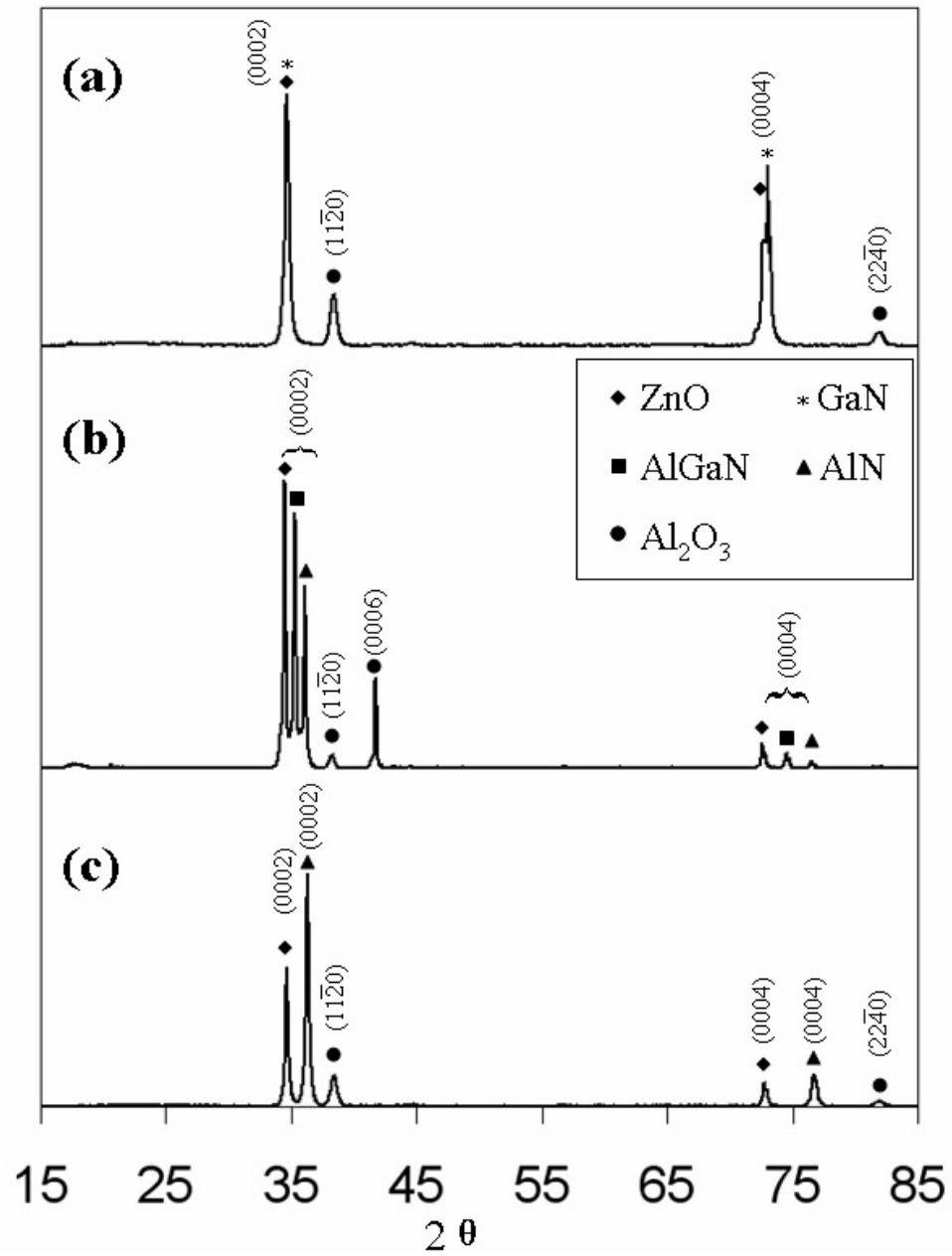
Figure 6.6: XRD spectra of aligned ZnO nanorods growing on GaN (a), $Al_{0.5}Ga_{0.5}N$ (b), and AlN (c) substrates.

Figure 6.6d and c. This figure also show that the diffraction peaks of $Al_{0.5}Ga_{0.5}N$ and AlN are gradually separated from the ZnO peaks due to the increased lattice mismatch, whereas the ZnO (0002) and (0004) peaks remain sharp and clear.
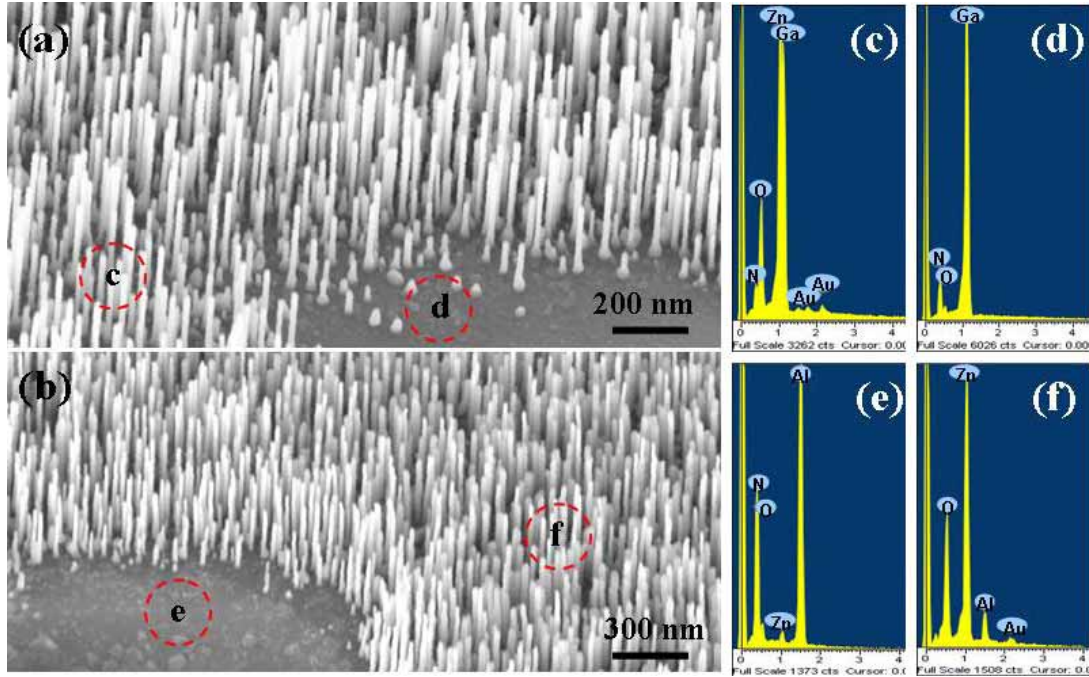
Figure 6.7: SEM images of ZnO nanorods growing on GaN (a) and AlN (b) substrates at the edge of catalyst layer; (c - f) EDS spectra of the corresponding circled region in (a) and (b).

The properties of catalytic particle initiated growth were further investigated using EDS during the SEM measurements. Figure 6.7a and b are SEM images of ZnO nanowires grown around the gold catalyst on GaN and AlN substrates, respectively, in which the catalyst boundary is clearly marked by the growth of aligned ZnO nanowires. EDS measurements were performed on the nanorod regions and the exposed substrate. Within the nanowire regions (Figure 6.7c and f), strong signals from zinc and oxygen were detected with a small gold signal originating from the Au film which acted as the catalyst and a portion of which remained at the tip of ZnO nanowires. Also small signals of Ga, Al and N were observed from the GaN and AlN substrates. However, on the exposed substrate (Figure 6.7d and e), only strong signals from the substrate materials
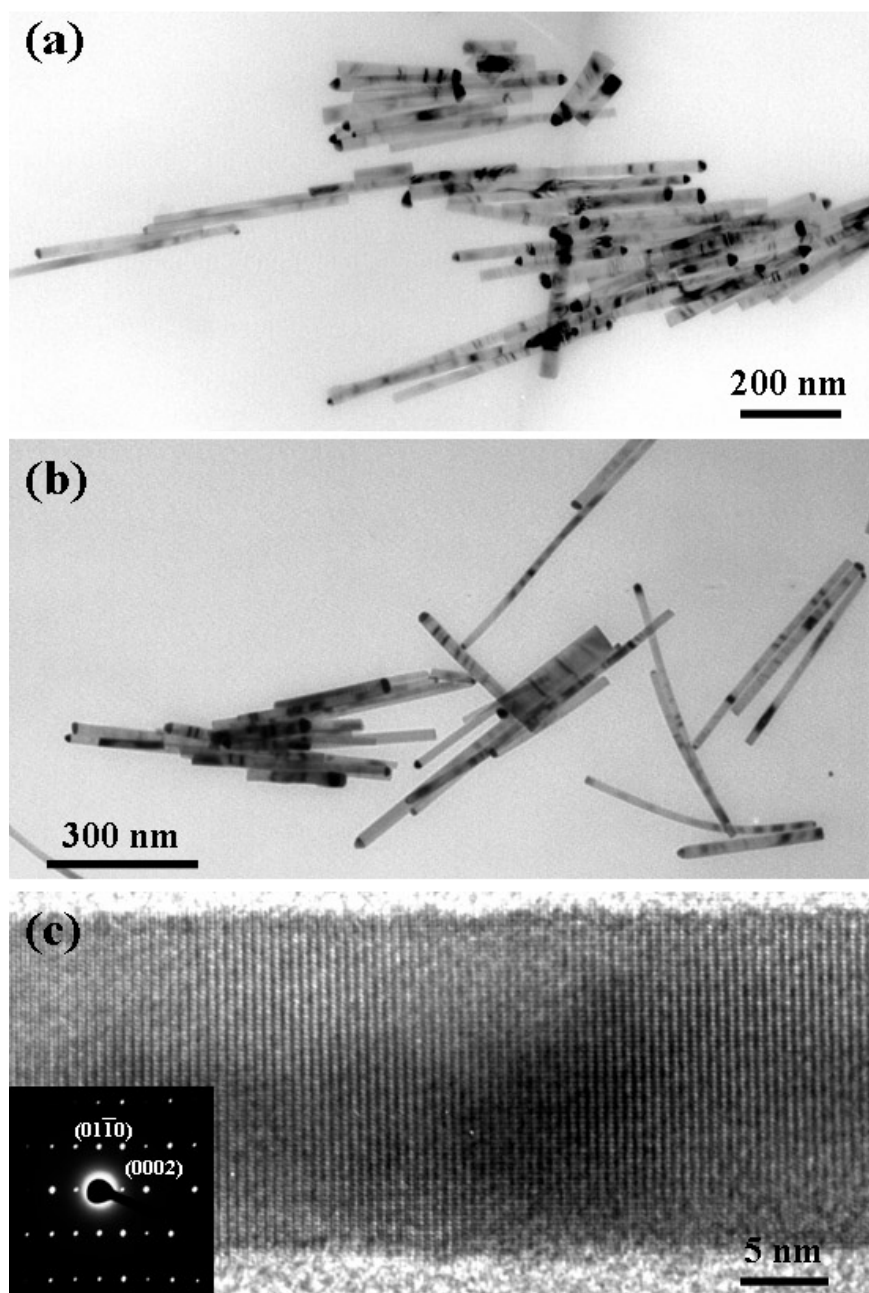
Figure 6.8: Low-magnification TEM image of ZnO nanorods grown on GaN (a) and AlN (b) substrates; (c) High-magnification TEM image of a single ZnO nanorod; inset: the corresponding electron diffraction pattern of the ZnO nanorod showing in (c).

were detected. Therefore, unlike the non-catalyst technique, such as MOCVD, which lacks of control over the growth position, the VLS process can precisely position the aligned ZnO nanowires by patterning the gold catalyst, while the uncovered substrate area remains chemically and structurally unchanged. Moreover, an almost perfect vertical alignment of ZnO nanowires without lateral growth can be achieved using the VLS technique demonstrated here.

TEM was also performed for size and crystal structure analysis. The lower magnification TEM images obtained for ZnO nanowires grown on GaN and AlN substrates are shown in Figure 6.8a and b, respectively. From ~200 nanowires recorded on TEM images, the average length of ZnO nanowires grown on GaN was measured to be 434 nm, while the ZnO nanowires grown on AlN substrate were a little longer, ~500 nm. However, their length distributions are very close — ±118 and ±120 nm for ZnO nanorods grown on GaN and AlN substrates, respectively. The average diameter was 28 ± 6 nm for ZnO nanorods grown on GaN is, and 22 ± 2 nm for those deposited on AlN. The smaller size of the ZnO nanorods on AlN is possibly due to the larger lattice mismatch between ZnO with AlN. The ZnO nanorods are single crystal (Figure 6.8c), the growth direction is [0001] and the six side facets are $\{11\overline{2}0\}$.

6.1.3 Epitaxial Relationships

From previous experimental results, it's becoming clear that the crystal structure of substrate is crucial for the orientation of nanowires grown by VLS process. Epitaxial relationship between the substrate surface and ZnO nanowires determines whether there will be an aligned growth and how well the alignment can be. Nanowires grown on silicon substrates are always randomly orientated because gold catalyst tends to form alloy with silicon at relatively low temperature and destroys the single-crystalline silicon
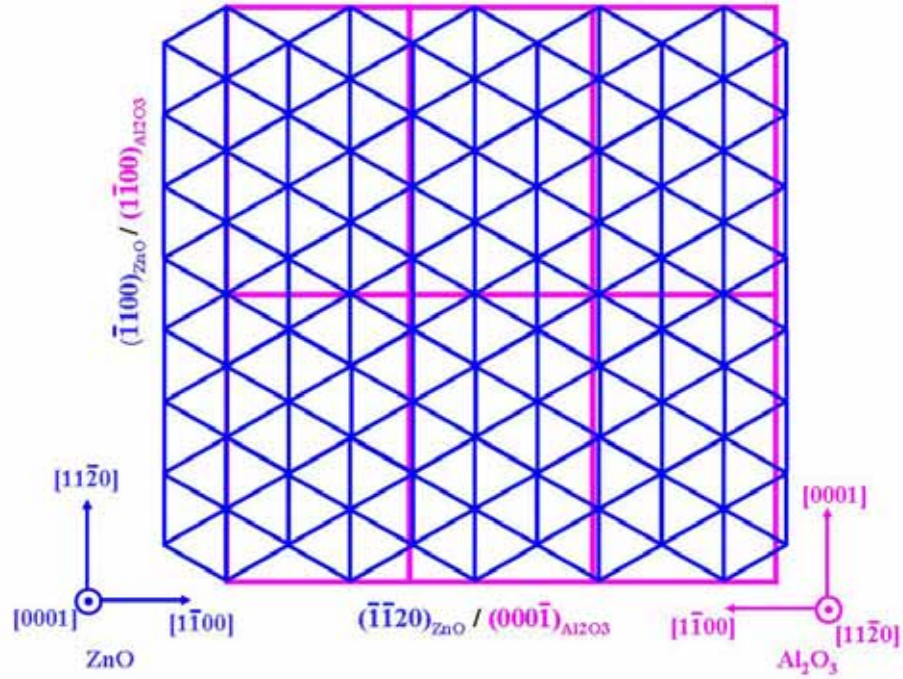
Figure 6.9: Schematic of the epitaxial relationship between *c*-plane of ZnO (blue) and *a*-plane of Al$_2$O$_3$ (pink).

surface. The successful alignment of ZnO nanowires on sapphire and nitride substrates is attributed to the very small lattice mismatches between the substrates and ZnO.

In the case of sapphire, (11$\bar{2}$0) plane orientated substrate is always used because the smallest lattice mismatch is along the *c*-axis of Al$_2$O$_3$ and *a*-axis of ZnO. The epitaxial relationship between ZnO nanowire and *a*-plane sapphire substrate is schematically shown in Figure 6.9, where (0001)$_{ZnO}$ || (11$\bar{2}$0) $_{Al_2O_3}$, [11$\bar{2}$0]$_{ZnO}$ || [0001] $_{Al_2O_3}$. The lattice mismatch between 4[01$\bar{1}$0]$_{ZnO}$ (4 × 3.249 = 12.996Å) and [0001] $_{Al_2O_3}$ (12.99 Å) is almost zero, which confined the growth orientation of ZnO nanowires. This relationship has also been confirmed by the electron diffraction pattern recorded on the interface of a ZnO nanowire and sapphire substrate[134], as shown in Figure 6.10.

127
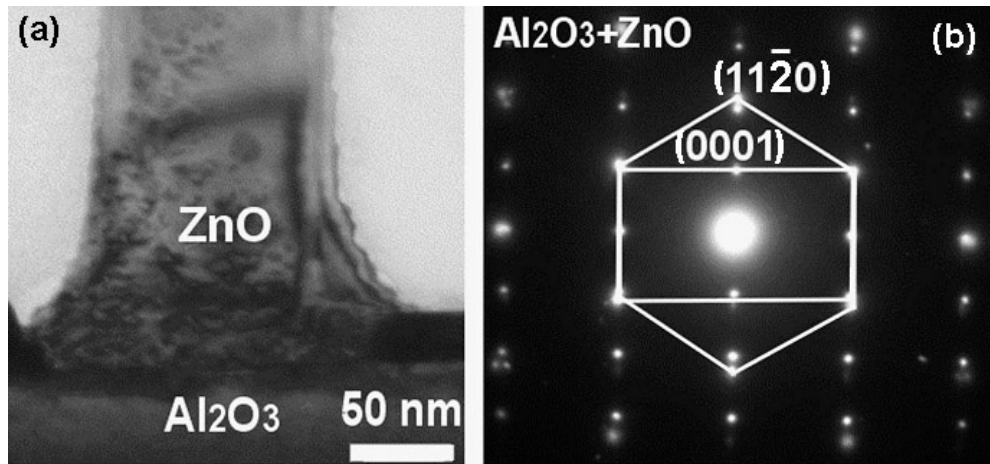
Figure 6.10: (a) TEM image of the junction between Al_2O_3 substrate and ZnO nanowire; (b) Electron diffraction pattern recorded on the junction region.

Nevertheless, since the $(11\bar{2}0)$ plane of Al_2O_3 is a rectangular lattice but the (0001) plane of ZnO is a hexagonal lattice, this epitaxial relationship can only hold in one direction. As illustrated in Figure 6.9, along the other direction, $[1\bar{1}00]$ direction, the lattice mismatch is fairly large, which will introduce some distortion on their lattice and cause stress around their interface. As a result, the lateral growth of ZnO side branches was always observed for *a*-plane sapphire substrates, especially on the edge of the growth area, where is no space restriction for lateral growth.[135]

As for the nitride substrates, GaN, AlN and AlGaN all have the same wurtzite structure as ZnO. So, the deposited ZnO nanowires are confined to their six equivalent $<01\bar{1}0>$ directions and only grow along the $[0001]$ direction, exactly following the substrate's crystal orientation, as shown in Figure 6.11. In this case, the epitaxial confinement is evenly distributed along the entire 2D atomic plane. As a result, even though the lattice mismatch becomes larger and larger from GaN (1.8%) to AlN (4.3%), the aligned growth was still kept very well. Moreover, the possibility for ZnO nanorods to undergo lateral growth is rare, even around the catalyst nucleation sites where
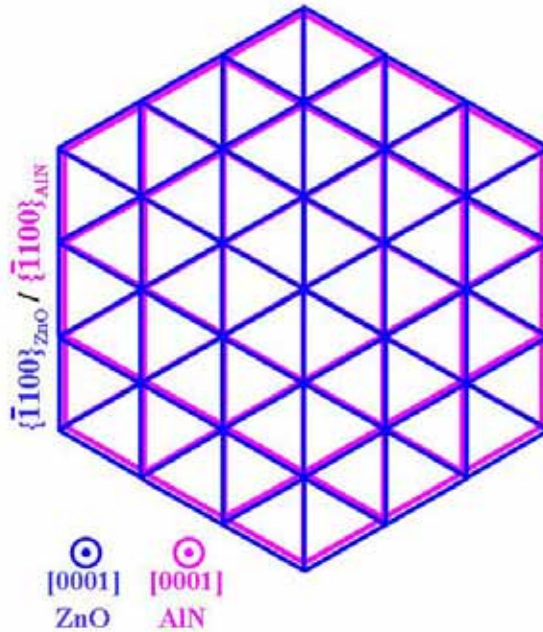
Figure 6.11: Schematic of the epitaxial relationship between *c*-plane of ZnO (blue) and *c*-plane of AlN (pink).

conditions are favorable for lateral growth, as shown in Figure 6.7a and b. Therefore, c-plane oriented $Al_xGa_{1-x}N$ substrates are ideal for the growth of aligned ZnO nanorods.

6.2 Growth Condition Investigation

As mentioned in the first section, many researchers, including us are employing VLS process for growing aligned ZnO nanowires on various substrates. However, the growth conditions reported are quite diverse and without a consistent pattern. For instance, some were grown under high vacuum,[55, 131, 132] whereas some were grown close to one atmosphere;[136] some substrates were put on the source materials,[134] whereas some substrates were put far away from the source.[131, 137] As a result, the size of the nanorods and the quality of the alignment varies drastically. There is a lack of a systematic

investigation on the experimental conditions under which ZnO nanorods are synthesized reproducibly at a large area.

Upon our successful fabrication of aligned ZnO nanowires on sapphire and nitrides substrates, a series of experiments were carried out under carefully designed growth conditions to discover a systematic guide line for synthesizing high quality aligned ZnO nanowires.

In our thermal evaporation system, there are many variables can be controlled to affect the final morphology, including furnace temperature, temperature gradient inside furnace, chamber pressure, pre-pumping pressure, oxygen concentration, flow rate of carrier gas, location of substrate and catalyst thickness. All of these effects would eventually determine the local partial pressure of ZnO vapor around the deposition region and resulted in different morphologies. Among those effects, some are just the equipment physical parameters, such as the temperature gradient and pre-pumping pressure, which were kept as constant during our experiments. Expect the catalyst thickness, other effects showed a cross interaction between each other. Therefore, our investigation of the optimal growth condition was generalized onto three basic terms: chamber pressure, oxygen partial pressure[138] and thickness of catalyst layer[139].

6.2.1 Chamber Pressure and Oxygen Partial Pressure

In our experiments, an undoped c-plane oriented GaN film with a thickness of 2 μm that was grown on an *a*-plane sapphire single-crystal substrate was used as the substrate. A thin layer of gold was deposited on the top of GaN via plasma sputtering, which acted as catalysts to guide the growth of ZnO nanowires. The source materials were a mixture of equal amounts (by weight) of ZnO power and graphite power, which was grounded and placed in an alumina boat. Then the boat was loaded in the center of an alumina tube (150 cm long, 4 cm inner diameter), where the substrate was placed 10 cm

away from the source material at the downstream side. The tube was placed in a horizontal tube furnace (model F79345 from Barnstead/Thermolyne Co.) with cooling water running through the outside of the tube at the ends. After pre-pumping the system down to 2×10^{-2} mbar, a premixed gas (Ar and O_2) was introduced into the system with a flow rate of 50 sccm to bring the pressure back to a certain point between 1.5 and 300 mbar according to the designed experiments. The furnace was then heated to 950 °C at a heating rate of 50 °C/min and the temperature was held at the peak temperature during the growth for 30 min. Finally, the system was slowly cooled to room temperature under flowing gas. All of the experimental conditions remained fixed for the series of experiments except two variables: the volume ratio of O_2 to Ar gas (1% to 4%), and the chamber pressure (0.3-100 mbar).

From the results, we found the oxygen partial pressure and the system total pressure played key roles in the growth of ZnO nanowires. With different oxygen volume percentage and different chamber pressure, the quality and growth behavior of the ZnO nanowires are strongly affected. We have carried out over 100 growth experiments under different growth conditions, which were designed to quantitatively define the best combination of the O_2 partial pressure and the chamber pressure for growth of aligned ZnO nanowires. For consistency, all of the samples were collected at the 880 °C temperature zone, which is 10 cm away from the source materials. The O_2 volume percentage in the chamber varied from 1 to 4 vol %, and the system pressure varied from 1.5 to 300 mbar. Since the growth system was first pumped down to 2×10^{-2} mbar, the system pressure was brought back to a growth pressure at a value between 1.5 and 300 mbar, the oxygen coming from the residue air only contributed 0.28-0.0014% toward the entire oxygen content, which was much less than the percentage of O_2 in the flow gas. Therefore, the partial pressure of O_2 was considered to be the volume percentage of the O_2 introduced in the flow gas.
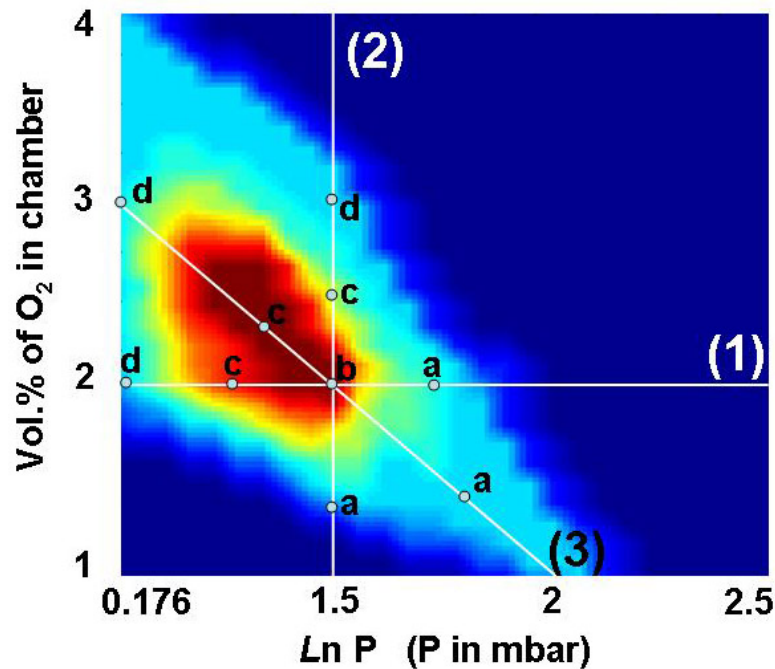
Figure 6.12: "Phase diagram" that correlates oxygen volume percent in the growth chamber (e.g. partial pressure) and the growth chamber pressure (plotted in logarithm and P is in unit of mbar) for growing aligned ZnO nanowires. The point matrix was broadened and smoothed by MatLab to form a quasi-continuous phase diagram. The synthesis Line (1) is the line with constant oxygen volume percentage; line (2) is the line with constant system pressure; line (3) is the line with linearly varying oxygen volume percentage and system pressure.

The experimental results are summarized in Figure 6.12, which is a "phase diagram" for the O_2 volume percentage in the chamber and system pressure, under which the optimum conditions for growing aligned ZnO nanowires are presented. The term of "phase diagram" used here is given a new meaning of representing the "road map" for controlled synthesis of nanowires. This phase diagram was determined for the furnace system described in the Experimental Section. As shown in Figure 6.12, the horizontal axis is the logarithm of the total chamber pressure; the vertical axis is the oxygen volume percentage in the chamber, and the quality of the grown ZnO nanowires is represented by different colors. The quality of the nanowires is characterized by their uniformity, density, length, and alignment. In the phase diagram, dark red represents the best growth

condition, where a perfect alignment of ZnO nanowires with a high density and uniform length and thickness were achieved. The growth is good in the red area, where the density is lower and the nanowires are shorter. In the green and light blue area, the growth is poor, where only a little amount of short nanowires was found. No growth was found in the dark blue region. This phase diagram provides the road map for growing high quality aligned ZnO nanowires.

To clearly demonstrate the effects of total chamber pressure and O_2 volume percentage to the final results, three sequences are highlighted in the phase diagram: fixed O_2 volume percentage but with variable chamber pressure (line 1); fixed system pressure but with variable O_2 volume percentage (line 2); and linear increased O_2 volume percentage with decreasing system pressure (line 3). Four representative points on each line are picked up to present the quality of the grown nanowires under the defined growth conditions.
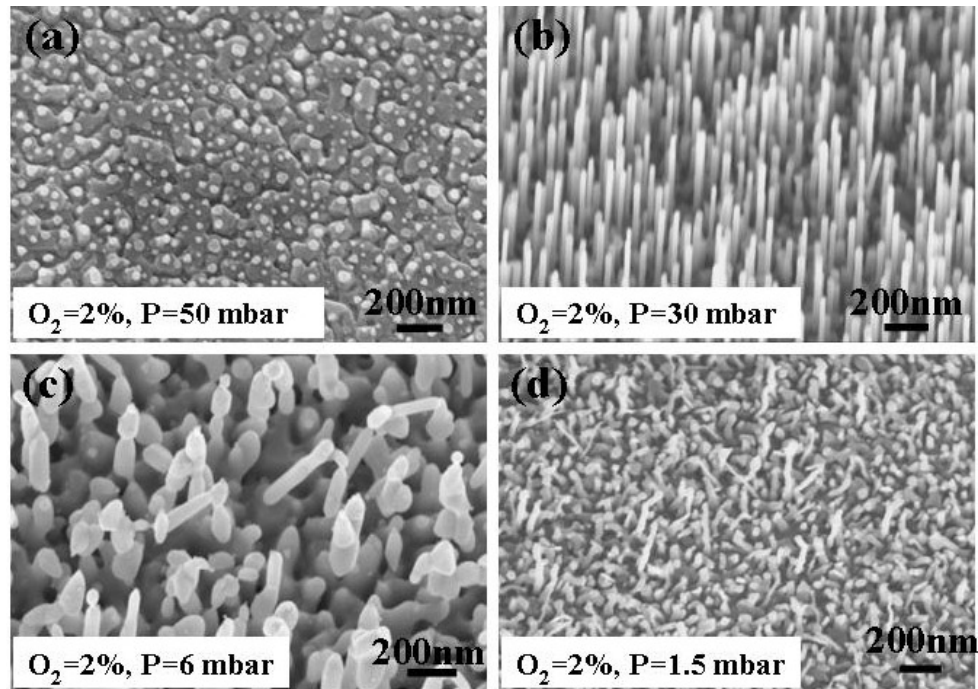
Figure 6.13: SEM images of ZnO nanowires grown under the conditions of 4 green points along line (1) in Figure 6.12 under constant oxygen volume percentage (2%) but variable chamber pressure: (a) 50 mbar; (b) 30 mbar; (c) 6 mbar; (d) 1.5 mbar.

133

Figure 6.13 presents SEM images of four samples received under the conditions of 2% fixed O_2 volume percentage (1 sccm oxygen, 49 sccm argon) but 4 different chamber pressures: 50 mbar, 30 mbar, 6 mbar, and 1.5 mbar as shown in Figure 6.13a-d, respectively. In Figure 6.13a, which represents the results with the highest system pressure among the four experiments, no nanowire was formed but only gold catalyst particles were found, which was confirmed by EDS. With the decreasing of system pressure to 30 mbar, a perfect alignment of ZnO nanowires was achieved, as shown in Figure 6.13b. When the system pressure dropped to 10 mbar, ZnO nanowires became shorter and randomly orientated, as shown in Figure 6.13c. By further dropping the system pressure to 1.5 mbar, only a few thin nanowires were deposited on a continuous ZnO film. This regular change in the ZnO morphology is contributed to the relative increased Zn vapor concentration while the system pressure decreased.

In the carbon-thermal evaporation process, the Zn vapor source is dominated by reaction

$$ZnO(s) + C(s) \longleftrightarrow Zn(v) + CO(v) \tag{6.2}$$

This reaction is favorable in high temperature. Once the vapors are transported to the cooler region where the substrate is located, the Zn vapor is deposited on the surface of the catalyst and reoxidized, resulting in the growth of the nanowire. Since the amount of Zn vapor is determined by the local temperature, thus, the rate at which the Zn vapor is produced can be assumed to be a constant under different chamber pressures. Therefore, when the total system pressure drops, the partial pressure of the Zn vapor increases. When the system pressure is too high, Zn vapor may not reach supersaturation, and thus, no deposition occurs on the surface of the catalyst particles, resulting in no growth at all (Figure 6.13a). When the system pressure is too low, Zn vapor may be over supersaturated, the vapor deposits not only on the surface of the Au catalyst but also the surface of the GaN substrate, resulting in formation of nanowires as well as a thin film on the substrate surface (Figure 6.13d). High quality aligned ZnO nanowires can only be

achieved when a reasonable supersaturation level of Zn vapor is reached at a moderate system pressure, which is around 30 mbar under our growth condition.
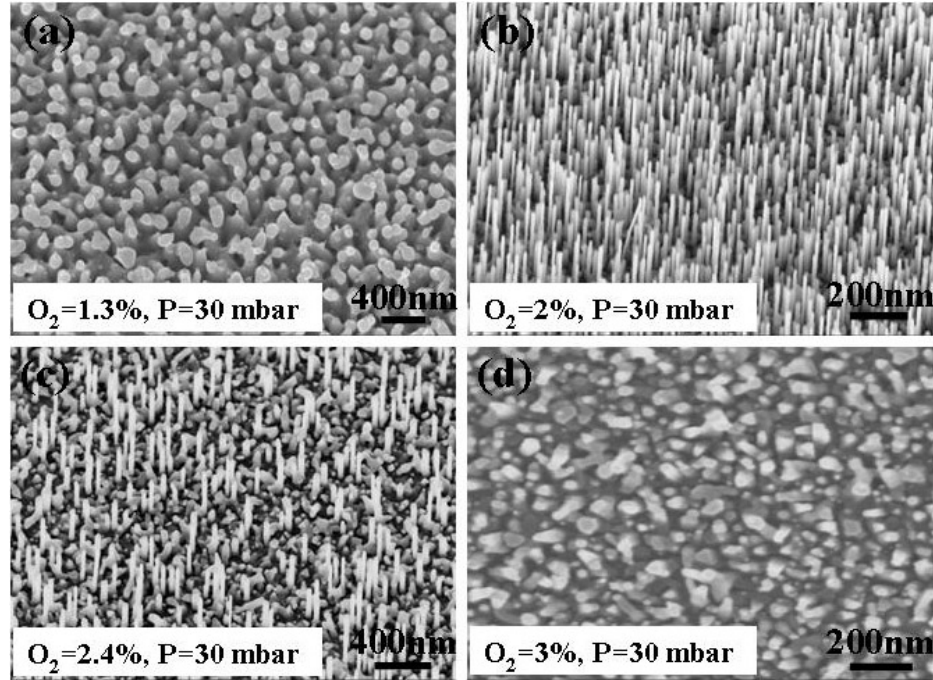
Figure 6.14: SEM images of ZnO nanowires grown under the conditions of 4 green points along line (2) in Figure 6.12 under constant chamber pressure (30 mbar) but variable oxygen volume percentage: (a) 1.3% ; (b) 2%; (c) 2.4%; (d) 3%.

The effect of O_2 partial pressure is illustrated in Figure 6.14, in which SEM images of a-d represent the typical results of ZnO deposition at O_2 volume percentage of 1.3%, 2%, 2.5%, and 3%, respectively, with a fixed chamber pressure of 30 mbar. At a very low O2 volume percentage (1.3%), only small ZnO dots were nucleated, as shown in Figure 6.14a. By increasing the O_2 volume percentage to 2%, good alignment of ZnO nanowires was achieved (Figure 6.14b). When the O_2 volume percentage increased to 2.5%, as shown in Figure 6.14c, the density of ZnO nanowires dropped dramatically, as well as their lengths. The growth of ZnO nanowires almost vanished once the O_2 volume percentage was set at 3% (Figure 6.14d).

There are three possible reactions that O_2 is involved in carbon assisted thermal evaporation process

$$2C + O_2 \longleftrightarrow 2CO \qquad\qquad (6.3)$$

$$2CO + O_2 \longleftrightarrow 2CO_2 \qquad\qquad (6.4)$$

$$2Zn + O_2 \longleftrightarrow 2ZnO \qquad\qquad (6.5)$$

Zn vapor is still provided by eq. 6.2. From the Ellingham diagram, reaction 6.2 occurs only when the temperature is higher than 970 ºC, whereas in our experiments, the furnace was just heated to 950 °C; thus, the question is what makes the local temperature high enough for reaction 1 to be possible? In the beginning when there was no other gas in the system, the main reaction involving O_2 is reaction 6.2, which generated heat as well as CO. The heat could be absorbed locally by the source materials (ZnO plus graphite) and possibly facilitate reaction 6.2 to produce Zn vapor. On the other hand, local concentration of CO could also increase, which could hinder the Zn vapor generation. Under the influence of these two effects, reaction 6.2 cannot be fully accelerated, and as a result, when the O_2 partial pressure was very low, insufficient Zn vapor was released to reach a reasonable supersaturation point for producing ZnO nanowires, as the situation shown in Figure 6.14a.

Once the partial pressure of O_2 was increased, additional O_2 can react with CO to form CO_2 (eq. 6.4), which lowered the concentration of CO and generated heat as well. Both of these two effects facilitated reaction 6.2. Therefore, supersaturation of Zn vapor can be reached, leading to growth of high quality aligned ZnO nanowires, as shown in Figure 6.14b. However, when the partial pressure of O_2 was further increased, additional O_2 could react with Zn vapor generated from the source materials immediately to form a ZnO film/grain. We have examined this situation by introducing a lot more O_2 into the system and found a layer of large ZnO nanowires/grain was formed on the surface of the source powders. Consequently, the Zn vapor decreased again near the substrate and little growth was found (Figure 6.14d). In general, only moderate O_2 volume percentage (~2 vol%) results in good aligned ZnO nanowires.

Four typical results of ZnO deposition carried out under linearly increased O_2 partial pressure with decreased chamber pressure are illustrated in Figure 6.15. The experimental conditions selected are as follows: (a) 1.6% O_2 at 50 mbar system pressure; (b) 2% O_2 at 30 mbar system pressure; (c) 2.5% O_2 at 7 mbar system pressure; (d) 3% O_2 at 1.5 mbar system pressure. Except point a, where both O_2 partial pressure and system pressure were intended to give a low Zn vapor concentration, all of the other three points in the phase diagram exhibited a reasonable growth of ZnO nanowires. This is because the decreasing of Zn vapor caused by increased O_2 could be compensated by reducing the chamber pressure; thus, the reasonable supersaturation level of Zn vapor can be maintain in a relatively large range.
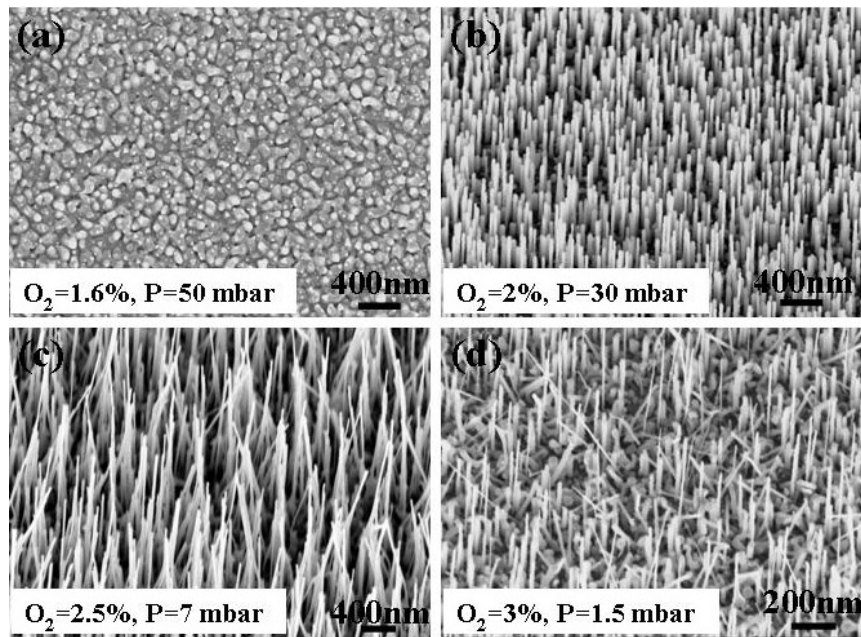
Figure 6.15: SEM images of ZnO nanowires grown under the conditions of 4 green points along line (3) in Figure 6.12 by linearly adjusting the chamber pressure and oxygen partial pressure. (a) 1.6% oxygen volume percentage, 50 mbar chamber pressure; (b) 2% oxygen volume percentage, 30 mbar chamber pressure; (c) 2.5% oxygen volume percentage, 7 mbar chamber pressure; (d) 3% oxygen volume percentage, 1.5 mbar chamber pressure.

In general, distinct from the conventional understanding about VLS growth process, we found that both the partial pressure of O_2 and total system pressure exhibited

distinct effects on the final morphologies of deposited ZnO nanostructures. In our furnace system, the optimal condition for growing aligned ZnO nanowires was found to be 2% O_2 at 30 mbar system pressure at a local growth temperature of 880 °C.

6.2.2 Thickness of Catalyst Layer

After the systematic study on the growth of ZnO nanowires on AlGaN substrate, the catalyst effect was studied. By varying the thickness of the deposited gold film through thermal evaporation, we found the density of aligned ZnO nanowires exhibited an almost linear relationship with the catalyst thickness.

In order to investigate the effects of the thickness of Au catalyst, eight stripes of gold layer with thicknesses from 1 to 8 nm at 1 nm gradient were deposited onto a 2 cm × 1 cm $Al_{0.5}Ga_{0.5}N$ substrate through thermal evaporation process, where the thickness was measured by a quartz crystal thickness monitor with a resolution of 0.1 nm. The fabrication of ZnO nanowires was carried out under the optimal experimental condition we developed the previous section. In general, a mixture of equal amounts (by weight) of ZnO and graphite powders were used as source materials and were loaded in an alumina boat, which was located at the center of an alumina tube. To facilitate the reaction 2% (1sccm) oxygen was mixed with argon carrier gas at a flow rate of 49 sccm, and the substrates were placed down stream in a temperature zone of ~850˚C. A horizontal tube furnace was used to heat the source materials to 950˚C at a rate of 50˚C/min and the temperature was held at the peak temperature for 30 minutes under a pressure of 30 mbar. The growth was terminated by turning off the furnace, and then the system was slowly cooled down to room temperature under an argon flowing gas.

Under the conditions specified above, all of the nanowires were grown simultaneously and under identical experimental conditions. The inset in Figure 6.16 is an optical picture of the substrate, from which the eight stripes can be clearly
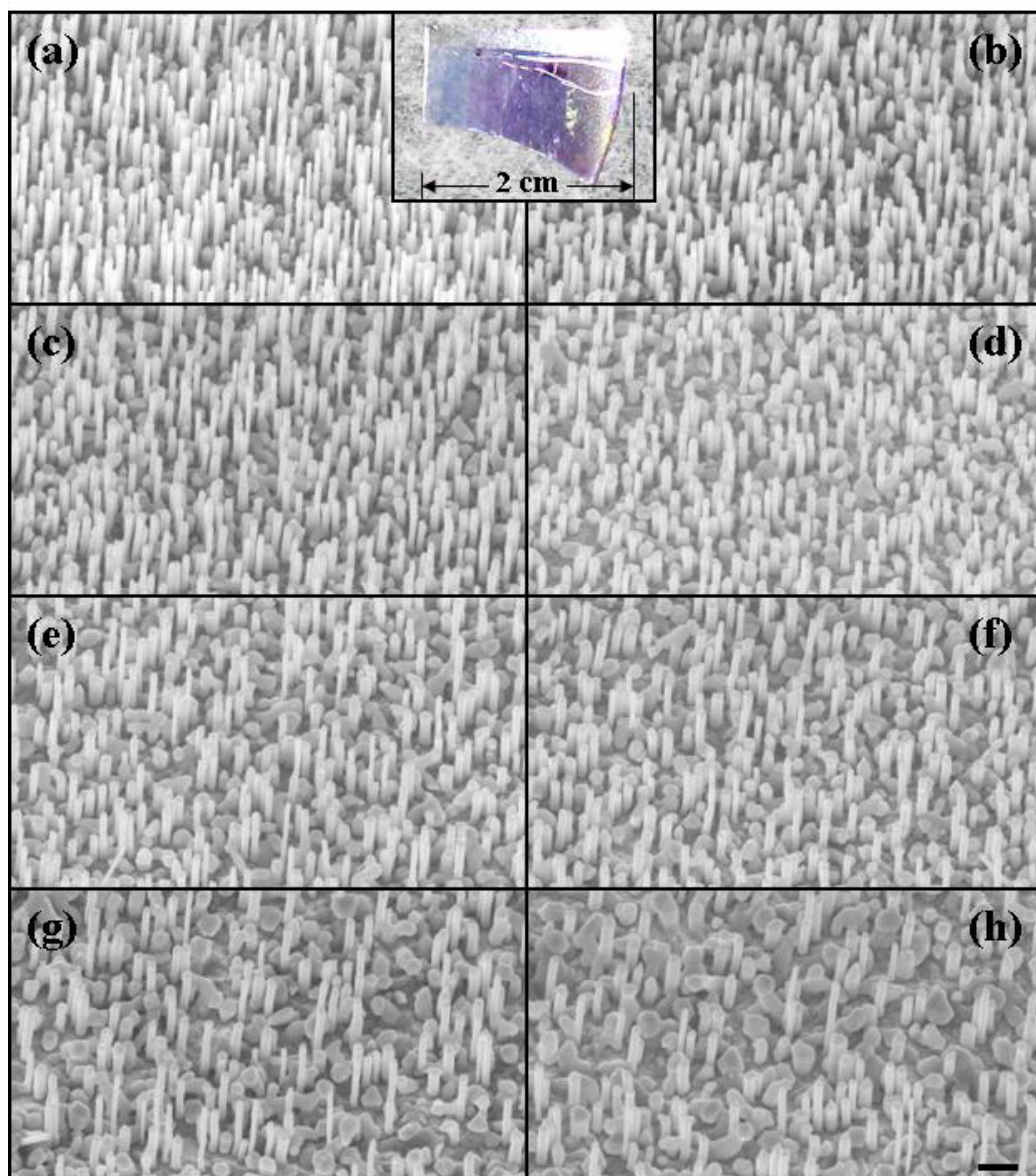
Figure 6.16: (a-h) SEM images of the aligned ZnO nanowires catalyzed by gold layer with thickness from 1 to 8 nm, respectively. Inset: Optic photo of the substrate showing eight stripes of the aligned ZnO nanowires corresponding to images (a)-(h) from left to right.

distinguished. From right to left, the color of the stripes varies from light blue to purple, which represent the aligned ZnO nanowires catalyzed by Au layer of thicknesses from 1 to 8 nm. Each stripe of the as-synthesized ZnO nanowires exhibited distinct difference even though there was only 1 nm change in the thickness of the deposited Au film. Since the blue color is from ZnO and red color is contributed by gold, it can be assumed the thinner layer of gold catalyst resulted in more ZnO nanowires, which has been further confirmed by SEM characterization. Each stripe of the as-synthesized ZnO nanowires exhibited obvious difference even though there was only 1 nm change of thickness between two adjacent stripes.

Figure 6.16a-h represents the typical SEM images recorded from the nanowires grown in the areas of the eight stripes at an identical magnification. Clearly, the 1-nm gold layer gives the highest density of aligned ZnO nanowires (Figure 6.16a), while the thickest gold layer results in the lowest density of nanowires (Figure 6.16h). With the decreasing of the density of the ZnO nanowires, more and more larger particles can be found on the substrate. As confirmed by EDS analysis equipped on the SEM, those particles are mostly composed of gold, which made the substrate appears more reddish in the optical image. However, despite the large difference in density, all of the ZnO nanowires exhibit very close width and length distribution.

Quantitative analysis were thereafter performed to reveal the density and thickness relationships of the aligned nanowires. The density was measured by top-view SEM images, as shown in the inset of Figure 6.17a. Each bright spot corresponds to a perpendicular ZnO nanowire with a gold catalyst particle on top. By counting the number of bright dots on five randomly taken SEM images, the average number of nanowires per square micrometers was calculated. The nanowire density at each thickness of gold catalyst layer is shown in the left-hand side axis in Figure 6.17a with an averaged error of ~10%. An almost linear drop in density from 112 to 15 with increasing catalyst thickness can be observed. The width of nanowires was measured by TEM. After transferring the
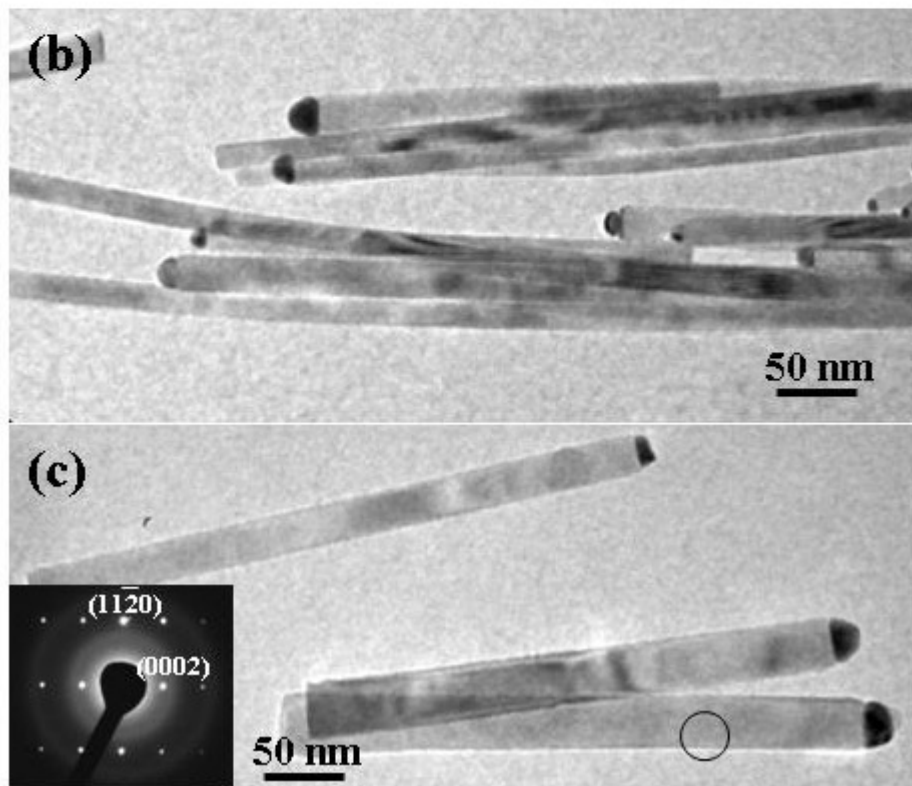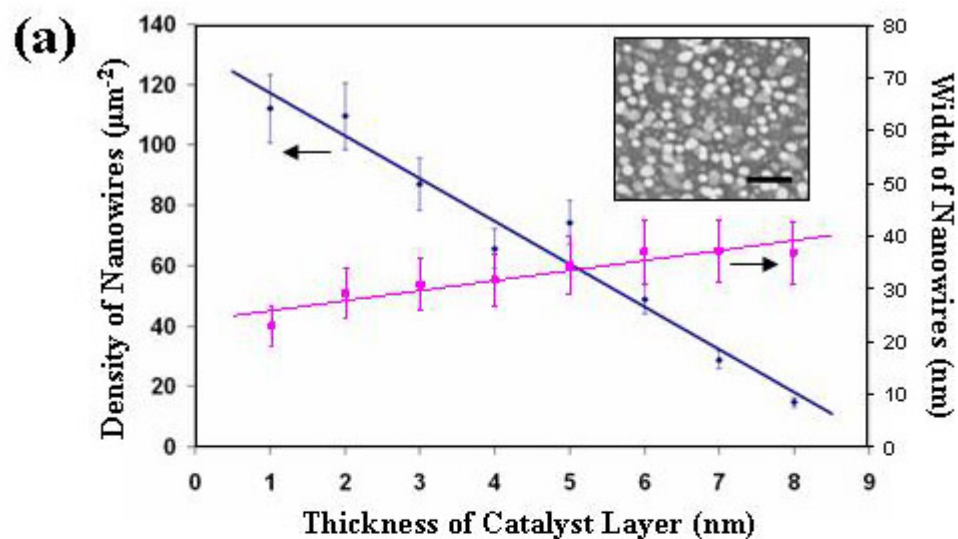
Figure 6.17: (a) Variation of density (left vertical axis) and width (right vertical axis) of the aligned ZnO nanowires with the thickness of gold catalyst layer. Inset: top-view SEM image of the aligned ZnO nanowires used for density calculation, the scale bar represent 200 nm. (b, c) TEM images of ZnO nanowires catalyzed by 1 nm and 8 nm gold layer, respectively. Inset is the select area electron diffraction pattern recorded on a nanowire body indicated by the circle in image (c).

aligned nanowires on each stripe to different TEM grids, more than 10 TEM images were taken for each sample to calculate the average width. The result is shown in Figure 6.17a. The standard deviations of the samples are ~16% from >100 randomly chosen nanowires. Unlike the density, the average width remains between 30 - 40 nm despite the change in catalyst thickness. In order to present the variation in nanowire width, representative TEM images with the same magnification for the two extreme cases, nanowires catalyzed by 1-nm- and 8-nm-thick gold, were taken and are shown in Figure 6.17b and c, respectively. One nanowire in Figure 2c exhibits a similar width as that in Figure 6.17b, while the other two are about 10~15 nm wide, indicating a larger absolute width distribution for the case of 8-nm-thick gold. A selective area electron diffraction pattern was taken on the nanowire as indicated by a circle in Figure 6.17c. As shown in the inset of Figure 2c, the nanowires were grown along the [0001] direction, which is the fastest growth direction for the VLS growth of ZnO.

Owing to the linear relationship between the density of nanowires and the thickness of the catalyst layer, thickness control of gold catalyst could be a very simple and effective way to achieve density control of aligned nanowires over a large surface area. In order to reveal why the density varies but the width remains constant, the wetting behavior of gold layer on $Al_{0.5}Ga_{0.5}N$ substrate was investigated when heated to the growth temperature. Two additional pieces of $Al_{0.5}Ga_{0.5}N$ substrates with the same gold catalyst distribution were prepared. Under the same furnace growth condition, one piece of the substrate was heated to the growth temperature without introducing source material to reveal the formation of catalyst dots; while the other one was heated to the same temperature with source material in the growth chamber for only a few minutes to reveal the initial growth stage of the nanowires. Based on the data we have received, the growth situation can be presented into three categories, as shown in Figure 6.18.

The first category is the *separated dots initiated growth*, where the gold layer is only 1-2 nm in thickness. As shown in Figure 6.18a, after being heated to the growth
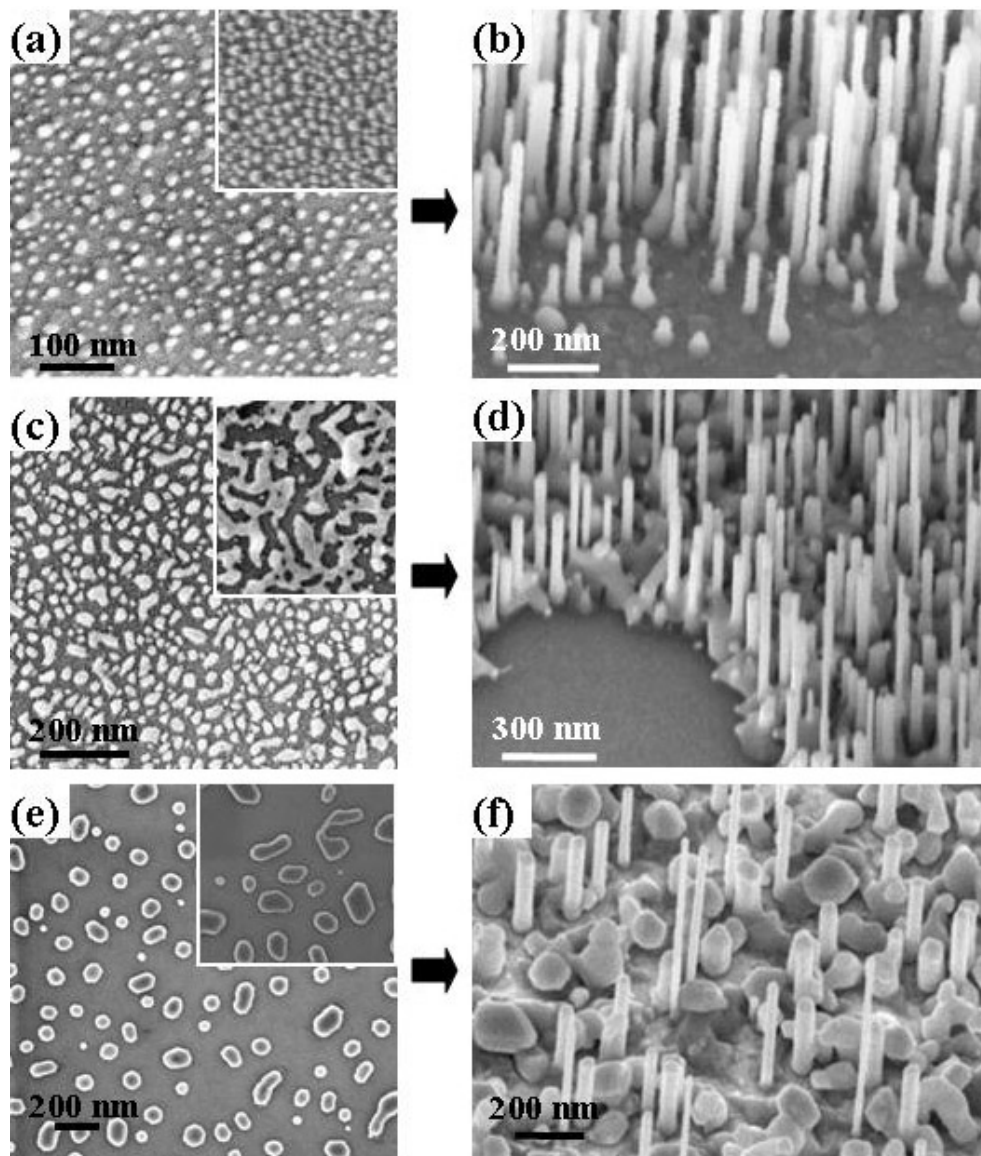
Figure 6.18: Three categories of the growth mechanisms based on the thickness of gold layer. (a, c, e) SEM images showing the wetting situation of gold catalyst on $Al_{0.5}Ga_{0.5}N$ substrate; Insets are the SEM images with the same magnification showing the wetting situation when the vapor source presented. (b, d, f) SEM images of the aligned ZnO nanowires catalyzed by the corresponding gold layer.

condition, the 1-2 nm gold layer melted into tiny gold dots (10-20 nm) evenly distributed on the substrate surface. Once the source vapor was present, larger particles were observed due to the coarsening effect resulting from the formation of a supersaturated "alloy", as shown in the inset of Figure 6.18a. However, all of the particles remained separated from each other, resulting in a higher density and individual ZnO nanowire growth from the substrate surface (Figure 6.18b).

The second category is *continuous layer initiated growth* when the thickness of the gold deposition layer was 3-6 nm. As shown in Figure 6.18c, the gold layer melted into separated islands with different sizes at the deposition temperature. Most of the large islands then merge into a continuous network on the substrate surface when alloying gold with the source vapor at the initial stage (inset of Figure 6.18c), while the small islands were still left isolated. As the deposition continued, the isolated small islands initiated the growth of nanowires, while the network formed a complete layer covering the substrate and connecting the base of all the nanowires (Figure 6.18d). The gold in the network would eventually be precipitated out forming small dots or very short rod during the cooling process. Therefore, the density of nanowires that can be grown in this case is relatively less. However, since every single ZnO nanowire is interconnected by the Au and/or ZnO layer at the root, this can be an alternative pathway to electrically connecting the aligned ZnO nanowires for electronic nano-devices and field emission. This is a unique advantage for solving the bottom electrical contact problem. It is also has the great merit of replacing the expensive semiconducting substrates by sapphire while preserving the electrical contact, offering a great potential for industrial application.

The third category is called the scattered islands initiated growth when the thickness of gold layer is greater than 7 nm. In this case, when melted, the catalyst layer is thick enough to form big gold particles (~100 nm). The large gold particles were widely separated; also a very small number of gold dots were left, as shown in Figure 6.18e. Even after forming an alloy with the source vapor, this morphology remained

144

unchanged (inset of Figure 6.18e). In the deposition process, only the small dots could initiate the growth of ZnO nanowires; and the big particles led the growth of ZnO films/ junks lying on the substrate, resulting in the lowest density of aligned ZnO nanowires.

The above discussion are based on moderate growth conditions as described in the experimental section, under which the evaporation of source materials was relatively slow so that the catalyst layer had enough time to melt and form an alloy step by step,
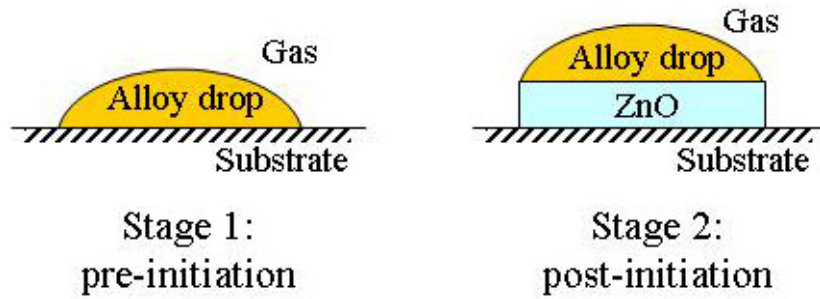
Figure 6.19: (a) Schematic of the initiation of ZnO nanowire growth. (b) SEM image of ZnO columns growth from a 10-nm-thick hexagonal gold pattern (inset) in a very high vapor concentration.

which can be considered as a thermal equilibrium process. In order to explain why only small dots initiate growth, the thermodynamic mechanisms were studied based on the pre- and post- nucleation of the ZnO nanowire, as illustrated in Figure 6.19. The alloy droplet is assumed to be supersaturated at stage 1; stage 2 presents the moment when the first layer of ZnO is precipitate, during which the change in supersaturation is compensated by the diffusing of source vapor from the gas phase into the alloy. The free energies of these two stages are presented by G1 and G2, respectively, as following:

$$G_1 = V_A G_{V1}^A + V_G G_{V1}^G + A_{AS}\gamma_{AS} + A_{AG}\gamma_{AG} + A_{GS}\gamma_{GS} \tag{6.6}$$

$$G_2 = V_A G_{V2}^A + V_G G_{V2}^G + A_{AZ}\gamma_{AZ} + A_{ZS}\gamma_{ZS} + A_{ZG}\gamma_{ZG} + A_{AG}\gamma_{AG} + A_{GS}\gamma_{GS} + V_Z G_V^Z \tag{6.7}$$

where V_A, V_G and V_Z are the volume of the alloy droplet, gas phase and ZnO respectively; G_{V1}^A, G_{V1}^G and G_{V2}^A, G_{V2}^G are the free energy per unit volume of alloy and gas phase at the

first and second stage respectively; G_V^Z is the free energy per unit volume of the precipitated ZnO crystal; A and γ are the area and free energy of the interfaces between gas, alloy, substrate and ZnO surfaces as indicated by their initials in the subscripts. The formation of ZnO results in a free energy change $\Delta G = G_2 - G_1$. By assuming the alloy composition remains the same ($G_{V1}^G = G_{V2}^G$) and the area of precipitated ZnO is the same as the contact area between the alloy and the substrate ($A_{AS} = A_{AZ} = A_{ZS}$), the ΔG can be given by:

$$\Delta G = V_G(G_{V2}^G - G_{V1}^G) + A_{AS}(\gamma_{AZ} + \gamma_{ZS} - \gamma_{AS}) + A_{ZG}\gamma_{ZG} + V_Z G_V^Z \qquad (6.8)$$

In order to initiate precipitating of ZnO, ΔG has to be negative, so we have:

$$V_G(G_{V1}^G - G_{V2}^G) > A_{AS}(\gamma_{AZ} + \gamma_{ZS} - \gamma_{AS}) + A_{ZG}\gamma_{ZG} + V_Z G_V^Z \qquad (6.9)$$

The left-hand side of the inequality is the change in the free energy of the vapor phase; on the right-hand side, the first term is determined by the initial size of the catalyst A_{AS} and last two terms are negligible at the initiation nucleation stage since the size of the ZnO/gas interface A_{ZG} and the volume of ZnO V_Z are very small. So equation (4) can be simplified to:

$$G_{V1}^G - G_{V2}^G > C \cdot A_{AS}, \quad C = (\gamma_{AZ} + \gamma_{ZS} - \gamma_{AS})/V_G \qquad (6.10)$$

where C is a constant. From this equation, small A_{AS}, e.g. small gold dots, are thermodynamically favorable sites for the initiation of aligned ZnO nanowires. Since the surface area A_{AS} for small size gold particles is rather small, equation (5) is usually satisfied. Therefore, growth on small size gold particles is thermodynamically favorable.

On the other hand, small gold particles are very likely to be in the liquid state at the growth temperature due to the reduced melting point for smaller particles. From the experiments of Buffat[2], the melting point of gold layer below 5 nm is much lower (<800 ℃) than the melting temperature of bulk gold (1064 ℃). These molten small gold particles resulted in the nucleation and growth of aligned ZnO nanowires due to the VLS growth, whereas for the large gold islands, they most likely to be in the solid state thus

growth by the VLS process is not possible. In our experiments, most of the nanowires are around 30 - 40 nm and therefore we may disregard the deposition thickness of the gold film.

In general, we found that a slight variation of the thickness of gold catalyst will result in a significant change in the density of grown aligned ZnO nanowires. This could be an effective and simple pathway to achieve density control without using the sophisticated techniques such as catalyst patterning. This study demonstrates two remarkable results: growth of aligned nanowire arrays on a ceramic substrate with a simultaneous formation of a continuous conducting electrode at the roots; and an easy and effective way for controlling the density of the grown nanowires on large surfaces for industrial applications. These results are important for device applications.

6.3 Properties and Potential Applications

Aligned 1D ZnO nanostructures has been believed to greatly facilitate the commercialization of semiconducting nanowires extraordinary properties into real nano-devices as sensor arrays, piezoelectric antenna arrays, optoelectronics, and interconnects. Due to their perpendicular alignment, external electrical, magnetical or optical impact can be easily applied on the ZnO nanowires arrays with the same effects on most of the ZnO nanowires. So a very tiny change of the optical or electrical property on a single nanowire can be magnified by the aligned structure instead of be cancel out by a random distribution. Therefore, these aligned 1D ZnO nanowires arrays have highly enhanced sensibility and responsibility, with which the commercialization requirements could be reached.

Based on our aligned ZnO nanowire grown on sapphire and nitride substrates, PL spectra were measured to reveal their light emitting properties as potential LEDs or

Lasers. A self-attracting phenomenon has also been discovered, which is probably caused by the uneven electrons distribution around the gold catalyst/ZnO nanowire junctions. In addition, by filling the spaces between the patterned and aligned ZnO nanowires, a 2D photonic crystal with luminescence property has been realized.

6.3.1 Light Emitting Properties

The light emitting properties of aligned ZnO nanowires were characterized by measuring the PL spectra under different detecting angles, on different substrate and different nanowire densities. All of the PL measurements were performed at room temperature.
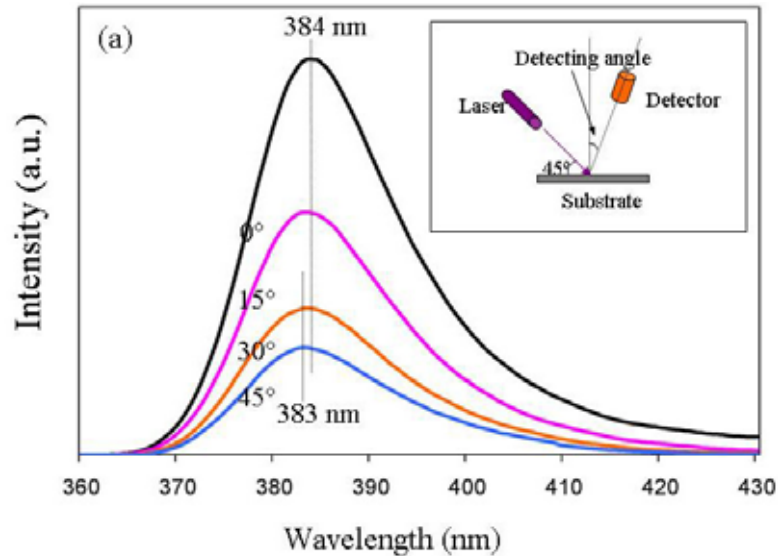
Figure 6.20: PL spectra acquired from an aligned ZnO nanowire array grown on sapphire substrate as a function of the angle between the detector and a direction normal to the substrate. The inset shows the experimental set up.

The angular PL measurements were carried out on the hexagonal patterned aligned ZnO nanowires grown on sapphire substrate. The excitation source was a 337 nm N_2 pulsed laser with 15 Hz pulse frequency, 800 ps pulse duration at an average energy

of 50 mW. The laser was incident onto the sample at an angle of 45°, while the detection angle was defined as the angle between the detector and the direction normal to the substrate, as shown in the inset in Figure 6.20. The emission spectra were recorded at four different detection angles, 0°, 15°, 30° and 45° (Figure 6.20). The aligned ZnO nanowires exhibit a peak at 384 nm at $\theta = 0°$. As the detection angle was increased, the luminescence intensity dropped dramatically, which indicates that the luminescence was emitted mainly along the perpendicular direction of the substrate. Moreover, the luminescence peak shifted very slightly from 384 nm to 383 nm when the detection angle increased from 0° to 45°. This may also be caused by the polarization of the emitted light from the aligned nanowires.[140]

In addition to sapphire substrate, the PL spectra of aligned ZnO nanowires were also measured on on GaN, AlGaN and AlN substrates using a 266 nm Nd:YAG Q-switched laser with an average power of 1.9 mW as the excitation light source. All of the samples exhibited a strong luminescence peak at ~378 nm corresponding to the near bandgap emission of ZnO and an identical peak shape with a peak width at half intensity of ~15 nm (Figure 6.21a~c). For the PL spectrum of ZnO nanorods on GaN, a small peak at 362.7 nm was also detected, which corresponds to the bandgap of GaN (3.44 eV). Due to the increased bandgap when Al was introduced into the GaN lattice, the PL peaks from the substrate are blue shifted and thus no additional substrate-related peaks were observed from ZnO nanorods grown on AlGaN and AlN substrates.

Although the PL peaks have an identical shape, their peak intensity varies significantly. The highest PL signal intensity, which was more than 10 volts, was measured from ZnO nanorods grown on AlN (Figure 6.21c) and the lowest from ZnO nanorods grown on GaN, only ~ 4 volts as shown in Figure 6.21a. The PL peak intensity from ZnO nanorods grown on AlGaN, exhibited an intermediate peak intensity of ~7 volts (Figure 6.21b). Since the density of nanorods grown on GaN, AlGaN and AlN substrates are calculated from the SEM images to be 146, 70 and 157 per μm^2,
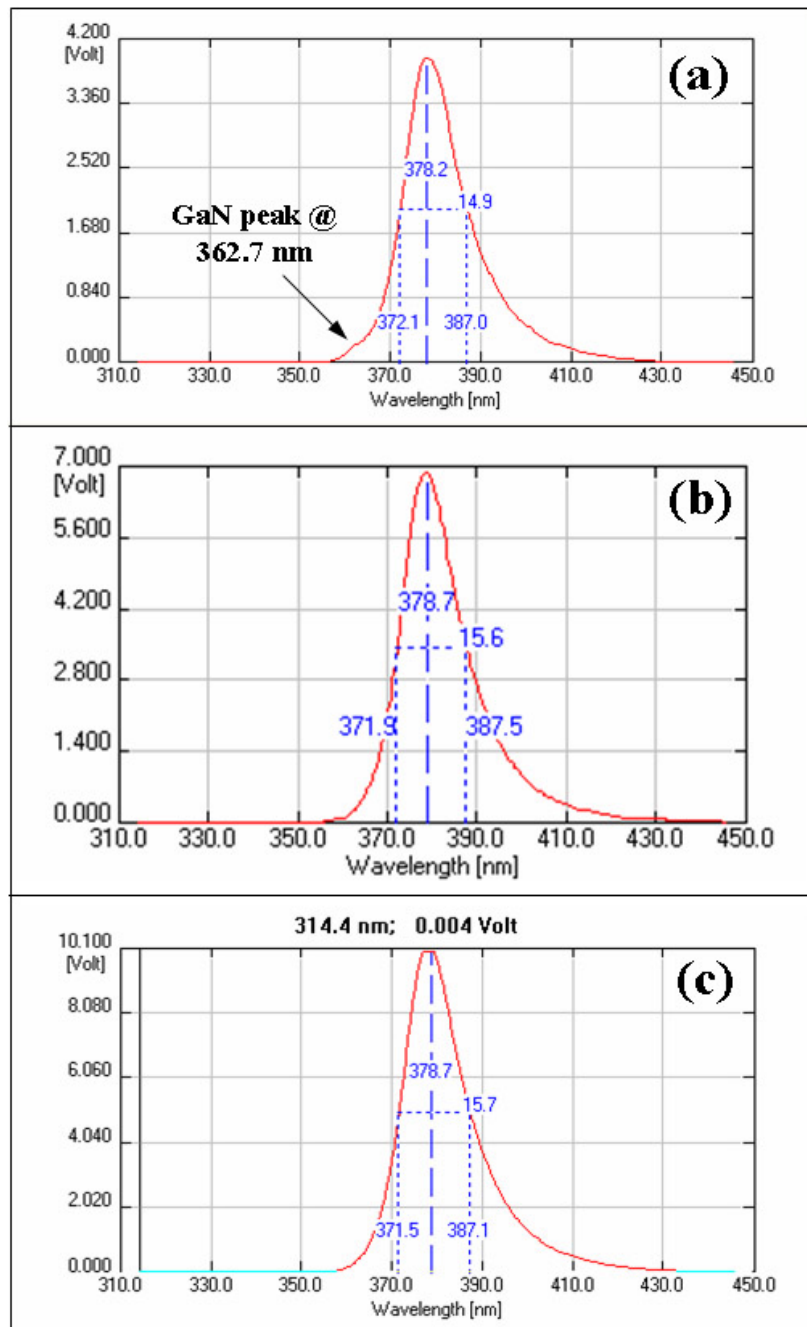
Figure 6.21: PL spectra of aligned ZnO nanowires grown on GaN (a), $Al_{0.5}Ga_{0.5}N$ (b), and AlN (c) substrates.

respectively, the relative PL intensities are not linearly related to the nanorod density. Due to the wide bandgap of AlN (6.20 eV), the luminescence from ZnO can not be absorbed by AlN, but the proximity of the bandgap of GaN to ZnO can cause absorption of the emission from the nanorods grown on GaN.

In order to reveal the density related light emitting properties, PL measurements were performed on the aligned ZnO nanowires catalyzed by gold layer with a thickness from 1 to 8 nm, which induced density variance was shown in section 6.2.2. Strong luminescence peaks are observed at 377 nm from all of the eight curves, while the intensities are varied, as shown in Figure 6.22. This is consistent to the constant diameter of the nanowires for all of the samples. In general, the intensity decreased when the density was dropping, as shown in the inset of Figure 6.22. The highest intensity is from the nanowires catalyzed by 1 nm gold layer, which has the highest density as well.
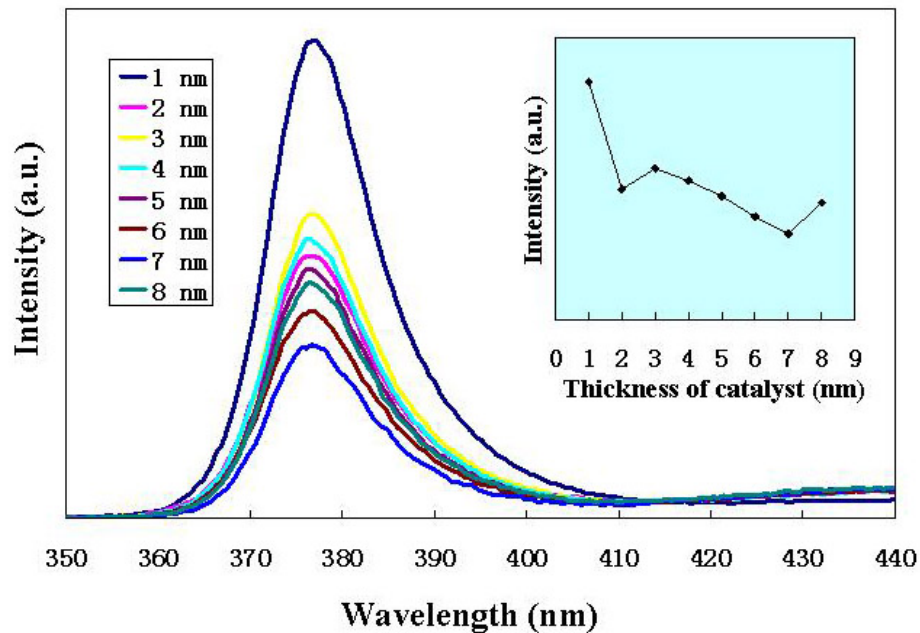
Figure 6.22: PL spectra of the eight stripes of the aligned ZnO nanowires with decreasing densities that were catalyzed by gold layer from 1 to 8 nm. Inset: Variation of the intensity of PL peaks with the change of catalyst thickness.

However, the lowest intensity is not from the sample with the lowest density. On the contrary, the sample catalyzed by 8 nm gold shows an enhancement on its luminescence intensity. This is probably owing to the increased reflectivity of the emitted light by the big gold particles lying on the substrate. The bouncing back of intensity from sample 2 to 3 may also be attributed to the increased reflectivity due to the formation of a continuous ZnO bottom layer.

6.3.2 Electromechanical Properties

The aligned ZnO nanowires fabricated through VLS process always have gold particles on their tips so that a natural metal-semiconductor junction (M-S) is formed. An interesting phenomenon of self-attraction among the aligned M-S junction arrays under an electron beam has been discovered during SEM characterization.[141]

The aligned ZnO nanowires sample was made on sapphire substrate with a hexagonal pattern, showing in Figure 6.23a. The nanowires exhibit an average diameter of ~20 nm and length ranging from 300 nm to 1 μm. The distribution of the nanowires follows the pre-fabricated pattern, but they grow from a continuous ZnO crystal layer at the bottom. An interesting phenomenon is that, after a short period of observation, some of the nanorods start to bend and make contact with each other. In all of these cases, the gold tip of one nanorod bends to be contact with the body of another. Usually both nanorods have slightly different lengths. The SEM images shown in Figure 6.23b and c, which were taken at a tilting angle of 30º, clearly show this process. Comparing the three circled regions, shows that all of the ZnO nanowires are straight and vertical at the beginning (Fig. 6.23b). However, after 30 seconds illumination by the electron beam, some of the tips of the nanowires suddenly bundled together, as shown in the final picture, figure 1c. Specifically, as shown in the circled regions in figure 6.23d and e, one
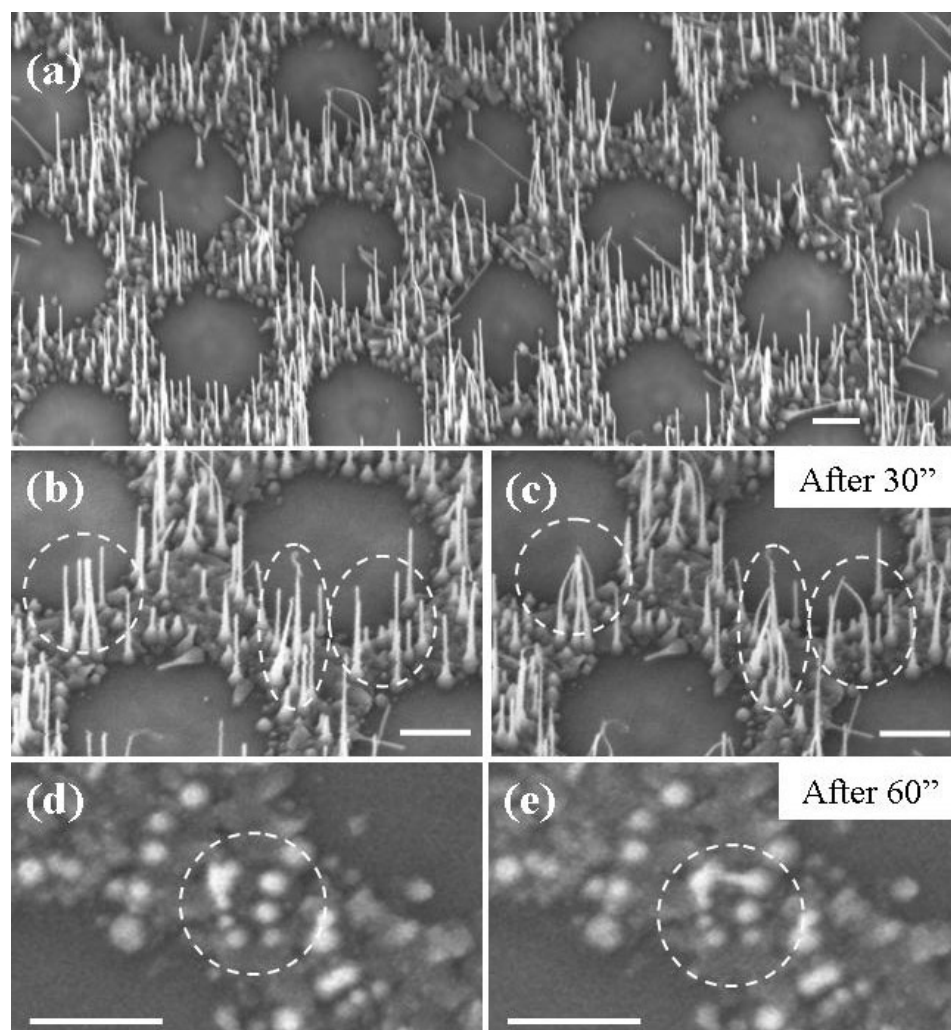
Figure 6.23: (a) A low-magnification SEM image of aligned ZnO nanowires; (b, c) 30º side view of self-attraction phenomenon; (d, e) Top view of self-attraction phenomenon. The scale bars represent 300 nm.

nanowire bends and makes contact with two nanowires on its left after 1 minute electron beam illumination.

The configuration of the bunched nanowires is very stable. Figure 6.24a shows the initial contact of four ZnO nanowires. When taken out of the SEM chamber and re-examined after 7 days in air (figures 6.24b and c), the configuration was preserved as shown in figure 6.24a. The largest distance between the bunched nanowires is ~150 nm.
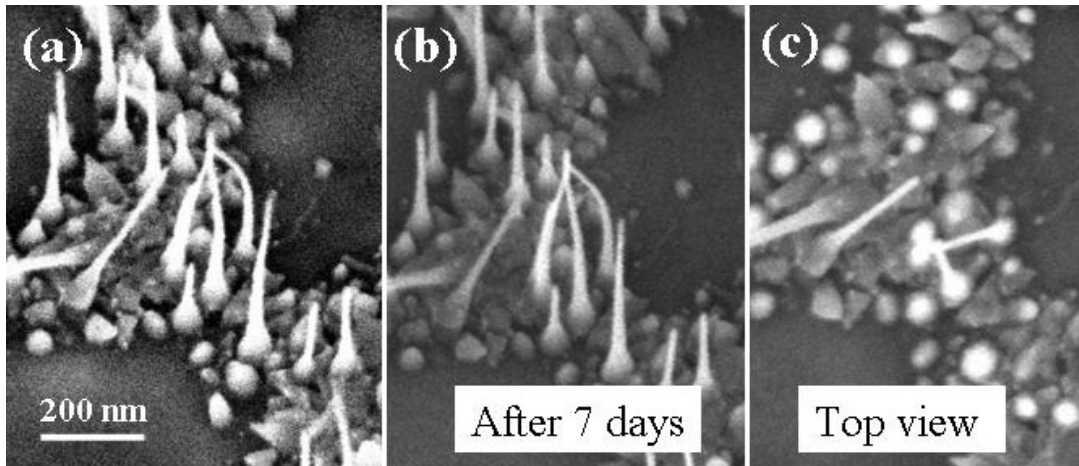
Figure 6.24: The ZnO nanowires contacting situation remains after days.

In order to explain this phenomenon, the crystallography of the ZnO nanowires was first confirmed by TEM characterization. Figure 6.25a shows a TEM image of a typical ZnO nanowire with a gold nanoparticle at its tip, which acts as the catalyst during VLS growth. The thickness of the nanowire is ~25 nm and the size of the gold nanoparticle is ~30 nm in diameter. The corresponding electron diffraction pattern (figure 6.25b) shows that the growth direction was along [0001] and that the side walls are $\{01\bar{1}0\}$ faceted. In the high resolution TEM image shown in figure 6.25c taken from the center region of a ZnO nanowire, the dislocation-free crystal structure can be clearly seen and there is no amorphous layer covering the nanorod. Since the $\{01\bar{1}0\}$ facets of ZnO
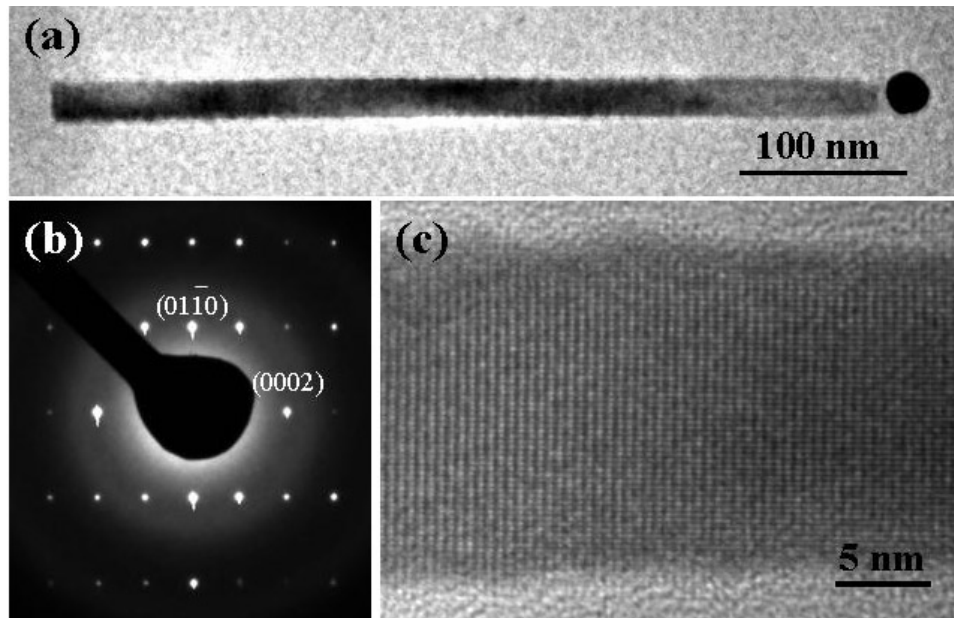
Figure 6.25: (a) A Low-magnification TEM image of a single ZnO nanowire; (b) Corresponding diffraction pattern; (c) A high-magnification TEM image of the ZnO nanowire.
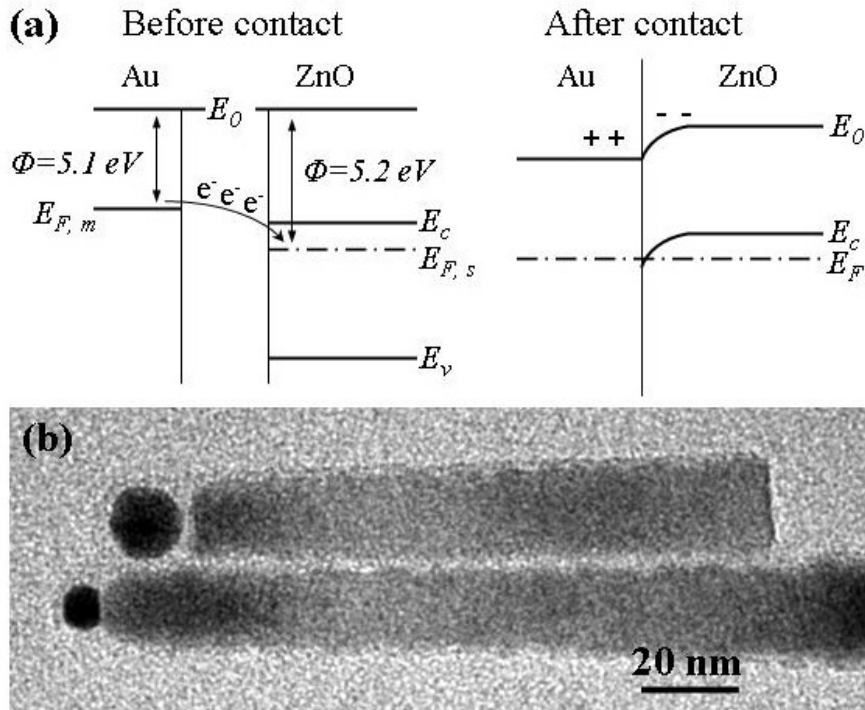
Figure 6.26: (a) Band gap structure of a Au and ZnO junction. (b) Two freely contacting ZnO nanowires.

wurtzite structure are non polar surfaces, the bending cannot be attributed to a local dipole moment created by surface polarization.[47]

From these observations, a metal-semiconductor junction model is proposed to explain the self-attracting effect. The work function of gold is 5.1 eV and our previous research revealed that the 1D ZnO nanostructure has a work function of 5.2~5.3 eV. Thus, as illustrated in figure 6.26a, the ZnO Fermi energy level is lower than that of gold because of its larger work function, so that electrons will flow from gold to ZnO during the formation of the metal-semiconductor junction to establish a constant Fermi energy level. This charge redistribution results in a positively charged Au particle and a negatively charged ZnO nanorod, with highest charge density region located adjacent to the junction.

When the ZnO nanowires are free standing, the electrostatic forces induced by the junction barrier are insufficient to overcome the elastic deformation force for bending. However, with the assistance of an external electron beam, electrons are excited from the valence band into the conduction band of ZnO. Thus, the electron concentration increases, whereas the holes in the valence band are filled by electrons flowing in from the Au tip, resulting in an increase in the local charge density on both sides of the Au/ZnO junction. Thus, the dipole moment increases even though some recombination of electrons with holes occurs in the ZnO. If the lengths of adjacent Au/ZnO nanowires differ, they will attract each other due to the asymmetric attractive and repulsive forces between them. Evidence to support this model is shown in figure 6.26b which shows two free contacting ZnO nanowires when one nanowire's Au tip contacting the other's body just below the junction. All of the freely contacting nanowires are similar to the one presented in figure 6.26b. We have not found any two aligned nanowires that are contacted head-to-head and body-to-body. This is important for our proposed model.

The model proposed to calculate the magnitude of the forces responsible for the bending is shown in figure 6.27a. Each Au/ZnO nanowire can be viewed as a dipole; the
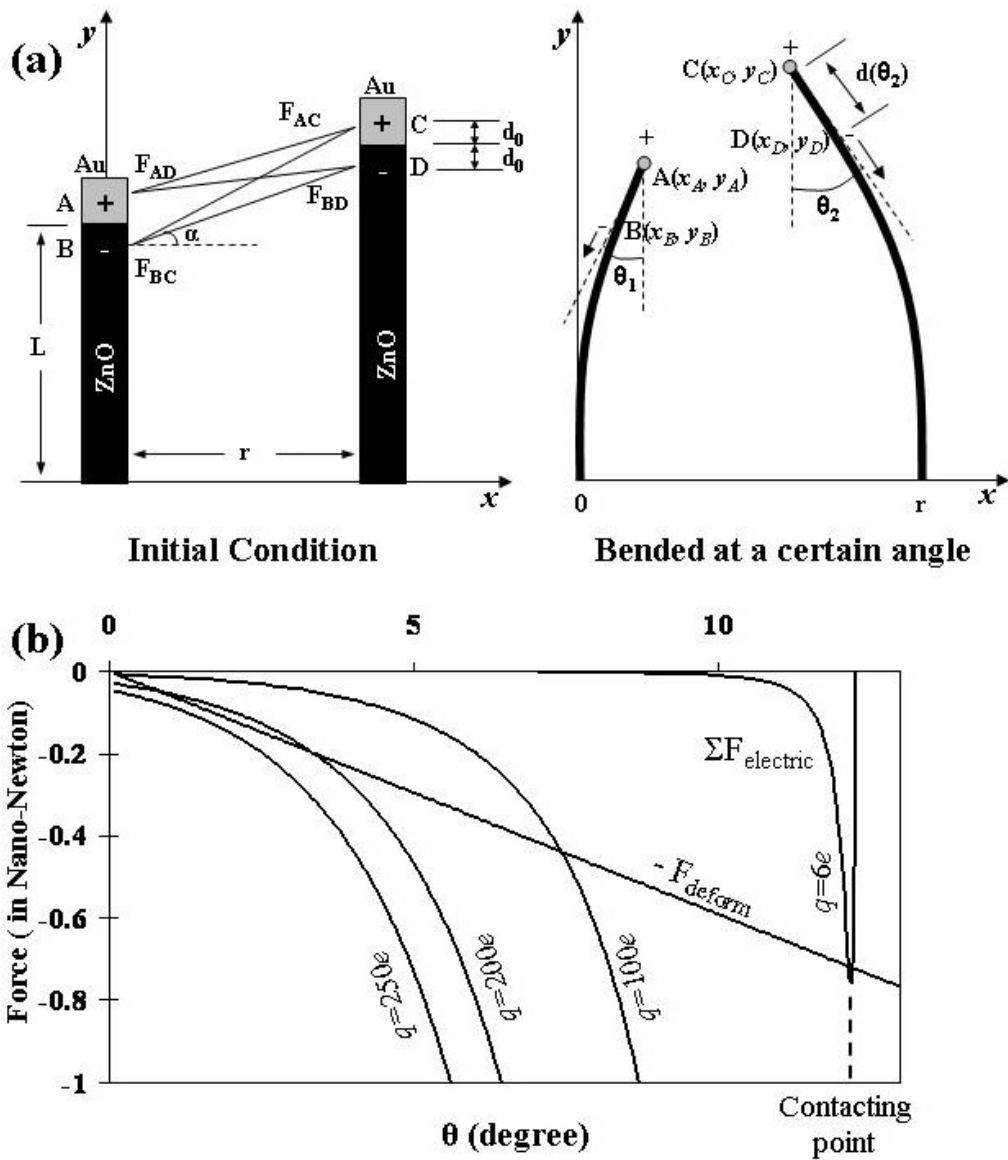
Figure 6.27: (a) Schematic model of the interaction between two ZnO nanowires. (b) The calculated electric attraction force and elastic force based on bending angle.

total force between two dipoles is attractive only if the nanowires have different lengths, such that the gold tip of one contacts the body of the other just below the junction interface. For free-standing nanowires, once the electrostatic attraction overcomes the elastic bending force, bending is possible.

To simplify the case, we just consider the interaction between two nanowires. The left side of figure 6.27a shows the initial state for two nanowires with lengths L_1 and L_2, respectively, separated by a distance r. The positive and negative charges are treated as point charges that are initially located the same distance from the Au/ZnO interface (points A and C for gold particles 1 and 2, points B and D for nanowires 1 and 2, respectively). This distance is represented by d_0. Now four different electric interactions exist: two forces of repulsion between like charges, F_{AC} and F_{BD}; two attractive forces between opposite charges, F_{AD} and F_{BC}. Assuming all the charges have the same magnitude, q, and considering only forces along the x direction are effective in bending the nanowires, each effective electrostatic force can be presented by Coulomb's equation:

$$F = \frac{q^2}{4\pi\varepsilon_0 R^2}\cos\alpha \qquad (6.11)$$

where ε_0 is the permittivity of space, R is the distance between two point charges and α is the angle between the force and x-axis. As shown on the right side of figure 6.27a, the bending angle θ, the angle between the y-axis and the tangent at the nanowire tip, is used for defining any intermediate state during the bending process. The relationship between the bending angle θ and the force F required to overcome the induced elastic energy is:

$$\theta = \frac{FL^2}{2EI} \qquad (6.12)$$

where L is the length, E is Young's modulus and I is the moment of inertia of the ZnO nanowire with a hexagonal cross-section. Since there are no other external force, the bending forces experienced by the two nanowires must be equal. During bending, we assume that the positive charges are confined due to the very small size of the gold

particles, whereas the negative charges can flow along the ZnO nanowires due to charge interactions. This is especially the case when the Au tip of one nanowire becomes close to the body of another nanowire. Then we can simply assume that the distance from the negative charge center to the interface increases lineally with increasing bending angle

$$d(\theta) = d_0 + \frac{\Delta L - d_0}{\theta_0}\theta \tag{6.13}$$

where ΔL and d_0 are the initial and final distances from the negative charge to the interface and θ_0 is the bending angle at which the two nanorods are in contact. This assumption meets the condition that the center of negative charge on the ZnO nanowire is closest to the center of the positive charge on the other nanorod tip, when both are in contact.

Based on all the assumptions mentioned above and assuming the shape of the bended nanorods is a part of a circle, the position of the four charge centers at any intermediate moment can be presented as follows:

$$
\begin{aligned}
x_A &= \frac{L_1 + d_0}{\theta_1}(1 - \cos\theta_1), y_A = \frac{L_1 + d_0}{\theta_1}\sin\theta_1 \\
x_B &= \frac{L_1 - d(\theta_1)}{\theta_1}(1 - \cos\theta_1), y_B = \frac{L_1 - d(\theta_1)}{\theta_1}\sin\theta_1 \\
x_C &= r - \frac{L_2 + d_0}{\theta_2}(1 - \cos\theta_2), y_C = \frac{L_2 + d_0}{\theta_2}\sin\theta_2 \\
x_D &= r - \frac{L_2 - d(\theta_2)}{\theta_2}(1 - \cos\theta_2), y_D = \frac{L_2 - d(\theta_2)}{\theta_2}\sin\theta_2
\end{aligned}
\tag{6.14}
$$

The distance R and angle α in equation 6.11 can be expressed using these coordinates information. Thus, the balancing of the electrostatic force and the elastic deformation force can be calculated in term of θ with any given L_1, L_2, r, d_0 and q. The curved lines in figure 6.27b are the electrostatic force calculated as a function of the bending angle for L_1 = 400 nm, L_2 = 500 nm, r = 100 nm, d_0 = 10 nm and q = 6e, 100e, 200e and 250e (e = 1.6×10^{-19} C), respectively. The straight line is the elastic deformation force for a Young's modulus of E_{ZnO} = 50 GPa.[64] This force is plotted in reversed sign in order to compare its

magnitude with the electrostatic attraction force. The attractive force increases slowly for small θ and increases dramatically when the two nanorods are in close proximity. For a small electron concentration, forming a contact between two nanorods is unlikely (cases q=6~200e). However, when the number of electrons exceeds 250, the attractive force becomes large enough to overcome the bending induced elastic force over the entire θ range. In this case, the ZnO nanorods are strongly attracted, and suddenly come together, as observed. Once the two nanorods are in contact, discharging may occur at the contacting point. However, short-range bonding such as van der Waals force can be induced that hold them together even days after the experiment.

In general, a new self-attracting phenomenon has been observed on vertical aligned ZnO nanorods under the effects of electron beam. This discovery opens a new way to manipulate nanomaterials and control nanodevices and could be applied in electron beam, electric field or opto-electron related nano-triggers, nano-switches and nano-sensors.

6.3.3 2D Photonic Crystals

2D photonic crystal (PC) is dielectric media with two-dimensional periodicity, which is normally an ordered array of dielectric rods or air-holes in a dielectric slab.[142] A wide variety of applications in optoelectronics have been explored using 2D PCs, such as waveguides[143], superprisms[144], laser diodes[145], and photonic integrated circuits[146]. Traditionally, 2D PCs are fabricated by electron-beam lithography, which is a top-down process that is limited to relatively small areas and high cost[147], possibly hindering its application and commercialization. The aligned and patterned growth of ZnO nanowires has been proved as a simple and cost effective approach for growing 1D nanostructure arrays on a relatively large scale. However, these as-synthesized 1D nanostructures have a large percentage of air space and vanishing photonic bandgap, and are not suitable for
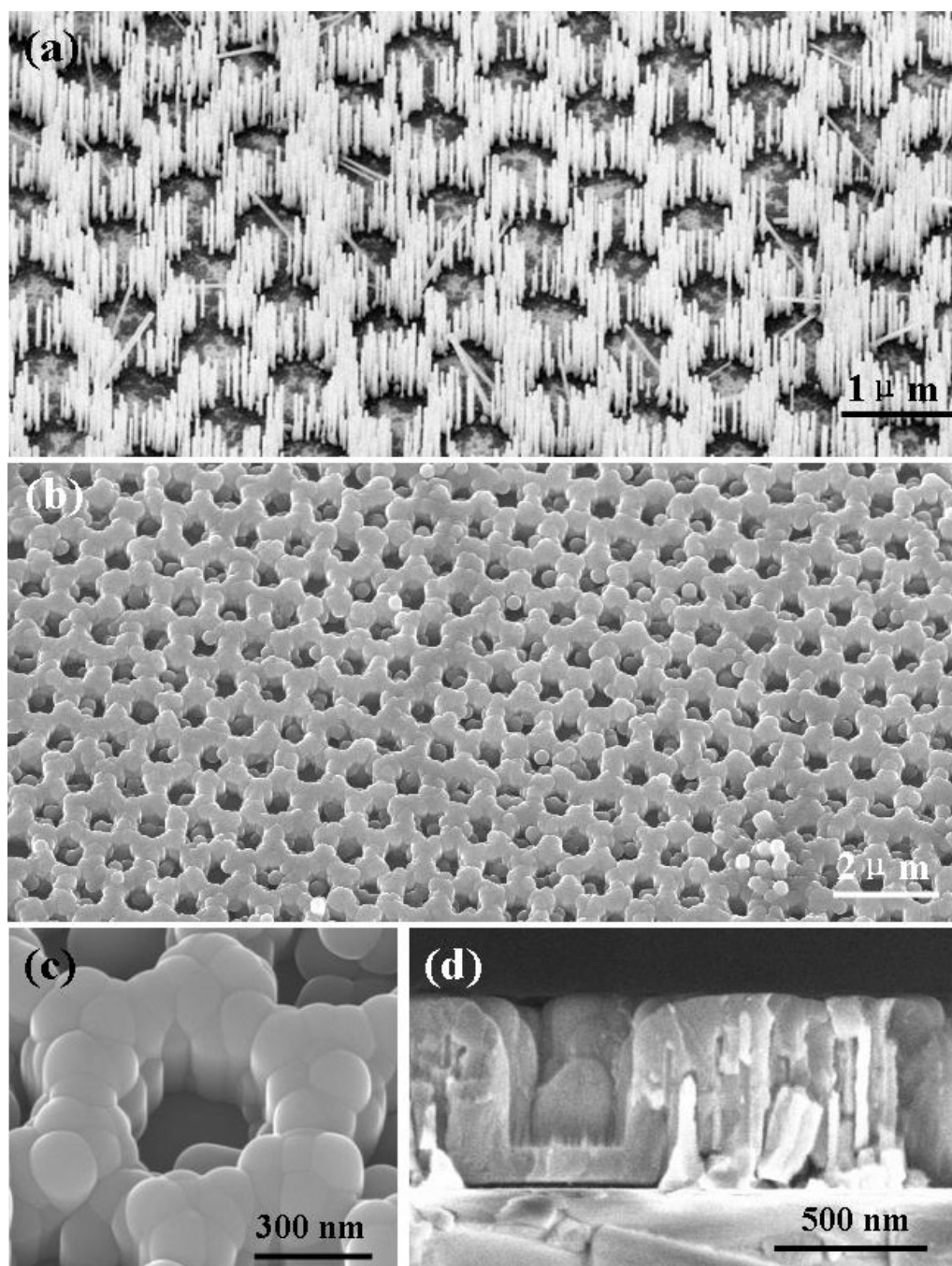
Figure 6.28: SEM images of the TiO$_2$/ZnO quasi-2D photonic crystal structure. (a) Short and densely aligned ZnO nanowire array on a sapphire substrate. (b) Low magnification SEM image of the TiO$_2$ coated ZnO nanorod array. (c) High magnification SEM image showing a single air hole surrounded by ZnO nanowires imbedded in TiO$_2$ walls. (d) Cross-section of the TiO$_2$ coated ZnO nanorod array.

161

photonic applications. However, by partially filling the space between the patterned and aligned ZnO nanowires with TiO_2 through an ALD process, a continuous ZnO/TiO_2 matrix with a highly ordered air hole array was formed. This periodic structure showed a reflection peak at the theoretically predicted bandgap region, while the near-UV emission of ZnO was unaffected by the TiO_2 coating. This technique demonstrates an effective and economical bottom-up process for 2D PC fabrication.

The 2D periodic structure was achieved by a two-step process: growth of patterned nanowire arrays with large air holes, then infiltration of the nanowire arrays with TiO_2 to form an air-TiO_2/nanowire photonic crystal. A honeycomb-like pattern of dense and well-aligned ZnO nanowire arrays was produced, as shown by the SEM image in Figure 6.28a. The length of the ZnO nanowires was ~500 nm and their diameters ranged from ~20–30 nm. In the second step, the ZnO nanowires were uniformly coated by a layer of TiO_2 using low temperature ALD. The SEM image of the TiO_2 coated ZnO nanorod array is shown in Figure 6.28b. All of the ZnO nanorods were coated with TiO_2, forming a continuous dielectric film patterned with a hexagonal air hole array. This configuration is very close to the structure of a 2D PC slab that can exhibit a full photonic bandgap. Because the height of this slab is ~600 nm, which is less than the minimum height for guiding infrared radiation, the structure is a quasi-2D PC structure.

The TiO_2 coated surface is presented by the high magnification SEM image shown in Figure 6.28c. The interior surface of the air holes is actually a combination of closely spaced dielectric cylinders, as a result of the uniform growth of TiO_2 around each ZnO nanowire. Figure 6.28d is a cross section of the TiO_2/ZnO 2D PC, which clearly shows that the space between the ZnO nanowires is completely filled by TiO2 due to the deep penetration of the ALD reactants. Owing to the uniform length of the ZnO nanowires, the TiO_2 coating exhibits a flat top surface. The thickness of the conformal TiO_2 coating measured at the substrate region is ~110 nm, which is uniform over all features, on both the sapphire substrate and the vertical ZnO nanowires. Since the length

of the ZnO nanowires are >500 nm in lengths, the ~100 nm-thick layer of TiO_2 deposited

on the substrate does not affect the entire structure for 2D PC. The total thickness of the

quasi-2D PC is ~600 nm including the thickness of the TiO_2 layer on the substrate. The

space between the TiO_2 layer and the substrate was created when the sample was cleaved

for the SEM study.

TEM was used to characterize the crystal structure of the TiO_2 coated ZnO

nanowires. The TEM sample was acquired at a broken edge as shown in Figure 6.28d.

Most of the TiO_2 layer was fractured off, and the ZnO nanowire observed in the TEM

image is covered only by a very thin layer of TiO_2, as shown in Figure 6.29a. The dark

tip at the front of the ZnO nanowire is the gold catalyst, which has a similar size as the

nanowire. A corresponding diffraction pattern reveals that the growth of the ZnO

nanowire was along the [0001] direction. Other than the diffraction spots from the ZnO,

no additional diffraction spots were observed, which confirms that the TiO_2 coating layer
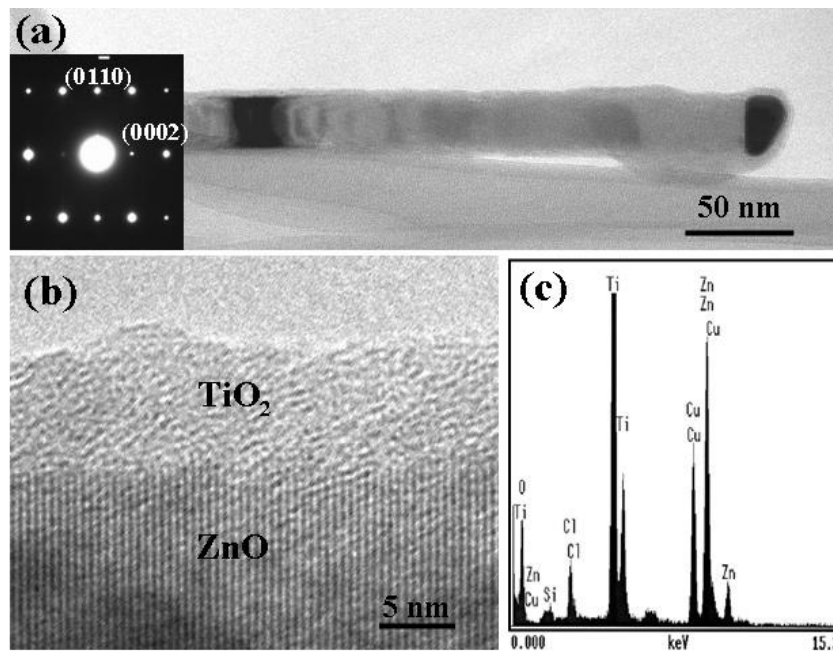
Figure 6.29: (a) A low magnification TEM image showing a ZnO nanorod removed from the TiO_2 coating and the corresponding electron diffraction pattern. (b) A high magnification TEM image of the side region of the ZnO nanorod showing an amorphous TiO_2 film covering the ZnO crystal. (c) ESD spectrum of the TiO_2 coated region.

was amorphous. Further evidence of the film structure is shown by a high resolution

TEM picture in Fig. 6.29b. The lattice fringes correspond to (0002) planes of a ZnO

crystal, on the top of which a clear TiO2 amorphous layer is shown. At the interface

region, no lattice deformation was observed. Although ZnO and TiO_2 can easily form an

alloy at elevated temperatures[148], the films are stable at the low TiO_2 deposition

temperature of 100ºC. The elements were confirmed by EDS acquired from the edge

region. As shown in Figure 6.29c, strong signals from Zn, Ti and O are recorded together

with a small amount of Cl due to the incomplete ALD reaction between $TiCl_4$ and H_2O at

the relatively low deposition temperature.

The photonic band structure of the fabricated photonic crystal has been studied

theoretically and experimentally. Based on the experimental configuration of the TiO_2

coated ZnO nanowire arrays, the band structure was first calculated for a model presented

in Figure 6.30a, in which a 2D PC structure with a triangular lattice of truncated air holes

was assumed. The dielectric matrix of the PC was treated as a uniform media with an

average refractive index of amorphous TiO_2 and ZnO weighted by their volume ratios. In

our case, by measuring 10 randomly recorded SEM images, the density of ZnO

nanowires was counted as ~120 per μm^2 and their average diameter and length were 30

nm and 500 nm, respectively. The volume of the TiO_2 matrix was estimated by assuming

the air holes were cylindrical, where the average distance between two neighboring air

holes was $a = 900$ nm and the average internal diameter of the air holes was ~480 nm.

Thus, the volume ratio of ZnO was calculated to be 8%. Considering the refractive

indexes of ZnO and TiO_2 to be 1.99 and 2.25 in the infrared region, respectively, the

effective refractive index was given by $n = 1.99 \times 8\% + 2.25 \times (1 - 8\%) = 2.23$.

Similarly, the average dielectric constant of the matrix is also estimated to be $\varepsilon = 4.97$.

The following structural data were used in the calculation of the 2D PC band structure:

lattice parameter $a = 900$ nm; internal diameter of the air holes $d = 480$ nm; slab
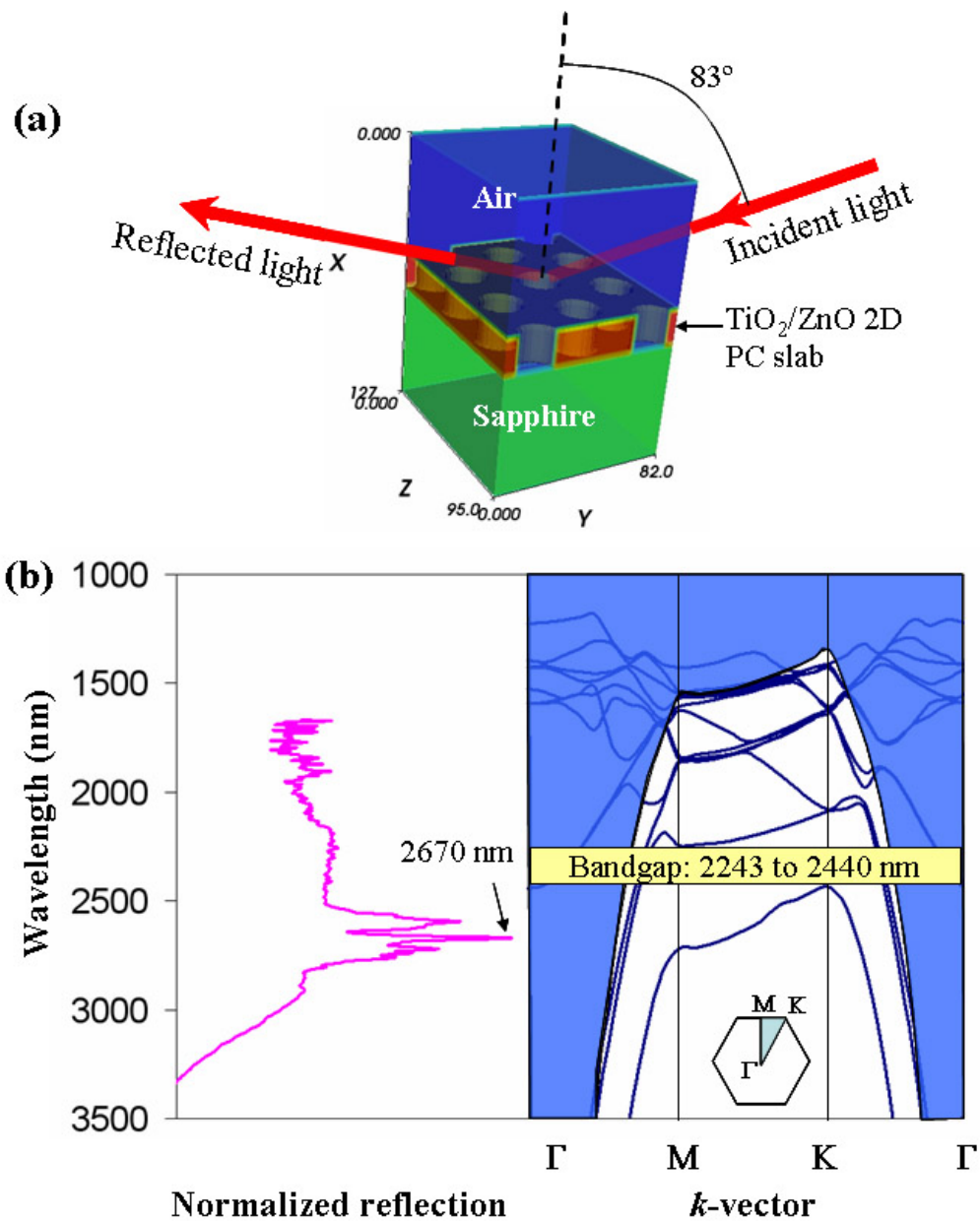
Figure 6.30: (a) A schematic model of the TiO$_2$/ZnO quai-2D PC for calculation, where the reflection measurement condition is also illustrated. (b) Left: Reflection spectrum of the TiO$_2$/ZnO quasi-2D PC slab after the reference was removed. Right: Calculated photonic band structure of the quasi-2D PC slab.

thickness $h = 600$ nm. Then the radius and slab thickness in terms of the lattice parameter were given by: $r = 0.267a$ and $h = 0.67a$.

Calculations were performed using the plane wave expansion method using a publicly available code[149] with a supercell as depicted in Figure 6.30a. Centered in the vertical dimension of the supercell is the 2D PC slab, mounted on a sapphire substrate ($\varepsilon = 2.96$) and surrounded by air above, all of which are infinitely extended in the y and z directions. Because of the nature of the calculation, the supercell is repeated in the x direction; hence, the air space between the slabs must be sufficient so that coupling of the guided modes between the slabs is minimized. This means that the modes that are not guided in the slab couple to one another and their solutions become part of the background continuum of modes that is shown by the shaded region in the band structure of Figure 6.30b. The band structure for the TE-like solutions is shown and a pseudo-bandgap region between the first and second bands is predicted in the normalized frequency range, $\omega a/2\pi c$, from 0.367 to 0.401, which corresponds to wavelengths from 2,440 to 2,243 nm. In this frequency range, there will be a dip in the photon density of states that will manifest itself as a peak in the reflectivity spectrum.

It was reported that the photonic band structure can be determined by reflection spectra[150], in which, the reflection peaks at different incident angles composed a large part of the band configuration. In our experiments, the photonic bandgap of the quasi-2D PC slab was measured by infrared spectroscopy at a large fixed incident angle (83°) to the normal direction, so as to enhance the interaction between the light and the lattice. Reflection spectra were acquired from both the TiO_2/ZnO quasi-2D PC slab and a thin layer of amorphous TiO_2 deposited on a flat sapphire substrate, which was used as a reference. The left-hand side of Figure 6.30b is the normalized reflection spectrum after rationing against the reference spectrum. A reflection peak was observed at 2,670 nm with a full width at half maximum of ~220 nm. Comparing this peak valve with the

calculated bandgap center at 2,342 nm, gives a mismatch of ~12%, which may be accounted for by the following factors.

The theoretical calculation was base on several assumptions and simplifications, which can change the distribution of the band structure. The theoretical bandgap was calculated for light transmitted within the 2D PC slab perpendicular to the normal direction, while experimentally the light was reflected off the slab surface at a large angle. This non-perpendicular light transportation causes a shift on the wavelength of reflection light, which is corresponding to the band distribution at certain transportation angle.[150, 151] According to this, our the data from this one fixed angle measurement is not sufficient to generate the whole band structure to match our theoretical calculation, however, the reflection peaks from the spectrum are able to clearly show the existing of the photonic bandgap. Experimentally, there are a few issues associated with the mismatch and relatively noisy spectra. Due to the large lattice parameter, the bandgap lies at fairly long wavelengths, where chemical species such as H_2O can also influence the reflection signal. The short length of this quasi-2D PC limits the light-lattice interaction, and as shown in Figures 6.28a and 6.28c, the air holes are not perfectively cylindrical, which results in random scattering effects.

As predicted by the theoretical calculation, the bandgap can be moved into the visible by changing the lattice parameter to ~100 nm. Being supported by single crystal ZnO nanowires, the matrix can be rigid even when its thickness becomes as thin as 30 nm, which is required by using this technique to fabricate a 2D PC with a bandgap in the visible spectral region. Achieving such a small feature is very expensive using lithographically based techniques. Therefore, through a bottom-up process, this technique created a new pathway for the large scale fabrication of 2D PC devices capable of operating over a wide wavelength range in a much more economical way.

In order to investigate the light emitting property of the quasi-2D PC slab with embedded ZnO nanowires, the photoluminescence was measured on the ZnO
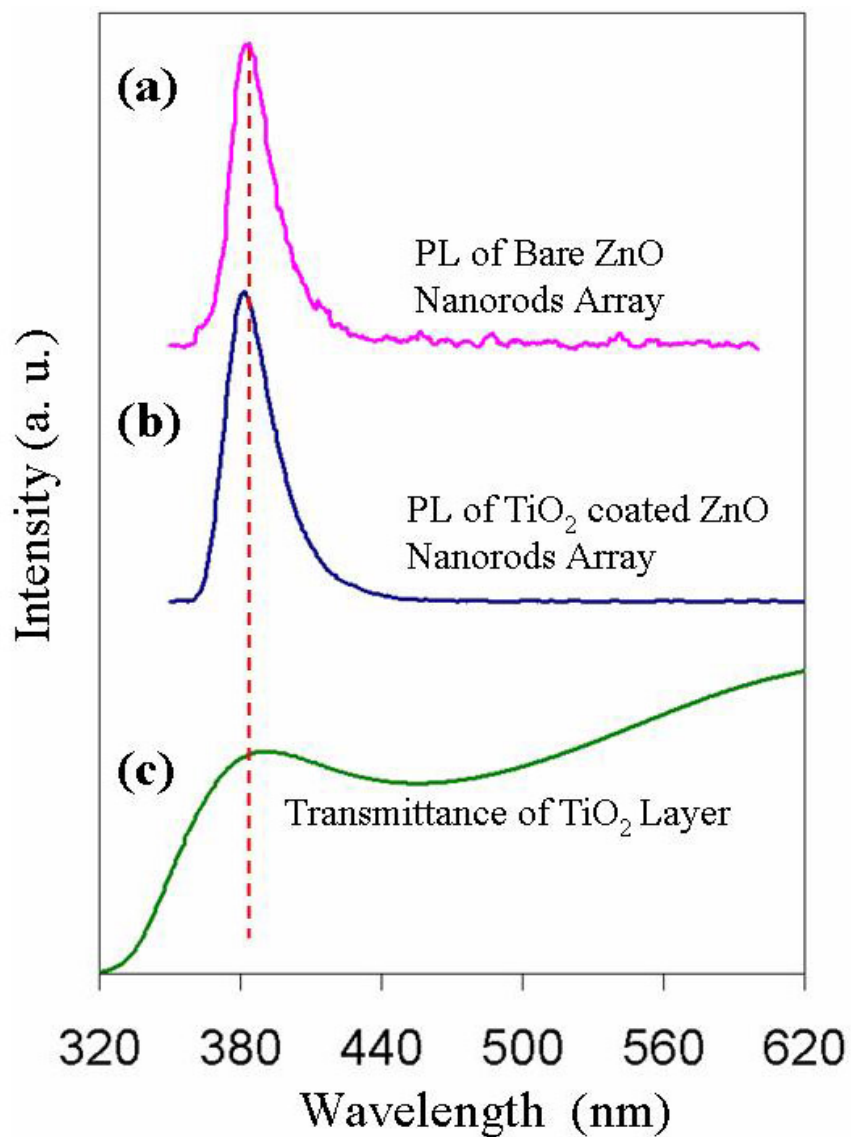
Figure 6.31: (a) Photoluminescence spectrum of a bare ZnO nanowire array. (b) Photoluminescence spectrum of a TiO$_2$/ZnO quasi-2D PC slab. (c) Transmission spectrum of an amorphous TiO$_2$ layer.

nanowire array before and after TiO_2 coating. As shown in Figure 6.31, the bare ZnO nanowire array has a PL peak at 384 nm. After being coated with a ~110 nm TiO2 layer, a PL peak with almost the same intensity was still observed at 383 nm. A transmittance spectrum was also measured on a 100 nm-thick, amorphous TiO_2 thin layer from the near-UV to visible region. As shown in curve c in Figure 6.31, amorphous TiO_2 exhibits an enhanced transmission at 380~390 nm, which matches very well with the PL peak from ZnO nanowires. Thus, the near-UV emission from the ZnO nanowires can be transmitted through the TiO_2 coating with little loss and is expected to show an identical PL peak with comparable intensity at the same wavelength as the non-coated ZnO nanowires. On the other hand, ZnO nanowires can be excited by UV radiation to lase at a wavelength of ~385 nm[55, 131], thus the TiO_2 coating will not affect the optical performance of the ZnO nanowires.

In summary, using a patterned and aligned ZnO nanowire array as a coating template, a bottom-up process for the fabrication of luminescent TiO_2/ZnO 2D PCs has been created. This periodic structure showed a reflection peak close to the theoretically predicted bandgap region. The photoluminescence of ZnO was not quenched by the TiO_2 coating. The bandgap can be controlled by varying the period of the PS sphere template, which is feasible down to ~100 nm, thus a 2D PC with a bandgap in the visible light region is possible. The technique is a totally self-assembly bottom-up process and can be effectively and economically scaled up for large-sized 2D PC fabrication.

CHAPTER 7

FUTURE WORK RECOMMENDATIONS

Patterning nanostructures through the low-cost self-assembly process has shown great potential in nano-device fabrication and integration. It is very likely to bring current ideal-proof nano-devices from scientific models to commercialized products once the assembly mechanisms are better understood and the defects are reduced to a device-function tolerable level. Moreover, besides facilitating the device fabrication, the aligned and well ordered configuration of nanostructures can also induce enhanced properties and new applications. Some novel applications have been described in previous chapters, such as the size-selector of nanoparticles, masks for nanolithography and photonic crystals. More sophisticated devices can also been realized by the self-assembled nanostructures described in this dissertation. Although the work is still in blueprint or initiation stage, it is necessary to be pointed out as promising targets of future research. Starting from the patterned nanobowl and nanowire structures respectively, high-efficient solar cell and sensor arrays are considered to be the achievable goals in near future.

7.1 High-Efficient Dye-Sensitized Solar Cell from TiO$_2$ Nanobowl Arrays

Harvesting energy directly from sunlight using photovoltaic technology is being increasingly recognized as an essential component of future global energy production. The essential cost-driving factor for the production of classical photovoltaic devices is the expensive investment in costly semiconductor processing technologies. This unfavorable cost has so far prohibited the technology from having a significant impact on global

energy production. Organic-based solar cells, such as dye-sensitized solar cells, provide a technically and economically viable alternative concept to present p-n junction photovoltaic devices.[116]
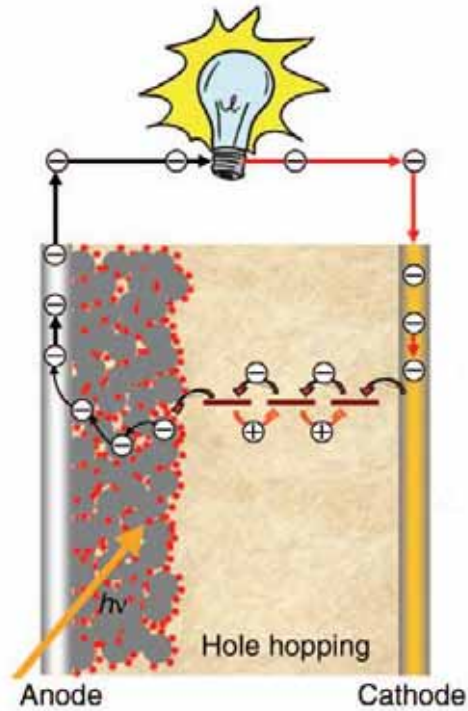
Figure 7.1: Schematic drawing of the operation principle of a dye-sensitized mesoporous heterojunction solar cell. The gray dots represent the mesoscopic oxide particles, covered with a monolayer of dye (small red dots). The yellow region is organic hole conductor.

Dye-sensitized solar cells defer from the conventional semiconductor devices in that they separate the function of light absorption from charge carrier transport. Figure 7.1 shows a basic schematic for the sensitized heterojunction photovoltaic cell. A monolayer of dye is attached to the surface of a mesoscopic film of a wide bandgap oxide semiconductor, such as TiO_2, and serves to harvest solar light. Upon excitation, an electron is injected into the conduction band of the semiconductor oxide. The electrons migrate across the nanoparticle network to the current collector (anode). They subsequently pass through the external circuit, where they perform electrical work and then proceed to the counter electrode (cathode). An organic hole conductor serves to

regenerate the sensitizer and transport the positive charges to the counter electrode, where they recombine with the electrons. Overall, there is no net chemical change under solar exposure; light is converted to electric power by this solid-state molecular photovoltaic system.

High power conversion efficiencies is the foremost aspect for the truly commercialization of organic-based solar cells. In order to achieve this, several fundamental issues must be addressed.

Bandgap: Current organic-based solar cells have exhibited high (>70%) quantum efficiency, defined as the ratio of the number of photons of a given wavelength incident on the device to the number of charges delivered to the external circuit, for blue photons. However, efficiently harvesting red photons, which contain a significant fraction of the energy in the solar spectrum, has proven challenging. Optical bandgaps of the light absorbing components must be reduced to approach the nominally optimal value of 1.4 eV while retaining good charge carrier mobility.

Interfaces: An improved understanding of the fundamental processes of charge transfer and carrier recombination across interfaces is critical. Contact resistance between layers must be minimized in order to reduce the device series resistance, which is important in determining the fill factor and thus the power conversion efficiency. Additionally, physical properties such as wetting between organic and inorganic components and adhesion between layers are important for both the device performance and lifetime.

Charge transport: Obtaining higher charge carrier mobilities will allow for the use of thicker active layers while minimizing carrier recombination and keeping the series resistance of the device low.

Controlling the morphologies and improving the optoelectronic properties of the light-absorbing and charge-transporting materials facilitate overcoming these fundamental obstacles to higher efficiency. Fabrication of bulk heterojunctions with well-

ordered arrays of organic and inorganic semiconductors is a promising route to increasing the efficiency of polymer photovoltaic cells. In such structures, almost all excitons formed are close enough to the organic-inorganic interface to be dissociated by electron transfer, all charge carriers have an uninterrupted pathway to the electrodes, and polymer chains are aligned to increase their charge carrier mobility.
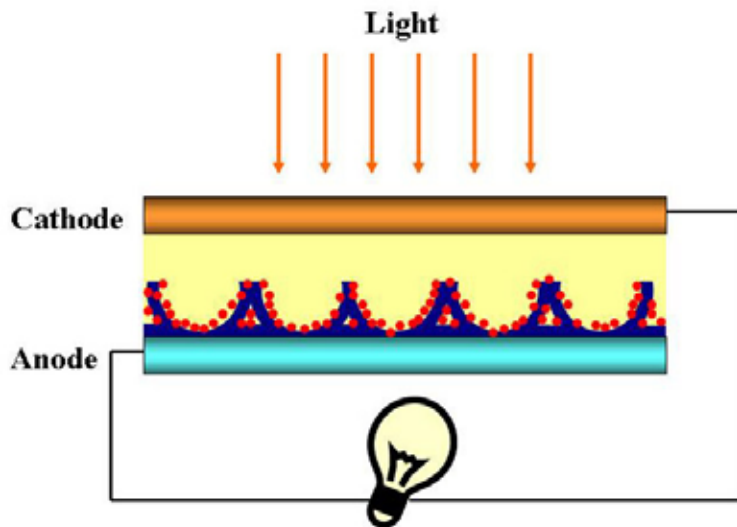
Figure 7.2: Schematic illustration of a dye-sensitized solar cell base-on TiO_2 nanobowl arrays. The blue curves represent the TiO_2 nanobowl array, covered with a monolayer of dye (small red dots). The yellow region represents organic hole conductor.

As described in Chapter 5, robust and highly-ordered anatase TiO_2 nano-bowl arrays have been successfully fabricated, which have a larger open surface area that could significantly increase the efficiency of surface related activities. The technique demonstrated can also be applied to different substrates, such as silicon, glass, metals or even polymer. This will realize the creation of a new type of dye-sensitized solar cell using TiO_2 nanobowl arrays as the semiconducting layer. As illustrated in Figure 7.2, by growing a TiO_2 nanobowl layer on a transparent conducting substrate, and coating the bowls with a layer of dye molecules covered by organic hole conductors and another electrode, a ultra-thin dye-sensitized solar cell is fabricated. How successful can the anatase TiO_2 nanobowl arrays be implemented into photovoltaic technology? In the

following, the expected technological properties of the dye-sensitized solar cell based on TiO_2 nanobowls will be discussed regarding to the primary commercial success factor—the efficiency.

Efficiency is the essential parameter for solar cells with respect to maximizing energy production and minimizing cost. Low device efficiency demands a larger photovoltaic active area in order to produce the same energy output. Comparing to the traditional mesoporous TiO_2 thin film made from TiO_2 nanocrystals, anatase TiO_2 nanobowl arrays can potentially be a more efficient electron conductor in a dye-sensitized solar cell.

First of all, the nanobowl array is like a set of millions of tiny satellite dishes, where almost all of the light that hits the surface will be reflected between the walls and be absorbed eventually. Consequently, even though the height of the nanobowl layer is only a few hundred nanometers, high absorption rate can be achieved owing to this unique morphology.

A contradiction exiting in a traditional TiO_2 nanocrystal dye-sensitized solar cell is that: TiO_2 close to the anode exhibits a high photovoltaic effect because of the highest light intensity, where, however, the electrons supplied from the cathode is limited due to the long pass through the organic hole transport material between the TiO_2 nanoparticles. On the other hand, TiO_2 can receive an almost infinite electron supply at the region close to the cathode, where the light intensity is the lowest and the photovoltaic reactions are limited. The efficiency of electron generation in a traditional dye-sensitized solar cell is limited by this contradiction, which now can be solved by using TiO_2 nanobowl layer. While keeping a comparable absorption rate, the TiO_2 nanobowl array can provide an equal high photovoltaic effect on all of its surfaces because electrons don't need to travel a long way between TiO_2 nanocrystals to re-activate the dye close to the anode as they do in a traditional dye-sensitized solar cell.

Furthermore, as shown in Figure 7.2, the contact between the anode and the TiO_2 nanobowls is a film-to-film contact owing to the uniform growth through ALD technique. Thus, the conductance at the interface of electrode and TiO_2 layer can be highly increased. It has also been revealed that the electron mobility in films of nanocrystals is limited by nanocrystal-nanocrystal hopping.[152] The crystal analysis showed that the single-crystal grain in the TiO_2 nanobowl structure is >50 nm. Considering the height of the nanobowl is ~300nm, an electron injected on the TiO_2 surface only need to pass at most 5—6 grain boundaries to reach the anode. As a result, the scattering and recombination effects can be significantly reduced and higher electron generation rate and electron mobility can be achieved.

Structurally, the thickness of the TiO_2 walls can be precisely tuned by varying the number of ALD cycles, and the size of bowls can be adjusted by using different sized PS spheres as templates. This structural flexibility in addition to the performance enhancements mentioned above will eventually bring this new type of dye-sensitized solar cell to a higher efficiency.

In general, solid-state solar cells based on sensitized mesoscopic heterojunctions have undergone rapid development over the last five years. A large improvement in performance was achieved over this period, with the conversion efficiency being increased by more than a factor of 10 to reach an impressive 4% in full sunlight. There is room for further improvement in the future. In particular, cell performance should benefit from advances in developing mesoscopic films such as ordered arrays.[153] The ordered anatase TiO_2 nanobowl arrays can be an ideal electron conductor film that might significantly increase the conversion efficiency. I believe further experimental and theoretical research on the TiO_2 nanobowl design in the dye-sensitized solar cell will explore a brand new way to produce high-efficient and low-cost photovoltaic devices.

7.2 Sensor Arrays

1D nanostructures, including nanowire, nanobelt and nanotube, are becoming a new category of advanced sensing device or system.[67] So far, the theory and technique adopted by 1D nanostructure sensors is based on those of FETs. The idea for sensing with FETs was introduced several decades ago, although the limited sensitivity of these planar devices has precluded them from having a large impact. Using semiconducting 1D nanostructures as FET elements can overcome the sensitivity limitations of previous planar FET sensors since binding to the surface of a nanowire leads to depletion or accumulation of carriers in the 'bulk' of the nanometer-diameter structure (versus only the surface region of a planar device) and increases sensitivity to the point that single-molecule detection might be possible.

Recent developments in nanoscience and nanotechnology have shown that its core technology is ideally suited for different gas- and bio-sensor applications. The basic concept has been shown laboratorially for detecting different gases or biological molecules based on single one-dimensional semiconducting nanostructure. Although the concept has been proved for years, it is still challenging to realize an efficient large-scale fabrication process with reasonable cost that is feasible for commercialization. Another intrinsic issue related to the single-nanowire-based gas- and bio-sensor is that the electric properties of each nanowire are different due to the variation in thickness, defects and active length. Accordingly, the electric response to the same amount of target species might be different between different sensors made from the "same" nanowire. Therefore, it is difficult to set standard responses to tell between different species just based on a single nanowire, unless an averaged value can be achieved from the signals of a large number of nanowire sensors.

Based on the patterned and aligned semiconducting nanowires described in Chapter 6, a low-cost self-assembly method for large-scale fabrication of an integrated

176
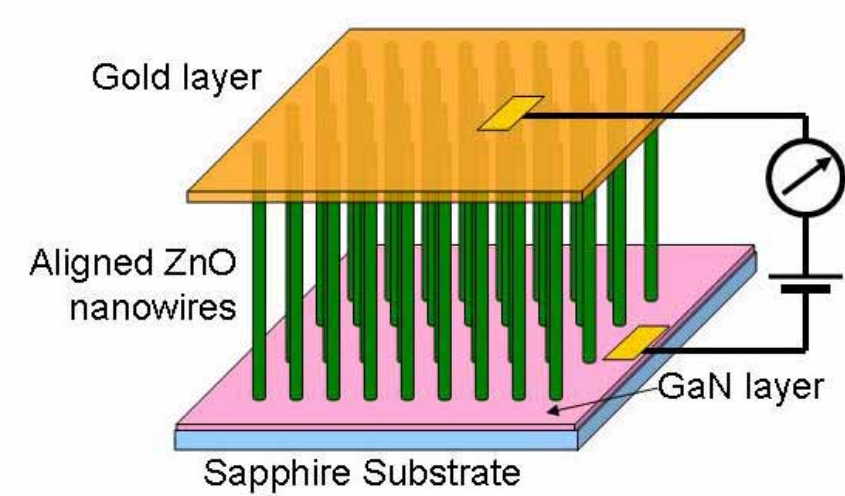
Figure 7.3: Schematic of a sensor array based on aligned ZnO nanowires.
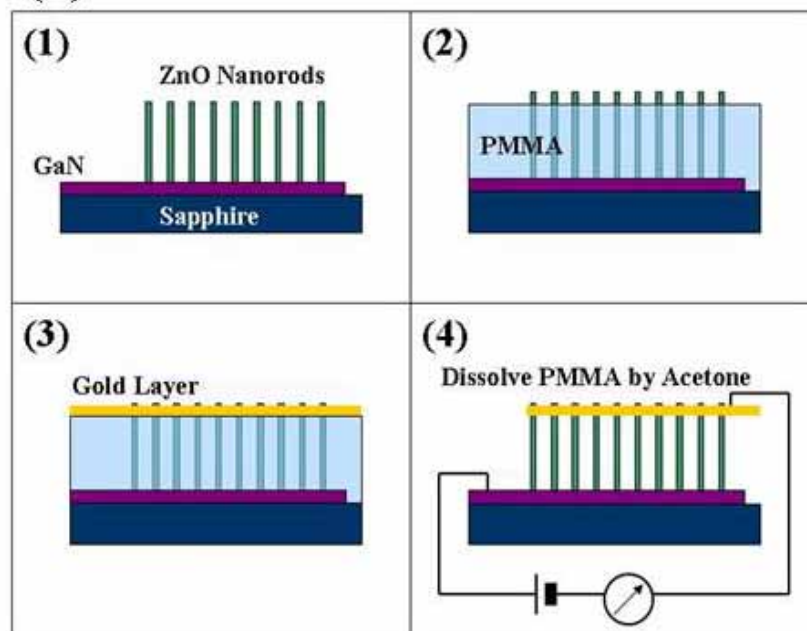
Figure 7.4: Schematic fabrication process of sensor arrays based on aligned ZnO nanowires.

gas- and bio-sensor array can be developed to overcome these challenges. In the proposed fabrication process, lithography technique that was traditionally utilized for electrodes assembly will be abandoned. Instead, a high-efficient self-assembly technique will be selected to locate the source and drain electrodes for number of sensor circuits simultaneously. Furthermore, a large quantity of nanowires instead of just one will be automatic aliened between the electrodes. A schematic structure of our proposed sensor array is shown in Figure 7.3. As a result, the electric signals generated through these circuits are naturally averaged, which are repeatable and reliable and can be considered as representative responses to various target species.

The experimental process is illustrated in Figure 7.4. After achieving the aligned ZnO nanowires on a semiconducting GaN substrate, a uniform PMMA layer can be spin-coated with the thickness smaller than the height of the nanowires. Therefore, the tips of most nanowires are exposed out of the PMMA layer, onto which a gold layer is deposited. The PMMA layer is thereafter dissolved in toluene to expose ZnO nanowires between the substrate and top gold layer. The gold layer can also be deposited through a mask such as TEM grid, thus multi top-electrodes are achieved, which can be simply connect to the bottom electrode by electric wires. The nanowires under each top-electrode can be treated as an individual sensor element and functionalized simultaneously. Even if some of them are broken, the rest still can provide valid sensing signals. Thus it is a much more reliable sensor system, which will eventually meet the requirements of the applications in variable circumstance. If the nanowires under different top electrodes are coated with different probe molecules, an on-chip sensor system for multi-tasks can be realized.

The possibility to introduce another electrode onto the nanowires to form a circuit has already been demonstrated. The preliminary experimental observation of the fabrication of this configuration is shown in Figure 7.5. The gold layer is supported by the standing nanowires and electrically connects all of them. This result is both
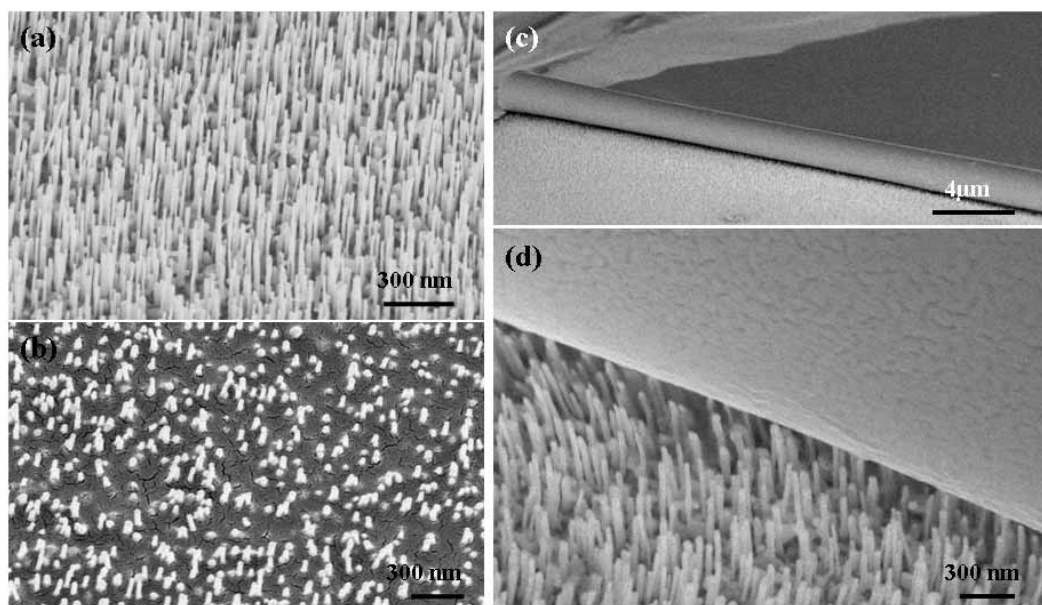
Figure 7.5: SEM images of the preliminary results. (a) aligned ZnO nanowires growing on GaN substrate; (b) PMMA coated ZnO nanowires; (c, d) gold electrode staying on the top ZnO nanowires after removing PMMA layer.

encouraging and intriguing, and ready for a better structural confinement for a better understanding of various electrical properties on the nanometer scale activate nanowires and the junctions. Moreover, this method can potentially be used to selectively functionalize different nanowires in a densely-packed array with different probe molecules.

Based upon the discussions above, I believe the aligned nanowire sensor arrays will exhibit extraordinary advantages both in their function and cost. This new type of nanostructure based sensor system is the first prototype that doesn't need microscopic control and lithography technique to either locate the nanostructure or pattern the electrodes. With high reliability and repeatability, the prototype of this sensor array, once realized laboratorially, will be ready for large-scale mass production for commercialization and this self-assembly fabrication process will eventually become a major technique in the field of nano-devices fabrication.

CHAPTER 8

CONCLUSION

Owing to the inventions and developments of powerful tools, such as TEM, SEM, AFM, and SPM that enable researchers to observe and manipulate objectives in the levels of atom, molecule or supermolecule; owing to the creation and discovery of novel nanostructures that provide interesting and functional targets for scientific studies; owing to the establishing of new theories that predict and explain the new or improved phenomena in nanometer scale, nanotechnology is experiencing a flourishing development in a large variety of fields covering all of the areas from science to engineering and to biology. As an active field in nanotechnology, the work presented in this dissertation is mostly focused on the fundamental study about the fabrication and assembly of functional oxide nanostructures.

Due to the intensive research that has been directed to nanoscience and nanotechnology, new morphologies as well as novel properties and phenomena have been discovered. However, it is still essential to increase the yields and improve the uniformity of the products for commercialization. Consequently, this dissertation is started with the study of the relationship between morphologies and experimental conditions. It has been found that the size and shape of the resulting 1D ZnO nanostructures varied according to the change of local vapor composition and concentration. Generally, a low growth temperature resulted in a low vapor density, which led to a small-size nanobelt (can be as small as 6 nm in width). A high growth temperature would induce a fast growth of big nanowires and other impurities might also become available during the high-temperature deposition. Thus a complex structure, such as mesoporous or core-shell nanowires, was realized.

After successfully fabricating the morphology controlled ZnO 1D nanostructures, a self-assembly process has been studied to achieve long-range ordered nanostructures for parallel processing and integrating nanodevices. As the fundamental template, a large-area monolayer of highly-ordered PS spheres was fabricated based on a water-surface-tension-assisted self-assembly process. Thereafter, for the first time, highly ordered anatase TiO_2 nanobowl arrays have been created. The process utilizes the PS spheres monolayer as a template. TiO_2 walls are uniformly coated around the sphere surface by atomic layer deposition, by which the thickness of TiO_2 walls can be precisely controlled. The final nano-bowl arrays were achieved after ion milling, etching and annealing. Besides their inherited well-ordered arrangement, the nano-bowls exhibit smooth interior and exterior surfaces and uniform size and thickness. The nanobowls have been demonstrated for selecting spheres smaller than the bowl's inner diameter. This approach can be extended to a wide range of coating materials and substrates with controlled wall thickness and size. Further research has improved this bottom-up process for fabricating large-scale, free-standing nanobowl sheets with high flexibility. By introducing an organic buffer layer between the nanobowls and the substrate, the full nanobowl layer (in centimeter range) can be lifted up and deposited on any other substrate or placed up-side-down forming small nano-cell arrays. The nanobowl sheet were also successfully loaded onto a copper TEM grid, which can be utilized as a reusable mask for making catalyst or quantum dots arrays with precisely controlled size, distribution and density. The formation of both up-side-down nanobowls and nanobowl masks presented successful examples of integrating top-down and bottom-up processes, which is the future of nanotechnology. The technique has a great potential for scaled-up, mass production and commercial applications.

Using the PS spheres monolayer and the nanobowl sheet as masks to pattern gold catalyst, large-scale patterned and vertical aligned ZnO nanowires were successfully achieved on sapphire and nitride substrates. The alignment was achieved by the epitaxial

181

relationship between the {0001} surfaces of ZnO and the substrate surfaces. Due to the better lattice and crystal structure match between ZnO and $Al_xGa_{1-x}N$ substrate, an almost perfect aligned growth was achieved on those nitride substrates.

Besides the crystallography of substrates, furnace conditions also exhibited significant effects on the alignment. Therefore, a systematic research was conducted to optimize the growth condition for achieving high quality aligned ZnO nanowires. Based on hundreds of experiments, a "phase diagram" that correlates the partial pressure of oxygen with chamber pressure for growing aligned ZnO nanowires on GaN substrate via VLS process was generated. Distinct from the conventional understanding about VLS growth process, it was found that both of the partial pressure of O_2 and total system pressure exhibited distinct effects on the final morphologies of deposited ZnO nanostructures. In our furnace system, the optimal condition for growing aligned ZnO nanorods was found to be 2% O_2 and 30 mbar system pressure at local deposition temperature of 880°C. The effect of catalyst has also been studied. It was found that a slight variation of the thickness of gold catalyst resulted in a significant change in the density of the aligned ZnO nanowires. This could be an effective and simple pathway to control nanowire density without using the sophisticated techniques such as catalyst patterning. The growth processes of ZnO nanowires on the AlGaN substrate has been studied based on the wetting behavior of gold catalyst on the substrate with or without source vapor. The growth can be classified into three categories: separated dots initiated growth, continuous layer initiated growth and scattered particle initiated growth. These discoveries provided a road map for large-scale, controlled synthesis of ZnO nanowires on both sapphire and nitride semiconductor substrates with the potential to meet the needs of practical applications and commercialization.

Practically, patterned or aligned 1D nanostructures can be potentially applied as sensor arrays, piezoelectric antenna arrays, optoelectronic devices, and interconnects. Furthermore, the bandgap of $Al_xGa_{1-x}N$, which can be either *n*- or *p*-type doped, is

tunable from 3.44 eV to 6.20 eV by changing the Al composition from 0 to 1. A bandgap tunable hetero-junction array of ZnO nanorods on a thin nitride film can thus be achieved making them an ideal candidate structure for light-emitting diode arrays. As a result, the photoluminescence property of the vertical aligned ZnO nanowires was examined to reveal the angular and substrate dependences. In addition to the optical property, an interesting electromechanical property was observed and studied. Due to the uneven electron distribution at the junction between semiconducting ZnO nanowire and gold tip, a self-attraction phenomenon was induced between vertical aligned ZnO nanowires under the illumination of electron beams. This discovery opened a new way to manipulate nanomaterials and control nanodevices and could be applied in electron beam, electric field or opto-electron related nano-switches and nano-sensors.

Further applications were developed by using the patterned and aligned ZnO nanowire array as a coating template for fabricating luminescent TiO_2/ZnO 2D PCs. The periodic structure showed a reflection peak close to the theoretically predicted bandgap region. The bandgap can also be tuned from IR to visible light wavelength region by varying the period of the PS sphere template. The technique is a self-assembly bottom-up process, which can be effectively and economically scaled up for large-sized 2D PC fabrication.

In general, this dissertation presented a systematic study on the low-cost self-assembly fabrication techniques for patterning functional nanostructures. In addition, some novel applications have also been investigated, such as a size-selector for nanoparticles, masks for nanolithography and templates for photonic crystals. However, patterning nanostructures through the low-cost self-assembly technique possesses much more potential in nano-device fabrication and integration. Beyond the work conducted in this dissertation, more sophisticated devices were recommended as a promising target of future research. Using the patterned TiO_2 nanobowl for high-efficient dye-sensitized solar cell and applying aligned nanowires for sensor arrays were carefully analyzed and

183

considered to be two achievable goals in near future. Due to the low cost and high efficiency, self-assembly techniques will eventually become the dominant fabrication method in future nanotechnology. The work presented in this dissertation may set a foundation for many industrial applications from controlled synthesis to nanomanufacturing.

REFERENCES

[1]   Alivisatos, A. P., Harris, A. L., Steigerwald, N. J. and Brus, L. E., J. Chem. Phys. 89, 4001 (1988).

[2]   Buffat, P. and Borel, J. P., Phys. Rev. A 13, 2287 (1976).

[3]   Wang, Z. L., Dekker Encyclopedia of Nanoscience and Nanotechnology 1773 (2004).

[4]   Lieber, C. M., MRS Bull. 28, 486 (2003).

[5]   Herman, M. A. and Sitter, H., *Molecular Beam Epitaxy: Fundamentals and Current Status* Sringer, Berlin (1996).

[6]   Zory Jr., P. S., *Quantum Well Lasers* Academic, San Diego (1993).

[7]   Alivisatos, A. P., MRS Bull. 2, 15 (1998).

[8]   Klimov, V. I., Mikhailovsky, A. A., Xu, S., Malko, A., Hollingsworth, J. A., Leatherdale, C. A., Eisler, H. K. and Bawendi, M. G., Science 314, 290 (2000).

[9]   Klein, D. L., Roth, R., Lim, A. K. L., Alivisatos, A. P. and McEuen, P. L., Nature 389, 699 (1997).

[10]   Colvin, V. L., Schlamp, M. C. and Alivisatos, A. P., Nature 370, 354 (1994).

[11]   Wang, Z. L., *Nanowires and Nanobelts: Materials, Properties and Devices* Kluwer Academic Publishers, Boston (2003).

[12]   Iijima, S., Nature 354, 56 (1991).

[13]   Dresselhaus, M. S., Dresselhaus, G. and Saito, R., Phys. Rev. B 45, 6234 (1992).

[14]   Mintmire, J. W., Dunlap, B. I. and White, C. T., Phys. Rev. Lett. 68, 631 (1992).

[15]   Zhang, X. F., Zhang, X. B., Tendeloo, G. V., Amelinckx, S., Beeck, M. O. d. and Landuyt, J. V., J. Crys. Growth 130, 368 (1993).

[16]   Iijima, S. and Ichihashi, T., Nature 363, 603 (1993).

[17]   Saito, R., Fujita, M., Dresselhaus, G. and Dresselhaus, M. S., Appl. Phys. Lett. 60, 2204 (1992).

[18]   Pan, Z. W., Xie, S. S., Chang, B. H., Wang, C. Y., Li, L., Liu, W., Zhou, W. Y. and Li, W. Z., Nature 394, 631 (1998).

[19]   Bandow, S., Hirahara, K., Hiraoka, T., Chen, G., Eklund, P. C. and Iijima, S., MRS Bull. 29, 260 (2004).

[20]   Hamada, N., Sawada, S. and Oshiyama, A., Phys. Rev. Lett. 68, 1579 (1992).

[21]   Haddon, R. C., Sippel, J., Rinzler, A. G. and Papadimitrakopoulos, F., MRS Bull. 29, 252 (2004).

[22]   Hu, J., Odom, T. W. and Lieber, C. M., Acc. Chem. res. 32, 435 (1999).

[23]   Xia, Y., Yang, P., Sun, Y., Wu, Y., Mayers, B., Gates, B., Yin, Y., Kim, F. and Yan, H., Adv. Mater. 15, 353 (2003).

[24]   Cui, Y., Lauhon, L. J. and Gudiksen, M. S., Appl. Phys. Lett. 78, 2214 (2001).

[25]   Xia, J. B. and Cheah, K. W., Phys. Rev. B 55, 15688~15693 (1997).

[26]   Ma, D. D. D., Lee, C. S., Au, F. C. K., Tong, S. Y. and Lee, S. T., Science 299, 1874 (2003).

[27]   Ma, D. D. D., Lee, C. S. and Lee, S. T., Appl. Phys. Lett. 79, 2468 (2001).

[28]   Pan, Z. W., Dai, Z. R. and Wang, Z. L., Science 291, 1947 (2001).

[29]   Dai, Z. R., Gole, J. L., Stout, J. D. and Wang, Z. L., J. Phys. Chem. B 106, 1274 (2001).

[30]   Dai, Z. R., Pan, Z. W. and Wang, Z. L., J. Phys. Chem. B. 106, 902 (2002).

[31]   Kong, X. Y. and Wang, Z. L., Solid State Commu. 128, 1 (2003).

[32]   Pan, Z. W., Dai, Z. R. and Wang, Z. L., Appl. Phys. Lett. 80, 309 (2002).

[33]   Li, X. L., Liu, J. F. and Li, Y. D., Appl. Phys. Lett. 81, 4832 (2002).

[34]   Li, Y. B., Bando, Y. and Sato, T., Chem. Phys. Lett. 359, 141 (2002).

[35]   Wen, S. G., Zhang, W. X. and Yang, S. H., Langmuir 19, 5898 (2003).

[36]   Fang, X. S., Ye, C. H., Peng, X. S., Wang, Y. H., Wu, Y. C. and Zhang, L. D., J. Mater. Chem. 13, 3040 (2003).

[37]   Ma, C., Moore, D., Li, J. and Wang, Z. L., Adv. Mater. 15, 228 (2003).

[38]   Ma, C., Ding, Y., Moore, D., Wang, X. D. and Wang, Z. L., J. Am. Chem. Soc. 126, 708 (2004).

[39] Wang, Z. L., Kong, X. Y. and Zuo, J. M., Phys. Rev. Lett. 91, 185502 (2003).

[40] Xiang, X., Cao, C. B. and Zhu, H., Solid State Commu. 126, 315 (2003).

[41] Seo, H. W., Bae, S. Y., Park, J., Yang, H., Kang, M., Kim, S., Park, J. C. and Lee, S. Y., Appl. Phys. Lett. 82, 3752 (2003).

[42] Wu, Q., Hu, Z., Wang, X. Z., Chen, Y. and Lu, Y. N., J. Phys. Chem. B 107, 9726 (2003).

[43] Wang, J. and Li, Y., Chem. Comm. 18, 2320 (2003).

[44] Shi, H. T., Qi, L. M., Ma, J. M., Cheng, H. M. and Zhu, B. Y., Adv. Mater. 15, 1647 (2003).

[45] Ronning, C., Gao, P. X., Ding, Y., Wang, Z. L. and Schwen, D., Appl. Phys. Lett. 84, 783 (2004).

[46] Kong, X. Y. and Wang, Z. L., Nano Lett. 3, 1625 (2003).

[47] Kong, X. Y., Ding, Y., Yang, R. S. and Wang, Z. L., Science 303, 1348 (2004).

[48] Arnold, S. M. and Kounce, S. E., J. Appl. Phys. 27, 964 (1956).

[49] Frank, F. C., Discuss. Faraday Soc. 5, 48 (1949).

[50] Sears, G. W., Acta Metall. 3, 361 (1955).

[51] Blakely, J. M. and Jackson, K. A., J. Chem. Phys. 37, 428 (1962).

[52] Dai, Z. R., Pan, Z. W. and Wang, Z. L., Adv. Func. Mater. 13, 9 (2003).

[53] Wagner, R. S. and Ellis, W. C., Appl. Phys. Lett. 4, 89 (1964).

[54] Morales, A. M. and Lieber, C. M., Science 279, 208 (1998).

[55] Huang, M. H., Mao, S., Feick, H., Yan, H., Wu, Y., Kind, H., Weber, E., Russo, R. and Yang, P., Science 292, 1897 (2001).

[56] Wu, Y. and Yang, P., J. Am. Chem. Soc. 123, 3165 (2001).

[57] Huang, M. H., Wu, Y., Feick, H., Tran, N., Weber, E. and Yang, P., Adv. Mater. 13, 113 (2001).

[58] Gudiksen, M. S., Wang, J. and Lieber, C. M., J. Phys. Chem. B 105, 4062 (2001).

[59] Frank, S., Poncharal, P., Wang, Z. L. and DeHeer, W. A., Science 280, 1744 (1998).

[60] Zhu, Y. W., Zhang, H. Z., Sun, X. C., Feng, S. Q., Xu, J., Zhao, Q., Xiang, B. and Wang, R. M., Appl. Phys. Lett. 83, 144 (2003).

[61] Gao, R. P., Wang, Z. L., Bai, Z. G., deHeer, W. A., Dai, L. M. and Gao, M., Phys. Rev. Letts. 85, 622 (2000).

[62] Wang, Z. L., Poncharal, P. and DeHeer, W. A., J. Phys. Chem. Solids 61, 1025 (2000).

[63] Poncharal, P., Wang, Z. L., Ugarte, D. and DeHeer, W. A., Science 283, 1513 (1999).

[64] Bai, X. D., Wang, E. G., Gao, P. and Wang, Z. L., Nano Lett. 3, 1147 (2003).

[65] Carlotti, G., Socino, G., Petri, A. and Verona, E., Appl. Phys. Lett. 51, 1889 (1987).

[66] Mao, S. X., Zhao, M. H., Wang, Z. L. and 993-995., Appl. Phys. Lett. 83, 993 (2003).

[67] Patolsky, F. and Lieber, C. M., Materials Today 8, 20 (2005).

[68] Arnold, M. S., Avouris, P., Pan, Z. W. and Wang, Z. L., J. Phys. Chem. B 107, 659 (2002).

[69] Avouris, P., Chem. Phys. 281, 429 (2002).

[70] McAlpine, M. C., Friedman, R. S., Jin, S., Lin, K., Wang, W. U. and Lieber, C. M., Nano Lett. 3, 1531 (2003).

[71] Cui, Y. and Lieber, C. M., Science 291, 851 (2001).

[72] Lauhon, L. J., Gudiksen, M. S., Wang, D. and Lieber, C. M., Nature 420, 57 (2002).

[73] Solomon, P. M., Annu. Rev. Mater. Sci. 30, 681 (2000).

[74] Hafeman, D. G., Science 240, 1182 (1988).

[75] Comini, E., Faglia, G., Sberveglieri, G., Pan, Z. W. and Wang, Z. L., Appl. Phys. Lett. 81, 1869 (2002).

[76] Cui, Y., Wei, Q., Park, H. and Lieber, C. M., Science 293, 1289 (2001).

[77] Hahm, J. and Lieber, C. M., Nano Lett. 4, 51 (2004).

[78] Alivisatos, A. P., Science 271, 933 (1996).

[79]   Wang, X. D., Ding, Y., Summers, C. J. and Wang, Z. L., J. Phys. Chem. B 108, 8773 (2004).

[80]   Law, M., Sirbuly, D. J., Johnson, J. C., Goldberger, J., Saykally, R. J. and Yang, P., Science 305, 1269 (2004).

[81]   Johnson, J. C., Choi, H. J., Knutsen, K. P., Schaller, R. D., Yang, P. and Saykally, R. J., Nat. Mater. 1, 106 (2002).

[82]   Agarwal, R., Barrelet, C. J. and Lieber, C. M., Nano Lett. 5, 917 (2005).

[83]   Vanheusden, K., Warren, W. L., Seager, C. H., Tallant, D. R., Voigt, J. A. and Gnade, B. E., J. Appl. Phys. 79, 7983 (1996).

[84]   Johnson, J. C., Yan, H., Yang, P. and Saykally, R. J., J. Phys. Chem. B 107, 8816 (2003).

[85]   AsifKhan, M., Olson, D. T., VanHove, J. M. and Kuznia, J. N., Appl. Phys. Lett. 58, 1515 (1991).

[86]   Bidnyk, S., Schmidt, T. J., Little, B. D. and Song, J. J., Appl. Phys. Lett. 74, 1 (1999).

[87]   Thomas, D. G. and Hopfield, J. J., Phys. Rev. 128, 2135 (1962).

[88]   Magde, D. and Mahr, H., Phys. Rev. Lett. 24, 890 (1970).

[89]   Colbow, K., Phys. ReV. 141, 742 (1966).

[90]   Liu, C., Zapien, J. A., Yao, Y., Meng, X., Lee, C. S., Fan, S., Lifshitz, Y. and Lee, S. T., Adv. Mater. 15, 838 (2003).

[91]   Choi, Y. C., Kim, W. S., Park, Y. S., Lee, S. M., Bae, D. J., Lee, Y. H., Park, G. S., Choi, W. B., Lee, N. S. and Kim, J. M., Adv. Mater. 12, 746 (2000).

[92]   Ma, C., Berta, Y. and Wang, Z. L., Solid State Commun. 129, 681 (2004).

[93]   Krumeich, F., Muhr, H. J., Niederberger, M., Bieri, F., Schnyder, B. and Nesper, R., J. Am. Chem. Soc. 121, 8324 (1999).

[94]   Huh, M., Kim, S., Ahn, J., Park, J. and Kim, B., NanoStruct. Mater. 11, 211 (1999).

[95]   Wang, X. D., Gao, P. X., Li, J., Summers, C. J. and Wang, Z. L., Adv. Mater. 14, 1732 (2002).

[96]   Hornebecq, V., Mastai, Y., Antonietti, M. and Polarz, S., Chem. Mater. 15, 3586 (2003).

[97]   Cooper, A. I., Adv. Mater. 15, 1049 (2003).

[98]   Takeuchi, S., Iwanaga, H. and Fujii, M., Philos. Mag. A 69, 1125 (1994).

[99]   Dai, Y., Zhang, Y., Wang, Z. L. and Solid State Commun. 2003, 629, Solid State Commun. 126, 629 (2003).

[100] Xu, X., Guo, C., Qi, Z., Liu, H., Xu, J., Shi, C., Chong, C., Huang, W., Zhou, Y. and Xu, C., Chem. Phys. Lett. 364, 57 (2002).

[101] Ji, Z. G., Kun, L., Song, Y. L. and Ye, Z. Z., J. Crystal Growth 255, 353 (2003).

[102] Yu, S. H. and Yoshimura, M., Adv. Mater. 14, 296 (2002).

[103] Wang, Y. W., Zhang, L. D., Liang, C. H., Wang, G. Z. and Peng, X. S., Chem. Phys. Letts. 357, 314 (2002).

[104] Haynes, C. L., McFarland, A. D., Smith, M. T., Hulteen, J. C. and Duyne, R. P. V., J. Phys. Chem. B 106, 1898 (2002).

[105] Hulteen, J. C. and Duyne, R. P. V., J. Vac. Sci. Technol. A 13, 1553 (1995).

[106] Veinot, J. G. C., Yan, H., Smith, S. M., Cui, J., Huang, Q. and Marks, T. J., Nano Lett. 2, 333 (2002).

[107] Rybczynski, J., Ebels, U. and Giersig, M., Colloids Surf. A 219, 1 (2003).

[108] Kempa, K., Kimball, B., Rybczynski, J., Huang, Z. P., Wu, P. F., Steeves, D., Sennett, M., Giersig, M., Rao, D. V. G. L. N., Carnahan, D. L., Wang, D. Z., Lao, J. Y., Li, W. Z. and Ren, Z. F., Nano Lett. 3, 13 (2003).

[109] Volokitin, Y., Sinzig, J., deJongh, L. J., Schmid, G., Vargaftik, M. N. and Moiseev, I. I., Nature 384, 621 (1996).

[110] Andres, R. P., Bielefeld, J. D., Henderson, J. I., Janes, D. B., Kolagunta, V. R., Kubiak, C. P., Mahoney, W. J. and Osifchin, R. G., Science 273, 1690 (1996).

[111] Wang, X. D., Lao, C. S., Graugnard, E., Summers, C. J. and Wang, Z. L., Nano Lett. 5, 1784 (2005).

[112] Wang, X. D., Graugnard, E., King, J. S., Wang, Z. L. and Summers, C. J., Nano Lett. 4, 2223 (2005).

[113] Suntola, T. and Simpson, M., *Atomic Layer Epitaxy* Chapman and Hall, (1990).

[114] Ritala, M. and Leskela, M., *Handbook of Thin Film Materials Vol. 1* Academic Press, (2002).

[115] Leskela, M. and Ritala, M., Thin Solid Films 409, 138 (2002).

[116] O'regan, B. and Grätzel, M., Nature 353, 737 (1991).

[117] Linsebigler, A. L., Lu, G. and Yates, J. T., Chem. Rev. 95, 735 (1995).

[118] King, J. S., Graugnard, E. and Summers, C. J., Adv. Mater. 17, 1010 (2005).

[119] Ma, T., Inoue, K., Yao, K., Noma, H., Shuji, T., Abe, E., Yu, J., Wang, X. and Zhang, B., J. Electronanl. Chem 537, 31 (2002).

[120] Kosiorek, A., Kandulski, W., Chudzinski, P., Kempa, K. and Giersig, M., Nano Lett. 4, 1359 (2004).

[121] Kosiorek, A., Kandulski, W., Glaczynska, H., Giersig, M. and Small 2005, Small 1, 439 (2005).

[122] Zhang, J., Wang, Z. L., Liu, J., Chen, S. and Liu, G. Y., *Self-Assembled Nanostructures* Kluwer Academic Publishers, (2002).

[123] Park, W. I. and Yi, G. C., Adv. Mater. 16, 87 (2004).

[124] Park, W. I., Yi, G. C., Kim, J. W. and Park, S. M., Appl. Phys. Lett. 82, 4358 (2003).

[125] Wang, Z. L., J. Phys.: Condens. Matter. 16, R829 (2004).

[126] Wang, Z. L., Materials Today 7, 26 (2004).

[127] Ozgur, U., Alivov, Y., Liu, C., Teke, A., Reshchikov, M. A., Dogan, S., Avrutin, V., Cho, S. J. and Morkoc, H., J. Appl. Phys. 98, 041301 (2005).

[128] Duan, X. and Lieber, C. M., Adv. Mater. 12, 298 (2000).

[129] Park, W. I., Kim, D. H., Jung, S. W. and Yi, G. C., 80, 4232 (2002).

[130] Choy, J. H., Jang, E. S., Won, J. H., Chung, J. H., Jang, D. J. and Kim, Y. W., Adv. Mater. 15, 1911 (2003).

[131] Wang, X. D., Summers, C. J. and Wang, Z. L., Nano Lett. 4, 423 (2004).

[132] Wang, X. D., Song, J. H., Li, P., Ryou, J. H., Dupius, R. D., Summers, C. J. and Wang, Z. L., J. Am. Chem. Soc. 127, 7920 (2005).

[133] Zhu, T. G., Chowdhury, U., Wong, M. M., Denyszyn, J. C. and Dupuis, R. D., J. Crys. Growth 248, 548 (2003).

[134] Fan, H. J., Fleischer, F., Lee, W., Nielsch, K., Scholz, R., Zacharias, M., Gösele, U., Dadgar, A. and Krost, A., Superlattices Microst. 36, 95 (2004).

[135] Yang, P., Yan, H., Mao, S., Russo, R., Johnson, J., Saykally, R., Morris, N., Pham, J., He, R. and Choi, H., Adv. Func. Mater. 12, 323 (2002).

[136] Lee, J. S., Kang, M. I., Kim, S., Lee, M. S. and Lee, Y. K., J. Cryst. Growth 249, 201 (2003).

[137] Hg, H. T., Chem, B., Li, J., Han, J., Meyyappan, M., Wu, J., Li, S. X. and Haller, E. E., Appl. Phys. Lett. 82, 2023 (2003).

[138] Song, J. H., Wang, X. D., Riedo, E. and Wang, Z. L., J. Phys. Chem. B 109, 9869 (2005).

[139] Wang, X. D., Song, J. H., Summers, C. J., Ryou, J. H., Li, P., Dupuis, R. D. and Wang, Z. L., Submitted (2005).

[140] Johnson, J. C., Yan, H., Yang, P. and Saykally, R. J., J. Phys. Chem. B 107, 8816 (2003).

[141] Wang, X. D., Summers, C. J. and Wang, Z. L., Appl. Phys. Lett. 86, 013111 (2005).

[142] Krauss, T. F., De La Rue, R. M. and Brand, S., Nature 383, 699 (1996).

[143] Park, W. and Summers, C. J., Appl. Phys. Lett. 84, 2013 (2004).

[144] Kosaka, H., Kawashima, T., Tomita, A., Notomi, M., Tamamura, T., Sato, T. and Kawakami, S., Rhys. Rev. B 58, R10096 (1998).

[145] Hirayama, H., Hamano, T. and Aoyagi, Y., Appl. Phys. Lett. 69, 791 (1996).

[146] Joannopoulos, J. D., Villeneuve, P. R. and Fan, S., Nature 386, 143 (1997).

[147] Chow, E., Lin, S. Y., Johnson, S. G., Villeneuve, P. R., Joannopoulos, J. D., Wendt, J. R., Vawter, G. A., Zubrzycki, W., Hou, H. and Alleman, A., Nature 407, 983 (2000).

[148] Marcì, G., Augugliaro, V., López-Muñoz, M. J., Martín, C., Palmisano, L., Rives, V., Schiavello, M., Tilley, R. J. D. and Venezia, A. M., J. Phys. Chem. B 105, 1026 (2001).

[149] Johnson, S. G. and Joannopoulos, J. D., Opt. Exp. 8, 173 (2001).

[150] Astratov, V. N., Whittaker, D. M., Culshaw, I. S., Stevenson, R. M., Skolnick, M. S., Krauss, T. F. and De La Rue, P. M., Phys. Rev. B 60, R16255 (1999).

[151] Coquillat, D., Torres, J., Peyrade, D., Legros, R., Lascaray, J. P., Le Vassor d'Yerville, M., Centeno, E., Cassagne, D., Albert, J. P., Chen, Y. and De La Rue, R. M., Opt. Exp. 12, 1097 (2004).

[152]   Ginger, D. S. and Greenham, N. C., Synth. Met. 124, 117 (2001).

[153]   Law, M., Greene, L. E., Johnson, J. C., Saykally, R. and Yang, P., Nat. Mater. 4, 455 (2005).